University of Southampton

Faculty of Natural and Environmental Sciences

Measurements and Concepts in Marine Carbonate Chemistry

Matthew Paul Humphreys, MA, MSci

Thesis for the degree of Doctor of Philosophy

March 2015

UNIVERSITY OF SOUTHAMPTON

ABSTRACT

FACULTY OF NATURAL AND ENVIRONMENTAL SCIENCES

Ocean and Earth Science

Doctor of Philosophy

MEASUREMENTS AND CONCEPTS IN MARINE CARBONATE CHEMISTRY

Matthew Paul Humphreys, MA, MSci

The marine carbonate chemistry system is the reactions and dynamic equilibria in seawater that involve dissolved carbon dioxide (CO_2) and the deprotonated forms of carbonic acid, which are bicarbonate ions and carbonate ions. This system affects other marine biogeochemical cycles and ecosystems through its strong influence on seawater pH. Currently, a rapid chemical perturbation is being driven by the accumulation of anthropogenic CO_2 in the ocean, which has taken up a significant fraction of the CO_2 emitted to the atmosphere by fossil fuel burning, cement manufacture and land-use change since pre-industrial times. To predict the future consequences, it is first essential to be able to accurately measure the present state of the system, and to understand how it operates. To contribute to these goals, I have firstly made new developments to the measurement techniques for two key system variables, namely total alkalinity and the stable isotopic composition of dissolved inorganic carbon. Secondly, I have combined results from recent research cruises along a hydrographic transect in the Northeast Atlantic with historical datasets in order to quantify the rate at which anthropogenic CO_2 has accumulated in the interior ocean over the past three decades, demonstrating that the regional accumulation rate is greater than the global average. I have used model output to assess uncertainties in these results that are caused by spatiotemporal heterogeneity in the distribution of observations. Thirdly, I have carried out a theoretical investigation into the influence of marine calcifying phytoplankton, like coccolithophores, on air-sea CO_2 exchange. I have shown that these organisms can behave either as CO_2 sources or sinks depending upon their relative rates of calcification and autotrophic production, their nutrient uptake stoichiometry, and local seawater conditions. Finally, I provide suggestions for developments to the work presented in this thesis that might help to overcome some challenges that are likely to face this field of research in the future.

Contents

List of tables

List of figures

Declaration of authorship

I, Matthew Paul Humphreys, declare that this thesis and the work presented in it are my own and has been generated by me as the result of my own original research.

Measurements and Concepts in Marine Carbonate Chemistry

I confirm that:

1. This work was done wholly or mainly while in candidature for a research degree at this University;
2. Where any part of this thesis has previously been submitted for a degree or any other qualification at this University or any other institution, this has been clearly stated;
3. Where I have consulted the published work of others, this is always clearly attributed;
4. Where I have quoted from the work of others, the source is always given. With the exception of such quotations, this thesis is entirely my own work;
5. I have acknowledged all main sources of help;
6. Where the thesis is based on work done by myself jointly with others, I have made clear exactly what was done by others and what I have contributed myself;
7. Part of this work has been published as:

Humphreys, M.P., Achterberg, E.P., Griffiths, A.M., McDonald, A., Boyce, A.J., 2015. Measurements of the stable isotope composition of dissolved inorganic carbon in the Northeastern Atlantic and Nordic Seas during summer 2012. Earth Syst. Sci. Data Discuss. 8, 57–82. doi:10.5194/essdd-8-57-2015

Signed:.....

Date:.....

Acknowledgements

The work presented in this thesis has been inspired and improved by a veritable host of colleagues and friends. In no particular order, special recognition must be given to:

Eric Achterberg, Toby Tyrrell and Kevin Oliver, for their supervision of my research, and for the incredible opportunities and experiences which my project has delivered;

Andrew Yool and Dieter Wolf-Gladrow, for taking the time to read and engage with my thesis, and for their insightful questions and suggestions that have improved it;

Jen Clarke, Sara Cregeen, James Morris, Mario Esposito and other assorted office-mates through the years, for providing an engaging habitat in which to work;

Alex Griffiths, for his pilot study on the Extended Ellett Line, and for his unflinching acceptance of an endless stream of delegated logistical tribulations;

Chris Daniels, for asking the titular question of Chapter 5, and for his valuable contributions to the development of its answer;

Matt Couldrey, Rosie Sheward, Penny Holliday, Victoire Rérolle, Alex Poulton and Sam Gibbs, for equipping me with their advanced understanding of subjects beyond the scope of my own knowledge, and for providing generous criticisms of my writing;

Eithne Tynan, Mariana Ribas-Ribas and the other scientists and crew on the research cruises in which I participated, for sharing both in the stress and in the adventure;

Alison McDonald and Adrian Boyce, for their laboratory expertise;

Becky Hampshire, Jan-Lukas Menzel Barraqueta and Harriet Compton, for helping me begin to learn how to supervise others;

Cynthia Brewer and the ColorBrewer team, whose colour palettes grace many of my illustrations;

The scientific denizens of Twitter, a cascade of stimulation;

Dave Milodowski, Marie Cavitte, Jayne Ede and Richard Armitage, for proofreading;

Kat Smith, for her support and encouragement, for sticking around, and for sometimes feigning interest in seawater carbonate chemistry;

And my family, for everything.

Definitions and abbreviations

α	Coefficient for stoichiometric ratio of nitrogen in POM
β	Coefficient for stoichiometric ratio of carbon in POM
γ	Coefficient for stoichiometric oxygen release during POM formation
$\delta^{13}\mathrm{C}$	Stable isotopic composition of carbon
$\delta^{13}\mathrm{C_{DIC}}$	Stable isotopic composition of dissolved inorganic carbon
$\delta^{13}\mathrm{C_{POC}}$	Stable isotopic composition of particulate organic carbon
δ_{corr}	Measured $\delta^{13}\mathrm{C}$ after linearity correction
δ_{meas}	Measured $\delta^{13}\mathrm{C}$ before linearity correction
ΔC^*	Tracer for anthropogenic component of DIC
$\Delta p\mathrm{CO_2}$	Difference between $p\mathrm{CO_2^{sw}}$ and $p\mathrm{CO_2^{atm}}$
$\Delta\mathrm{RC}$	Ratio between $\delta^{13}\mathrm{C_{DIC}}$ and DIC change after anthropogenic CO_2 addition
ΔS	Difference between production slope and isocap slope
ζ	Coefficient for stoichiometric ratio of hydrogen in POM
η	Coefficient for stoichiometric ratio of sulfate in POM
θ	Coefficient for stoichiometric ratio of phosphorus in POM
λ	Coefficient for stoichiometric water uptake during POM formation
μ_a	Dilution correction factor during acidimetric seawater titration
σ	A specific standard deviation value
σ_0	Potential density at sea surface pressure
${\sigma_0}^{\mathrm{A}}$	An example σ_0 layer
${\sigma_0}^{\mathrm{B1}}$	Part of an example σ_0 layer
${\sigma_0}^{\mathrm{B2}}$	Part of an example σ_0 layer
φ	Coefficient for stoichiometric ratio of oxygen in POM
ψ	Released CO_2:precipitated carbonate ratio during calcification
δ_{A}	Anthropogenic component of $\delta^{13}\mathrm{C_{DIC}}$
δ_{R}	Remineralisation component of $\delta^{13}\mathrm{C_{DIC}}$
a	Coefficient for equation for linear approximation of isocap slope
A	Peak area during $\delta^{13}\mathrm{C}$ measurements
A_0	Initial estimate of TA in mass units during acidimetric seawater titration

A_i	Estimate of TA in mass units after iteration *i* of Gran plot calculations
A_{xs}	Cross-sectional area between two potential density layers
AOU	Apparent oxygen utilisation
b	Coefficient for equation for linear approximation of isocap slope
c	Coefficient for equation for linear approximation of isocap slope
C	Certified value of δ^{13}C standards relative to V-PDB
CA	SUERC-ICSF internal δ^{13}C standard
CARINA	Carbon in Atlantic Ocean data product
C_{dil}	Correction factor for dilution by mercuric chloride
CRM	Certified reference material
C_{T}	Dissolved inorganic carbon (interchangeable with DIC)
CTD	Instrument to determine seawater conductivity, temperature and depth
d	Coefficient for equation for linear approximation of isocap slope
DIC	Dissolved inorganic carbon (interchangeable with C_{T})
$\mathrm{DIC}_{\mathrm{anth}}$	Anthropogenic component of DIC
$\mathrm{DIC}_{\mathrm{carb}}$	Carbonate pump component of DIC
$\mathrm{DIC}_{\mathrm{soft}}$	Soft tissue pump component of DIC
DMS	Dimethyl sulfide
DMSP	Dimethylsulfoniopropionate
DO	Dissolved oxygen
E_a	Electric potential across analyte during acidimetric seawater titration
$E°$	Standard electrode potential during acidimetric seawater titration
$E°_0$	Initial estimate of $E°$
$E°_i$	Estimate of $E°$ after iteration *i* of Gran plot calculations
EEL	Extended Ellett Line hydrographic transect
eMLR	Extended multi-linear regression
F	Faraday constant
FAA	Full Anthropogenic Annual subset of model output
F_{CO2}	Net sea-to-air flux of carbon dioxide
$f\mathrm{CO}_2^{\mathrm{atm}}$	Atmospheric fugacity of carbon dioxide
$f\mathrm{CO}_2^{\mathrm{sw}}$	Seawater fugacity of carbon dioxide

F_T	Dissolved inorganic fluorine
g	Linearity correction gradient for $\delta^{13}C$ measurements
g_a	Initial estimate for Gran function during acidimetric seawater titration
G_a	Gran function during acidimetric seawater titration
GLODAP	Global Ocean Data Analysis Project data product
IB	Iceland Basin
IPCC	Intergovernmental Panel on Climate Change
ISFET	Ion sensitive field effect transistor
k_0	Henry's constant for carbon dioxide
k_1	First stoichiometric dissociation constant of carbonic acid
k_2	Second stoichiometric dissociation constant of carbonic acid
k_B	Stoichiometric dissociation constant of boric acid
k_F	Stoichiometric dissociation constant of hydrofluoric acid
k_{P1}	First stoichiometric dissociation constant of phosphoric acid
k_{P2}	First stoichiometric dissociation constant of phosphoric acid
k_{P3}	Third stoichiometric dissociation constant of phosphoric acid
k_S	Second stoichiometric dissociation constant of sulfuric acid
k_w	Stoichiometric dissociation constant of water
L	Linearity-corrected $\delta^{13}C$ measurements prior to V-PDB calibration
$L(\sigma_0)$	Horizontal distance of above-seafloor idealised EEL route at potential density layer σ_0
$L(\mathrm{EEL})$	Total length of idealised EEL route
L_a	Correction function for CO_2 loss during acidimetric seawater titration
LDEO	Lamont-Doherty Earth Observatory
LGM	Last Glacial Maximum
m_a	Mass of acid titrant added during acidimetric seawater titration
MAB	SUERC-ICSF internal $\delta^{13}C$ standard
MATLAB	A numerical computing environment and programming language developed by MathWorks (Natick, USA)
MEDUSA	An intermediate complexity biogeochemical-ecosystem model
M_{sw}	Mass of seawater titrated during acidimetric seawater titration
N	Coefficient in Nernst equation

NA	SUERC-ICSF internal $\delta^{13}C$ standard
NAO	North Atlantic Oscillation
NAOI	North Atlantic Oscillation Index
NEMO	Nucleus for European Modelling of the Ocean
p	Coefficient for calibration of $\delta^{13}C$ to V-PDB
P	Pressure
PACIFICA	Pacific Ocean Interior Carbon data product
pCO_2	Partial pressure of carbon dioxide
pCO_2^{atm}	Atmospheric partial pressure of carbon dioxide
pCO_2^{sw}	Seawater partial pressure of carbon dioxide
PETM	Palaeocene-Eocene Thermal Maximum
pH	Free scale pH
PIC	Particulate inorganic carbon
POC	Particulate organic carbon
POM	Particulate organic matter
PON	Particulate organic nitrogen
POP	Particulate organic phosphorus
POS	Particulate organic sulfur
P_T	Dissolved inorganic phosphorus (interchangeable with TPO_4)
q	Coefficient for calibration of $\delta^{13}C$ to V-PDB
r	Coefficient for calibration of $\delta^{13}C$ to V-PDB
R	Ideal gas constant
$R_{C/O2}$	Stoichiometric ratio of carbon to oxygen in particulate organic matter
R_I	Isocap ratio
$R_{N/O2}$	Stoichiometric ratio of nitrogen to oxygen in particulate organic matter
R_P	Production ratio
RP	Rockall Plateau
RRS	Royal Research Ship
RT	Rockall Trough
S	Salinity
SAM	Subsampled Anthropogenic Monthly subset of model output

SCM	Subsampled Control Monthly subset of model output
SD	Standard deviation
S_{I}	Exact isocap slope
$S_{\mathrm{I}}^{\mathrm{lin}}$	Linear approximation to isocap slope
SOCAT	Surface Ocean CO_2 Atlas data product
S_{P}	Production slope
SPGI	Subpolar Gyre Index
SST	Sea surface temperature
S_{T}	Dissolved inorganic sulfur (interchangeable with TSO_4)
SUERC-ICSF	Scottish Universities Environmental Research Centre – Isotope Community Support Facility
t	Time
T	Seawater temperature
TA	Total alkalinity
TAA	Transect Anthropogenic Annual subset of model output
TA_{C}	Carbonate alkalinity
TA_{HgCl2}	Total alkalinity prior to correction for dilution by mercuric chloride
TB	Dissolved inorganic boron
TPO_4	Dissolved inorganic phosphorus (interchangeable with P_{T})
Tr	Gas transfer coefficient for air-sea CO_2 exchange
TSO_4	Dissolved inorganic sulfur (interchangeable with S_{T})
TTD	Transient Tracer Distribution
TTO-NAS	Transient Tracers in the Ocean – North Atlantic Study
UKOA	United Kingdom Ocean Acidification research programme
V_{HgCl2}	Volume of mercuric chloride solution added to a seawater sample
V_{sample}	Volume of a seawater sample
V-PDB	Vienna Pee Dee Belemnite international standard for $\delta^{13}C$
VINDTA	Versatile Instrument for the Determination of Total inorganic carbon and titration Alkalinity
X	Part of function for TA in terms of H^+ and aqueous CO_2 concentrations
Y	Part of function for TA in terms of H^+ and aqueous CO_2 concentrations
z	Correction factor for CO_2 loss during acidimetric seawater titration

$z(\sigma_0)$	Mean depth of potential density layer σ_0
Z	Part of function for TA in terms of H^+ and aqueous CO_2 concentrations

1

Introduction

Abstract

This chapter provides an overview of the main chemical species involved in the marine carbonate chemistry system and the reactions that occur between them. This system is changing at a rate that is perhaps unprecedented because of oceanic uptake of a significant fraction of all anthropogenic carbon dioxide emissions to the atmosphere, and this has many potential repercussions for marine biogeochemical cycles and ecosystems. There is a suite of system variables which can be measured using a variety of different techniques, and from values for any two of these the variables all of the others can be calculated. The results of many research programmes in recent decades are available in several quality-controlled compilations, which can be used to provide context for new studies and reveal long-term changes. Such analyses can be augmented using output from ocean general circulation models that resolve biogeochemical cycles. These variables, measurement techniques and data archives are briefly summarised here to provide context for the rest of the thesis, which is outlined at the end of this introductory chapter.

1.1 Seawater carbonate chemistry

Observations of the presence of carbon dioxide (CO_2) dissolved in seawater have been made for almost 200 years (Marcet, 1822), and its solution chemistry has been rigorously investigated during the intervening time such that its thermodynamics and kinetics are now well-understood (Zeebe and Wolf-Gladrow, 2001; Millero, 2007). The marine carbonate chemistry system can be described by the dynamic equilibria:

Equation 1.1 $$CO_{2(aq)} + H_2O \overset{k_1}{\rightleftharpoons} HCO_3^- + H^+ \overset{k_2}{\rightleftharpoons} CO_3^{2-} + 2H^+$$

where HCO_3^- and CO_3^{2-} are bicarbonate and carbonate ions respectively, and H^+ really represents the hydronium ion (H_3O^+). The sum of the aqueous CO_2, HCO_3^- and CO_3^{2-} concentrations is called dissolved inorganic carbon (DIC):

Equation 1.2 $$DIC = [CO_2] + [HCO_3^-] + [CO_3^{2-}]$$

where the square brackets here and hereafter denote the molality of the enclosed species in seawater solution. The concentration of undissociated carbonic acid (H_2CO_3) is completely negligible for all practical purposes (Zeebe and Wolf-Gladrow, 2001). In typical present-day surface ocean seawater, the stoichiometric equilibrium constants k_1 and k_2 have pk_a values of *circa* 6 and 9 respectively (Lueker et al., 2000) while the pH is about 8.1 (Takahashi et al., 2014a). Therefore HCO_3^- is the dominant species, forming about 90 % of DIC, while CO_3^{2-} and dissolved CO_2 make up about 10 % and less than 1 % respectively (Figure 1.1). The high pH and small contribution of aqueous CO_2 to DIC are possible because of seawater's total alkalinity (TA). This is defined as the excess of proton acceptors over proton donors during an acidimetric titration of seawater to a pH of 4.5 (Dickson, 1981; Wolf-Gladrow et al., 2007):

Equation 1.3
$$TA = [HCO_3^-] + 2[CO_3^{2-}] + [B(OH)_4^-] + [OH^-] + [HPO_4^{2-}] + 2[PO_4^{3-}] + [SiO(OH)_3^-] + [HS^-] + 2[S^{2-}] + [NH_3] - [H^+] - [HSO_4^-] - [HF]$$

Additional protolytes in the form of various dissolved organic compounds may also exist in seawater and also need to be taken into account when using Equation 1.3 (Bradshaw and Brewer, 1988; Hernández-Ayón et al., 2007; Muller and Bleie, 2008; Kim and Lee, 2009), although the concentrations and pk_a values which these compounds might have presently remain poorly-constrained by the measurements that are routinely carried out.

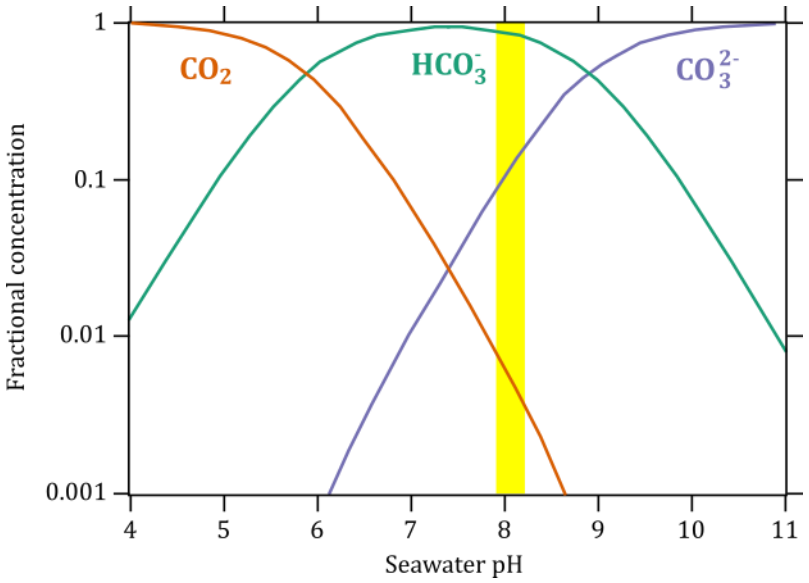

Figure 1.1. Schematic Bjerrum plot of the relationship between seawater pH and the relative concentrations of aqueous carbon dioxide (CO_2, orange), bicarbonate ion (HCO_3^-, green) and carbonate ion (CO_3^{2-}, violet). Typical surface ocean seawater pH at the present day is between about 7.9 and 8.2 (Takahashi et al., 2014a), as indicated by the vertical yellow bar. Note the logarithmic scale on the vertical axis. Re-drawn from Raven et al. (2005).

The component of TA that consists of bicarbonate and carbonate ions is called the carbonate alkalinity (TA_C):

Equation 1.4 $$TA_C = [HCO_3^-] + 2[CO_3^{2-}]$$

Seawater TA_C typically constitutes about 95 % of the TA. The TA_C can be estimated from TA by subtracting the measured or estimated concentrations of all of the other chemical species in Equation 1.3. The carbonate system therefore can be described by six variables – DIC, TA_C, $[CO_2]$, $[HCO_3^-]$, $[CO_3^{2-}]$ and pH – which are related to each other by four equations – Equations 1.2, 1.4, and the equilibrium conditions for Equation 1.1:

Equation 1.5

$$k_1 = \frac{[HCO_3^-][H^+]}{[CO_2]}$$

Equation 1.6

$$k_2 = \frac{[CO_3^{2-}][H^+]}{[HCO_3^-]}$$

The $[H^+]$ is usually reported using a pH scale, which is logarithmic, instead of as a concentration. The scale can be defined in several different ways. In marine chemistry, the simplest version that is commonly used is the 'Free' scale (Equation 1.7). In practice, other dissolved species can interfere with measurements of $[H^+]$, in particular bisulfate ions (HSO_4^-) and hydrogen fluoride (HF). The simplest way to account for the effect of these species is to include them in the definition of pH, and the 'Total' (Equation 1.8) and 'Seawater' (SWS, Equation 1.9) pH scales have been designed to this end.

Equation 1.7 $$pH_{Free} = -\log_{10}([H^+])$$

Equation 1.8 $$pH_{Total} = -\log_{10}([H^+] + [HSO_4^-])$$

Equation 1.9 $$pH_{SWS} = -\log_{10}([H^+] + [HSO_4^-] + [HF])$$

Once values for any two of the six variables are known, these four equations can be solved and thus the other four unknown variables evaluated (Zeebe and Wolf-Gladrow, 2001). The stoichiometric equilibrium constants k_1 and k_2 can be estimated as functions of temperature and salinity (e.g. Mehrbach et al., 1973; Dickson and Millero, 1987; Lueker et al., 2000). This calculation assumes that the system is in thermodynamic equilibrium, which should be valid for timescales longer than a few seconds (Zeebe and Wolf-Gladrow, 2001).

Exchange of CO_2 between the atmosphere and ocean is governed by the difference between the atmospheric and seawater partial pressures of CO_2 (pCO_2^{atm} and pCO_2^{sw} respectively). The pCO_2^{sw} is the partial pressure of CO_2 that would be found in air in equilibrium with a given parcel of seawater. It is directly proportional to $[CO_2]$:

Equation 1.10

$$pCO_2^{sw} = \frac{[CO_2]}{k_0}$$

where k_0 is Henry's constant for CO_2, which can be estimated as a function of seawater temperature and salinity (Weiss, 1974). The net direction of sea-to-air transfer of CO_2 is controlled by the sign of the difference between pCO_2^{atm} and pCO_2^{sw} (ΔpCO_2):

Equation 1.11 $$F_{CO2} = Tr \cdot (pCO_2^{sw} - pCO_2^{atm}) = Tr \cdot \Delta pCO_2$$

where F_{CO2} is the net CO_2 flux and Tr is a gas transfer coefficient. This coefficient is thought to have a power law relationship with the wind speed near the sea surface, although this is very difficult to constrain especially at higher wind speeds, and consequently a variety of formulations exist (Wanninkhof, 1992). It is also influenced by seawater temperature due to the temperature-dependence of both the Schmidt number – which is the ratio of viscosity to diffusivity – and CO_2 solubility (i.e. k_0) (e.g. Wanninkhof, 1992; Takahashi et al., 2009). From Equation 1.11, when pCO_2^{sw} is greater than pCO_2^{atm}, ΔpCO_2 is positive, and there is net evasion of CO_2 from the sea into the air; when pCO_2^{atm} is the greater, ΔpCO_2 is negative, and the sea takes up atmospheric CO_2. These fluxes are usually small – perturbations from air-sea CO_2 equilibrium are reversed with a typical *e*-folding time of about 240 days (Zeebe and Wolf-Gladrow, 2001, pp. 80–81) – compared to the rate at which other processes can affect ΔpCO_2, for example seasonal changes in seawater temperature or biological uptake of DIC, so most of the surface ocean has non-zero ΔpCO_2 and is not in equilibrium with pCO_2^{atm}. Nevertheless, the global mean of ΔpCO_2 is close to zero, but slightly negative owing to the ongoing anthropogenic increase in pCO_2^{atm} (Takahashi et al., 2009).

An important caveat is that for equilibrium calculations, the fugacity of CO_2 (fCO_2^{atm} and fCO_2^{sw}) should be used instead of its partial pressure; pCO_2^{sw} in Equation 1.10 is really fCO_2^{sw}. The fugacity takes into account deviation from the behaviour of an ideal gas; it is the partial pressure of a theoretical ideal gas with the same chemical potential as the actual gaseous CO_2. Numerically, the difference between the two is very small, with fCO_2^{sw} typically about 0.3 % smaller than pCO_2^{sw} (Zeebe and Wolf-Gladrow, 2001). This small offset makes no difference to any of the conclusions presented in this thesis, so the more widely-familiar concept of pCO_2^{sw} is used throughout.

The stable isotopic composition of oceanic DIC, specifically the ratio of carbon-13 to carbon-12 in DIC normalised to a reference standard ($\delta^{13}C_{DIC}$), is primarily controlled by air-sea gas exchange, temperature, and biological utilisation of DIC (Lynch-Stieglitz et al., 1995). Where there is net evasion of CO_2 from the surface ocean into the atmosphere, transfer of CO_2 containing the lighter carbon-12 isotope is kinetically favoured, leaving the seawater with higher $\delta^{13}C_{DIC}$. Where the net transfer is air-to-sea, seawater $\delta^{13}C_{DIC}$ declines because atmospheric CO_2 has a lighter isotopic composition than seawater DIC. Greater equilibrium fractionation between the atmosphere and ocean is favoured by colder conditions, so temperature

modulates the strength of the air-sea gas exchange effect on $\delta^{13}C_{DIC}$. From a biological perspective, autotrophic organisms in the surface ocean convert DIC into particulate organic carbon (POC), preferentially using carbon-12 through kinetic fractionation. The $\delta^{13}C_{DIC}$ in the surrounding seawater is therefore increased, while the isotopic composition of POC ($\delta^{13}C_{POC}$) is relatively light. Below the surface mixed layer, $\delta^{13}C_{DIC}$ is then reduced by remineralisation of exported POC with low $\delta^{13}C_{POC}$. In the global surface ocean, the air-sea gas exchange and biology typically affect $\delta^{13}C_{DIC}$ in an opposite sense to each other, resulting in a complex pattern in is distribution with a small range (Gruber et al., 1999). The timescale for equilibration of $\delta^{13}C_{DIC}$ with atmospheric CO_2 is an order of magnitude longer than that for DIC itself (Lynch-Stieglitz et al., 1995; McNeil et al., 2001a).

One key phenomenon arising from its chemical interactions in seawater solution is that CO_2 is unique amongst Earth's atmospheric gases in its partitioning between the atmosphere and ocean: as a total integrated inventory, the latter contains over 50 times as much carbon in DIC as the former does in CO_2 (Falkowski et al., 2000). If aqueous CO_2 did not react to form HCO_3^- and CO_3^{2-}, and pCO_2^{atm} remained at its present-day value, the ocean DIC inventory would be reduced to under 1 % of its current size, as under 1 % of DIC is aqueous CO_2. Alternatively, if all of the carbon currently stored in the ocean as HCO_3^- and CO_3^{2-} were returned to the atmosphere, pCO_2^{atm} would be many times greater than at the present day. This is exacerbated by the high solubility of CO_2 in water relative to other, non-polar atmospheric gases like oxygen and nitrogen. Considering the concern about the climatic consequences of a possible doubling or tripling of pCO_2^{atm} later in this century (IPCC, 2013), the profound influence that the inconspicuous dynamic equilibria in Equation 1.1 have upon the Earth surface system as a whole cannot be overstated.

1.2 Anthropogenic CO_2 emissions

The marine carbonate chemistry system is currently undergoing significant change. Anthropogenic emissions of CO_2 to the atmosphere, for example from burning fossil fuels (Andres et al., 2012), are responsible for an increase in pCO_2^{atm} (Francey et al., 2013; Raupach et al., 2013) to about 400 µatm, from its pre-industrial level of about 280 µatm (Ahn et al., 2012). This has a range of heavily-studied potential consequences for global climate (IPCC, 2013). Even after anthropogenic emissions cease, the pCO_2^{atm} is likely remain elevated above pre-industrial levels for tens of thousands of years (Archer, 2005).

The global ocean has mitigated the climatic implications by providing a sink for up to half of all anthropogenic CO_2 emissions in the past two centuries (Sabine et al., 2004; Khatiwala et al., 2009), and it continues to sequester on average about a quarter of these emissions each year (Manning and Keeling, 2006; Le Quéré et al., 2009). Oceanic CO_2 uptake causes a decline in pH, which is commonly known as ocean acidification, and which is accompanied by a decline in the carbonate ion concentration (a shift to the left in Figure 1.1). This is concentrated in the surface ocean and will persist for centuries after anthropogenic CO_2 emissions cease (Caldeira and Wickett, 2003), eventually being at least partly reversed by natural dissolution of carbonate sediments (Feely et al., 2004; Morse et al., 2007). The biological impacts that decreased pH may have in the intervening time are poorly understood; experiments have not found consistent responses between different species (Doney et al., 2009). The uncertainty in some species' responses is perhaps related to the conflict that while extra CO_2 might be expected to benefit primary production as a resource for photosynthesis, the simultaneous lower seawater pH may induce adverse energetic costs associated with internal pH regulation, particularly for calcifying organisms (Gaylord et al., 2015). Changes in the interactions between species in an ecosystem context and consequently community compositions are extremely difficult to predict, but are likely to be at least as important as direct physiological effects on individual species (Gaylord et al., 2015). These concerns are not purely academic; detrimental effects on the health and survival of some key species like oysters could also have significant economic consequences (Ekstrom et al., 2015). Changes in pH may affect the bioavailability of trace elements such as iron (Shi et al., 2010), and can also have even more obscure (to the marine chemist, at least) effects such as olfactory and auditory impairment in marine animals that causes changes in their behaviour (Simpson et al., 2011; Leduc et

al., 2013; Munday et al., 2014), and decreases in interior ocean sound absorption (Hester et al., 2008; Ilyina et al., 2010).

Chemically, the buffer capacity of seawater to take up atmospheric CO_2 is reduced at lower pH and at higher temperatures (Frankignoulle, 1994; Egleston et al., 2010), so on decadal timescales as pCO_2^{atm} continues to grow a decreasing fraction of it will be taken up into the ocean. On longer timescales (of several hundred thousand years), processes including dissolution of marine carbonate sediments and terrestrial silicate weathering will act as negative feedbacks, reducing pCO_2^{atm} back towards pre-industrial levels (Archer, 2005; Colbourn et al., 2015). To predict the size of the oceanic CO_2 sink into the future, it is therefore essential to first understand its distribution at the present day. Several methods exist for indirectly measuring the amount of DIC with an anthropogenic origin (DIC_{anth}) stored in the global ocean, as reviewed by Wallace (1995) and more recently by Sabine and Tanhua (2010). The earliest evaluations were performed in the late 1970s using a 'back-calculation' technique (Brewer, 1978; Chen and Millero, 1979). Back-calculation involves correcting present-day measurements of DIC in the interior ocean for changes resulting from dissolution of carbonate minerals and organic matter; the remaining excess in DIC over a theoretical 'preformed' DIC value, representing pre-industrial surface conditions in ventilation regions, is DIC_{anth}. However, the accuracy and precision of DIC and other measurements at the time this method was introduced and the uncertainties in preformed distributions were both too large for the results to be widely accepted (Shiller, 1981). The later ΔC^* approach of Gruber et al. (1996) was based on the same principles, but with more advanced estimates of the preformed distributions, and benefitting from an order-of-magnitude improvement in the accuracy and precision of routine DIC and TA measurements. It has been applied to determine the global distribution and inventory of DIC_{anth} (Sabine et al., 2004), and several studies have been performed comparing a range of more recent minor variations on the approach (e.g. Sabine and Feely, 2001; Álvarez et al., 2009; Vázquez-Rodríguez et al., 2009). The method remains limited in particular by its need to estimate pre-industrial fields for DIC, TA and other variables (Goodkin et al., 2011), and by assumptions like that diapycnal mixing in the ocean interior is negligible everywhere (Matsumoto and Gruber, 2005). The former limitation can be overcome by considering relative changes in DIC_{anth} between cruises, rather than trying to calculate it absolutely. For example, an 'extended' multi-linear regression (eMLR) technique – a development of the simpler multi-linear regression approach (Wallace,

1995) – can be used for two cruises separated in time but in the same location (Friis et al., 2005; Tanhua et al., 2007). In this approach, a multi-linear regression is applied to the data from each cruise to predict DIC from other hydrographic metavariables such as temperature, salinity and dissolved oxygen; one regression can then be subtracted from the other, and then applied to one of the sets of metavariables. The result is interpreted as DIC_{anth}, and the regression is assumed to account for changes in DIC like those due to changes in water mass distributions (Thacker, 2012). The method used to quantify DIC_{anth} accumulation from 1981 to 2013 at the Extended Ellett Line (EEL) hydrographic transect in the Northeast Atlantic in Chapter 4 is based ultimately upon the principles of the back-calculation methods, but applied like the eMLR method to quantify decadal changes in DIC_{anth}, not its absolute inventory.

Alternatively, the DIC_{anth} can be estimated without using carbonate chemistry measurements at all, for example using the Transient Tracer Distribution (TTD) method (Hall et al., 2002; Waugh et al., 2006). Here, anthropogenic CO_2 is assumed to behave as a passive, inert tracer, such that its distribution is proportional to that of other tracers with a similar atmospheric concentration history, like chlorofluorocarbons (CFCs). However, owing to an international ban on their use (the Montreal Protocol), emissions of CFCs have reduced significantly while anthropogenic CO_2 continues to increase, limiting applications of the TTD approach.

Finally, DIC_{anth} accumulation can be independently quantified by the corresponding decrease in $\delta^{13}C_{DIC}$ – the marine Suess effect (Keeling, 1979) – using techniques similar to the back-calculation and eMLR approaches, but modified to use $\delta^{13}C_{DIC}$ observations instead of DIC (Sonnerup et al., 1999; Quay et al., 2003, 2007). There have been significant changes in the depth-distribution of $\delta^{13}C_{DIC}$ in the interior ocean because of DIC_{anth}, like erosion of the gradient between high $\delta^{13}C_{DIC}$ near the ocean surface and low $\delta^{13}C_{DIC}$ at depth (Olsen and Ninnemann, 2010). In Chapter 4, the observed decrease in $\delta^{13}C_{DIC}$ provides independent support for the attribution of the multi-decadal increase in DIC observed at the EEL to its anthropogenic and other components.

1.3 Measurements

A plethora of methods exist to measure different components of the carbonate system. The most commonly measured variables are DIC, TA, pH and pCO_2^{sw}. Methods to measure other system variables do exist, but are less developed and less widespread. As the entire system can be calculated from values for any pair of its variables, these calculations can be tested by measuring three or more variables and comparing calculated with measured values. This approach has been taken to show that which specific pair of variables are measured does not affect the accuracy of the calculated variables (Ribas-Ribas et al., 2014). However, the choice of which pair is measured does affect the precision of the calculated variables, because of the different uncertainties in the measurements and how these propagate through the calculations. The accuracy of seawater DIC and TA measurements can be assessed using certified reference material (CRM) obtained from A.G. Dickson (Scripps Institution of Oceanography, USA). It is now common practice to adjust the results for DIC and TA samples such that CRM measurements made at the same time match the certified values.

1.3.1 Measurement principles and methods

For all variables for which discrete seawater samples are collected, borosilicate glass bottles with greased ground glass stoppers are typically used as containers, held shut by tape or elastic bands. An air headspace is introduced taking up 1 % of the bottle volume, and 0.02 % of the bottle volume of saturated mercuric chloride solution is added in order to sterilise the seawater, preventing post-sampling biological changes in its contents (Dickson et al., 2007).

1.3.1.1 Dissolved inorganic carbon

Seawater DIC is normally measured by acidifying a sample with phosphoric acid to convert all of the bicarbonate and carbonate ions to CO_2 and bubbling through with an inert carrier gas (often nitrogen) to transport all of the CO_2 to a measurement device. The amount of CO_2 can then be measured by techniques such as coulometric titration (e.g. Johnson et al., 1985) or infrared absorption (e.g. O'Sullivan and Millero, 1998). The full sampling and measurement procedure for DIC using the Versatile INstrument for Determination of Total inorganic carbon and titration Alkalinity (VINDTA), which uses a coulometric method, is briefly outlined in Section 4.2.1.1.

1.3.1.2 Total alkalinity

Total alkalinity is determined by a pH-monitored titration with hydrochloric acid following any of a variety of methods, which are discussed in detail in Chapter 2. A sampling and measurement procedure for TA using the VINDTA instrument is also briefly outlined in Section 4.2.1.1.

1.3.1.3 pH

A review of oceanic pH measurement techniques has recently been performed by Rérolle et al. (2012), and the four main varieties are briefly summarised here. Spectrophotometric methods are conceptually the simplest: a spectrophotometer is used to detect colour changes in a pH indicator added to seawater sample (e.g. Martz et al., 2003; Rérolle et al., 2013). Congruent pH measurements can also be obtained potentiometrically by using a glass electrode (Byrne et al., 1988; Dickson, 1993). Thirdly, pH measurements can be carried out using an ion sensitive field effect transistor (ISFET); ISFET-based sensors have been successfully deployed in the marine environment on autonomous floats (e.g. Argo floats) (Le Bris and Birot, 1997; Martz et al., 2010; Bresnahan Jr. et al., 2014). Finally, an assortment of optode-based sensors are being developed for seawater applications; in these, a fluorescence signal emitted by specific pH-sensitive compounds which are in contact with the sample is measured and can be used to determine pH (e.g. Schröder et al., 2005; Zhu et al., 2005; Clarke et al., 2015b).

1.3.1.4 Seawater partial pressure of carbon dioxide

Several different approaches can be taken to measure pCO_2^{sw} (Clarke et al., 2015a), but most common are equilibrator-based systems, whereby a seawater sample is allowed to equilibrate with a gas phase. These measurements are usually carried out on a continuous, flow-through water supply, without discrete samples being collected. The amount of CO_2 in the gas phase can then be measured, typically by infrared absorbance (e.g. Saito et al., 1995). New techniques based on optodes similar to those used for pH measurement are also being developed (e.g. Atamanchuk et al., 2014).

1.3.1.5 Carbonate ion concentration

Direct measurement of CO_3^{2-} is possible for example by spectrophotometric observations of its complexation with Pb(II) (Byrne and Yao, 2008), or directly by ultraviolet spectrophotometric titration; the latter can also provide information about

pairing of the carbonate ion with the major cations dissolved in seawater (Martz et al., 2009). Although these methods are promising, this measurement is not currently widespread.

1.3.1.6 Stable isotopes of DIC

Seawater $\delta^{13}C_{DIC}$ can be measured using a stable isotope ratio mass spectrometer, once the DIC has been converted into CO_2 and extracted using a technique involving acidification and an inert carrier gas (McNichol et al., 2010) similar to that used for DIC measurements (Section 1.3.1.1). The sampling, measuring and processing steps for this measurement for two recent cruises in the North Atlantic are described in detail in Chapter 3, and by Humphreys et al. (2015). The potential to carry out high-resolution surface ocean measurements at sea has also been investigated using other techniques like continuous wave cavity ringdown spectroscopy (Becker et al., 2012). Regardless of the measurement technique, $\delta^{13}C_{DIC}$ results are typically reported relative to the Vienna Pee Dee Belemnite (V-PDB) international standard (Coplen, 1995).

1.4 Data

1.4.1 Observations

1.4.1.1 Ocean interior

The main sources of historical carbonate chemistry observational data are the compilations of measurements from research cruises which have been assembled and quality-controlled by the scientific community. For example, the Global Data Analysis Project (GLODAP) (Key et al., 2004), Carbon in the Atlantic Ocean (CARINA) (Key et al., 2010) and Pacific Ocean Interior Carbon (PACIFICA) (Suzuki et al., 2013) syntheses contain high-quality marine carbonate chemistry measurements carried out during the last 30 to 40 years, along with important metadata like seawater temperature, salinity, macronutrient concentrations and dissolved oxygen. The measurements have been adjusted where necessary to ensure consistency between cruises, by comparing variables in the deepest part of the water column between 'cross-over' cruises which have intersecting routes (Tanhua, 2010). There is some overlap in the cruises included in these data products, and the methods by which the adjustments have been made vary from product to product. To resolve these issues, a new data product called GLODAPv2 is in preparation, which will contain all of the data from GLODAP, CARINA and PACIFICA along with that from hundreds of more recent cruises, all having undergone a consistent secondary quality-control and adjustment process. This will form an invaluable resource for future investigations. Data from GLODAP and CARINA have been used extensively in Chapter 4, and it is anticipated that that analysis will be updated to use GLODAPv2 once it is released.

The $\delta^{13}C_{DIC}$ data provided in GLODAP and CARINA have not undergone a secondary quality-control procedure, but alternative compilations that have do exist. For example, the synthesis produced by Schmittner et al. (2013) has been used in Chapter 4. The $\delta^{13}C_{DIC}$ measurements described in Chapter 3 have been submitted to a new compilation which is in preparation by Becker et al. (2015).

In addition to *ad hoc* research cruises, there are a handful of marine carbonate chemistry time-series sites where repeated measurements have been taken at sub-annual resolution (Bates et al., 2014). Their distribution is heavily biased towards the North Atlantic, but they provide key observational data to quantify multi-decadal trends in anthropogenic CO_2 uptake and associated pH decline (e.g. Dore et al., 2009; Olafsson et al., 2009; González-Dávila et al., 2010; Bates et al., 2012). They also provide results which can be compared with output from global coupled ocean-

atmosphere models for validation purposes (e.g. Le Quéré et al., 2010). As well as these time-series sites visited regularly by research ships, there are fixed-point sustained observatories which operate semi-autonomously from moorings and can measure carbonate chemistry variables at high temporal resolution, for example on the Porcupine Abyssal Plain in the Northeast Atlantic where pCO_2^{sw} has been measured at intervals as short as an hour, consecutively for at least 2 years (Körtzinger et al., 2008).

Recent developments in sensor technology have led to an extension of the Argo project (http://www.argo.ucsd.edu) to include biogeochemical measurements such as pH. The Argo project, which began in the early 2000s, consists of several thousand autonomous drifting profiling floats deployed throughout the global ocean, which measure physical hydrographic variables in the upper 2000 m of the ocean at a high resolution. If the biogeochemical sensors become more widespread they could play a vital role filling in the gaps in the more traditional observational data set, especially in infrequently-visited regions like the Southern Ocean and parts of the Pacific and in chronically under-sampled winter months.

1.4.1.2 Surface ocean

Semi-autonomous systems collecting surface ocean pCO_2^{sw} measurements have been widely deployed not only on scientific research vessels but also on cargo and passenger ships repeating regular routes across all oceans. These are compiled into quality-controlled data syntheses like the Surface Ocean CO_2 Atlas (SOCAT) (Pfeil et al., 2013; Bakker et al., 2014) and the Lamont-Doherty Earth Observatory (LDEO) database (Takahashi et al., 2014b). No other marine carbonate system variable is currently measured at this spatial or temporal resolution on a global scale. To remedy this, there is ongoing research into estimating pCO_2^{sw} and other carbonate system variables from more widely-available metadata such as sea surface temperature (SST) and chlorophyll-*a* concentration (e.g. Ono et al., 2004). For example, surface ocean TA can be robustly estimated from polynomial functions of salinity and SST in most open ocean regions (Lee et al., 2006).

1.4.2 Model output

Model output provides many opportunities to extend analyses of observational data. Despite the increasing abundance of observations, there remain significant spatial

and temporal gaps. For example, in Chapter 4, output from a simulation described by Yool et al. (2013b) of the Nucleus for European Modelling in the Ocean (NEMO), an ocean general circulation model (Madec, 2008), coupled with the biogeochemical model MEDUSA-2.0 (Yool et al., 2013a), are used to investigate if spatiotemporal heterogeneity in the distribution of observations has an adverse effect on calculated rates of change for certain variables, and to indicate how representative changes observed in a small region might be of changes in the wider surrounding ocean basins. Many other different model outputs containing marine carbonate chemistry variables are also available, notably the CMIP5 compilation of the Coupled Model Intercomparison Project (Taylor et al., 2011).

1.5 Thesis overview

The aims of this thesis are primarily to make developments to the measurement of marine carbonate chemistry variables, to use these measurements to constrain biogeochemical changes at a hydrographic transect that is previously unstudied in this context, and to provide novel insights into how concepts from the marine carbonate chemistry system can be usefully applied. More specifically, the existing methods for calculating TA from acidimetric titration data are not designed for the open-cell hardware set-up without active CO_2 purging that is commonly used for measurements, so I have adapted these methods to make them more suitable for this purpose. Measurements of $\delta^{13}C_{DIC}$ are much less abundant than those of the non-isotopic system variables yet they provide valuable extra insight into the processes governing seawater chemistry, so I have measured this variable in samples from two cruises in the North Atlantic, and made improvements to the accuracy and precision of the calibration procedure. I have combined these methodological developments with historical hydrographic data to investigate and quantify the uptake of anthropogenic CO_2 by the ocean in the Northeast Atlantic, which is a key region in this context. Finally, I have introduced a conceptual framework which aims to assess theoretically whether marine calcifying phytoplankton like coccolithophores act as sources or sinks of CO_2 to the environment.

These aims are addressed in the chapters of this thesis as follows. Chapters 2 and 3 are about measurements: the former of TA, and the latter of $\delta^{13}C_{DIC}$. Chapter 2 presents a novel synthesis of existing methods for determining TA from open-cell titration data (Gran, 1952; Hansson and Jagner, 1973; Bradshaw et al., 1981; Butler, 1992; Dickson et al., 2003). Although the approach is complete in its present form and can be used to accurately calculate TA, there is scope for further development and independent publication of this chapter in the future. Chapter 3 reports measurements $\delta^{13}C_{DIC}$ of samples collected during recent research cruises. Significant adjustments to the processing of the raw data, including calibration and quality-control, were made to the original procedures used by the laboratory at which the measurements were carried out (Scottish Universities Environmental Research Centre – Isotope Community Support Facility, East Kilbride, UK), improving efficiency and accuracy. A version of the chapter is currently a discussion paper under review for the journal Earth System Science Data (Humphreys et al., 2015). Chapter 4 integrates the methods and data from Chapters 2 and 3 into an investigation of uptake of anthropogenic CO_2 by the oceans, a key application of marine carbonate

chemistry data. Changes at the Extended Ellett Line hydrographic transect in the Northeast Atlantic over the past 3 decades are evaluated using observational data from recent UK research cruises (Sherwin, 2009; Read, 2010, 2011; Griffiths, 2012; Griffiths and Holliday, 2013) and from quality-controlled syntheses of historical cruise data (Key et al., 2004, 2010; Schmittner et al., 2013). Output from a coupled ocean general circulation-ecosystem and biogeochemical model (Yool et al., 2013b) is incorporated in order to assess the reliability of the observational results. Once the new synthesis data product GLODAPv2 is released, it will be incorporated into the analysis and this chapter will be submitted for publication. Finally, Chapter 5 examines a critical biological application of the principles and concepts of carbonate chemistry, namely the behaviour of coccolithophores in the surface ocean as sources or sinks of CO_2, from a chiefly theoretical standpoint. A shortened version of this chapter is in preparation for publication, with its focus shifted mainly onto the implications of the results.

2

Calculating seawater total alkalinity from open-cell titration data using a modified Gran plot technique

Abstract

To improve the efficiency and transparency of calculating seawater total alkalinity from potentiometric titration data, a new code has been written: Calkulate. This runs in the MATLAB (MathWorks) program, and determines total alkalinity (TA) using a 'modified Gran plot' approach. This approach has been further developed to take into account the now common practices of carrying out open-cell titrations and independently measuring the dissolved inorganic carbon concentration (DIC). This is achieved by using DIC as an input value and modelling its decrease during the titration to account for CO_2 loss to the air. The code has been tested using real titration data from a recent UK research cruise in the Northeastern Atlantic, and cross-over analysis with cruises from the GLODAP and CARINA quality-controlled data syntheses suggests that the calculated TA values are accurate: for samples collected deeper than 1500 m, the mean offset between all TA measurements for this cruise determined using Calkulate and TA data on the same potential density surfaces from 7 nearby cruises in the data syntheses was -0.08 μmol kg^{-1}, over an order of magnitude smaller than the typical measurement precision for TA. Methods to calibrate TA measurements using this script to ensure consistency between laboratories are discussed and compared. Different sources of uncertainty are evaluated, and their relative impact depends upon how the acid titrant molarity has been determined: if this is done independently of certified reference material (CRM) measurements, then an accurate value for the volume of sample being titrated is particularly essential; if not, then this has a much smaller influence on the results. The Calkulate script is provided in Appendix 1.

2.1 Introduction

Total alkalinity (TA) is one of the four commonly-measured carbonate chemistry system variables. Dickson (1992) provides a thorough review of the history of the concept's development, which is defined by Dickson (1981) as:

Equation 2.1

$$\begin{aligned} \mathrm{TA} = [\mathrm{HCO_3^-}] + 2[\mathrm{CO_3^{2-}}] + [\mathrm{B(OH)_4^-}] + [\mathrm{OH^-}] + [\mathrm{HPO_4^{2-}}] + 2[\mathrm{PO_4^{3-}}] + [\mathrm{SiO(OH)_3^-}] \\ + [\mathrm{HS^-}] + 2[\mathrm{S^{2-}}] + [\mathrm{NH_3}] - [\mathrm{H^+}] - [\mathrm{HSO_4^-}] - [\mathrm{HF}] \end{aligned}$$

where the square brackets here and hereafter indicate the molality of the enclosed chemical species. Measurements of TA are usually based upon the titration of a seawater sample with hydrochloric acid (HCl), but a variety of methods exist both for the titration procedure and also for the interpretation of the titration results. The choice of which combination of these methods is taken to determine TA is usually made based on convenience, and it should not bias the measurement. The titration is monitored *via* pH, which can be measured using either a spectrophotometric or a potentiometric technique. The titration can be closed-cell, where gases cannot be exchanged with the surroundings, or open-cell, where they can. In the former case, the dissolved inorganic carbon (DIC) concentration can also be calculated from the titration data; in the latter, CO_2 is sometimes actively purged from the sample prior to measurement, and sometimes not. The acid titrant can be added in repeated small increments, with the pH recorded throughout the titration and the shape of the titration curve used to calculate TA; or, it can be added until a specific end-point pH value is reached, and TA calculated from the amount of acid used. In the former case, at least three different methods have been successfully used to determine the titration equivalence point and hence TA in seawater samples: modified Gran plots (Gran, 1952; Hansson and Jagner, 1973; Bradshaw et al., 1981), non-linear least-squares curve fitting (Dickson, 1981; Johansson and Wedborg, 1982), and difference derivatives (Hernández-Ayón et al., 1999). For certain subsets of these methods, studies have demonstrated that consistent TA results can be obtained regardless of which specific approach is used. For example, Barron et al. (1983) applied several different approaches to simulated titration data, to show that both modified Gran plot and curve fitting methods can successfully evaluate seawater TA to a precision of 0.1 %. Mintrop et al. (2000) found no systematic difference between TA measured using open-cell and closed-cell titrations, and none between using incremental acid addition with curve fitting and addition to an end-point pH value. Dickson et al.

(2003) separately found no systematic offset between TA measured using closed-cell and open-cell titrations. Sterile seawater samples with reliable certified TA values, called certified reference material (CRM), are available to assess the accuracy and consistency of measurements between different laboratories and methods (Dickson et al., 2003).

A common hardware set-up used for oceanographic TA measurements at the present day is the Versatile Instrument for the Determination of Total Alkalinity (VINDTA), produced by Marianda (Kiel, Germany). The VINDTA carries out a potentiometric, open-cell titration of each seawater sample, without active purging of CO_2, and using regular incremental additions of HCl. Each acid addition is called a 'titration step', and between each step there is a pause of around 20-30 seconds for the acid to mix with the sample and for the electric potential measured across the seawater to stabilise. The VINDTA software uses a non-linear least-squares curve fitting approach to calculate TA from the titration data. For this calculated TA to be accurate, input variables including the HCl titrant concentration and density, and the seawater sample's salinity and total phosphate concentration, must be known at the time of analysis. This is not always the case, as TA measurements are frequently carried out before quality-controlled metadata become available. Re-calculation of TA with updated metadata is possible using the VINDTA software, or with an alternative code converted from FORTRAN to run in MATLAB (MathWorks) by D.C.E. Bakker (University of East Anglia, UK). While both of these pieces of software are useful tools, their application can be inefficient for the large and complex datasets frequently generated during research cruises and large sampling programmes. Both use methods designed for closed-cell titrations; DIC is determined as well as TA. In addition, they are not easy to modify in order to amend the equations or values used for equilibrium constants and ionic concentrations, or to take inputs of titration data not produced by a VINDTA instrument. To begin to address these issues, a new MATLAB (MathWorks) code called Calkulate was developed and is presented in this chapter. The equations and method used by Calkulate are described, the influence of uncertainty in different inputs on calculated TA is assessed, and the code is tested by application to real cruise data.

2.2 Theory and methods

The equations presented in this section are primarily a synthesis of the works of Gran (1952), Hansson and Jagner (1973), Bradshaw et al. (1981), Butler (1992) and Dickson et al. (2003). The Calkulate code (Appendix 1) uses a modified 'Gran plot' method (Gran, 1952) to determine seawater TA from VINDTA titration data. This approach was modified to include the major ionic interactions in typical seawater by Dyrssen and Sillén (1967) and Hansson and Jagner (1973), and was used to determine TA for all *circa* 6000 samples collected during the GEOSECS research programme (Bradshaw et al., 1981). For potentiometric titrations, it is an iterative process in which the value of TA is refined by repetition of part of the calculation until the change in its value between iterations becomes negligible. In general, a Gran plot is a graphical interpretation of titration data in which the titration end-point can be located using an equation called a Gran function (e.g. Figure 2.1b). For TA, the end-point is defined by Equation 2.1 as the point where TA = 0, but the progress of the TA titration is monitored only by measurement of the pH at each step. A plot of pH against the cumulative amount of acid titrant added (m_a) is non-linear, and the titration end-point corresponds to an inflection point (Figure 2.1a). Because of the relatively large increase in m_a at each step in VINDTA titrations, the position of this inflection point cannot be accurately determined. The Gran function is therefore used instead: it is designed such that it is linear with respect to acid addition, and it is equal to 0 at the end-point itself (Figure 2.1b); the m_a-axis intercept is located at the titration end-point, as the amount of acid required to be added to a seawater sample to reduce its TA to 0 is equal to that sample's original TA. In a closed-cell titration, DIC can also be determined using a different Gran function, but this is not true of VINDTA titrations because the open-cell set-up permits the exchange of carbon dioxide (CO_2) between the sample and the laboratory air during the titration. However, CO_2 is not actively purged from the sample prior to measurement, and there is not necessarily sufficient time for the sample DIC to fully equilibrate with the laboratory air at each titration step, so it is not immediately obvious how to account for this in the equations. The existing codes to calculate TA from titration data therefore do not include a correction scheme for changes in DIC during the titration, so the one suggested by Butler (1992) has been implemented in Calkulate.

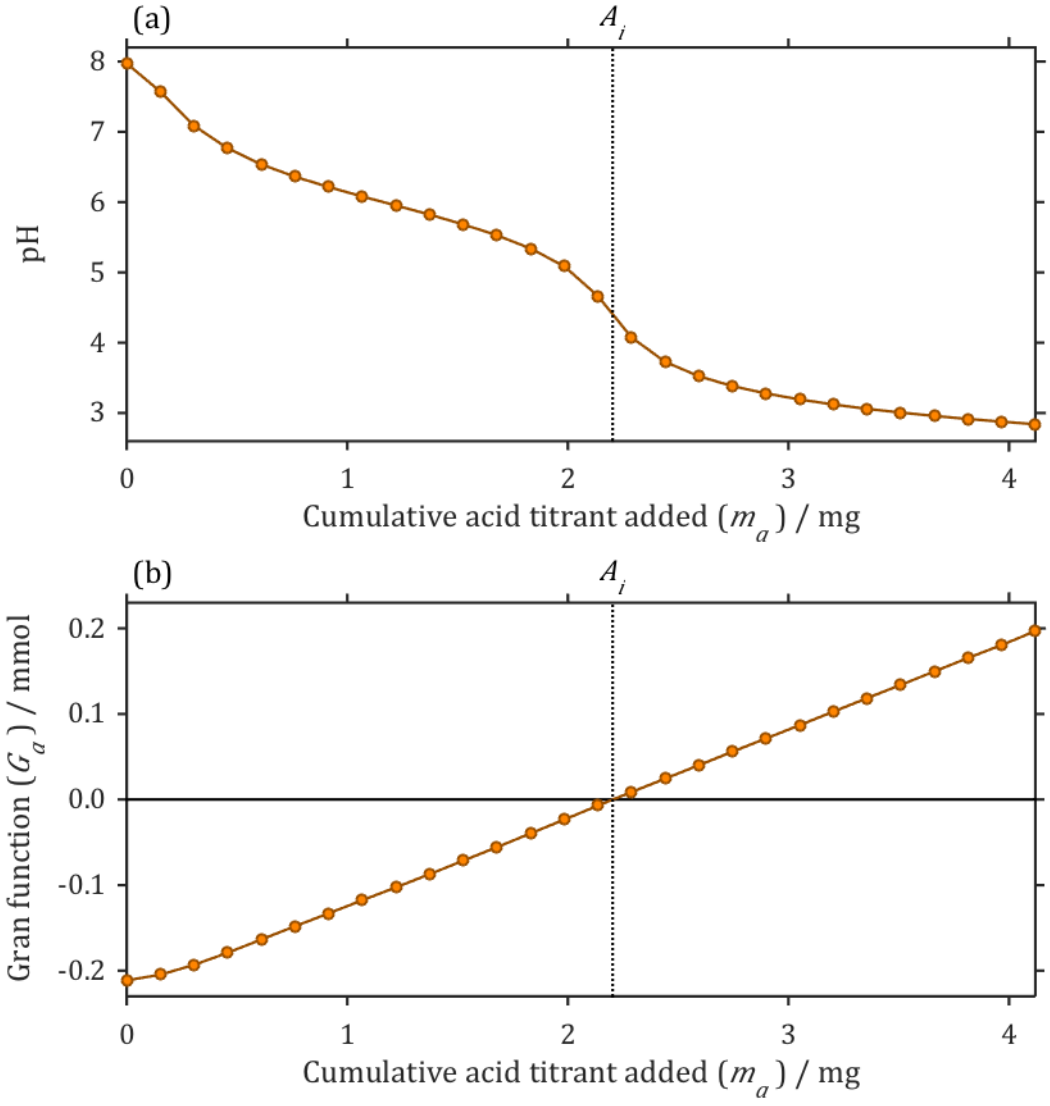

Figure 2.1. Changes in (a) pH and (b) the Gran function (G_a) throughout an example seawater total alkalinity (TA) titration as a function of the cumulative amount of acid titrant added (m_a) (i.e. a Gran plot). The filled circles indicate the actual acid addition steps. The vertical dotted line indicates the location of the titration end-point, which is where $m_a = A_i$ and $G_a = 0$.

On notation: a subscript *i* indicates that the preceding variable changes upon each iteration of the calculations described in Section 2.2.5. A subscript *a* indicates that the preceding variable changes throughout the titration, and so is evaluated separately at each acid addition step. This is omitted for the stoichiometric equilibrium constants: although these are evaluated separately at each titration step, changes from step to step are driven entirely by temperature fluctuations and not by the acid addition, so for clarity these variables are not labelled with subscript *a*.

2.2.1 Acquisition of titration data

Calkulate requires data for three variables which change throughout the titration: the cumulative volume of acid added to the seawater analyte, the electric potential measured in the sample, and its temperature. The VINDTA instrument produces these titration data as text files with a .dat file extension, which Calkulate can directly import. If titration data have been generated differently, for example by a different hardware system or by computer simulation, then Calkulate can still be used provided that the input data is converted into a compatible format. Calkulate also requires the acid titrant's molarity and density, and the volume of the seawater sample being titrated along with its salinity, DIC concentration (C_T) and dissolved inorganic phosphate (P_T) concentration. A volume correction factor can be also be provided for the burette which delivers the acid titrant to the sample, if this has been independently calibrated.

There is an optional input to replace the temperature recorded in the titration data file created by the VINDTA to a uniform value. This option was introduced because communication errors between one specific VINDTA instrument at the National Oceanography Centre, Southampton and its thermometers have resulted in titrations having false temperature data recorded; if left uncorrected, these would significantly bias the TA calculation. All samples are routinely warmed to 25.0 °C in a water bath prior to analysis, and this water is circulated through a jacket surrounding the titration cell, so 25.0 °C can be used as a replacement value with some confidence in these cases.

2.2.2 Concentrations and constants

The expressions used to calculate the concentrations of relevant dissolved chemical species not given as inputs (Section 2.2.2.1), and the necessary stoichiometric equilibrium constants (Section 2.2.2.2), are mostly those recommended by Dickson et al. (2007), but additional options are also provided. For example, the ionic concentrations present in synthetic seawater can be used instead of those based on measurements of typical natural seawater. In the code, the selection of constants and concentrations are handled by a switch block which is robust and easy to modify to include new equations or values as required.

For conversions between seawater volume and mass, the density of the sample at the analysis temperature is calculated using the international one-atmosphere equation of state of seawater (Millero and Poisson, 1981).

2.2.2.1 Chemical concentrations

Concentrations of dissolved inorganic carbon and phosphorus (C_T and P_T, Equations 2.2 and 2.3) are required as Calkulate inputs; these are routinely measured independently of total alkalinity. The concentrations of dissolved inorganic sulfur (S_T, Equation 2.4) and fluorine (F_T, Equation 2.5) are also required, but these are not routinely measured; however, they can be relatively reliably predicted from salinity (Dickson et al., 2007), the sources of which are given in Table 2.1. Calkulate uses the Warner (1971) relationship for F_T rather than the Riley (1965) value, because the latter study – although recommended by Dickson et al. (2007) – is principally about observations of anomalous F_T concentrations, while the former is concerned with obtaining a value representative of 'normal' seawater. In either case, the difference between the two is sufficiently small that the effect of this choice on calculated TA is negligible: for a typical seawater sample, switching from one relationship to the other changes the calculated TA by less than 0.03 μmol kg^{-1} (about 0.001 % of typical seawater TA). These relationships are typically reported in terms of a ratio with chlorinity. To convert these into ratios with salinity, a salinity:chlorinity ratio of 1.80655:1 was used, following Dickson et al. (2007).

Equation 2.2 $$C_T = [CO_2] + [HCO_3^-] + [CO_3^{2-}]$$

Equation 2.3 $$P_T = [H_3PO_4] + [H_2PO_4^-] + [HPO_4^{2-}] + [PO_4^{3-}]$$

Equation 2.4 $$S_T = [HSO_4^-] + [SO_4^{2-}]$$

Equation 2.5 $$F_T = [HF] + [F^-]$$

Element	Calkulate default	Alternative(s) provided
Sulfur (S_T)	Morris and Riley (1966)	Kester et al. (1967)*
Fluorine (F_T)	Warner (1971)	Riley (1965) Kester et al. (1967)*

Table 2.1. Sources of equations for chemical concentrations used by Calkulate. In each row the underlined citation is recommended by Dickson et al. (2007). *Kester et al. (1967) values are for their synthetic seawater recipe.

2.2.2.2 Stoichiometric equilibrium constants

The equilibria relevant to the TA measurement involve protons and: bisulfate and sulfate ions (Equation 2.6); hydrogen fluoride and fluoride ions (Equation 2.7); carbon dioxide, bicarbonate and carbonate ions (Equations 2.8 and 2.9); phosphoric acid, dihydrogen phosphate, hydrogen phosphate and phosphate ions (Equations 2.1, 2.11 and 2.12); and water and hydroxide ions (Equation 2.13):

Equation 2.6 $$HSO_4^- \overset{k_S}{\rightleftharpoons} H^+ + SO_4^{2-}$$

Equation 2.7 $$HF \overset{k_F}{\rightleftharpoons} H^+ + F^-$$

Equation 2.8 $$CO_2 + H_2O \overset{k_1}{\rightleftharpoons} H^+ + HCO_3^-$$

Equation 2.9 $$HCO_3^- \overset{k_2}{\rightleftharpoons} H^+ + CO_3^{2-}$$

Equation 2.10 $$H_3PO_4 \overset{k_{P1}}{\rightleftharpoons} H^+ + H_2PO_4^-$$

Equation 2.11 $$H_2PO_4^- \overset{k_{P2}}{\rightleftharpoons} H^+ + HPO_4^{2-}$$

Equation 2.12 $$HPO_4^{2-} \overset{k_{P3}}{\rightleftharpoons} H^+ + PO_4^{3-}$$

Equation 2.13 $$H_2O \overset{k_W}{\rightleftharpoons} H^+ + OH^-$$

Various equations in terms of temperature and salinity, mostly empirically-determined, are available to estimate the stoichiometric equilibrium constants. Those used (and available as alternatives) in Calkulate are given in Table 2.2. Once calculated from the sample temperature and salinity, all of the equilibrium constants

are converted into the Free pH scale (Zeebe and Wolf-Gladrow, 2001, pp. 57–61), and all subsequent calculations are carried out on that scale.

Constant(s)	Equation(s)	Calkulate default	Alternative(s) provided
k_S	2.6	Dickson (1990a)	Waters and Millero (2013)
k_F	2.7	Perez and Fraga (1987)	Dickson and Riley (1979)
k_1, k_2	2.8, 2.9	Lueker et al. (2000)	Goyet and Poisson (1989)*
k_{P1}, k_{P2}, k_{P3}	2.1, 2.11, 2.12	Dickson et al. (2007)	-
k_w	2.13	Dickson et al. (2007)	-

Table 2.2. Sources of equations for equilibrium constants used by Calkulate. In each row the underlined citation is recommended by Dickson et al. (2007). *Goyet and Poisson (1989) determined k_1 and k_2 using synthetic seawater following the Kester et al. (1967) recipe.

2.2.3 Nernst equation

The Nernst equation can be used to convert between the measured electric potential for the seawater analyte at each titration step (E_a) and the proton concentration ($[H^+]_a$):

Equation 2.14 $$E_a = E° + N \ln([H^+]_a)$$

where $E°$, the standard electrode potential, is a constant to be determined from the titration data. Its value depends on the pH scale being used (Marion et al., 2011), and the hardware set-up used for the measurement; $E_a \rightarrow E°$ as $[H^+]_a \rightarrow 1$. The coefficient N is given by:

Equation 2.15

$$N = \frac{RT}{F}$$

where R is the ideal gas constant, F is the Faraday constant and T is the absolute temperature of the seawater sample in units of K. The values of R and F used by Calkulate are the 2010 CODATA recommended values (as reported by http://physics.nist.gov/cuu/Constants): 8.3144621 J mol^{-1} K^{-1} and 96.4853365 kC mol^{-1} respectively.

2.2.4 Initial estimates of TA and $E°$

To ensure convergence during the iterative part of the process, reasonable initial estimates of TA and $E°$ must be made. This is achieved by using the original, 'unmodified' Gran function (Gran, 1952). The Gran function (g_a, labelled variously F_1 and F_2 by other authors) used for this initial estimate is calculated from the titration data (Equation 2.16). This function should be linear after the titration end-point is passed (the point at which enough acid has been added to reduce the sample's TA to 0), and while the pH remains above about 3, sufficiently high to ensure that the electrode does not behave in a significantly non-Nernstian manner:

Equation 2.16 $$g_a = (M_{\mathrm{sw}} + m_a)\, e^{-E_a/N}$$

where M_{sw} is the mass of the seawater sample at the start of the titration, m_a is the cumulative mass of acid added, E_a is the electric potential measured in the seawater analyte at each point, and N is the Nernstian conversion factor (Equation 2.15). The m_a-axis intercept of a linear least-squares regression between the mass of acid titrant added m_a and g_a is the initial estimate of the total alkalinity in the seawater sample, (A_0), which is in units of acid mass, not concentration. The initial value of $E°$ ($E°_0$) is then estimated by rearranging Equation 2.14; after the titration end-point (i.e. where $m_a > A_0$), the amount of extra added HCl is roughly equal to [H^+], so $E°_0$ can be estimated by evaluating Equation 2.17 at each point in the titration curve where $m_a > A_0$ and taking the mean result:

Equation 2.17

$$E°_0 = \left\langle E_a - N \ln\left(\frac{(m_a - A_0)[\mathrm{HCl}]}{M_{\mathrm{sw}} + m_a}\right)\right\rangle \text{ for } m_a > A_0$$

where [HCl] is the molality of the acid titrant, and the angle brackets indicate the mean over all titration steps where $m_a > A_0$.

2.2.5 Iterative refinement of TA and $E°$

Once the initial estimates A_0 and $E°_0$ have been made, their values are refined using an iterative process. First, pH (Free scale) is calculated at each titration step from E_a and the most recent estimate of $E°$ ($E°_{(i\text{-}1)}$):

Equation 2.18

$$\mathrm{pH}_a = \frac{(E_a - E°_{(i-1)})}{\log_{10}(N)}$$

The proton concentration [H⁺] is then calculated from pH:

Equation 2.19 $$[\mathrm{H}^+]_a = 10^{-\mathrm{pH}_a}$$

From [H⁺] and the various ionic concentrations (Table 2.1) and equilibrium constants (Table 2.2), the concentrations of all other species at each titration step can be determined. Only the species which contribute to TA and which are present at non-negligible concentrations after the titration has progressed past the titration end-point (i.e. pH < pk_1) are of concern. The relevant equations are:

Equation 2.20

$$[\mathrm{HCO}_3^-]_a = \frac{\mu_a\, L_a\, C_\mathrm{T}\, k_1}{[\mathrm{H}^+]_a + k_1}$$

Equation 2.21

$$[\mathrm{HSO}_4^-]_a = \frac{\mu_a\, S_\mathrm{T}\, [\mathrm{H}^+]_a}{[\mathrm{H}^+]_a + k_\mathrm{S}}$$

Equation 2.22

$$[\mathrm{HF}]_a = \frac{\mu_a\, F_\mathrm{T}\, [\mathrm{H}^+]_a}{[\mathrm{H}^+]_a + k_\mathrm{F}}$$

Equation 2.23

$$[\mathrm{OH}^-]_a = \frac{k_\mathrm{w}}{[\mathrm{H}^+]_a}$$

Equation 2.24

$$[\mathrm{H_3PO_4}]_a - [\mathrm{HPO}_4^{2-}]_a = \frac{\mu_a\, P_\mathrm{T}\, ([\mathrm{H}^+]_a^3 - k_{\mathrm{P1}}k_{\mathrm{P2}}[\mathrm{H}^+]_a)}{[\mathrm{H}^+]_a^3 + k_{\mathrm{P1}}[\mathrm{H}^+]_a^2 + k_{\mathrm{P2}}k_{\mathrm{P3}}[\mathrm{H}^+]_a + k_{\mathrm{P1}}k_{\mathrm{P2}}k_{\mathrm{P3}}}$$

where μ_a is the acid dilution correction factor:

Equation 2.25

$$\mu_a = \frac{M_{\mathrm{sw}}}{M_{\mathrm{sw}} + m_a}$$

and where L_a (in Equation 2.20 only) is the correction factor for CO_2 loss during the titration (Butler, 1992):

Equation 2.26

$$L_a = \frac{[\mathrm{H}^+]_a^2 + k_1[\mathrm{H}^+]_a + k_1k_2}{(1+z)[\mathrm{H}^+]_a^2 + k_1[\mathrm{H}^+]_a + k_1k_2}$$

where z controls the rate of CO_2 loss; Butler (1992) suggests that z could take a value of 0.1. Note that Butler (1992) refers to L_a using the symbol F_z.

The Gran function (G_a) is then evaluated throughout the titration using the calculated concentrations:

Equation 2.27

$$G_a = (M_{\mathrm{sw}} + m_a)([\mathrm{H}^+]_a + [\mathrm{HSO}_4^-]_a + [\mathrm{HF}]_a + [\mathrm{H_3PO_4}]_a - [\mathrm{HPO}_4^{2-}]_a - [\mathrm{HCO}_3^-]_a - [\mathrm{OH}^-]_a)$$

The symbol for this Gran function (Equation 2.27) uses a capital G to distinguish it from the initial estimate, which used a lowercase g (Equation 2.16). Equation 2.27 is Dickson's expression for TA (Equation 2.1) (Dickson, 1981), multiplied by -(M_{sw} + m_a) to make it linear throughout the titration, and with only species with non-negligible concentrations after the end-point included. A linear least-squares regression is carried out between this updated G_a and the added acid mass (m_a) in the pH range from 3 to 4. As before, the m_a-axis intercept is the next estimate of TA, labelled A_i where the subscript i begins at 1 and increases by 1 with each iteration. A new value is generated for $E°$ ($E°_i$) using this new A_i and an equation similar to Equation 2.17, but improved to include the effect of HSO_4^- and HF on the electrode pH measurement:

Equation 2.28

$$E°_i = \langle E_a - N \ln\left(\frac{(m_a - A_i)[\mathrm{HCl}] - ([\mathrm{HSO}_4^-]_a + [\mathrm{HF}]_a)M_{\mathrm{sw}}}{M_{\mathrm{sw}} + m_a}\right)\rangle \text{ for } m_a > A_i$$

The entire process described in this section, beginning with Equation 2.18, is then repeated with the new values. Ideally, the process would be iterated until the

difference in A_i each time became smaller than a pre-defined value that is significantly smaller than the measurement precision, such as 0.01 % (Hansson and Jagner, 1973). At present, Calkulate simply repeats this step 10 times and outputs the final value for A_i, converted into concentration units, as the sample TA; unless there are significant errors in the titration data, 10 repetitions is more than enough to achieve changes in A_i between iterations of less than 0.01 %.

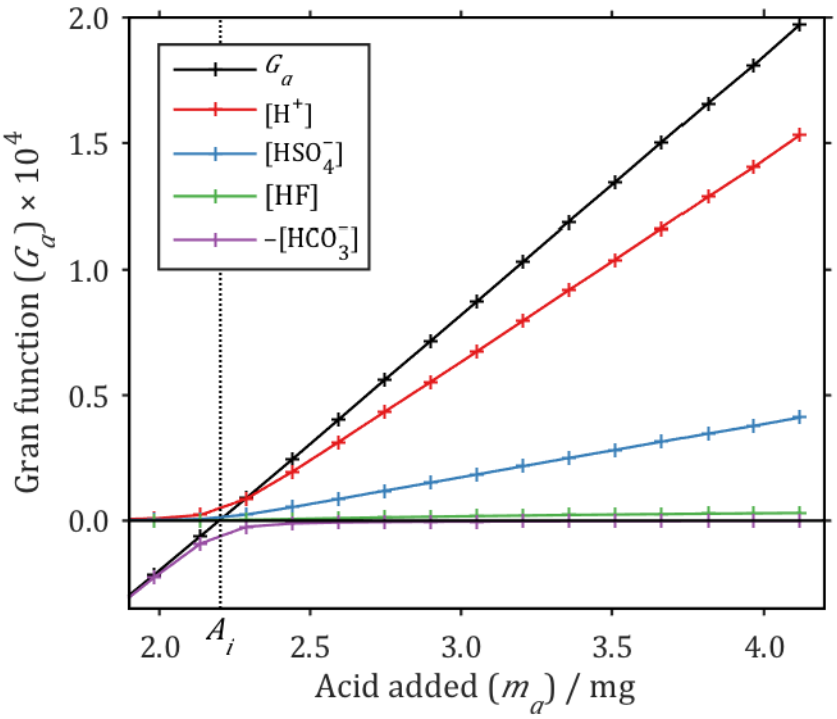

Figure 2.2. The Gran function (G_a, black line) evaluated using Equation 2.27, and the relative contributions from its components, for the latter part of an example VINDTA titration. The components [H^+] (red), [HSO_4^-] (blue), [HF] (green) and [HCO_3^-] (purple) are the concentrations of those species multiplied by (M_{sw} + M_a). The + markers indicate the actual acid addition steps. The contributions of [H_3PO_4] − [HPO_4^{2-}] and [OH^-] are too small to distinguish from 0 on this scale, so have not been shown. The vertical dashed line marked A_i indicates the total alkalinity.

2.2.6 Mercuric chloride correction

The Calkulate script does not include a correction for mercuric chloride addition to seawater samples. Mercuric chloride solution is added in order to sterilise the seawater and thus prevent biological changes to $\delta^{13}C_{DIC}$ after sampling; it has zero TA, but when added to seawater samples it does reduce TA by dilution (Dickson et al., 2007). Consequently, a minor correction can be applied to the final result for TA returned by Calkulate:

Equation 2.29

$$\mathrm{TA} = \mathrm{TA}_{\mathrm{HgCl2}} \cdot C_{\mathrm{dil}} = \mathrm{TA}_{\mathrm{HgCl2}} \cdot \left(1 + \frac{V_{\mathrm{HgCl2}}}{V_{\mathrm{sample}}}\right)$$

where TA is the final corrected value, $\mathrm{TA}_{\mathrm{HgCl2}}$ is the output from Calkulate, C_{dil} is the dilution factor, V_{HgCl2} is the volume of mercuric chloride solution originally added to the sample, and V_{sample} is the volume of the original sample. Best-practice procedures suggest that V_{HgCl2} should be 0.02 % of V_{sample} for a saturated mercuric chloride solution (e.g. 50 µL added to a 250 mL sample), in which case C_{dil} is 1.0002. This correction should not be applied to CRM measurements, as their certified TA is measured after mercuric chloride addition and therefore should already include it.

2.3 Discussion

2.3.1 Determination of the acid molarity

The molarity of the acid titrant should be independently determined and used as an input to calculate TA. For example, coulometric titration can be used for acid calibration (Taylor and Smith, 1959; Dickson et al., 2003). Alternatively, acid with a certified molarity can be obtained from A.G. Dickson (Scripps Institution of Oceanography, USA) and used as a reference to accurately determine the molarities of acids produced in-house. The volumes of the pipette which measures the seawater sample that is titrated and the burette which delivers acid titrant to the titration cell should be precisely determined. Analysis of certified reference material (CRM) also obtained from A.G. Dickson (Dickson et al., 2003) can then be used to evaluate the measurement accuracy for TA. Of particular importance to determine accurately are the acid molarity, the burette volume and the pipette volume, because percentage uncertainty in these inputs propagates into a similar magnitude uncertainty in calculated TA. Uncertainties in the other inputs have a significantly smaller influence on TA (Table 2.3).

However, all of this information may not be available in practice, especially when TA is being re-calculated from archival titration data. If the acid molarity is unknown, it can be estimated from CRM titrations, although this means that the CRM can no longer be used to assess accuracy. Nevertheless, this is a very common situation, to which a solution is required. The data from a CRM titration can be input to Calkulate several times with a different acid molarity each time. The approximate acid molarity is known, so a small range about this value should be used for the different inputs. Each input acid molarity will give a different output TA, and if a small enough range is used then a second-order polynomial fit can be made between acid molarity and output TA. This fit can then be used to find the acid molarity which produces the certified TA value. If the acid molarity found in this way falls outside the range of inputs used to generate the fit, the process should be repeated with an adjusted range.

Variable	Input value	Change in TA for 0.1 % change in input / %
Acid molarity	0.1054 mol L^{-1}	0.0991
Burette volume	4.9799 mL	0.0989
Pipette volume	99.416 mL	0.0989
Salinity	33.651	0.0024
C_T	2026.91 µmol kg^{-1}	0.0005
Acid density	1.0212 kg L^{-1}	0.0002
z (Equation 2.26)	0.1	4×10^{-5}
P_T	0.42 µmol kg^{-1}	6×10^{-8}

Table 2.3. Percentage changes in calculated total alkalinity (TA) resulting from a 0.1 % change in the input values to Calkulate, to evaluate the uncertainty propagation from these inputs. Rows are in descending order of importance in terms of percentage: changes in acid molarity have the greatest influence on calculated TA, while changes in P_T have the smallest.

If any of the other hardware-related inputs are missing, for example the accurate pipette volume, then this same method can still be used under certain conditions. Most critically, the pipette volumes *et cetera* must not have changed between the analysis of the CRM used to estimate the acid molarity, and the analyses of samples to which that acid molarity is applied. If this is the case, the value which has been determined is no longer truly an acid molarity, but rather a generic correction factor which takes into account all of the inaccuracies in these inputs. Because their effects on calculated TA are non-linear, if accurate measurements are not available for these hardware-related inputs then values as close as possible to the real ones should be used, to minimise error. Accuracy can then be assessed indirectly using cross-over analysis between cruises (see Section 2.3.3). Arguably, this method of CRM calibration does offset (to some extent) the disadvantage of not being able use CRMs to directly assess accuracy; small inaccuracies in the hardware-related inputs do not lead to errors in calculated TA as long as the true values of these inputs have not changed between CRM and sample analysis. If the acid molarity has been independently measured, it is absolutely essential that every single input is precisely correct.

Uncertainties in both C_T and P_T have sufficiently small influences on TA such that, if either is unknown, it should still be possible to calculate TA with confidence using an estimated value. Estimates could be generated for example by interpolation, if there is a missing measurement in the middle of a vertical profile, or by multi-linear regression with other hydrographic variables such as temperature and salinity.

Although uncertainty in acid density has a very small influence on calculated TA (Table 2.3), the VINDTA hardware design could be improved by thermostatting the acid titrant, because changes in its temperature will affect its density and consequently how many moles of acid are delivered to the seawater sample in each titration step. As in any titration, knowing the exact amount of titrant that has been added to the analyte is critical for an accurate result.

2.3.2 CO_2 loss correction

The coefficient z suggested by Butler (1992) to account for loss of CO_2 from the sample to the surrounding air during the titration (Equation 2.26) has a non-negligible influence on the calculated TA (Figure 2.3a). Loss of CO_2 causes a decrease in C_T which should be taken into account to calculate $[HCO_3^-]_a$ (Equation 2.20). The equation proposed by Butler (1992) (Equation 2.26) is based on the premise that loss of CO_2 will be a linear function of the change in $[CO_2]$ from the start of the titration. A somewhat arbitrary value of 0.1 was originally suggested for z, but a value appropriate for typical VINDTA measurements could be estimated through a relatively simple experiment. According to Equation 2.26, DIC remains relatively constant during the latter part of the titration, after the titration end-point (after about 2.3 mL of acid added in Figure 2.3b). A titration could be carried out using the VINDTA, and a subsample taken directly from the titration cell towards the end of the titration. A measurement of the DIC in this subsample would provide a route to estimate an appropriate value for Butler's z. A DIC instrument requiring only a few mL of seawater sample for each measurement could be suitable for this purpose (e.g. the Apollo SciTech Inc. DIC Analyzer AS-CS). By carrying out repeated titrations of subsamples of the same batch of seawater and measuring DIC at a different point during each titration, the form of the equation proposed by Butler (1992) to correct for CO_2 loss could also be validated. Until this has been carried out, the coefficient z

should be set to zero, which means that no correction is made, consistent with the original methods (Hansson and Jagner, 1973; Bradshaw et al., 1981).

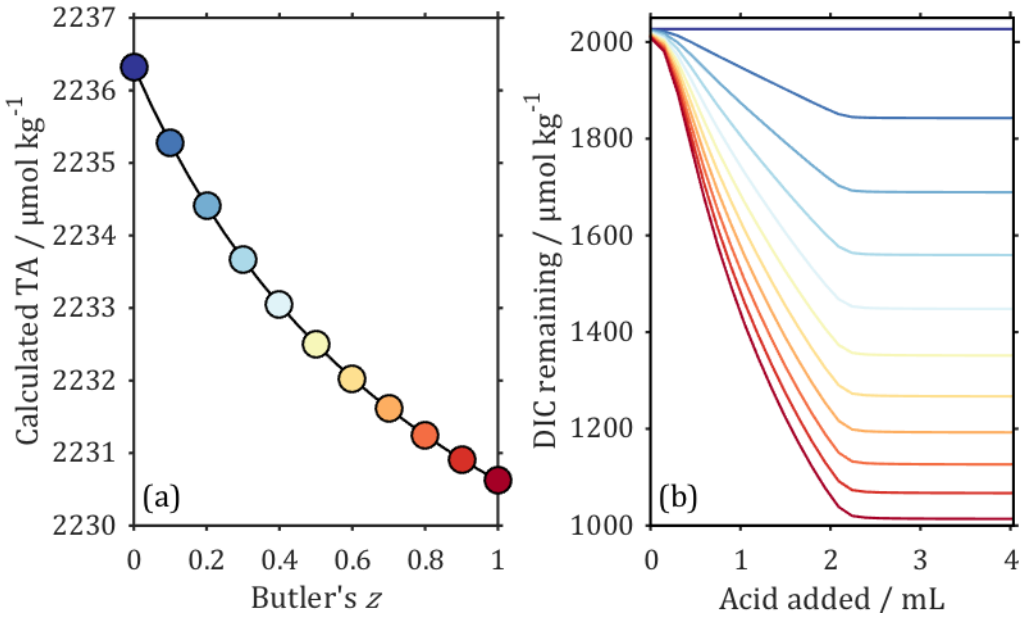

Figure 2.3. Effect of varying z (Equation 2.26) on (a) calculated total alkalinity (TA) and (b) dissolved inorganic carbon (DIC) throughout an example titration. The filled circles in (a) correspond to the lines of the same colour in (b). It is entirely possible for z to take values outside the range of its axis in (a), although negative z would mean that DIC was increasing throughout the titration.

2.3.3 Application to real titration data

Once all of the measurements from a research cruise have been carried out, their consistency with other laboratories can be assessed by cross-over analysis. This involves comparing the results with nearby measurements from other research cruises. Tanhua (2010) has developed a MATLAB (MathWorks) toolbox to perform cross-over analysis of TA and other variables with data from the GLODAP (Key et al., 2004) and CARINA (Key et al., 2010) syntheses. This toolbox compares the new TA measurements with those in GLODAP and CARINA which are horizontally within 200 km, deeper than 1500 m, and at a similar potential density, and calculates the mean offset between the new measurements and each cruise in the data syntheses. The horizontal limit (200 km) is a trade-off between capturing enough historical data to perform an analysis, while remaining local enough to the new data that the results are meaningful. The vertical limit (1500 m) is set such that seasonal and interannual

variability in TA is minimised. For the CARINA synthesis, offsets in TA of up to 6 μmol kg^{-1} between cruises were considered acceptable (Tanhua et al., 2010).

Application of this cross-over analysis (Tanhua, 2010) to some of the recent data sets produced for the Extended Ellett Line hydrographic transect in the Northeast Atlantic (Holliday and Cunningham, 2013; Chapter 4) revealed offsets in TA greater than this 6 μmol kg^{-1} limit. For example, the mean offset between TA from RRS *Discovery* cruise D365 in 2011 (Read, 2011; Hartman et al., 2014a) and the seven cross-over cruises in GLODAP and CARINA was -10.68 μmol kg^{-1}. The raw titration data files were obtained for D365 (the analysis had been carried out at the National Oceanography Centre, Southampton) and Calkulate was applied to re-calculate these data. The acid concentrations were determined from the CRM analyses accompanying the sample measurements, as described in Section 2.3.1. The same cross-over analysis was performed on the re-calculated TA data; the mean offset against the same seven cruises was -0.08 μmol kg^{-1}. Clearly, there was nothing wrong with the original measurements, but a problem had arisen during the processing, probably in part due to the opacity of the only code available. The TA data for D365 were therefore updated to the re-calculated values prior to the analysis described in Chapter 4.

2.4 Conclusions

The code described in this chapter and presented in Appendix 1 is a working product which has been used to reliably calculate total alkalinity (TA) from open-cell titration data. This script improves upon existing alternatives particularly in terms of flexibility, computational efficiency, and applicability specifically to open-cell titrations. However, there is scope for continued improvement and development. Firstly, measurements of dissolved inorganic carbon (DIC) could be carried out during titrations to establish a value for the CO_2 loss coefficient z and validate the model used to represent it, as described in Section 2.3.2. Secondly, this procedure can be simplified for titrations where pH is monitored using a spectrophotometric method. For that application, all steps involving E_a and $E°$ would be excluded, no 'initial estimate' of A_0 would be made, and the iterative section would be repeated only once: the first value calculated for A_i is its final estimate. Thirdly, the script could be converted to use the non-linear least-squares curve-fitting approach to evaluate TA. Although the curve-fitting approach is arguably less intuitive, it is virtually identical in a mathematical sense to the Gran plot method. It also uses an iterative process, but might be more efficient computationally as the iteration is performed by lower-level code.

3

Measurements of the stable carbon isotope composition of dissolved inorganic carbon in the Northeastern Atlantic and Nordic Seas during summer 2012

This chapter is currently a discussion paper under review for the journal Earth System Science Data (Humphreys et al., 2015).

Abstract

The stable carbon isotope composition of dissolved inorganic carbon ($\delta^{13}C_{DIC}$) in seawater was measured in samples collected during two cruises in the Northeastern Atlantic and Nordic Seas from June to August, 2012. One cruise was part of the UK Ocean Acidification research programme, and the other was a repeat hydrographic transect of the Extended Ellett Line. In combination with measurements of other variables on these and other cruises, these data can be used to constrain the anthropogenic component of dissolved inorganic carbon (DIC) in the interior ocean, and to help to determine the influence of biological carbon uptake on surface ocean carbonate chemistry. The measurements have been processed, quality-controlled and submitted to an in-preparation global compilation of seawater $\delta^{13}C_{DIC}$ data, and are available from the British Oceanographic Data Centre. The observed $\delta^{13}C_{DIC}$ values fall in a range from −0.58 to +2.37 ‰, relative to the Vienna Pee Dee Belemnite (V-PDB) standard. From duplicate samples collected during both cruises, the one-sigma precision for the 552 results is ± 0.086 ‰, which is similar to other published studies of this kind. Data doi:10.5285/09760a3a-c2b5-250b-e053-6c86abc037c0 (Northeastern Atlantic), doi:10.5285/09511dd0-51db-0e21-e053-6c86abc09b95 (Nordic Seas).

3.1 Introduction

To predict the future response of the ocean carbon sink to continued changes to the atmospheric CO_2 partial pressure (pCO_2^{atm}), it is essential first to understand the existing spatial distribution of anthropogenic dissolved inorganic carbon (DIC). A variety of methods have been employed to achieve this (Sabine and Tanhua, 2010), including: back-calculation from DIC, total alkalinity and oxygen measurements (Brewer, 1978; Chen and Millero, 1979; Gruber et al., 1996); correlation with distributions of other anthropogenic transient tracers such as chlorofluorocarbons (Hall et al., 2002); and multi-linear regressions between observational data from pairs of cruises separated in time (Tanhua et al., 2007). Multi-decadal measurements have shown that increases in the pCO_2^{atm} and ocean DIC have been accompanied by reductions in their carbon-13 content relative to carbon-12 ($\delta^{13}C$, Equations 3.1 and 3.2), a phenomenon known as the Suess effect (Keeling, 1979). This occurs because anthropogenic CO_2 is isotopically lighter (i.e. it has a lower $\delta^{13}C$ signature) than pre-industrial and present-day atmospheric CO_2, as a result of its biological provenance; it provides another way to investigate the spatial distribution of anthropogenic DIC and quantify its inventory (Quay et al., 1992, 2003, 2007; Sonnerup et al., 1999, 2007). Additionally, because the $\delta^{13}C$ of DIC ($\delta^{13}C_{DIC}$) takes approximately 10 times longer to equilibrate with the atmosphere than DIC itself (Lynch-Stieglitz et al., 1995), their relative rate of change in the interior ocean can constrain the length of time a given water mass last spent at the ocean surface (McNeil et al., 2001a, 2001b; Olsen et al., 2006). Finally, $\delta^{13}C_{DIC}$ measurements are important for verification of predictions made by ocean carbon cycle models (Sonnerup and Quay, 2012).

This chapter presents measurements of seawater $\delta^{13}C_{DIC}$ from two cruises during summer 2012. The first cruise (RRS *James Clark Ross*, cruise JR271) was carried out by the Sea Surface Consortium, part of the UK Ocean Acidification research programme (UKOA). These $\delta^{13}C_{DIC}$ measurements will contribute towards quantifying the impact of ocean acidification upon the ocean carbon cycle and the biogeochemical processes which affect it, a high-level objective for this Northeastern Atlantic/Nordic Seas cruise and the UKOA. The second cruise (RRS *Discovery*, cruise D379) was a repeat occupation of the Extended Ellett Line (EEL) hydrographic transect in the Northeastern Atlantic. These are the first $\delta^{13}C_{DIC}$ measurements made during an EEL cruise, establishing a baseline for future work on the transect. These measurements

have been used to independently support the quantitative attribution of changes in DIC at the EEL to anthropogenic and other drivers (Chapter 4).

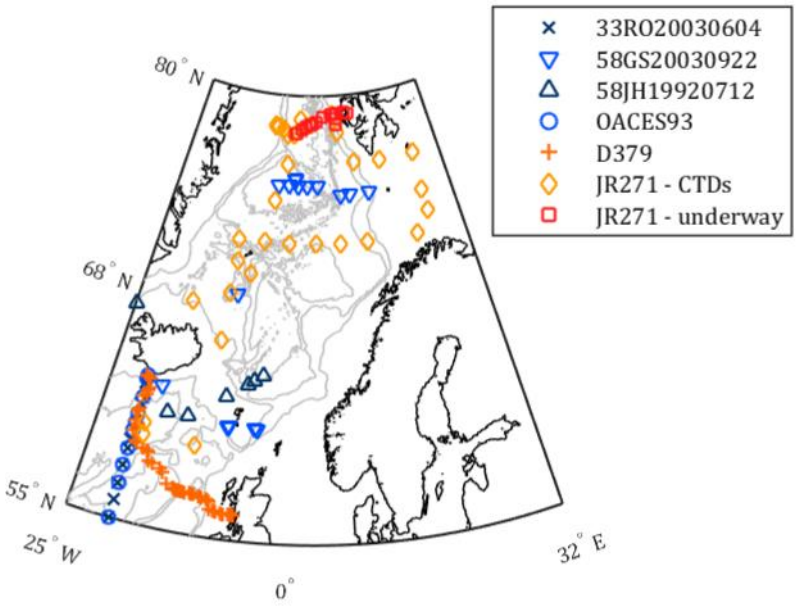

Figure 3.1. Sample locations for cruises D379 (orange plusses) and JR271 (CTD stations: gold diamonds; underway: red squares), along with nearby historical $\delta^{13}C_{DIC}$ data locations from the Schmittner et al. (2013) compilation, for context: cruises 33RO20030604 (dark blue crosses), 58GS20030922 (blue inverted triangles), 58JH19920712 (dark blue triangles) and OACES93 (blue circles). Grey contours indicate bathymetry at 500 m intervals from the GEBCO_2014 grid, version 20141103, http://www.gebco.net.

3.2 Sample collection

3.2.1 Cruise details

Samples for $\delta^{13}C_{DIC}$ measurements were collected during two cruises. (1) RRS *James Clark Ross* cruise JR271, which took place between 1st June and 2nd July 2012 in the Northeastern Atlantic and Nordic Seas (Leakey, 2012). During JR271, the maximum depth sampled at most stations was shallower than 500 m, because the overall sampling strategy for that cruise and research programme involved assessment of ocean acidification on surface ocean biogeochemical processes. The underway surface water samples collected during JR271 were from a transect across the Fram Strait at approximately 79°N, the northernmost part of the cruise. (2) RRS *Discovery* cruise D379, which took place between 31st July and 17th August 2012, in the Northeastern Atlantic (Griffiths, 2012). Sample collection during D379 was carried out by Alex M. Griffiths (University of Southampton). The Extended Ellett Line (EEL) transect covered by D379 runs from Scotland to Iceland via the Rockall Trough and plateau, and the northernmost section of the route (at 20°W) overlaps the northern end of the A16 World Ocean Circulation Experiment (WOCE) hydrographic transect. The samples collected cover the full depth range. For both cruises, the sample locations are illustrated by Figure 3.1, and information about the number and types of samples collected is given in Table 3.1.

3.2.2 Collection and storage methods

Prior to sample collection, the containers were thoroughly rinsed with deionised water (MilliQ water, Millipore, >18.2 mΩ cm^{-1}). Samples were collected from the source (either Niskin bottle or underway seawater supply) via silicone tubing, following established best-practice protocols (Dickson et al., 2007; McNichol et al., 2010). The containers were thoroughly rinsed with excess sample directly before filling until overflowing with seawater, taking care not to generate or trap any air bubbles. Two different sample containers were used: (1) 100 mL soda-lime glass bottles with ground glass stoppers (Dixon Glass, UK), lubricated with Apiezon® L grease and held shut with tape; (2) 50 mL glass vials with plastic screw-cap lids and polytetrafluoroethylene/silicone septa. Saturated mercuric chloride solution equivalent to 0.02 % of the sample container volume was added to sterilise each sample before sealing. A 1 mL air headspace was also introduced to the bottles, but

the vials were sealed completely full of seawater. The samples were stored in the dark until analysis.

Cruise	Samples	CTD stations		Underway	Total
		Bottles	Vials	Bottles	
JR271	Unique samples	210	0	17	227
	Incl. duplicates	221	0	17	238
D379	Unique samples	62*	263	0	325
	Incl. duplicates	66	284	0	350
Both (Totals)	Unique samples	272	263	17	552
	Incl. duplicates	287	284	17	588

Table 3.1. Quantities and types of samples collected during cruises JR271 and D379, and types of sample containers used. D379 duplicates where one sample was collected in each type of container are counted in the 'Unique samples – Bottles' cell (asterisked). The rows labelled 'Both (Totals)' show the total number of samples collected during both cruises.

3.3 Sample analysis

The $\delta^{13}C_{DIC}$ samples were analysed at the Scottish Universities Environmental Research Centre Isotope Community Support Facility (SUERC-ICSF) in East Kilbride, UK between June and August 2013.

3.3.1 Definitions

The abundance of carbon-13 (^{13}C) relative to that of carbon-12 (^{12}C) in a given substance *X* is given by Equation 3.1. For each sample *X*, R_X is then normalised to a reference *standard* using Equation 3.2 to give that sample's $\delta^{13}C$.

Equation 3.1

$$R_X = \frac{[^{13}C]_X}{[^{12}C]_X}$$

where $[^{13}C]_X$ and $[^{12}C]_X$ are the concentrations of ^{13}C and ^{12}C respectively in *X*.

Equation 3.2

$$\delta^{13}C = \frac{R_X - R_{standard}}{R_{standard}} \cdot 1000\ ‰$$

3.3.2 Analysis procedure

Samples were analysed in a batch process. For each batch, $\delta^{13}C$ was measured in 88 Exetainer® glass vials, each of 12 mL volume. At least 18 vials per batch were set aside for calibration standards ('standard vials'), while the rest were used for seawater samples ('sample vials').

Most of the standards were analysed before any samples, at the start of each batch ('initial standards'), except for a pair near the middle and at the end ('mid-point standards' and 'end-point standards' respectively). Three SUERC-ICSF in-house standards (powdered carbonate/bicarbonate solids called MAB, NA and CA; see Table 3.2) were used to calibrate the $\delta^{13}C_{DIC}$ results to the Vienna Pee Dee Belemnite (V-PDB) international standard (Coplen, 1995). These in-house standards have previously been calibrated against the NBS 19 international standard by researchers at SUERC-ICSF. The initial standards consisted of a range of masses of all 3 of the in-house standards. The mid- and end-point standards, used for drift correction, were of similar mass and the same type (MAB for batches 1 and 2, and NA thereafter).

Name	Chemical composition	C = Certified $\delta^{13}C$ V-PDB / ‰
MAB	$CaCO_3$	+ 2.48
NA	$NaHCO_3$	– 4.67
CA	$CaCO_3$	– 24.23

Table 3.2. The SUERC-ICSF in-house calibration standards. In the final column, *C* refers to Equation 3.4.

A total of 103 seawater samples were subsampled twice and analysed consecutively ('analysis duplicates'). This was carried out for all samples in the first 2 batches, and every 10th sample thereafter.

The analysis procedure was necessarily slightly different for the standards and samples because of their different states (solid and liquid respectively). The standard and sample vials were soaked and rinsed with deionised water, then dried overnight at 65 °C. The calibration materials were weighed into the standard vials, whilst 80 µL of concentrated phosphoric acid (mixed with phosphorus pentoxide to generate 100 % acid saturation) was added to each sample vial, to convert all of the dissolved carbonate and bicarbonate in the seawater sample (added later) into CO_2. All vials were then closed using plastic screw-cap lids with PTFE/silicone septa to make an air-tight seal. These lids were not removed until the entire analysis process was complete. All addition or removal of fluids from the vials after this point was via injection of a needle through the septa.

The air in each vial was replaced, to remove CO_2, by flushing with helium for 15 minutes ('overgassing'). This was an automated process carried out by a CTC Analytics PAL system. After overgassing, 1 mL of the phosphoric acid/phosphorus pentoxide diluted with deionised water to 10 % concentration (by volume) was added to each standard vial. For each sample, a syringe was rinsed 3 times with the sample and then used to transfer 1 mL of that sample into the vial. All of the vials were then left for at least 24 hours for the standard or sample to fully react with the acid and equilibrate with the gas headspace.

Finally, the gas headspace in each vial was automatically sampled by the PAL System, and the $\delta^{13}C$ of the CO_2 measured 10 times by a Thermo Scientific Delta V mass spectrometer attached to a Thermo Scientific Gasbench 2. The set of 10

measurements for each sample or standard are henceforth referred to as ‘technical replicates’.

3.4 Measurement processing

3.4.1 Batch-by-batch processing

The raw $\delta^{13}C$ results were processed using MATLAB (MathWorks) software in five steps: (1) erroneous measurement removal, (2) averaging, (3) peak area correction, (4) calibration to V-PDB, and (5) drift correction. Except where specified, these steps were applied to each analysis batch independently, using only data from that specific batch.

3.4.1.1 Erroneous measurement removal

To begin, erroneous $\delta^{13}C$ measurements were removed from the sets of technical replicates. These typically occurred when the CO_2 concentration in a replicate was too high or low, resulting in the peak area falling outside of the calibration range. Therefore, only measurements with a peak area between 10 and 145 were retained, and if fewer than 6 of the original 10 technical replicates for a given sample fell in the acceptable peak area range, the entire sample was discarded.

3.4.1.2 Averaging

After erroneous measurements were removed, the mean $\delta^{13}C$ and peak area was calculated from each sample's technical replicates. These mean values were used for the remainder of the data processing.

3.4.1.3 Peak area correction

Plots of peak area against raw $\delta^{13}C$ reveal relationships which are different for each of the 3 calibration standards (Figure 3.2) and for seawater (Figure 3.3). Peak area is controlled by CO_2 concentration, so a range of peak areas can be generated by using a range of masses of calibration standards, or volumes of seawater, in different analyses, and these results can be used to quantify and correct for the relationships between peak area and raw $\delta^{13}C$. All corrections were linear and made to a peak area of 35, which is approximately equal to the mean peak area for all seawater samples across all analysis batches. For the calibration standards, the corrections were derived using the initial standards. For each batch, a linear least-squares regression between peak area and raw $\delta^{13}C$ was derived for each standard. Regressions were discarded if the range of input peak areas either (1) did not include the value 35, or (2) was smaller than 30. The mean gradient for each of the three standards (excluding

discarded regressions) was then calculated across all batches and used to make the peak area correction for each standard (Figure 3.2).

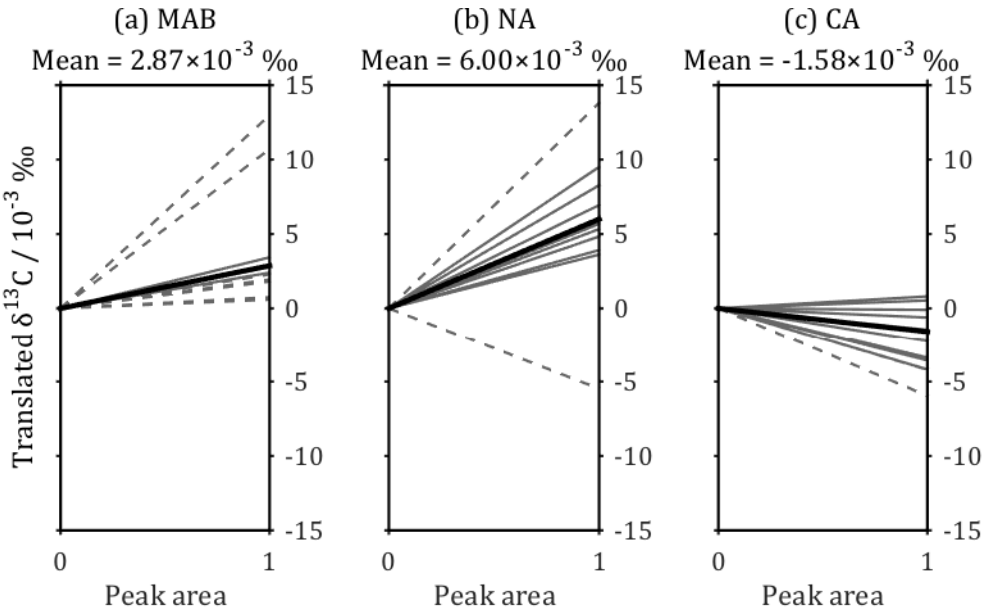

Figure 3.2. Peak area versus $\delta^{13}C$ relationships used for the peak area correction of the calibration standards (a) MAB, (b) NA and (c) CA (Table 3.2). The grey lines are the linear least-squares best fit for each analysis batch, but translated to have a vertical axis intercept of 0 (so that the value of the line at peak area = 1 is equal to the gradient). The dashed lines indicate batches excluded from calculation of the mean gradient for each standard (thick black line; see text for exclusion criteria).

For the seawater samples, 6 subsamples of a large homogeneous seawater sample were taken in volumes from 0.50 to 1.50 mL (in 0.25 mL increments). These were measured consecutively during analysis batch #6, and a linear least-squares regression of $\delta^{13}C$ against peak area was used to make the linearity correction for all seawater samples from all batches (Figure 3.3). All corrections were made using an equation of the form:

Equation 3.3 $$\delta_{\mathrm{corr}} = \delta_{\mathrm{meas}} - g(A - 35)$$

where δ_{corr} is the corrected $\delta^{13}C_{DIC}$ value; δ_{meas} is the original, uncorrected $\delta^{13}C_{DIC}$ value; A is the peak area; and g is the appropriate correction gradient. For the standards MAB, NA and CA, g is 2.87×10^{-3}, 6.00×10^{-3} and -1.58×10^{-3} respectively (Figure 3.2), while for the seawater samples, g is 1.04×10^{-2} (Figure 3.3).

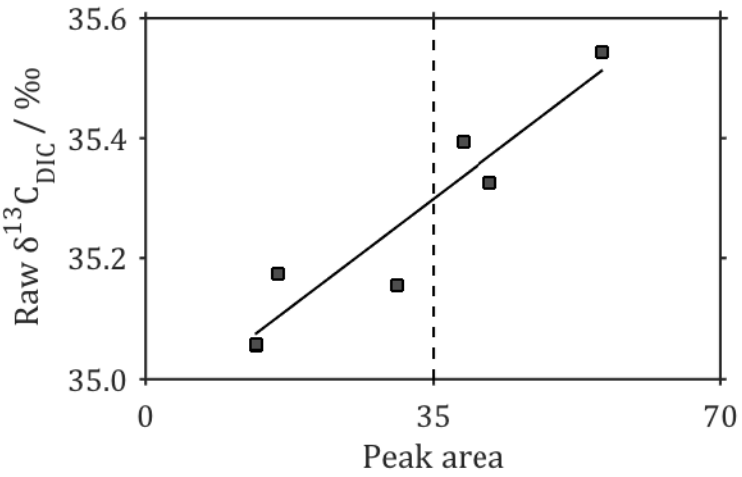

Figure 3.3. Peak area versus $\delta^{13}C$ relationship for homogeneous seawater sampled at a range of volumes from 0.5 to 1.5 mL (grey squares). The black best-fit line shows the relationship used to correct all seawater samples for peak area, with gradient 0.0104 and vertical-axis intercept 34.9346. The vertical dashed line at peak area = 35 indicates the peak area to which corrections have been made.

3.4.1.4 Calibration to V-PDB

The mean of the peak-area-corrected $\delta^{13}C$ for each of the 3 calibration standards was calculated (L), using only the measurements of the initial standards. A non-linear fit (Equation 3.4) between L and the corresponding certified values relative to V-PDB (C, Table 3.2) was used to determine constants p, q and r for each batch, and then calibrate the samples to the V-PDB international standard (Coplen, 1995). The fit used an equation of the form:

Equation 3.4 $$L^2 + C^2 + pL + qC + r = 0$$

3.4.1.5 Drift correction

An interpolation between three points was used to correct for instrument drift during each batch. The index was the analysis position, with the mean analysis positions for the initial, mid-point and end-point standards as sample points for the interpolation. The initial point was assigned a value (drift) of 0, and mid-point and end-point values were calculated by subtracting the mean calibrated $\delta^{13}C$ for each of the mid-point and end-point standard pairs from their certified values (Table 3.2). Piecewise cubic Hermite interpolating polynomial (PCHIP) fits (Fritsch and Carlson, 1980) between analysis position and drift were generated and used to correct all results other than the initial standards. The PCHIP fits generate a smooth, continuous function with a

continuous first derivative that do not predict outputs falling outside the range of input values and that fit the data better than other functions (e.g. linear fits), judged by eye.

3.4.2 Quality control

After calibration, the mean $\delta^{13}C_{DIC}$ and its standard deviation (SD) was calculated for all seawater samples in all batches. Four of the 608 measurements had extremely low $\delta^{13}C_{DIC}$ values, more than 6 SDs away from the mean. These measurements were discarded; they are assumed to represent sample containers where the air-tight seal failed and so the DIC is contaminated with atmospheric CO_2, which has a much lower $\delta^{13}C$ than typical ocean DIC (Lynch-Stieglitz et al., 1995). The $\delta^{13}C_{DIC}$ measurements were finally combined with their cruise metadata, using the mean values for pairs of analysis and sample duplicates, and the differences between the two samples in each duplicate pair calculated for statistical evaluation.

3.4.3 Data availability

The final, calibrated $\delta^{13}C_{DIC}$ results have been archived with the British Oceanographic Data Centre and are publicly accessible, free of charge (Humphreys et al., 2014a, 2014b). Measurements of additional hydrographic variables for cruise D379 are similarly available from the Carbon Dioxide Information Analysis Center (Hartman et al., 2014b). The $\delta^{13}C_{DIC}$ results have also been submitted to an ongoing global compilation of seawater $\delta^{13}C_{DIC}$ data (Becker et al., 2015) as part of which they will undergo a secondary quality-control procedure.

3.5 Discussion and statistics

3.5.1 Erroneous measurement removal

The process of removing erroneous measurements from the raw data eliminated approximately 1 % of the seawater sample technical replicates, but reduced the mean and maximum standard deviation (SD) of these sets of replicates by one and three orders of magnitude respectively. Limiting the range of acceptable peak areas was responsible for almost all of the reduction in the mean SD and significantly reduced the maximum SD. Intermittent very low peak areas were suspected to be a consequence of transient liquid blockages in the tubing that drew the gaseous samples from the vials into the mass spectrometer. The second step of discarding samples with fewer than 6 technical replicates in this acceptable peak area range made little difference to the mean SD, but resulted in a further significant reduction to the maximum SD (Table 3.3). Figure 3.4 illustrates the SD of all sets of technical replicates for samples throughout the analysis.

Measurement removal step	Number of measurements	Number of sample sets	Mean tech. rep. SD / ‰	Max. tech. rep. SD / ‰
All raw data	7410	741	0.240	66.60
10 < peak area < 145	7349	740	0.029	0.616
Valid tech. reps ≥ 6	7329	734	0.028	0.058

Table 3.3. Summary of the erroneous measurement removal process for all of the seawater samples. Numbers in each row are for all data after application of the measurement removal step indicated in the first column. 'Tech. rep. SD' = standard deviation of uncalibrated $\delta^{13}C_{DIC}$, calculated for each sample's set of 10 technical replicates.

3.5.2 Calibration to V-PDB

Initially, a linear fit was used to calibrate the raw $\delta^{13}C$ measurements to the V-PDB standard. However, application of this calibration to the same standards that it was generated from resulted in overestimations of the MAB and CA standards, and underestimations for NA, relative to the certified values. The over/underestimates were consistent in polarity across all batches, with mean values of +0.08 ‰, –0.10 ‰

and +0.03 ‰ for MAB, NA and CA respectively. This was resolved by using a non-linear calibration fit. A circular fit (Equation 3.4) was used, rather than an ordinary polynomial, because it maintains constant curvature in the calibration space, which has the same units (‰) on both axes. With the non-linear fit, for all standards across all 11 batches, the mean ± SD of the difference between calibrated and certified $\delta^{13}C$ was 0.00 ± 0.06 ‰ (MAB, 59 analyses), 0.00 ± 0.11 ‰ (NA, 73 analyses) and 0.00 ± 0.08 ‰ (CA, 47 analyses) (Figure 3.5).

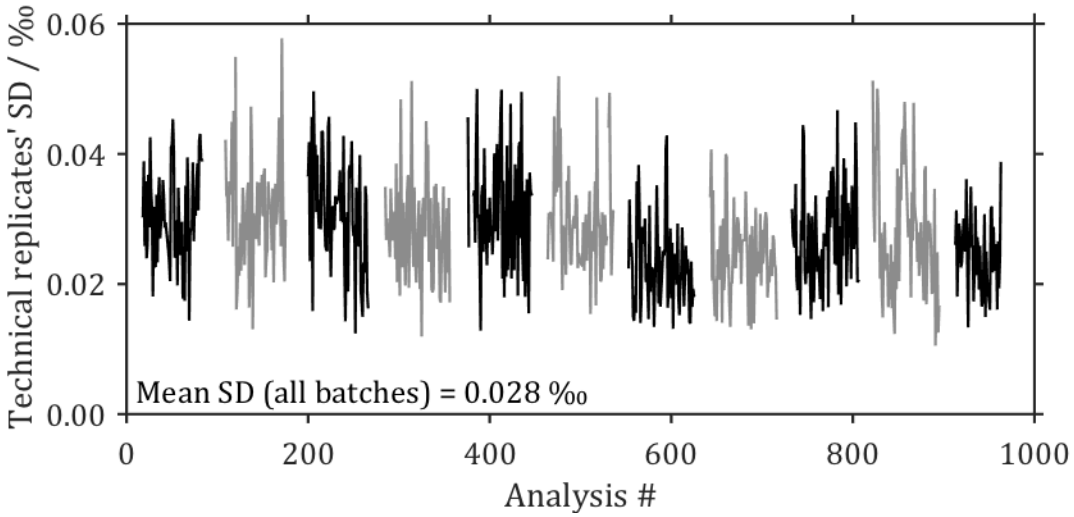

Figure 3.4. Standard deviation (SD) of technical replicates for each seawater sample, after erroneous peak removal. Alternating black and grey sections indicate separate analysis batches.

It would be beneficial for future analyses to develop a set of dissolved standards with certified $\delta^{13}C_{DIC}$ for calibration purposes, to avoid having a different analytical method for the standards than for the samples. Certified reference material (CRM) seawater produced by A.G. Dickson (Scripps Institution of Oceanography, USA) does not have a certified $\delta^{13}C_{DIC}$, but the procedures by which it is created and stored to ensure that the DIC and TA do not change should also mean that $\delta^{13}C_{DIC}$ is consistent between different bottles of the same batch. This could perhaps be used as a starting point for creating a standard which can be treated in the same way as the samples.

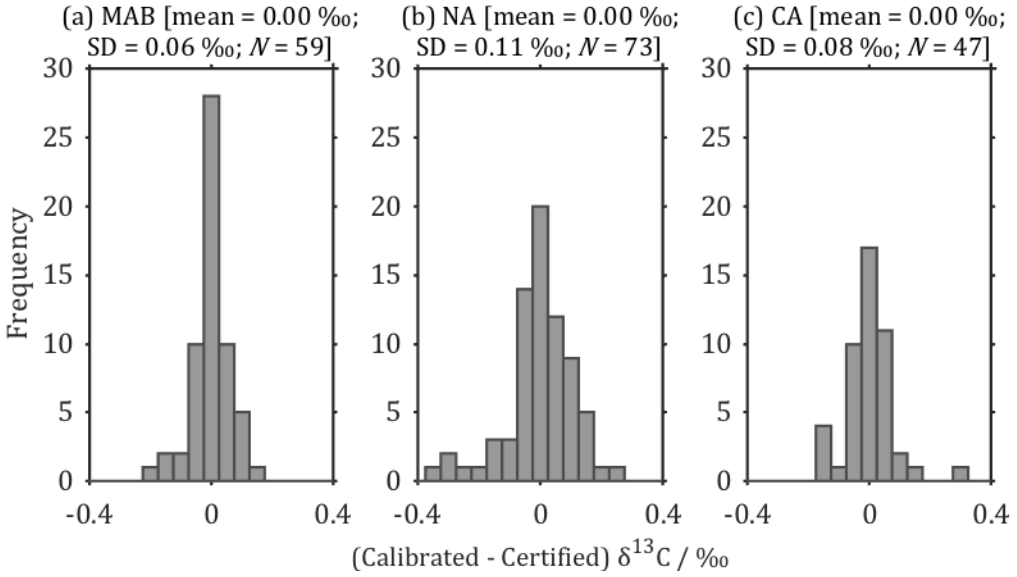

Figure 3.5. Distributions of the difference between calibrated and certified $\delta^{13}C$ for calibration standards (a) MAB, (b) NA and (c) CA (Table 3.2) in all batches. SD = standard deviation; N = number of analyses.

3.5.3 Precision from duplicates

Comparison with published estimates of precision for $\delta^{13}C_{DIC}$ measurements is complicated by the various different definitions used in the literature. In this study, the mean absolute difference in calibrated $\delta^{13}C_{DIC}$ for all analytical duplicate pairs was 0.053 ‰. This is very close to published values which we believe to be equivalently defined. For example, Olsen et al. (2006) quote a long-term precision for $\delta^{13}C$, based on replicates, of 0.05 ‰.

To evaluate the true measurement precision, including error introduced by the sampling process, it is necessary to use the sample duplicates rather than the analytical duplicates (Table 3.4). The mean duplicate pair difference for samples in the same type of container across both cruises was 0.097 ‰. However, where the duplicate samples were collected in different containers (one in a bottle, one in a vial), the mean absolute duplicate pair difference took the higher value of 0.168 ‰. This suggests that the small differences in the sampling method for the different containers introduced a small but measurable increase in the error. To test if there was a systematic offset in $\delta^{13}C_{DIC}$ measured in the different container types, we subtracted the vial value from the bottle value for these duplicate pairs with non-matching containers, and performed a one-sample *t*-test for the null hypothesis that the resulting distribution had a mean value of 0. It was not possible to reject the null

hypothesis at the 95 % certainty level, so we did not find a consistent offset between the container types.

Cruise	Sample container	Number of pairs	Mean absolute difference / ‰
D379	Same	16	0.109
JR271	Same	11	0.080
Both	Same	27	0.097
D379	Different	9	0.168

Table 3.4. Mean absolute differences between sampling duplicates. The 'sample container' column indicates whether the duplicates were collected in the same type of container as each other, or different containers (i.e. one in a vial, one in a bottle).

The expected SD of many measurements of the same sample (i.e. one-sigma precision) can be estimated from the mean of the duplicate pair absolute differences by dividing the latter by $2/\sqrt{\pi}$ (Thompson and Howarth, 1973), as follows. Each duplicate pair is considered to be two samples randomly drawn from a normal distribution, with an SD equal to the one-sigma measurement precision (σ), and a mean equal to the 'true' $\delta^{13}C_{DIC}$ value. If the 'duplicate pair differences' are calculated by subtracting the $\delta^{13}C_{DIC}$ of the first sample in each pair from that of the second, the resulting normal distribution of these differences (across all duplicate pairs) should have a mean of 0 and a SD of $\sigma\sqrt{2}$. The absolute differences therefore form a half-normal distribution; a generic half-normal distribution has a mean value of the SD of the normal distribution that it is half of multiplied by $\sqrt{2}/\sqrt{\pi}$. In this case, the SD is $\sigma\sqrt{2}$, and so the mean of the half-normal distribution – that is, the mean of the absolute differences between duplicate pairs – is $2\sigma/\sqrt{\pi}$. Thus, the one-sigma precision (σ) can be estimated from the mean of the duplicate pair absolute differences by dividing the latter by $2/\sqrt{\pi}$.

For this study, for the duplicates from both cruises which were in the same type of container, the precision is therefore 0.086 ‰ (based on mean absolute difference of 0.097 ‰, Table 3.4). Like the analytical precision, this compares well with equivalent published values. For example: Olsen et al. (2006) found an SD of 0.07 ‰ for 16

samples taken in seawater with 'very similar physical and chemical water mass characteristics'; McNichol et al. (2010) record a 'replication' of ±0.03 ‰ from measurements of duplicate seawater samples from the Niskin bottle; and Griffith et al. (2012) calculated a 'pooled SD' for 8 duplicate $\delta^{13}C_{DIC}$ samples of 0.23 ‰.

3.5.4 Results distribution

The measured $\delta^{13}C_{DIC}$ values during both cruises D379 and JR271 are illustrated by Figures 3.6 and 3.7. All of the $\delta^{13}C_{DIC}$ measurements were in the range from to –0.58 to +2.37 ‰, relative to V-PDB. A detailed description of the distribution of $\delta^{13}C_{DIC}$ is beyond the scope of this chapter, but the results from the Extended Ellett Line hydrographic transect (cruise D379, Figure 3.7) are discussed further in Chapter 4.

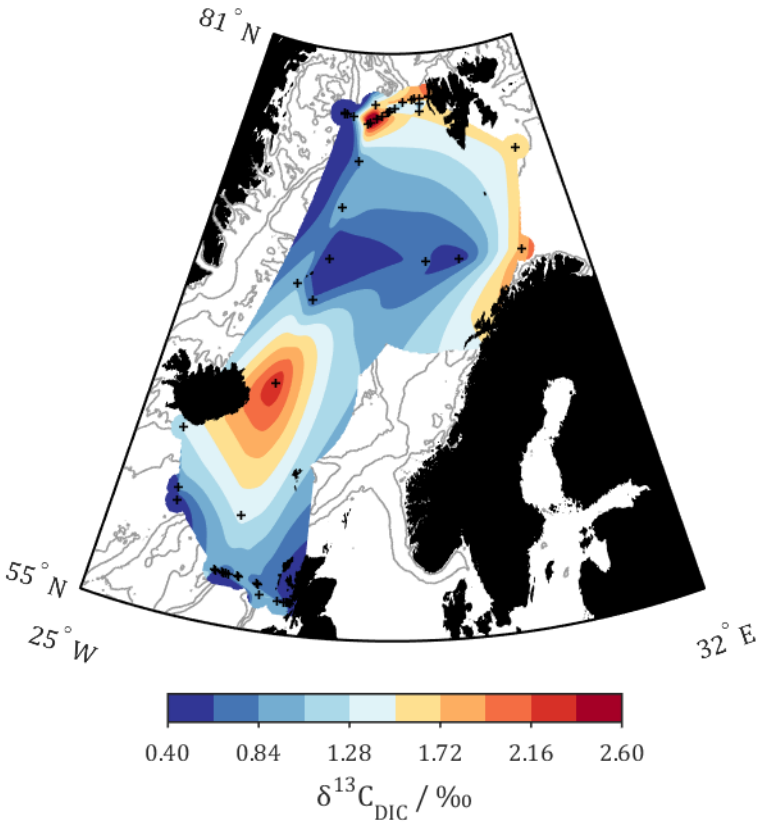

Figure 3.6. Measured $\delta^{13}C_{DIC}$ for all samples from both cruises collected at a depth shallower than 10 m. Actual sampling points are indicated by black plusses.

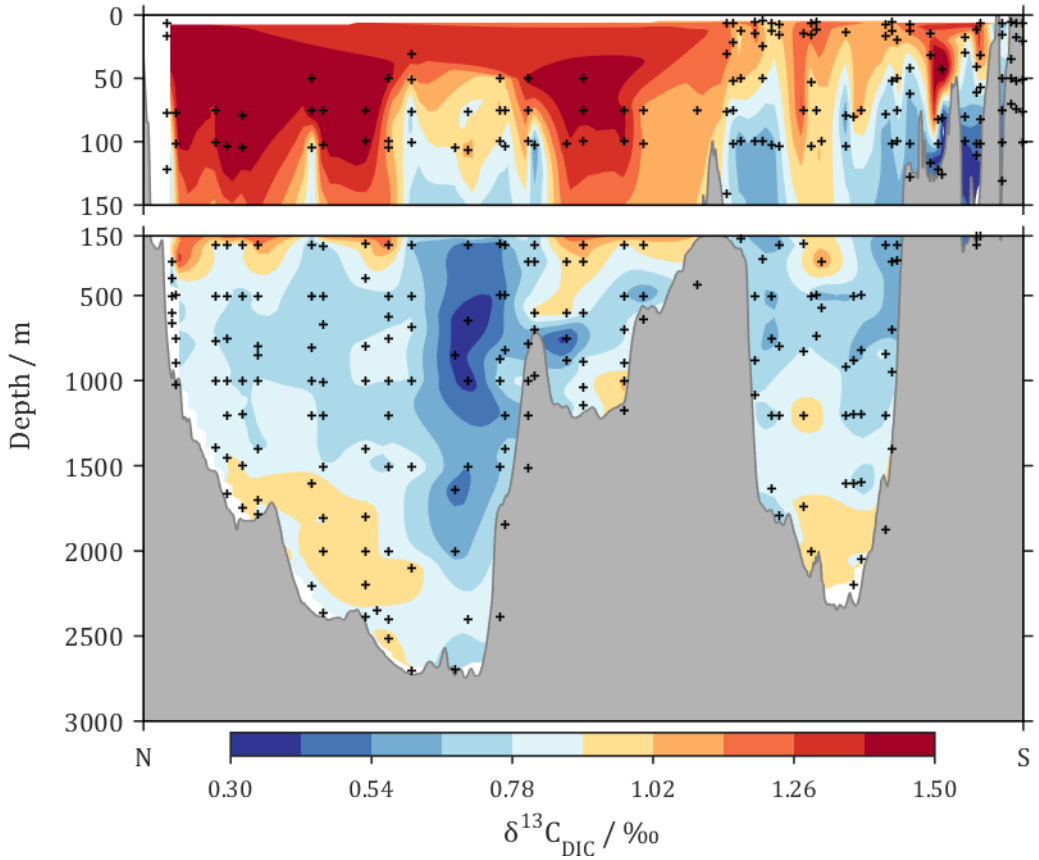

.

Figure 3.7. Measured $\delta^{13}C_{DIC}$ for all samples from cruise D379. Actual sampling points are indicated by black plusses. Section runs from Iceland to Scotland from left to right; see Figure 3.1 for precise route. Bathymetry data are from the GEBCO_2014 grid, version 20141103, http://www.gebco.net, and are approximate to the cruise route

4

Combined observational and model assessment of anthropogenic carbon accumulation along the Extended Ellett Line hydrographic transect, Northeast Atlantic Ocean, from 1981 to 2013

Abstract

Marine carbonate chemistry measurements have been carried out annually since 2009 during UK research cruises on the Extended Ellett Line (EEL), an oceanographic transect in the Northeast Atlantic Ocean. The EEL intersects several water masses which are key to the global thermohaline circulation, and therefore it samples a critical region to monitor physical and biogeochemical change. Results from these EEL cruises have been combined with several quality-controlled data syntheses to produce a hydrographic time-series for the EEL transect from 1981 to 2013, and to detect multi-decadal increases in dissolved inorganic carbon (DIC) throughout the water column with a near-surface maximum rate of 1.65 ± 0.47 μmol kg^{-1} yr^{-1}. Integrating by volume and using corresponding changes in dissolved oxygen (DO) and total alkalinity (TA) as proxies for other processes controlling DIC reveals an anthropogenic CO_2 accumulation rate of 1.71 ± 0.15 mg-C m^{-3} yr^{-1} (i.e. approximately 0.14 ± 0.01 mmol-C m^{-3} yr^{-1}), which is about 114 % of the global mean. This represents only 22.3 ± 2.2 % of the total DIC increase; the remainder is associated with increased remineralised organic matter content, which may be driven by lateral changes in water mass distributions induced by subpolar gyre contraction, evidenced by simultaneous changes in DO, TA, and the stable isotopic composition of DIC. Output from a general circulation-ecosystem model demonstrates that spatial and temporal heterogeneity in the observations' distribution does not adversely affect the calculated rates of change on multi-decadal timescales, and indicates that the EEL observations may track ongoing distal changes in the North Atlantic and Nordic Seas.

4.1 Introduction

Open-ocean time-series sites which monitor marine carbonate chemistry provide essential observational data to quantify long-term trends in anthropogenic CO_2 uptake and acidification (e.g. Dore et al., 2009; Olafsson et al., 2009; González-Dávila et al., 2010; Bates et al., 2012), and also to validate output from global coupled ocean-atmosphere models (Le Quéré et al., 2010). However, only a handful of these sites exist globally (Bates et al., 2014). In this chapter, a new time-series of carbonate chemistry measurements is presented for the Extended Ellett Line (EEL), an open-ocean transect in the Northeast Atlantic. The EEL runs from Iceland to Scotland via the Rockall Plateau (Figure 4.1), and repeated physical measurements have been carried out there since 1975 (Holliday and Cunningham, 2013). The transect captures the flow of warm, salty water from the North Atlantic into the Nordic Seas, and around half of the returning deep, cold overflow current, with the remaining overflow returning south via the west of Iceland (Hansen and Østerhus, 2000). This is a critical region to monitor because of the importance of the high latitude North Atlantic for both oceanic uptake and storage of anthropogenic CO_2, estimated to account for 23 % of global oceanic anthropogenic CO_2 storage despite covering only 15 % of the global ocean surface area (Sabine et al., 2004; Khatiwala et al., 2009). As the EEL will continue to be surveyed by UK research vessels, this analysis provides a baseline which can be extended in future years as more data becomes available.

This new time-series consists of measurements carried out during annual EEL cruises from 2009 to 2013, augmented by hydrographic data from several quality-controlled compilations (Key et al., 2004, 2010; Schmittner et al., 2013). It has been used to quantify the rate of change of dissolved inorganic carbon (DIC) throughout the water column along the EEL, and corresponding changes in apparent oxygen utilisation (AOU) and total alkalinity (TA) have isolated its anthropogenic component (Section 4.4.1). The partitioning of the DIC change into this and other components is supported by observed changes in the stable isotopic composition of DIC (Section 4.4.2). Output from a coupled ocean general circulation-biogeochemical model demonstrates the robustness of the calculated rates of change, their independence from the spatiotemporal heterogeneity of the observations, and suggests that changes observed at the EEL may match similar magnitude changes throughout the surrounding ocean basins, confirming its importance for continued future monitoring (Section 4.4.3).

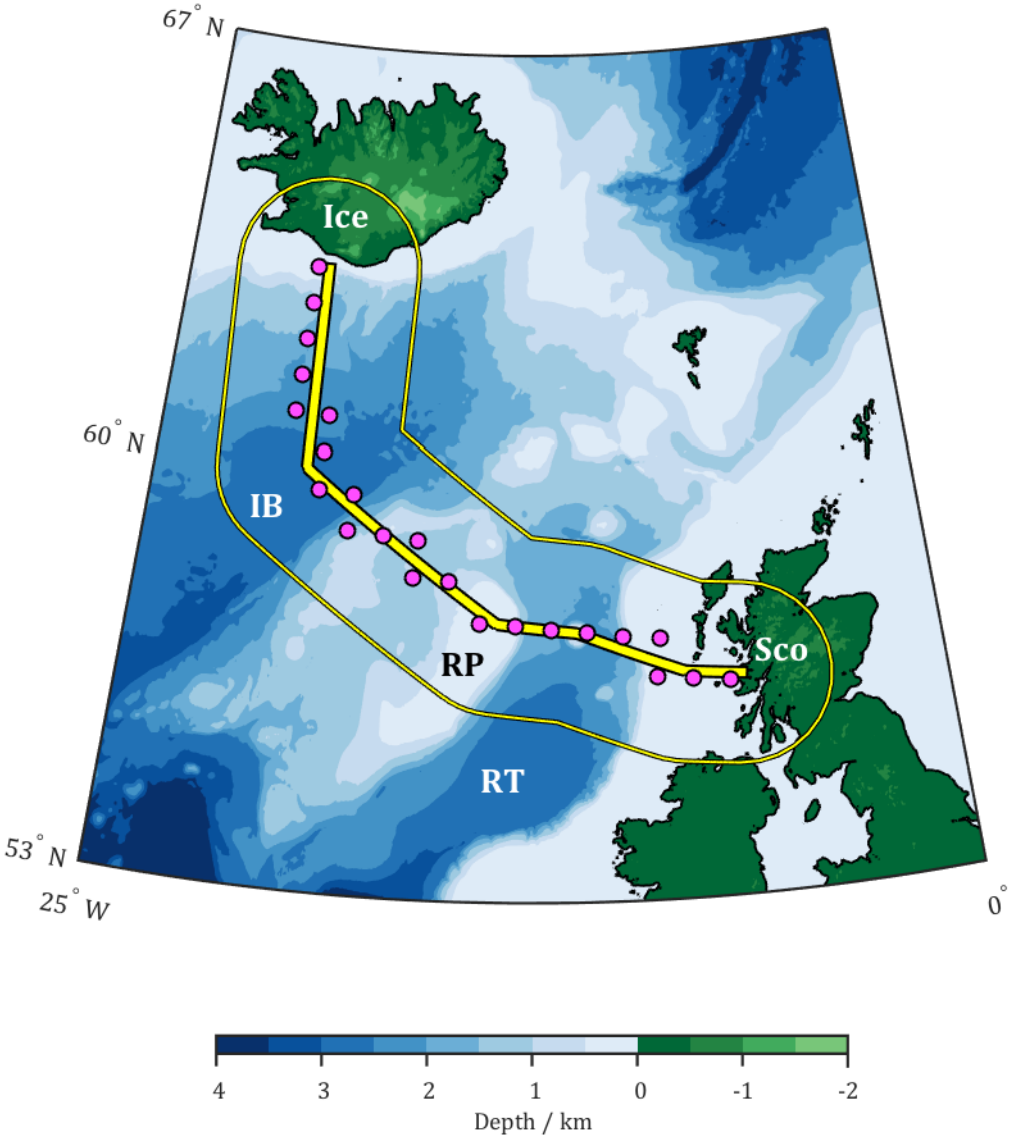

Figure 4.1. Bathymetry of the Extended Ellett Line (EEL) region from the GEBCO_2014 grid (version 20141103, www.gebco.net). Idealised EEL route (Table 4.1) and surrounding 167 km-radius zone around it (from within which data were selected for this analysis – Section 4.3.1.1), are indicated by the thick and thin yellow lines respectively. Magenta circles show locations of the 'model stations' selected to represent the ideal EEL: the TAA data set. Abbreviations: IB = Iceland Basin; RP = Rockall Plateau; RT = Rockall Trough; Ice = Iceland; Sco = Scotland.

4.2 Methods and data acquisition

4.2.1 Observations

4.2.1.1 Carbonate chemistry measurements

The EEL was occupied annually from 2009 to 2013 by RRS *Discovery* cruises D340 (Sherwin, 2009), D351 (Read, 2010), D365 (Read, 2011) and D379 (Griffiths, 2012), and RRS *James Cook* cruise JC086 (Griffiths and Holliday, 2013). Carbonate chemistry sample collection and measurements were carried out by V.M.C. Rérolle (D340 & D351), M. Esposito (D351 & D365), A.M. Griffiths (D379) and J.-L. Menzel Barraqueta (JC086), the latter two under my supervision. Samples for DIC and TA were collected from the CTD rosette via silicone tubing into 250 ml borosilicate glass bottles following established best practice procedures (Dickson et al., 2007). Immediately after sample collection, a 2.5 ml air headspace and 50 µl of saturated mercuric chloride solution were added to each bottle. Bottles were then immediately sealed with ground glass stoppers lubricated with Apiezon® L grease, and held shut with tape. Analysis was carried out at the National Oceanography Centre, Southampton using a VINDTA 3C system. For the DIC measurement, all DIC is converted to CO_2 by acidifying samples with 10 % phosphoric acid, and the CO_2 is removed by purging with nitrogen gas. The total amount of CO_2 in the gas stream is then determined by coulometric titration. To measure TA, an open-cell potentiometric titration with 0.1 M hydrochloric acid is carried out on the sample, and a modified Gran approach used to estimate TA from the titration data (Bradshaw et al., 1981; also see Chapter 2). DIC and TA results were calibrated using certified reference material obtained from A.G. Dickson (Scripps Institution of Oceanography, USA). Approximately 1 in 10 samples were collected in duplicate, to estimate the measurement precision: ± 3 µmol kg^{-1} for DIC and ± 2 µmol kg^{-1} for TA. These data have been archived with the Carbon Dioxide Information Analysis Center (Hartman et al., 2014a, 2014b, 2014c). Note that the TA results for cruise D365 used in this chapter differ from those provided by Hartman et al. (2014a) for the reasons discussed in Section 2.3.3 – they have been recalibrated in order to correct systematic offsets with measurements from previous cruises.

4.2.1.2 $\delta^{13}C_{DIC}$ measurements

During cruise D379, samples were collected to measure the stable isotopic composition of DIC ($\delta^{13}C_{DIC}$) by A.M. Griffiths. Full details of the sample collection and analysis are provided in Chapter 3 and by Humphreys et al. (2015), and the data set is freely accessible (Humphreys et al., 2014b).

4.2.1.3 Other measurements

Continuous depth profiles of temperature (*T*), conductivity, pressure (*P*) and dissolved oxygen (DO) were recorded at each sampling station using SeaBird 911 CTDs. Conductivity and DO data were calibrated using at-sea analysis of discrete samples from Ocean Test Equipment samplers by salinometer (Autosal, Guildline) and Winkler titration respectively. The calibration of sensors gave uncertainties of ±0.003 to 0.005 in salinity (*S*) and ±5 μmol kg^{-1} in DO for these cruises (Sherwin, 2009; Read, 2010, 2011; Griffiths, 2012; Griffiths and Holliday, 2013).

4.2.2 Data syntheses

Data from the GLobal Ocean Data Analysis Project (GLODAP) (Key et al., 2004) and CARbon dioxide IN the Atlantic Ocean (CARINA) (Key et al., 2010) syntheses were combined with the measurements carried out during the recent EEL occupations from 2009 to 2013. Carbonate chemistry data in GLODAP from the Transient Tracers in the Ocean – North Atlantic Study (TTO-NAS) (Brewer et al., 1985) were adjusted following Tanhua and Wallace (2005).

The $\delta^{13}C_{DIC}$ data in GLODAP and CARINA (Key et al., 2004, 2010) have not undergone a secondary quality-control process, so we have instead used the compilation prepared by Schmittner et al. (2013). This consists of a high-quality subset of the GLODAP and CARINA results, augmented by data from additional cruises (Gruber et al., 1999). The estimated accuracy of these $\delta^{13}C_{DIC}$ values is between 0.1 and 0.2 ‰ (Schmittner et al., 2013).

4.2.3 Model output

The output of a simulation described in detail by Yool et al. (2013b) was obtained (referred to as the 'anthropogenic simulation'). This had been run from the year 1860 to 2100, and consisted of the size-based intermediate complexity ecosystem model MEDUSA-2.0 (Yool et al., 2013a) coupled to the physical model version 3.2 of the Nucleus for European Modelling of the Ocean (NEMO) (Madec, 2008). The horizontal resolution is approximately 1° × 1° (with 292 × 362 grid points), and vertical space is divided into 64 levels which increase in thickness from about 6 m at the surface to 250 m at a depth of 6 km. Each vertical column of grid points is referred to as a 'model station'. Surface forcing of NEMO used output from the HadGEM2-ES Earth-System model (Collins et al., 2011), and the DIC and TA fields in MEDUSA-2.0 were initialised using the GLODAP climatology (Key et al., 2004). Atmospheric $p\mathrm{CO}_2$ followed historical data from 1860 through 2005, and then switched to Representative Concentration Pathway 8.5 (Riahi et al., 2011) for the rest of the simulation. Basic validation of the output, by comparison with recent observations, was performed by Yool et al. (2013b). Output from a second 'control simulation' was also obtained, which had the same set-up except that the mean atmospheric $p\mathrm{CO}_2$ was held at a pre-industrial value of 286 μatm throughout.

4.2.4 Bathymetry

Bathymetric data from the GEBCO_2014 30 arc-second grid (version 20141103, www.gebco.net) were obtained for the EEL and its immediate surrounding area. The bathymetry of the idealised EEL route (Table 4.1) was derived from this data by linear interpolation of depth from the GEBCO_2014 latitude and longitude grids.

4.3 Data processing

4.3.1 Subsampling

4.3.1.1 Observations

All data in GLODAP, CARINA and from the recent EEL cruises falling within 167 km of an idealised EEL route, running in straight lines (great circles) through the waypoints listed in Table 4.1, were selected to create the 'observational' data set (Table 4.2). Many of the cruises in GLODAP and CARINA passing through the EEL region did not follow the EEL route, so 167 km was chosen as the optimal radius to satisfy the trade-off between capturing enough historical data to perform an effective analysis while still remaining local to the EEL. To avoid bias from differences in variable distributions, only data points with values for all of the following variables were used in the analysis: latitude, longitude, pressure (or depth), temperature, salinity, DIC and DO. Total alkalinity is not included in this list because its inclusion significantly reduces the number of data available, and as it does not show significant multi-decadal changes any resulting distribution bias is negligible.

Latitude / °N	Longitude / °W	Notes
63.30	020.00	North-western end of EEL transect, near Iceland
60.00	020.00	Mid-Iceland Basin; idealised EEL route departs from WOCE A16N transect
57.60	013.60	Rockall Plateau
57.45	011.10	Anton Dohrn Seamount, mid-Rockall Trough
56.75	007.85	European continental shelf
56.65	006.15	South-eastern end of EEL transect, near Scotland

Table 4.1. Waypoints along the idealised route for the EEL transect (Figure 4.1). The idealised route follows direct great-circle paths between these points.

The same processing was carried out separately for the Schmittner et al. (2013) data set plus D379 $\delta^{13}C_{DIC}$ measurements (Chapter 3), without the requirement for DIC and DO data at each point, to form the 'isotopes' data set (Table 4.3).

Cruise dates	Data source	Cruise code	Number of observations	
			Other variables	Total alkalinity
Jul 1981	TTO-NAS	TTONAS_4	53	53
Aug 1981	TTO-NAS	TTONAS_5	31	31
Apr-Jun 1989	CARINA	31AN119	29	23
Aug 1989	CARINA	64TY8908	53	50
Jul 1990	CARINA	64TY9003	138	0
Apr-May 1991	CARINA	164TY9104	684	0
Nov 1991-Oct 1992	CARINA	IrmingerSea	31	0
May 1992	CARINA	06MT021/3	11	11
Jul 1992	CARINA	58JH9207	27	0
Aug 1993	GLODAP	OACES93	144	137
Jul-Aug 1994	CARINA	58JH9408	125	0
Jul 1996	CARINA	06MT362	23	23
May 1997	CARINA	06MT392	37	29
Jun 1997	GLODAP	316N151_2	224	224
Jun-Jul 1999	CARINA	06MT452	117	0
Sep-Oct 2000	CARINA	64PE169	58	0
Jul 2001	CARINA	06MT504	100	95
Jun 2003	CARINA	CLIVAR A16N_2003	173	169
Jun 2009	EEL	D340	82	82
May 2010	EEL	D351	62	62
May 2011	EEL	D365	445	441
Aug 2012	EEL	D379	423	418
May 2013	EEL	JC086	429	423
Jul 1981-May 2013	**All sources**	**All cruises**	**3499**	**2271**

Table 4.2. Details for all cruises from which observational data were selected, excluding $\delta^{13}C_{DIC}$ data (Table 4.3). Data sources are 'TTO-NAS' (data from GLODAP, adjusted following Tanhua and Wallace (2005)), 'CARINA' (Key et al., 2010), 'GLODAP' (Key et al., 2004), and 'EEL' (recent cruises by UK research ships; description given in this paper). The 'cruise dates' and 'number of observations' columns refer only to the data used in this study, from within a 167 km radius of the idealised EEL route (Table 4.1).

Cruise dates	Data source	Cruise code	Number of observations
Aug 1993	Schmittner	OACES93	59
Jun 2003	Schmittner	33RO20030604	5
Oct 2003	Schmittner	58GS20030922	11
Aug 2012	EEL	D379	321
Aug 1993-Aug 2012	**All sources**	**All cruises**	**396**

Table 4.3. Details for all cruises from which observational $\delta^{13}C_{DIC}$ data were selected. Data sources are 'Schmittner' (Schmittner et al., 2013) and 'EEL' (recent cruises by UK research ships; description given in Chapter 3). The 'cruise dates' and 'number of observations' columns refer only to the data used in this study, from within a 167 km radius of the idealised EEL route (Table 4.1).

4.3.1.2 Model output

The model outputs were subsampled into several different data sets (Table 4.4). Firstly, monthly mean fields from both simulations (anthropogenic and control) were subsampled to match the spatiotemporal distribution of observational data as closely as possible, using a nearest-neighbour approach. These data sets are hereafter referred to as SAM and SCM (Subsampled Anthropogenic Monthly and Subsampled Control Monthly respectively). The SAM data set is therefore the model equivalent of the real EEL observations, and SCM is the same but with no anthropogenic CO_2. Secondly, annual mean fields from the anthropogenic simulation, from 1981 to 2013 inclusive within the region from 25°N to 75°N and 70°W to 10°E were extracted to form the data set called FAA (Full Anthropogenic Annual). Finally, all results at the closest model locations to the idealised EEL transect route (Figure 4.1) were selected from FAA to form the TAA data set (Transect Anthropogenic Annual). This TAA data set can be considered as representing the EEL sampled uniformly throughout the study period; rates of change of variables calculated using TAA are the standard against which the quality of the other model data sets are judged.

Data set abbreviation	Dates included	Locations included	Simulation	Resolution
SAM (Subsampled Anthropogenic Monthly)	Matching observations	Matching observations	Anthropogenic	Monthly
SCM (Subsampled Control Monthly)	Matching observations	Matching observations	Control	Monthly
FAA (Full Anthropogenic Annual)	1981-2013	25 to 72°N, 070°W to 010°E	Anthropogenic	Annual
TAA (Transect Anthropogenic Annual)	1981-2013	Model EEL transect (Figure 4.1)	Anthropogenic	Annual

Table 4.4. Summary of the model data sets and abbreviations used to refer to them.

4.3.2 Derived variables

Potential density at $P = 0$ (σ_0), *in situ* density (ρ), and potential temperature were calculated from T, S and P using the Gibbs-SeaWater Oceanographic Toolbox for MATLAB (MathWorks) (McDougall and Barker, 2011). Apparent oxygen utilisation (AOU) was calculated from potential temperature, S and DO using the combined fit coefficients of García and Gordon (1992).

4.3.3 Interpolations and rates of change

For the observational, SAM, SCM and TAA data sets: at each sampling station, measured DIC, TA, AOU, S, $\delta^{13}C_{DIC}$ and depth were interpolated at σ_0 values ascending in units of 0.001 from 26 to 28, using piecewise cubic interpolations of the measurements (Fritsch and Carlson, 1980). Figure 4.2 illustrates these interpolations at an example sampling station from the observational dataset, while Figure 4.4 shows the same for the 'matching' data in SAM. Potential density is a better interpolant than depth as it tracks vertical movements of water masses in the time between successive observations; it has previously been effectively used with this interpolation method for the same purpose of comparing variables between cruises (e.g. Tanhua et al., 2010). A small number of stations had fewer than the 4 unique measurements required to carry out the interpolation, so no interpolation was

carried out; instead, the measured values were assigned to the closest σ_0 level. No extrapolations were performed beyond the measured σ_0 range at any station. Linear least-squares regressions between each variable and the sampling date were used to determine the rate of change at every σ_0 level (e.g. Figure 4.3 for observations, Figure 4.5 for SAM). The mean value for each variable was also calculated for each σ_0 across all of the data. The rate of change of any variable X is reported as $dX/dt = R \pm U$, where R is the rate of change of X, and U is its uncertainty. The value of U is the '1-sigma' confidence interval (i.e. 68.3 % confidence) taking into account the increase in uncertainty driven by autocorrelation in the variables. This confidence interval is appropriate because it is the same level at which the precision of carbonate chemistry data is typically reported. Both R and U were calculated using the MATLAB (MathWorks) function regress2, written by I. Eisenman (Scripps Institution of Oceanography, USA; http://eisenman.ucsd.edu/code/matlab-toolbox/regress2.m), which is based on the methods of Bartlett (1935) and Bretherton et al. (1999), and which computes a linear regression but reports confidence intervals that account for the autocorrelation. Rates of change calculated at σ_0 levels which did not include any data from both the earliest and most recent years of data (1992 and 2012 respectively for $\delta^{13}C_{DIC}$, 1981 and 2013 for all other variables) were excluded from further analysis.

The same interpolation process was carried out for the FAA data set, but the rates of change were calculated independently for each model station. At each σ_0 layer, the rate of change of each variable in the TAA data set was subtracted from the corresponding FAA rate. These values, representing the difference between the rate of change of a variable X at each model station in FAA and its rate of change in the ideal model EEL (TAA), are referred to as $\Delta[dX/dt]$. Positive values indicate a greater rate in FAA than TAA, so the variable is increasing faster at the point in FAA than it is at the same σ_0 at the EEL itself. Rates of change considered representative of the North Atlantic and Nordic Seas for each σ_0 layer were calculated for each variable by finding the mean rate of change at all model stations in the range from 25 to 40°N and 070 to 030°W for the North Atlantic, and 66 to 72°N and 012°W to 001°E for the Nordic Seas.

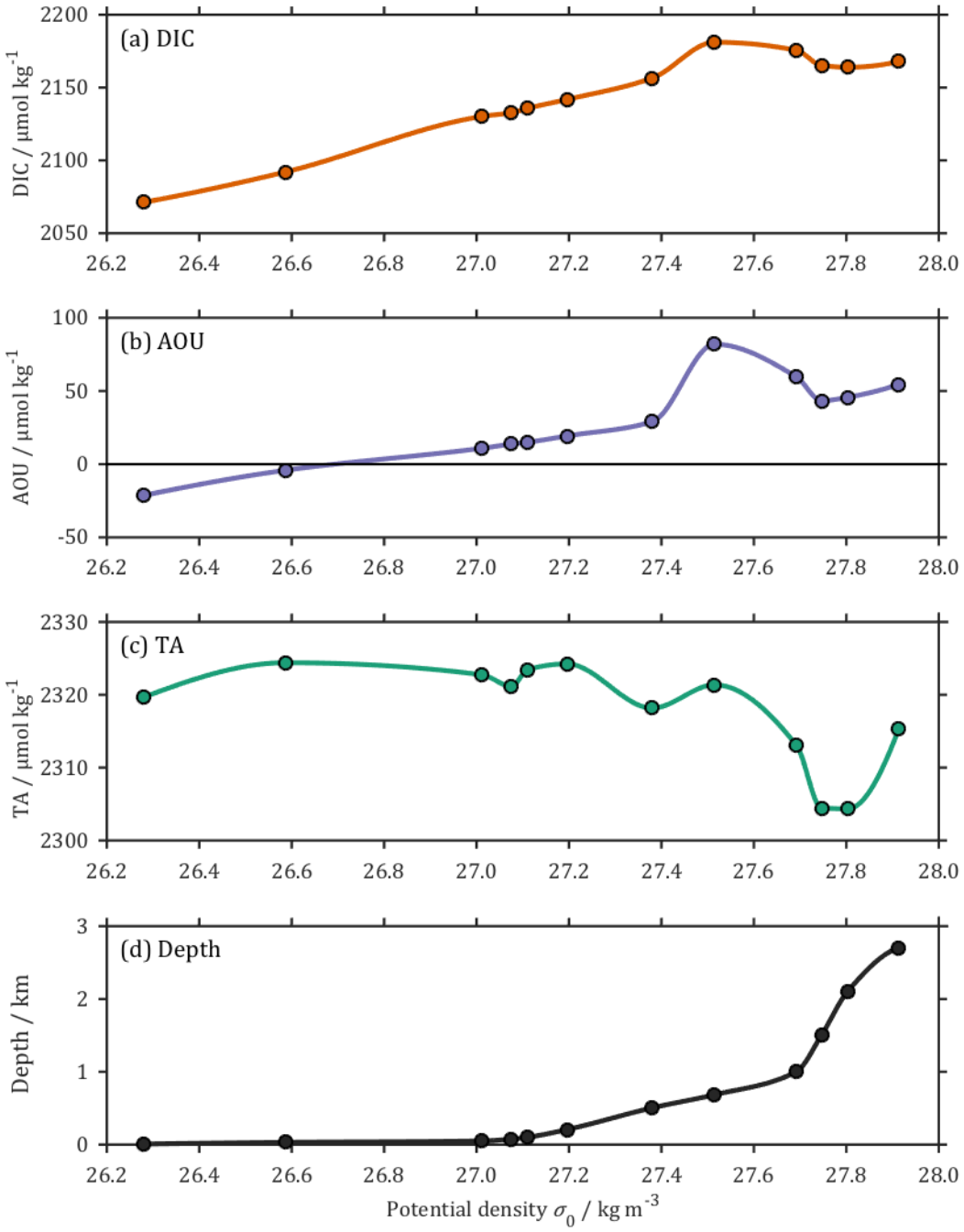

Figure 4.2. Measurements (circles) and interpolations against σ_0 used to calculate rates of change (lines) for (a) dissolved inorganic carbon (DIC), (b) apparent oxygen utilisation (AOU), (c) total alkalinity (TA) and (d) depth, for a typical sampling station (specifically EEL cruise D379, station B12, 12th August 2012).

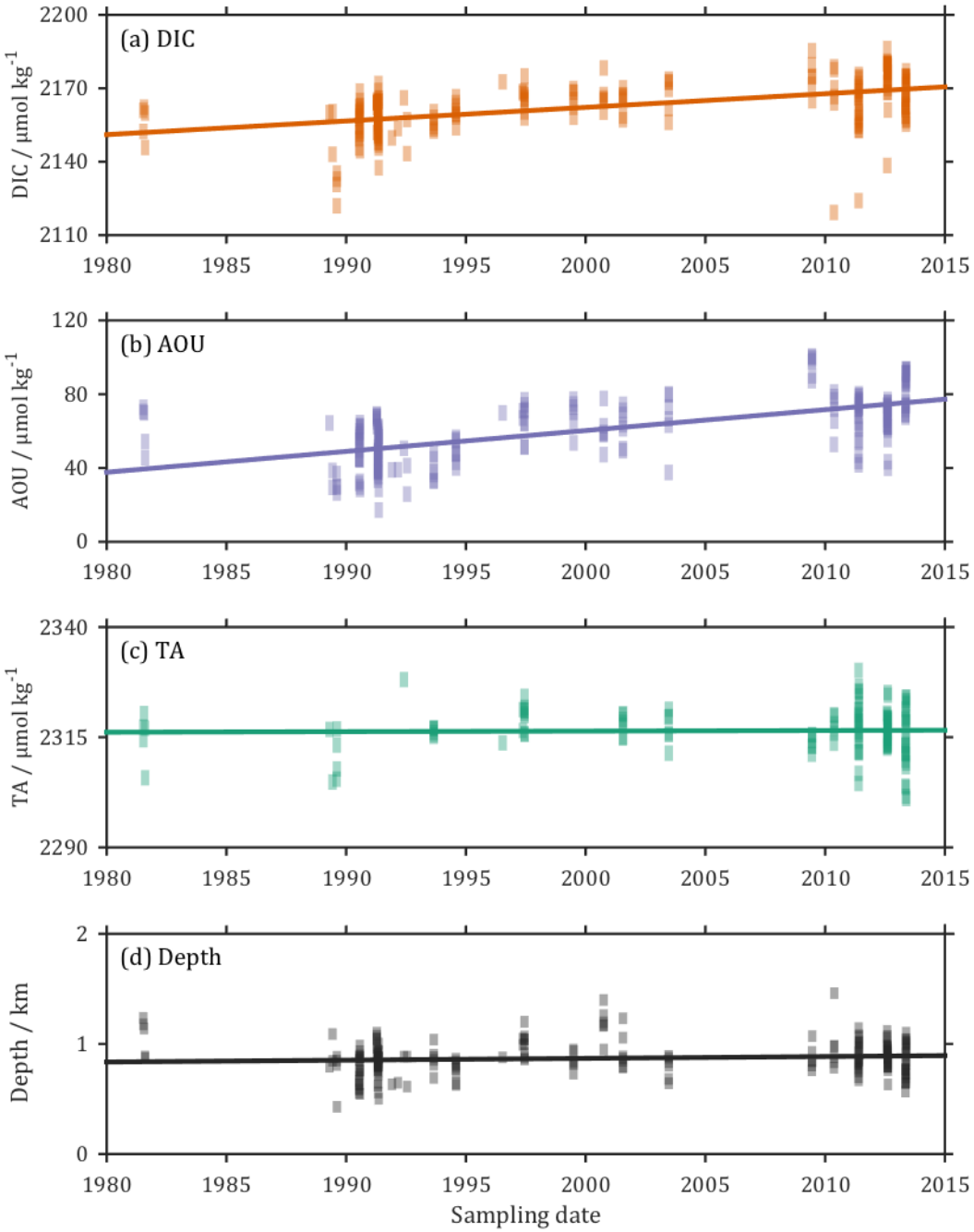

Figure 4.3. Example of data used to determine rates of change; includes all data within 167 km of the idealised EEL route, interpolated to σ_0 = 27.600. Individual data points are semi-transparent. Rates of change are: (a) dissolved inorganic carbon (DIC), 0.56 ± 0.06 µmol kg^{-1} yr^{-1}, r = 0.508, n = 226; (b) apparent oxygen utilisation (AOU), 1.13 ± 0.09 µmol kg^{-1} yr^{-1}, r = 0.651, n = 226; (c) total alkalinity (TA), 0.01 ± 0.05 µmol kg^{-1} yr^{-1}, r = 0.022, n = 132; and (d) depth, 1.65 ± 1.03 m yr^{-1}, r = 0.107, n = 226; where r is the correlation coefficient, and n the number of measurements.

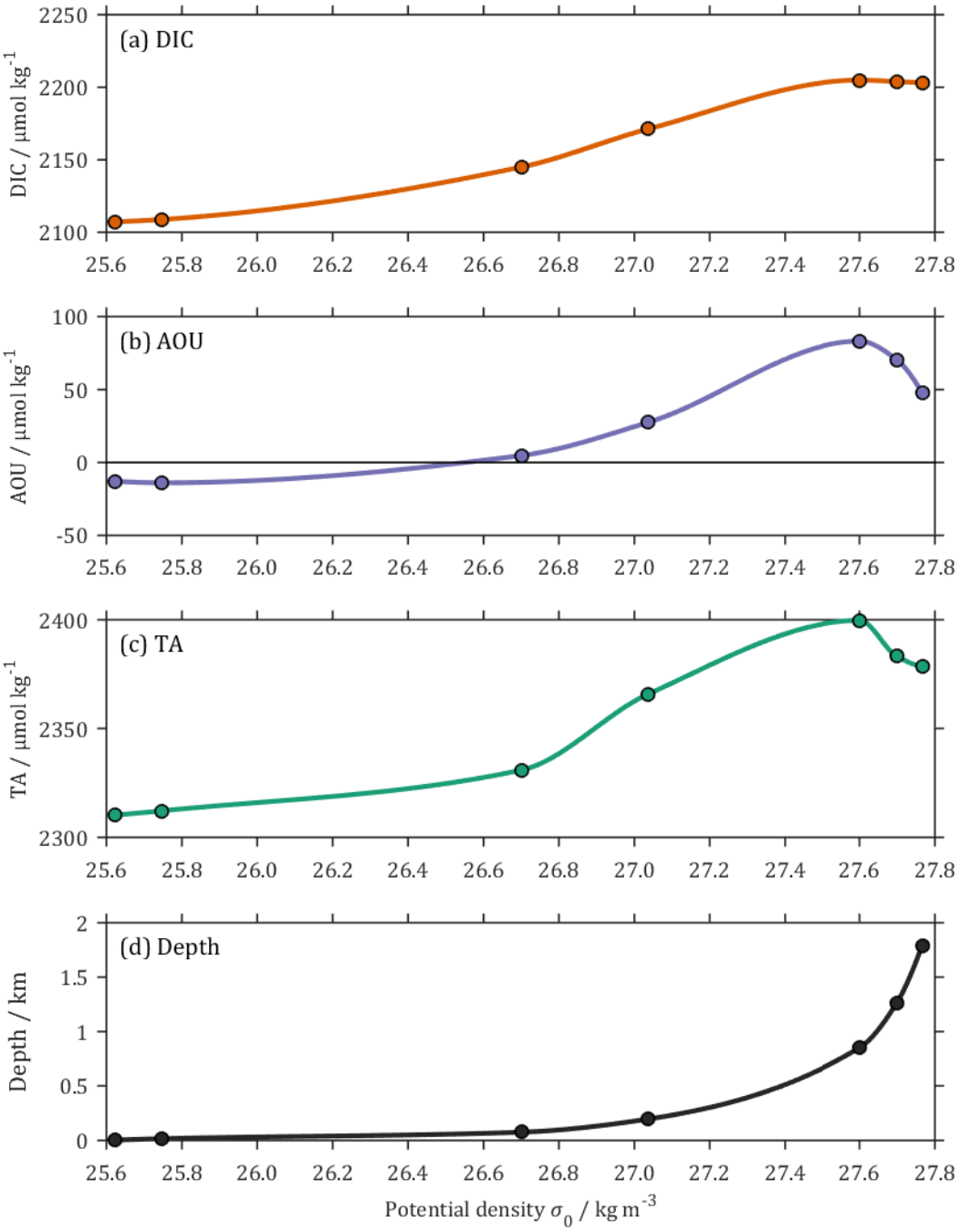

Figure 4.4. Model output (circles) and interpolations against σ_0 used to calculate rates of change (lines) for (a) dissolved inorganic carbon (DIC), (b) apparent oxygen utilisation (AOU), (c) total alkalinity (TA) and (d) depth, for the data in SAM matching the observations in Figure 4.2. Note that there are fewer data points here than in Figure 4.2; this is because of the lower vertical resolution of the model than the observations, so multiple observational data points are matched to the same model point.

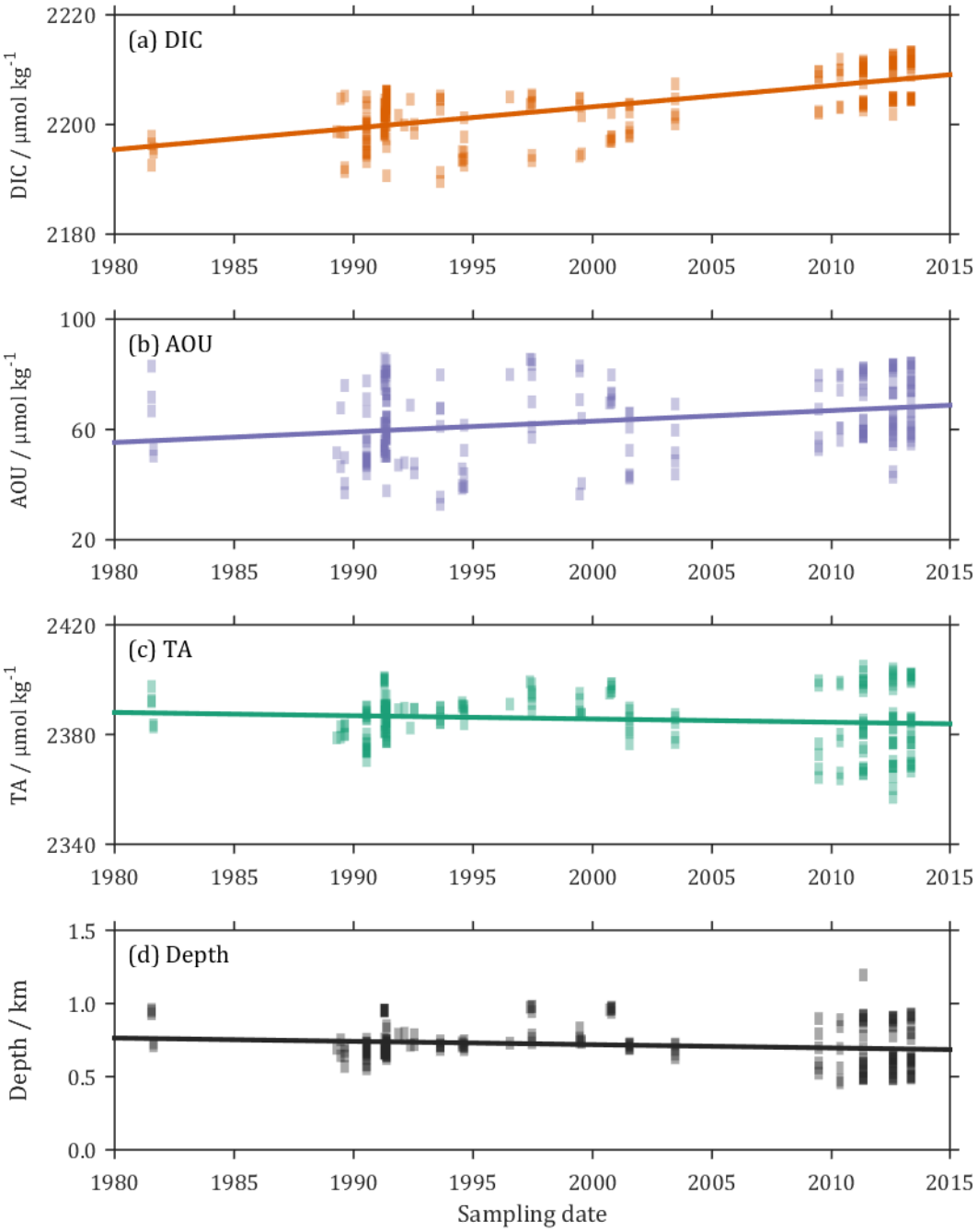

Figure 4.5. Example of model data from SAM used to determine rates of change; includes all data within 167 km of the idealised EEL route, interpolated to σ_0 = 27.600. Individual data points are semi-transparent. Rates of change are: (a) dissolved inorganic carbon (DIC), 0.39 ± 0.03 µmol kg^{-1} yr^{-1}, r = 0.694, n = 219; (b) apparent oxygen utilisation (AOU), 0.38 ± 0.09 µmol kg^{-1} yr^{-1}, r = 0.287, n = 219; (c) total alkalinity (TA), -0.12 ± 0.07 µmol kg^{-1} yr^{-1}, r = -0.118, n = 219; and (d) depth, -2.26 ± 0.90 m yr^{-1}, r = -0.168, n = 219; where r is the correlation coefficient, and n the number of measurements.

4.3.4 Column inventories

To quantify volume-integrated rates of change (column inventories) for each variable, the average depth of each σ_0 level was calculated by applying a smoothing spline interpolation to the mean depth at each σ_0 value, thus ensuring that the depth of each successive σ_0 value increased monotonically. The horizontal distance of the idealised EEL route which was above the seafloor at each of these mean depths was then measured using the interpolated GEBCO_2014 bathymetry. The cross-sectional area of the interval between each pair of σ_0 values was calculated as the product of the difference between the depths and the mean of the above-seafloor lengths (Figure 4.6). Rates of change with units of μmol kg^{-1} yr^{-1} were converted to μmol m^{-3} yr^{-1} using the mean *in situ* density (ρ) for all measurements in each interval, then multiplied by the cross-sectional area and unit thickness to give the total rate of change. The sum of this result over all layers gave the column inventory change in each variable. The reported uncertainties were calculated by combining the errors in rate of change across all σ_0 layers. This process was carried out separately for each data set. For the anthropogenic component of DIC (DIC_{anth}) inventory, all negative values of $dDIC_{anth}/dt$ were set to equal 0 prior to summation, a step common to this type of calculation (e.g. Vázquez-Rodríguez et al., 2009). This is necessary because negative values of small magnitude persist through the deeper part of the water column, constituting a large fraction of the total water volume, so they can mask the true anthropogenic signal from nearer to the surface.

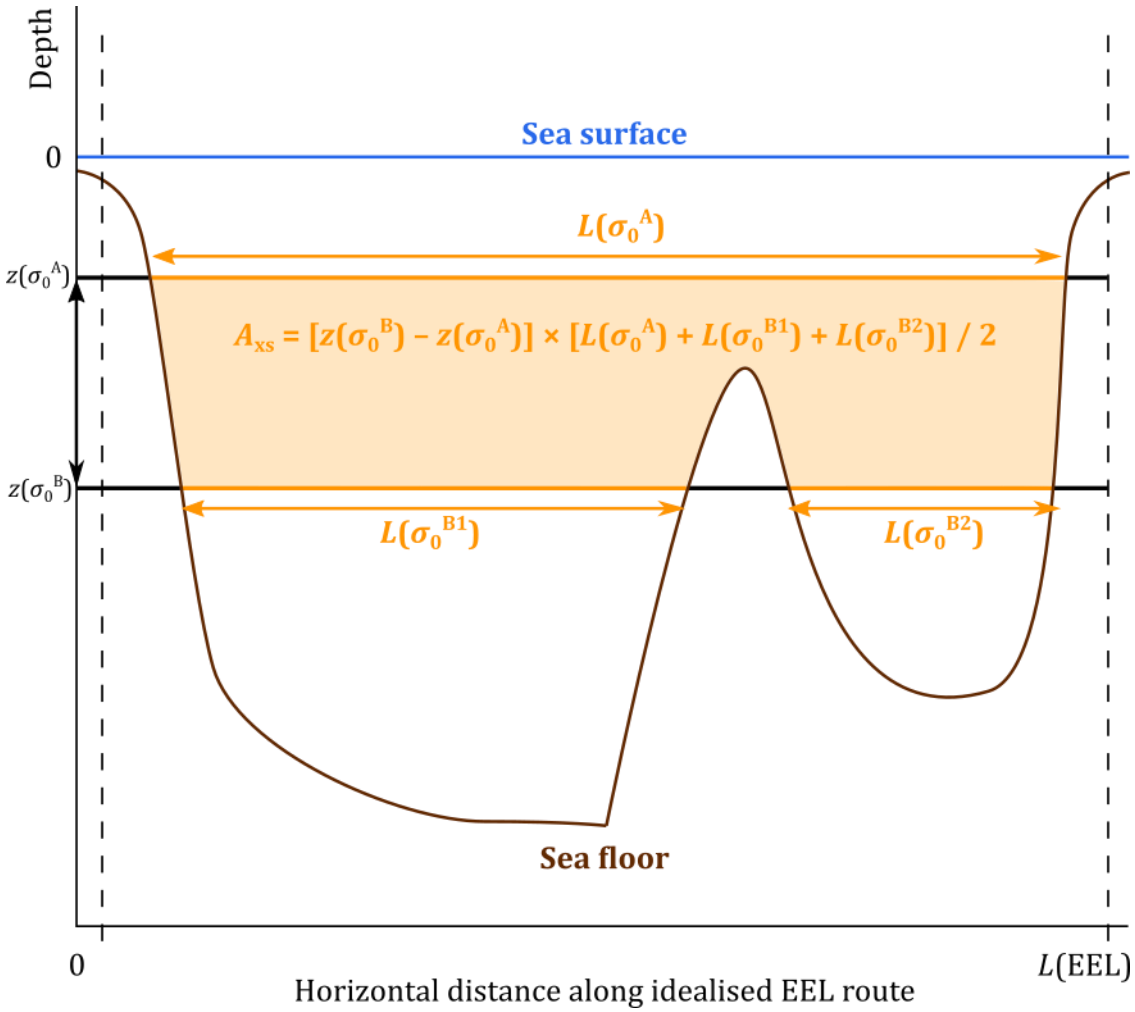

Figure 4.6. Schematic illustration of cross-sectional area calculations for determining column inventory changes. The mean depths ($z(\sigma_0^A)$ and $z(\sigma_0^B)$) of two σ_0 levels (σ_0^A and σ_0^B) are determined as described in the text (Section 4.3.4). The horizontal distances of the idealised EEL route (total length L(EEL)) that are above the sea floor at each of these depths (i.e. the orange horizontal lines) are $L(\sigma_0^A)$ and $L(\sigma_0^{B1}) + L(\sigma_0^{B2})$. The cross-sectional area (A_{xs}, orange shaded area) of the interval between σ_0^A and σ_0^B is calculated as the product of the difference between the depths and the mean of the above-seafloor lengths, as indicated by the equation for A_{xs}. This is carried out for every adjacent pair of σ_0 levels in order to calculate column inventories for the entire water column.

4.4 Results and discussion

4.4.1 Multi-decadal DIC increase

4.4.1.1 Isolating the anthropogenic component

Increases in DIC from 1981 to 2013 are observed throughout the water column. The $d\mathrm{DIC}/dt$ decreases with depth, from a maximum of 1.65 ± 0.47 μmol kg^{-1} yr^{-1} in the shallowest σ_0 layers, to a deep minimum of 0.02 ± 0.10 μmol kg^{-1} yr^{-1} (Figure 4.7a). This non-zero $d\mathrm{DIC}/dt$ implies that the processes controlling DIC – the carbonate pump, soft tissue pump, and the solubility pump (Gruber et al., 1996) – are not operating in steady state. We can use changes in other measured variables to deconvolve the total DIC change into these component processes.

Equation 4.1 $$d\mathrm{DIC}/dt = d\mathrm{DIC}_{\mathrm{carb}}/dt + d\mathrm{DIC}_{\mathrm{soft}}/dt + d\mathrm{DIC}_{\mathrm{sol}}/dt$$

The 'carbonate pump' is the formation and dissolution of calcium carbonate ($CaCO_3$). Increasing its rate of dissolution relative to formation would drive an increase in DIC, accompanied by an increase in TA of double the magnitude (Wolf-Gladrow et al., 2007). Its contribution to the total $d\mathrm{DIC}/dt$, $d\mathrm{DIC}_{\mathrm{carb}}/dt$, can therefore be determined as:

Equation 4.2 $$d\mathrm{DIC}_{\mathrm{carb}}/dt = 0.5 \cdot \left(d\mathrm{TA}/dt - R_{\mathrm{N/O2}} \cdot d\mathrm{AOU}/dt\right)$$

where the $d\mathrm{AOU}/dt$ term corrects for changes in TA driven by nitrate release during organic matter remineralisation, and $R_{\mathrm{N/O2}}$ (the stoichiometric ratio of nitrogen to oxygen in particulate organic matter) is -0.0941 ± 0.0081 (Anderson and Sarmiento, 1994). In the observations, changes in TA are very small: $d\mathrm{TA}/dt$ is between 0.23 ± 0.26 and -0.19 ± 0.10 μmol kg^{-1} yr^{-1}, and $d\mathrm{DIC}_{\mathrm{carb}}/dt$ is in the range between 0.16 ± 0.13 and -0.08 ± 0.05 μmol kg^{-1} yr^{-1} (Figure 4.7a). The observed DIC increase was therefore not significantly driven by changes in the carbonate pump.

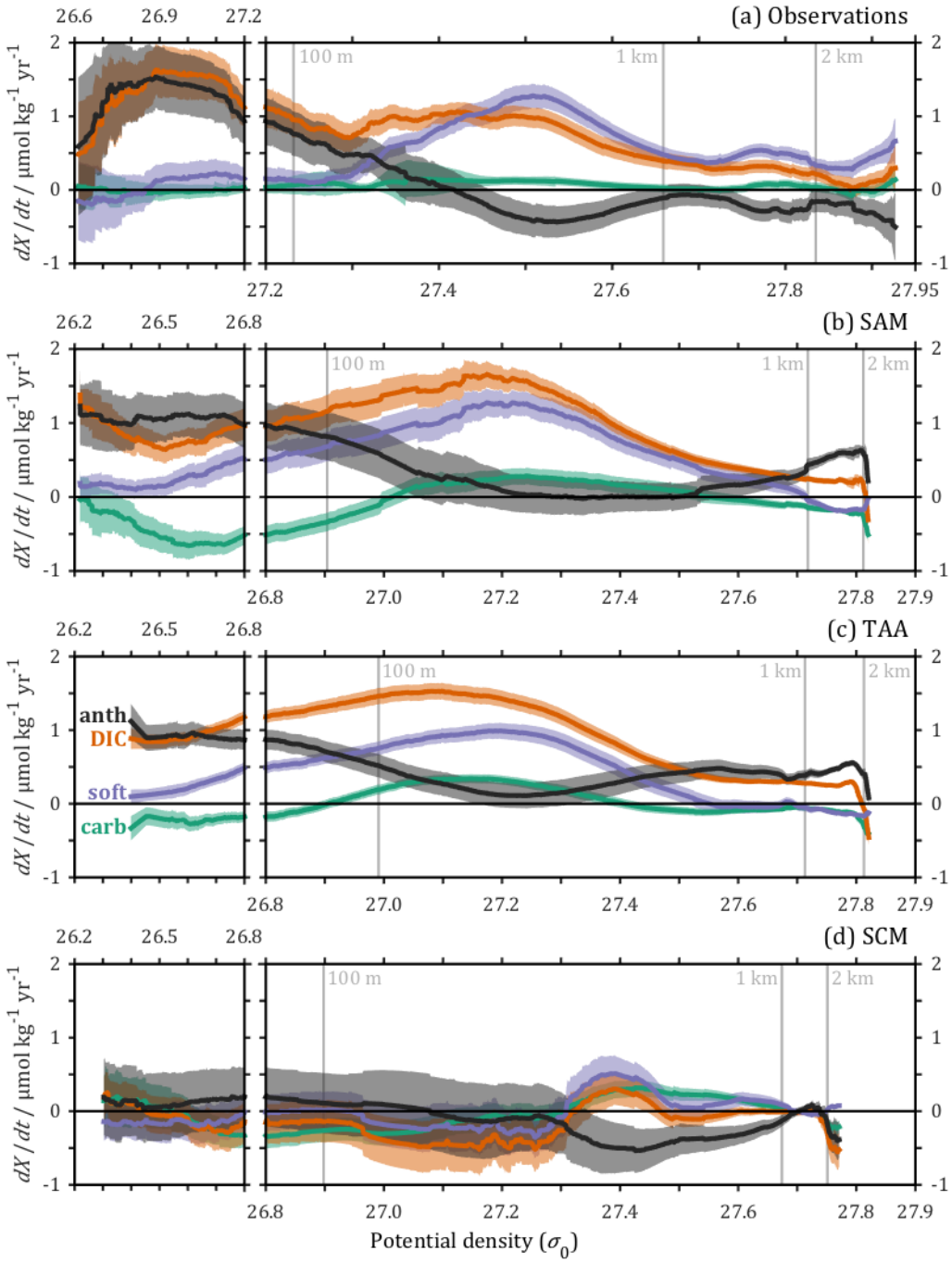

Figure 4.7. Rate of change of dissolved inorganic carbon DIC and its soft tissue pump (soft), carbonate pump (carb) and anthropogenic (anth) components (orange, blue-purple, green and black-grey respectively; see labels in (c)) throughout the water column for the (a) observations, (b) SAM, (c) TAA and (d) SCM data sets (Table 4.4). Shaded regions indicate ± one-sigma uncertainty. Vertical grey lines indicate σ_0 with mean depths of 100 m, 1 km and 2 km in each data set. Note different horizontal scale for (a).

Biological activity, concentrated near the ocean surface, converts dissolved inorganic nutrients to particulate organic matter (POM), some of which sinks and remineralises at depth, returning the nutrients to solution: the soft tissue pump. Remineralisation also takes up DO, thereby increasing AOU. The component of $d\mathrm{DIC}/dt$ caused by changes in organic matter remineralisation, $d\mathrm{DIC}_{\mathrm{soft}}/dt$, can therefore be estimated from $d\mathrm{AOU}/dt$:

Equation 4.3 $$d\mathrm{DIC}_{\mathrm{soft}}/dt = -R_{\mathrm{C/O2}} \cdot d\mathrm{AOU}/dt$$

where $R_{\mathrm{C/O2}}$ is the increase in DIC as a fraction of DO uptake during this process, which takes a constant value of -0.688 ± 0.092 (Anderson and Sarmiento, 1994). The rate of $d\mathrm{DIC}_{\mathrm{soft}}/dt$ is close to 0 in the upper water column, but it closely tracks $d\mathrm{DIC}/dt$ for σ_0 > 27.4 (Figure 4.7a).

The remaining DIC increase is concentrated in σ_0 layers close to the ocean surface (Figure 4.7a), and is attributed to increases in air-to-sea CO_2 transfer at the surface outcrop regions for these layers. Assuming no long-term trend in air-sea CO_2 disequilibrium from 1981 to 2013 (i.e. $d\mathrm{DIC}_{\mathrm{diseq}}/dt$ = 0), this increase represents the accumulation of $\mathrm{DIC}_{\mathrm{anth}}$:

Equation 4.4 $$d\mathrm{DIC}_{\mathrm{anth}}/dt = d\mathrm{DIC}_{\mathrm{sol}}/dt - d\mathrm{DIC}_{\mathrm{diseq}}/dt \approx d\mathrm{DIC}_{\mathrm{sol}}/dt$$

The choice of POM stoichiometry controls the values of $R_{\mathrm{C/O2}}$ and $R_{\mathrm{N/O2}}$, and so clearly influences the calculation of the partitioning of $d\mathrm{DIC}/dt$ into its carbonate and soft tissue components (Equations 4.2 and 4.3). The values which we have chosen to use for $R_{\mathrm{C/O2}}$ and $R_{\mathrm{N/O2}}$, -0.688 ± 0.092 and -0.0941 ± 0.0081 respectively, are based on global macronutrient measurements (Anderson and Sarmiento, 1994) and feature a higher O_2 coefficient than the 'original' stoichiometry of Redfield et al. (1963), which gives -0.768 for $R_{\mathrm{C/O2}}$ and -0.116 for $R_{\mathrm{N/O2}}$. Using a higher O_2 coefficient than in the original stoichiometry is supported by considerations of the composition of several groups of algal biomolecules (Anderson, 1995). Switching between these stoichiometries does not significantly alter our results for $d\mathrm{DIC}_{\mathrm{anth}}/dt$, relative to their uncertainty: the different stoichiometries result in a difference in the mean $d\mathrm{DIC}_{\mathrm{anth}}/dt$ across all σ_0 of 0.05 μmol kg^{-1} yr^{-1}, and a change in the volume-integrated inventory change for the entire EEL of about 8 % (with the newer stoichiometry giving the higher $\mathrm{DIC}_{\mathrm{anth}}$ inventory) – no larger than the uncertainty propagated into this inventory estimate directly from the rates of change, 9 %. Furthermore, the original value for $R_{\mathrm{C/O2}}$ (Redfield et al., 1963), which has a much bigger influence on

the DIC_{anth} calculation than $R_{N/O2}$ does, falls within the uncertainty of the more recent result (Anderson and Sarmiento, 1994). Consequently, this is not considered to be an important source of uncertainty in the results.

4.4.1.2 Changes throughout the water column

The anthropogenic DIC increase at the EEL is confined in and above the thermocline (σ_0 < 27.5), in accordance with previous global-scale observations of its distribution (Sabine et al., 2004). In this upper part of the water column, calculated $d\mathrm{DIC}_{\mathrm{anth}}/dt$ is consistent with similar analyses in the nearby or overlapping regions of the Iceland Basin (Pérez et al., 2010) and southern Rockall Trough (McGrath et al., 2012a). At greater depths, $d\mathrm{DIC}_{\mathrm{anth}}/dt$ is close to or slightly less than 0 (Figure 4.7a). This is a common feature for this type of method (e.g. Vázquez-Rodríguez et al., 2009).

Most of the soft-tissue component of the DIC increase is likely caused by changes in the distribution of water masses within σ_0 layers, rather than by increasing export and remineralisation of POM along the EEL itself. Although sufficient *in situ* data do not exist to directly confirm the presence or absence of a multi-decadal trend in POM export and remineralisation in the EEL region, the rate of this process is unlikely to be increasing fast enough (if at all) to cause the observed peak in $d\mathrm{DIC}_{\mathrm{soft}}/dt$: export rates can be estimated as a function of, amongst other things, surface chlorophyll-*a*, with higher concentrations accompanying higher export rates (e.g. Dunne et al., 2007); satellite observations have in fact detected a small decline in chlorophyll-*a* from 1998 to 2012 for the northern North Atlantic (Gregg and Rousseaux, 2014). Considering instead water mass distributions: at σ_0 less than 27.70, the EEL samples a mixture of waters from the subtropical and subpolar gyres; contraction of the subpolar gyre increases the relative size of the subtropical component, while expansion decreases it (Hátún et al., 2005). The subpolar gyre index (SPGI) can be interpreted as a measure of the degree of its contraction, with lower values indicating a more contracted gyre. Its value has decreased significantly during the period of our study, especially since the early 1990s (Hátún et al., 2005; Hughes et al., 2012), in a process which has separately been shown to drive a decrease in macronutrient concentrations in the Rockall Trough (Johnson et al., 2013). Bio-geographical shifts at virtually all trophic levels in the North Atlantic during the past century have also been linked to changes in the SPGI (Hátún et al., 2009). The increasing southern water contribution is a combination of Eastern North Atlantic Water, formed in the Bay of Biscay (McGrath et al., 2012b), and highly-saline Mediterranean Water (Burkholder

and Lozier, 2011; McGrath et al., 2012b). Data from GLODAP and CARINA indicate that DIC and AOU along σ_0 layers increase to the south of the EEL region, so an increasing southern influence on the water at the EEL would increase DIC and AOU at the EEL, as we observe.

Between σ_0 of 27.70 and 27.85, the EEL samples Labrador Sea Water (LSW). The properties of this water mass are highly variable both spatially and temporally in this region, because it undergoes extensive mixing with other water masses – including recirculating LSW ventilated in earlier years – during its transport from its source to the EEL region (Yashayaev et al., 2007). So, although an increase in DIC_{anth} in the LSW is not observed during the study period, any anthropogenic signal from the source region could have been suppressed by mixing with an older LSW, or other water mass with lower DIC_{anth} content. Again, increased *in situ* remineralisation is unlikely to be responsible for the observed increase in total DIC, as virtually all POM generated in the EEL region which is exported from the surface is remineralised at shallower depths, in the mesopelagic zone (Henson et al., 2012). Other studies have identified small increases in DIC_{anth} in LSW (Pérez et al., 2010; McGrath et al., 2012a), but for different spatial and temporal domains to those used in this study. This discrepancy may be an artefact of differences in the distribution of observations of this highly variable water mass between the two studies. No DIC_{anth} accumulation is observed from 1981 to 2013 in the water masses present below the LSW, in the deepest part of the water column, with σ_0 greater than 27.85, although there are still small increases in DIC and AOU. Since their formation in the Nordic Seas and subsequent flow through one of several narrow channels over the Greenland-Scotland ridge into the EEL region (Hansen and Østerhus, 2000), these waters – like the LSW – have been significantly altered by various mixing processes, preventing direct attribution of the DIC and AOU increases to a specific driver.

4.4.1.3 Column inventories

The global ocean anthropogenic CO_2 sink was about 2 Pg-C yr^{-1} for the period from 1981 to 2013 (Le Quéré et al., 2009), which corresponds to global average DIC_{anth} accumulation rates of approximately 1.5 mg-C m^{-3} yr^{-1} (Eakins and Sharman, 2010). For the idealised EEL route, volume-integrated $dDIC_{anth}/dt$ is 1.71 ± 0.15 mg-C yr^{-1} m^{-3}, which is slightly greater than the global average value and confirms the importance of this region for the sequestration of atmospheric anthropogenic CO_2

into the ocean. The equivalent volume-integrated $d\mathrm{DIC}/dt$ is 7.65 ± 0.34 mg-C yr^{-1} m^{-3}, so the $\mathrm{DIC_{anth}}$ increase accounts for 22.3 ± 2.2 % of the total DIC accumulation.

Measurements of chlorofluorocarbon (CFC) inventory changes in the North Atlantic have demonstrated that the dominant control on CFC column inventory variability can be changes in volume of different water masses at a given location, rather than changes in the CFC concentration within each water mass (Kieke et al., 2007; Steinfeldt et al., 2009); a similar result has been suggested for anthropogenic DIC (Pérez et al., 2010). However, the timescale of volumetric variability in these studies is sub-decadal; for the longer time period from 1981 to 2013 in the EEL observations, changes in σ_0 layer thicknesses are small, sufficiently so that including these changes in inventory calculations changes the final result by significantly less (typically an order of magnitude) than the size of its one-sigma uncertainty. The assumption that σ_0 layer volumes are static to calculate volume-integrated rates of change is therefore valid.

4.4.2 Stable isotopes of DIC

The stable isotopic composition of DIC ($\delta^{13}\mathrm{C_{DIC}}$) can be used as an independent test of the attribution of the changes in DIC to its anthropogenic and soft tissue components, as these are the two main processes influencing $\delta^{13}\mathrm{C_{DIC}}$ in the interior ocean. Firstly, uptake of anthropogenic CO_2 results in a decrease in $\delta^{13}\mathrm{C_{DIC}}$, known as the Suess effect, because fossil-fuel carbon is isotopically light relative to modern seawater (Keeling, 1979). Secondly, POC remineralisation also reduces $\delta^{13}\mathrm{C_{DIC}}$, because POC has a lighter isotopic signature than typical seawater: according to a meta-analysis study, surface ocean $\delta^{13}\mathrm{C_{POC}}$ is between -20 and -30 ‰ at the latitude and sea surface T of the EEL (Goericke and Fry, 1994), compared with typical seawater DIC values near 0 ‰ (Chapter 3; Humphreys et al., 2015; Schmittner et al., 2013). The carbonate pump does not significantly affect $\delta^{13}\mathrm{C_{DIC}}$, because marine carbonate mineral formation (calcification) does not significantly fractionate carbon: typically, the minerals have a $\delta^{13}\mathrm{C}$ composition similar to that of the surrounding seawater (Lynch-Stieglitz et al., 1995). Consequently, negative $d\delta^{13}\mathrm{C_{DIC}}/dt$ is observed throughout the water column, increasing from a minimum of -0.038 ± 0.026 ‰ yr^{-1} at near-surface σ_0 levels to a maximum of -0.002 ± 0.006 ‰ yr^{-1} at depth (Figure 4.8). Using a multi-linear regression

approach to account for changes in water mass distributions, Quay et al. (2007) identified mean $d\delta^{13}C_{DIC}/dt$ of -0.018 ± 0.002 ‰ yr^{-1} for the entire Atlantic surface mixed layer from 1981 to 2003, with the $d\delta^{13}C_{DIC}/dt$ decreasing to between -0.04 and -0.05 ‰ yr^{-1} in the subpolar region between 40°N and 60°N, which is consistent with the EEL results.

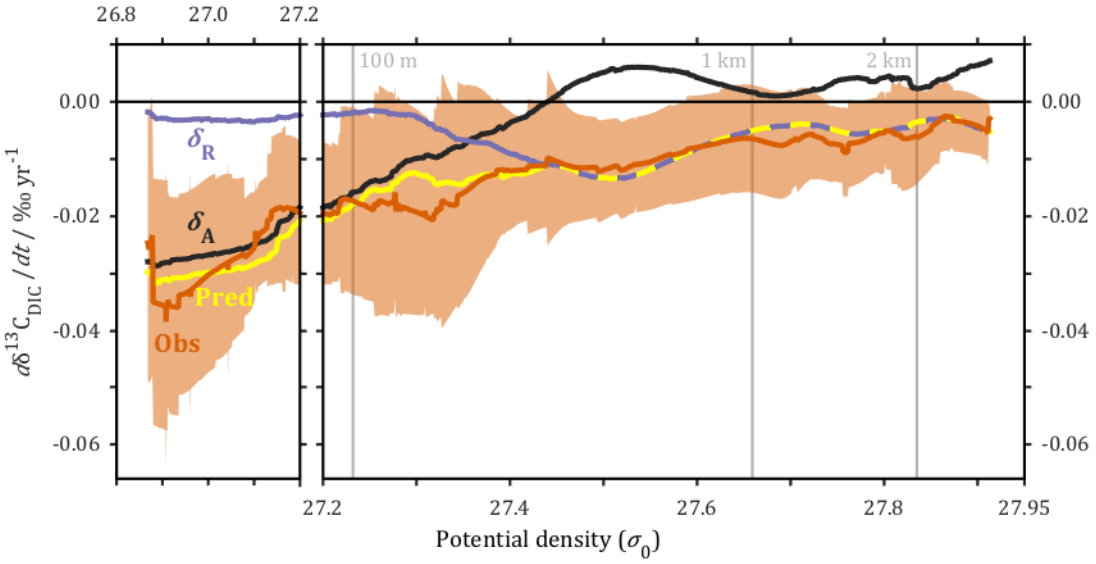

Figure 4.8. Observed and 'predicted' rate of change of $\delta^{13}C_{DIC}$ for the EEL. Orange-red line and shading shows rate ± one-sigma uncertainty evaluated directly from observations (labelled Obs); yellow line (labelled Pred) shows rate predicted from observed dDIC/dt and dAOU/dt using best-fit ΔRC and $\delta^{13}C_{POC}$. The anthropogenic ($\Delta\delta_A$) and remineralised ($\Delta\delta_R$) components of the prediction are shown separately (black-grey and blue-purple lines, labelled δ_A and δ_R respectively; Equations 4.5 and 4.6). Note that positive values for the anthropogenic component were replaced with 0, so the predicted $d\delta^{13}C_{DIC}/dt$ coincides with the remineralised component (alternating blue-purple/yellow line). Vertical grey lines indicate σ_0 with mean depths of 100 m, 1 km and 2 km.

There are far fewer $\delta^{13}C_{DIC}$ observations than for the other variables, and the length of the time-series is shorter, running from 1993 to 2012. Nevertheless, $d\delta^{13}C_{DIC}/dt$ can be related to changes in the other variables to independently test the attribution of dDIC/dt to its anthropogenic and remineralisation components. In each σ_0 layer, the total change in $\delta^{13}C_{DIC}$ from 1981 to 2013 ($\Delta\delta^{13}C_{DIC}$) is the sum of the changes from anthropogenic CO_2 accumulation ($\Delta\delta_A$) and POC remineralisation ($\Delta\delta_R$):

Equation 4.5 $$\Delta\delta^{13}C_{DIC} = \Delta\delta_A + \Delta\delta_R$$

The anthropogenic component $\Delta\delta_A$ can be calculated from the total changes in DIC (ΔDIC) and AOU (ΔAOU), and the ratio between anthropogenic changes in $\delta^{13}C_{DIC}$ and DIC, called ΔRC following e.g. McNeil et al. (2001a):

Equation 4.6 $$\Delta\delta_A = \Delta RC \cdot (\Delta DIC + \Delta AOU \cdot R_{C/O2})$$

The remineralisation component $\Delta\delta_R$ also depends on the initial DIC and $\delta^{13}C_{DIC}$ (DIC_i and δ_i respectively), and the isotopic composition of POC ($\delta^{13}C_{POC}$):

Equation 4.7

$$\Delta\delta_R = -\delta_i + \frac{DIC_i \cdot \delta_i - \delta^{13}C_{POC} \cdot \Delta AOU \cdot R_{C/O2}}{DIC_i + \Delta DIC}$$

The values of the DIC and $\delta^{13}C_{DIC}$ rate-of-change regression lines at the mid-point of the year 1981 were used for DIC_i and δ_i. Conversion between ΔDIC, ΔAOU and $\Delta\delta^{13}C_{DIC}$ and their rates of change is straightforward for the 32-year observational period. For any variable X:

Equation 4.8 $$\Delta X = 32 \cdot dX/dt$$

For each σ_0 layer, the observed rates of change of DIC, AOU and $\delta^{13}C_{DIC}$ were thus used to calculate values for ΔRC and $\delta^{13}C_{POC}$ of -0.019 ‰ (μmol kg^{-1})$^{-1}$ and -21.94 ‰ respectively, as least-squares best fit to all σ_0 layers. For this calculation, positive values for $\Delta\delta_A$ (implying negative anthropogenic DIC content) were set to 0, analogous to the column inventory calculations (Section 4.4.1.3). To visualise the results, $d\delta^{13}C_{DIC}/dt$ was then predicted using these best-fit values of ΔRC and $\delta^{13}C_{POC}$ along with observed dDIC$/dt$ and dAOU$/dt$ (Figure 4.8).

It was originally proposed that ΔRC might take a relatively globally-uniform value between -0.016 and -0.019 ‰ (μmol kg^{-1})$^{-1}$ (Heimann and Maier-Reimer, 1996). More recently, it has been demonstrated that ΔRC can deviate from this global average to exhibit significant spatial variation in certain regions (McNeil et al., 2001a; Olsen et al., 2006), because the air-sea equilibration time is an order of magnitude faster for DIC than for $\delta^{13}C_{DIC}$ (Lynch-Stieglitz et al., 1995). Körtzinger et al. (2003) calculated ΔRC throughout the North Atlantic, reporting -0.022 ± 0.002 ‰ (μmol kg^{-1})$^{-1}$ for the σ_0 layers observed in this study. The best-fit value for ΔRC calculated here, -0.019 ‰ (μmol kg^{-1})$^{-1}$, fits comfortably within this range of previously published results. Using the linear regression between sea surface temperature (SST) and $\delta^{13}C_{POC}$ described by Goericke & Fry (1994) for the northern

hemisphere and SST > 5 °C, and a value of 10.6 °C for SST (the mean of all EEL T observations for which $P \leq 10$ dbar), we would predict $\delta^{13}C_{POC}$ = -22.8 ‰ for the EEL, with an uncertainty on the order of ± 3 ‰, which is very similar to the least-squares best fit $\delta^{13}C_{POC}$ of -21.94 ‰. It is therefore concluded that the $d\delta^{13}C_{DIC}/dt$ observations do provide independent support for the quantitative attribution of dDIC/dt to its anthropogenic and remineralisation components, despite the relatively poor spatiotemporal coverage of $\delta^{13}C_{DIC}$ observations.

4.4.3 Model output

4.4.3.1 Subsampled model output and observational data

It is useful to briefly assess how well the values of modelled variables in the subsampled monthly mean outputs from the anthropogenic and control simulations (SAM and SCM respectively) agree with their matching distributions in the observations before discussing rates of change calculated from the model data sets. Although exactly matching absolute values are not required to compare rates of change, if the distributions of key variables were completely different then it would not be reasonable to expect their rates of change in the model to provide a useful analogue to the observations. An important caveat is that only one model has been used here; others might result in different outcomes.

There was no significant systematic offset between the latitude, longitude and date of the observations and their matching points in the SAM and SCM data sets (Figure 4.9a-c). In terms of depth, a small fraction of the observations are represented by significantly shallower model data (Figure 4.9d). This occurs because of the coarseness of the model grid relative to the length scale of real-world bathymetric features in this region; the model stations which were closest horizontally to these observations had maximum depths shallower than the observations themselves. However, in terms of the entire data set these points are few enough that the overall systematic offset remains insignificant: the mean difference between observed and matching-model depth was -22 m (negative sign indicating a shallower mean depth for the subsampled model than for the matching observations). This means that the model data sets which have been subsampled to 'look like' the observations do so successfully, spatially and temporally.

The physical and biogeochemical variables under investigation deviated further than the spatial and temporal metavariables from the observations in SAM and SCM. These subsampled model data sets share very similar σ_0 fields, both offset towards lighter values than their matching observations (Figure 4.10a) especially in the deepest part of the water column. This may be caused by the unrealistic northward penetration of Antarctic Bottom Water (AABW), which has been identified in some NEMO runs (Hieronymus and Nycander, 2013) in particular the one used here (Yool et al., 2013b), coupled with the tendency of such models to also underestimate the density of this AABW (Heuzé et al., 2013). The SAM and SCM AOU fields are also very similar to each other, and both represent their matching observations relatively well (Figure 4.10b). In SAM, DIC takes consistently high values relative to SCM (Figure 4.10c), so some anthropogenic CO_2 should be present and detectable in the SAM data set. The DIC in SAM is also consistently high relative to the observations, but the offset is fairly consistent across the entire DIC range, with the fit quality otherwise similar as for AOU. The TA fields from both simulations diverge considerably from reality, covering a much wider and higher range of values (Figure 4.10d), although they do correlate with each other. As this anomalous behaviour is present in the same way in both SAM and SCM, it should not adversely affect identification of the anthropogenic CO_2 signal in SAM.

In terms of rate of change, SAM does reasonably well represent the pattern for the observations in the upper water column (Figure 4.7b): $d\mathrm{DIC}_{\mathrm{anth}}/dt$ decreases away from surface from values between about 1.0 and 1.3 μmol kg^{-1} yr^{-1} to close to 0 at a σ_0 of about 27.5 in both SAM and the observations. The rates $d\mathrm{DIC}/dt$ and $d\mathrm{DIC}_{\mathrm{soft}}/dt$ are similarly well-matched. Deeper in the water column, there is a small increase in $\mathrm{DIC}_{\mathrm{anth}}$ in SAM that is not seen in the observations. This increase forms a broad peak between mean depths of about 1 and 2 km, with an amplitude of about 0.5 μmol kg^{-1} yr^{-1}. A similar pattern is observed in the same depth range for $\mathrm{DIC}_{\mathrm{anth}}$ in SCM (Figure 4.7d); its presence in the control simulation suggests that it may be an artefact caused by internal re-organisation of water masses and variables in the model in the absence of a long spin-up period. Alternatively, it may be associated with the northward AABW penetration previously identified as a possible cause of low σ_0 in the models relative to the observations (Heuzé et al., 2014; Hieronymus and Nycander, 2013). Other than where specified, SCM does not show significant changes in any of the tested variables, and the patterns with depth appear mostly random, suggesting that the $\mathrm{DIC}_{\mathrm{anth}}$ signal observed in SAM is indeed anthropogenic. The

$d\mathrm{DIC}_{\mathrm{carb}}/dt$, which is mostly dependent upon $d\mathrm{TA}/dt$ (Equation 4.2), exhibits changes in SAM which are absent from the observations throughout the water column; but, as for $\mathrm{DIC}_{\mathrm{anth}}$ in the deeper part of the water column, a similar pattern is found in SCM, which again suggests that it may result from ongoing drift from non-equilibrium initial model conditions.

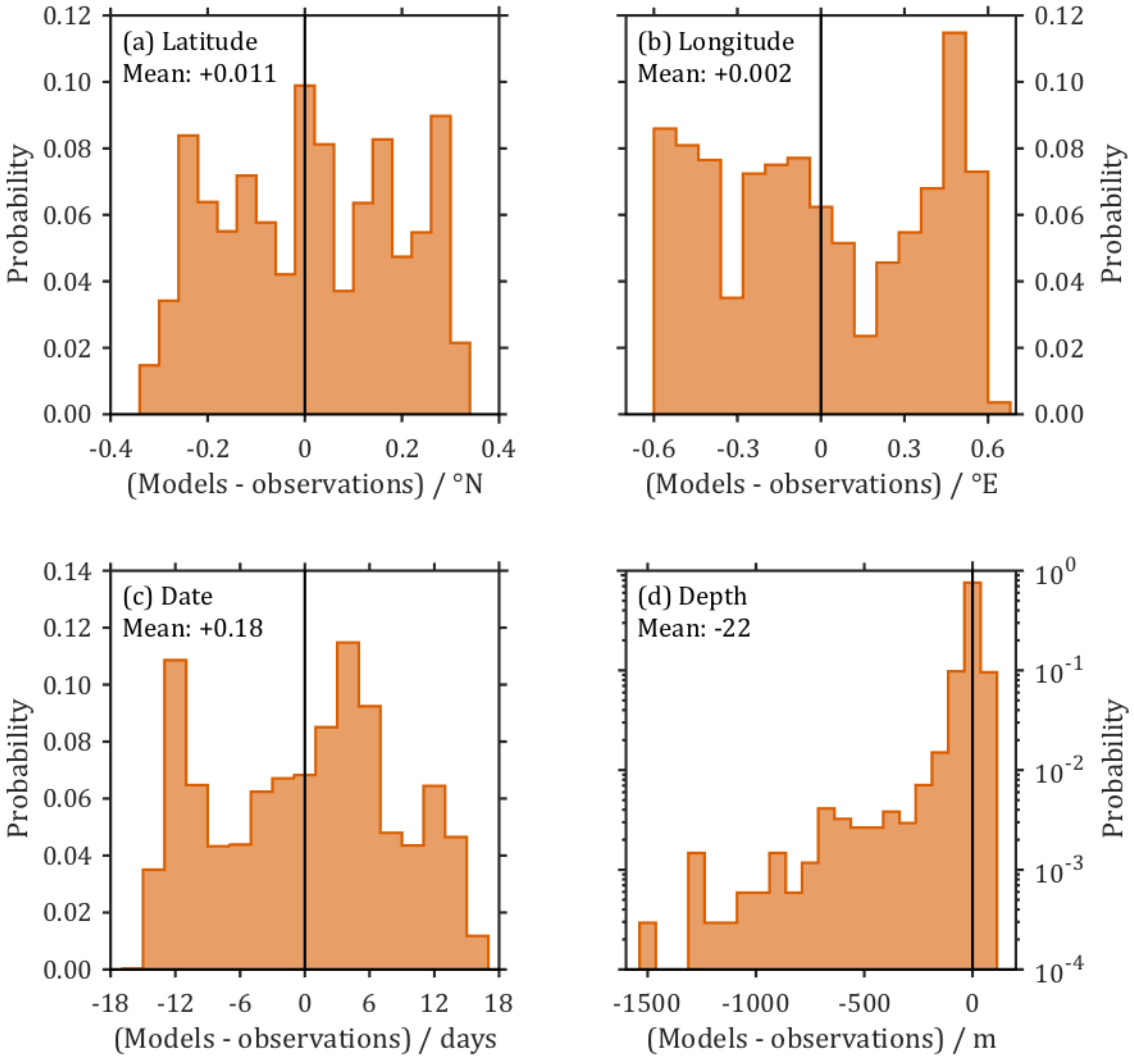

Figure 4.9. Probability distributions of offsets between observations and matching values from the subsampled monthly model outputs (SAM and SCM), for: (a) latitude; (b) longitude; (c) date; and (d) depth, note logarithmic vertical axis scale. The distributions for the anthropogenic and control simulations (SAM and SCM respectively) are identical for all of these metavariables.

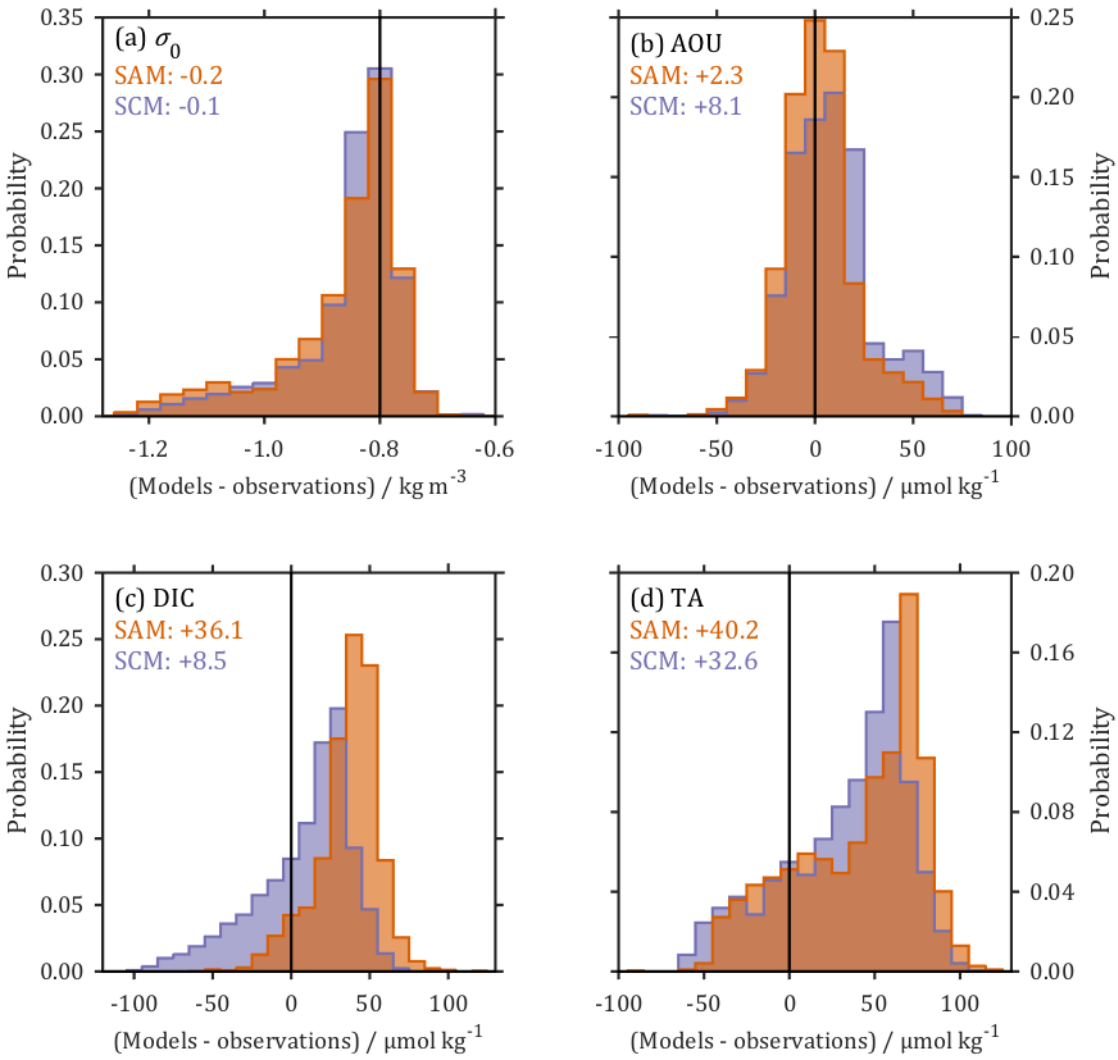

Figure 4.10. Probability distributions of offsets between observations and matching model values from the anthropogenic simulation (SAM, orange) and the control simulation (SCM, violet), for (a) potential density (σ_0), (b) apparent oxygen utilisation (AOU), (c) dissolved inorganic carbon (DIC), and (d) total alkalinity (TA). The SAM and SCM numerical values displayed in each panel are the mean offset for all of each data set.

4.4.3.2 Spatiotemporal sampling heterogeneity

The model data sets can be used to estimate the magnitude of the uncertainty resulting from spatiotemporal heterogeneity in the data distribution that is introduced into the observational rates of change, by comparing the rates of change calculated for the anthropogenic simulation subsampled to match the observations (SAM, Figure 4.7b) with those for the same simulation but with no missing values (TAA, Figure 4.7c). For each variable X, dX/dt at each σ_0 value in SAM is subtracted

from its value in TAA, and the mean ± standard deviation of these differences across all σ_0 is: -0.01 ± 0.15 for DIC, -0.29 ± 0.39 for TA, +0.22 ± 0.18 for AOU and -0.03 ± 0.19 for DIC_{anth}, all in μmol kg^{-1} yr^{-1}. These errors, particularly for DIC_{anth}, are up to an order of magnitude smaller than typical errors in rates of change. It is concluded that the spatiotemporal heterogeneity of the observational data distribution does not adversely affect the calculated rates of change for these variables.

4.4.3.3 North Atlantic Oscillation

It has been separately shown using observational data that multi-decadal trends in DO (and therefore AOU) can be identified despite substantial short-term interannual variability in a shorter, 19-year time-series transect close to the EEL, which samples several water masses also present at the EEL (Stendardo et al., 2015). However, difficulties are presented over shorter timescales. It has been suggested that a higher rate of DIC_{anth} accumulation can be identified in the Iceland Basin during the high North Atlantic Oscillation (NAO) index period from 1991 to 1998, compared with the lower NAO index (NAOI) period from 1997 to 2006 (Pérez et al., 2010). The NAOI can defined in several different ways, all associated with the atmospheric pressure difference between Iceland and the Azores, with a more positive NAOI indicating a greater difference in pressure (Hurrell et al., 2003). This pressure difference affects the local atmospheric circulation and surface wind speeds, and consequently can influence surface ocean currents and air-sea gas exchange (Thomas et al., 2008; Gruber, 2009). To test for a NAOI signal in the EEL time-series, the rate of change of DIC_{anth} was calculated using the same methods as for the observational, SAM and TAA data sets (Section 4.3.3), but restricted to these two date ranges (1991 to 1998 and 1997 to 2006). Although this produces an opposite result to Pérez et al. – that is, greater $d\mathrm{DIC}_{anth}/dt$ for the latter, low-NAOI period – and part of the increase in DIC_{anth} these workers observed was due to changes in σ_0 layer volumes rather than changes within σ_0 layers, the more important finding is that these calculated rates are not very meaningful. Because fewer data are available for the shorter time periods considered, the statistical significance of any apparent non-zero trends is much less reliable: for the full observational data set (1981 to 2013), the median uncertainty in $d\mathrm{DIC}_{anth}/dt$ across all σ_0 is 0.33 μmol kg^{-1}, while the equivalent figures for 1991 to 1998 and 1997 to 2006 are 1.94 μmol kg^{-1} and 1.99 μmol kg^{-1} respectively, so the uncertainty for these shorter time periods is the same magnitude as the long-term

DIC_{anth} rate of change (Figure 4.7). The atmospheric forcing used in the model simulations does not necessarily contain an NAO-like phenomenon, and even if there was one present it would not be expected to vary simultaneously with the real NAO. Consequently, an NAO effect cannot be directly observed in the model data sets. However, the model outputs can be used to indicate the unreliability of rates calculated using the EEL time-series data for these shorter time periods: the root-mean-square (RMS) difference between $d\mathrm{DIC}_{anth}/dt$ for the SCM and TAA data sets is 0.19 μmol kg^{-1} for 1981 to 2013, but it increases to 0.93 μmol kg^{-1} for 1997 to 2006 and is an order of magnitude greater for 1991 to 1998, taking a value of 2.39 μmol kg^{-1}. Clearly, the adverse impact of the spatiotemporal heterogeneity of the observations on calculated rates of change is significantly greater on these shorter timescales.

That is not to say that the NAO does not influence $d\mathrm{DIC}/dt$ and its components: indeed, in this study the positive $d\mathrm{DIC}_{soft}/dt$ has been attributed to contraction of the subpolar gyre, which is at least partly driven by the NAO – the wind patterns associated with a positive NAOI phase generally cause northward extension of the North Atlantic subtropical gyre (Gruber, 2009). Rather than disproving such a link, the demonstrated significant increase in uncertainty in rates of change over shorter timescales prevents these data from being used to support a direct link between the NAOI and the water column DIC at these shorter timescales. Even if it were possible to identify these relationships on these sub-decadal timescales, it may be more appropriate to attribute changes in water column DIC beneath the surface ocean mixed layer directly to subpolar gyre contraction rather than to positive NAO, and to use the subpolar gyre index (SPGI) rather than the NAOI to identify correlations. In the mixed layer, where the seawater is in direct contact with the atmosphere, direct relationships between the NAOI and hydrographic properties resulting from NAO control of surface wind fields might be expected (Thomas et al., 2008; Reverdin, 2010). However, the NAOI is defined in terms of atmospheric conditions, while the SPGI is oceanic; despite the ability of the NAO to influence the subpolar gyre, the relationship between the NAOI and SPGI is non-linear and asymmetric (the response of the subpolar gyre to a negative NAOI phase is not simply the opposite of its response to a positive) (Lohmann et al., 2008). As an oceanic property, the SPGI is therefore more likely to directly correlate with changes in DIC, even if the ultimate driver is the NAO.

4.4.3.4 Applicability of EEL rates to a wider area

Results from the TAA data set can be compared with FAA to investigate relationships between rates of change of variables observed at the EEL with changes in the surrounding ocean basins. The TAA data set contains all annual mean model output for the set of model stations identified as representing the EEL (Figure 4.1), while the FAA data set contains the same output but for a much wider area of the North Atlantic and Nordic Seas (Figure 4.12) with rates calculated separately at each station. This comparison shows that changes observed in the EEL water column are representative of changes on a much larger spatial scale, although which region the EEL best represents varies with σ_0. For illustrative purposes, the mean value of $\Delta[d\mathrm{DIC}/dt]$ (see Section 4.3.3) and its components (Equations 4.1 through 4.4) are taken at each σ_0 level across all model stations in the FAA data set within the latitude range from 25 to 40°N and longitude range from 070 to 030°W as representative of the North Atlantic, and from 66 to 72°N and 012°W to 001°E equivalently for the Nordic Seas (Figure 4.12). When the mean $\Delta[dX/dt]$ for a variable X is close to 0, the model station's dX/dt is similar to that observed at the EEL, which is then considered to represent that region well. Positive $\Delta[dX/dt]$ indicates a faster increase (or slower decrease) in X at the station than at the EEL, and the opposite for negative values.

For σ_0 in the range from 27.0 to 27.8 – most of the water column – $d\mathrm{DIC}/dt$ is between 0.5 and 1.5 μmol kg^{-1} yr^{-1} higher in the Nordic Seas than in the North Atlantic, but the position of the EEL on this gradient shifts with depth (Figure 4.11a). In the upper part of the water column (σ_0 < 27.35, e.g. Figure 4.12a), $\Delta[d\mathrm{DIC}/dt]$ is close to 0 for the Nordic Seas, but at higher σ_0 (e.g. Figure 4.12b) the EEL rate more closely resembles the North Atlantic. The divide between 'upper' and 'lower' water column in this context, at σ_0 between 27.3 and 27.4, corresponds to a depth of roughly 300 to 500 m at the EEL, and the bottom of the thermocline. Both the soft-tissue (Figure 4.11b) and carbonate (Figure 4.11c) components exhibit similar patterns as the total DIC change – that is, the EEL is changing more like the Nordic Seas in the upper water column, and like the North Atlantic at greater depths. However, because of how these components are combined to calculate the anthropogenic contribution to DIC change (Equation 4.1), the pattern is reversed for $\mathrm{DIC_{anth}}$: its accumulation in the upper water column is at a similar rate to the North Atlantic, while it matches the Nordic Seas at greater depths.

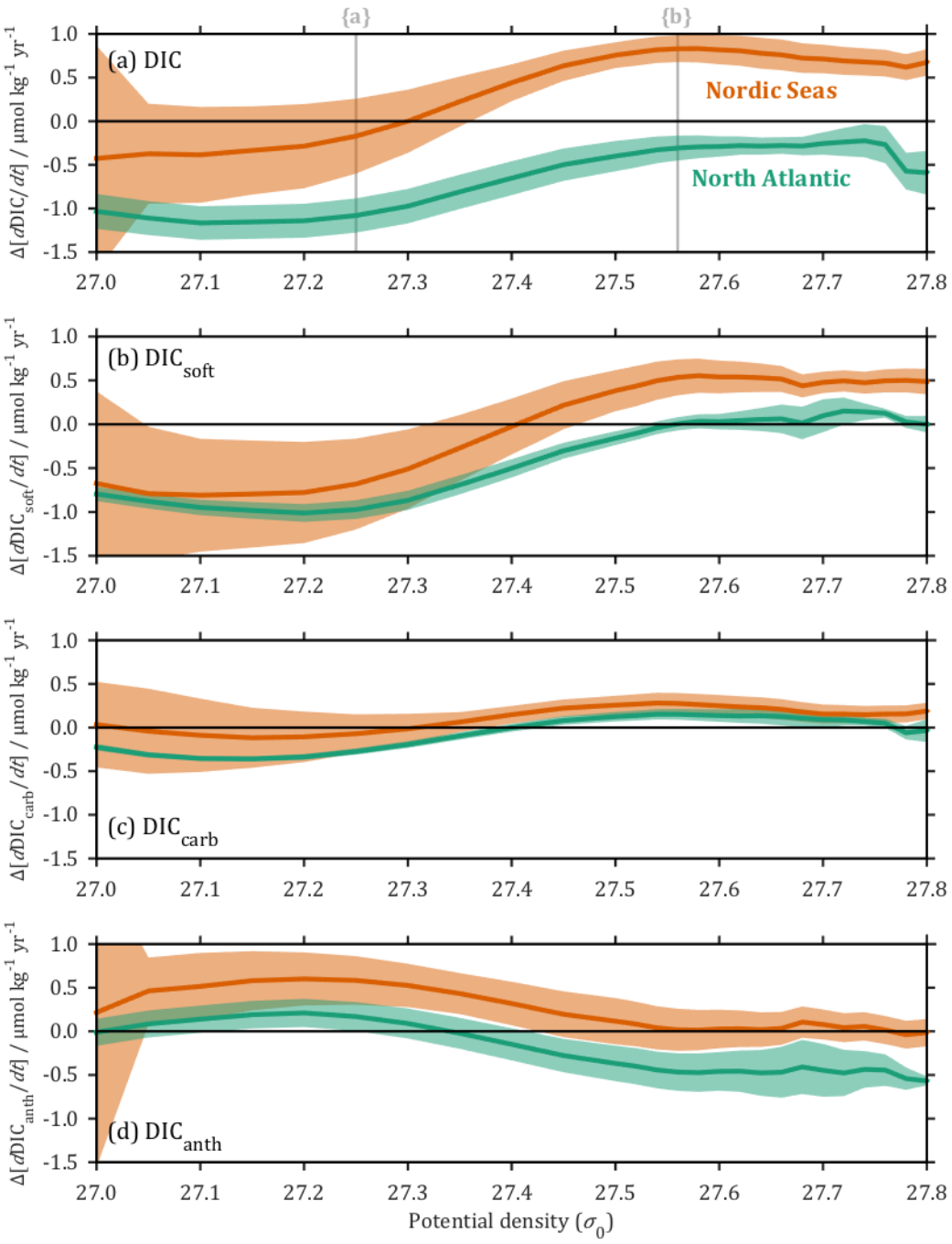

Figure 4.11. Mean rate of change of (a) dissolved inorganic carbon (DIC), and its components (b) DIC_{soft}, (c) DIC_{carb} and (d) DIC_{anth} in the full anthropogenic annual data set FAA in selected regions, relative to equivalent rate in the ideal model EEL transect data set TAA at the same potential density (σ_0). Positive values indicate that the faster rate is in the FAA data set. 'Nordic Seas' data (orange) is from 66 to 72°N and 012°W to 001°E; 'North Atlantic' (green) is from 25 to 40°N and 070 to 030°W (Figure 4.12). Shaded areas show ± 2 standard deviations about the mean values. In (a), the grey vertical lines marked {a} and {b} indicate the σ_0 values for Figures 4.9a and 4.9b respectively.

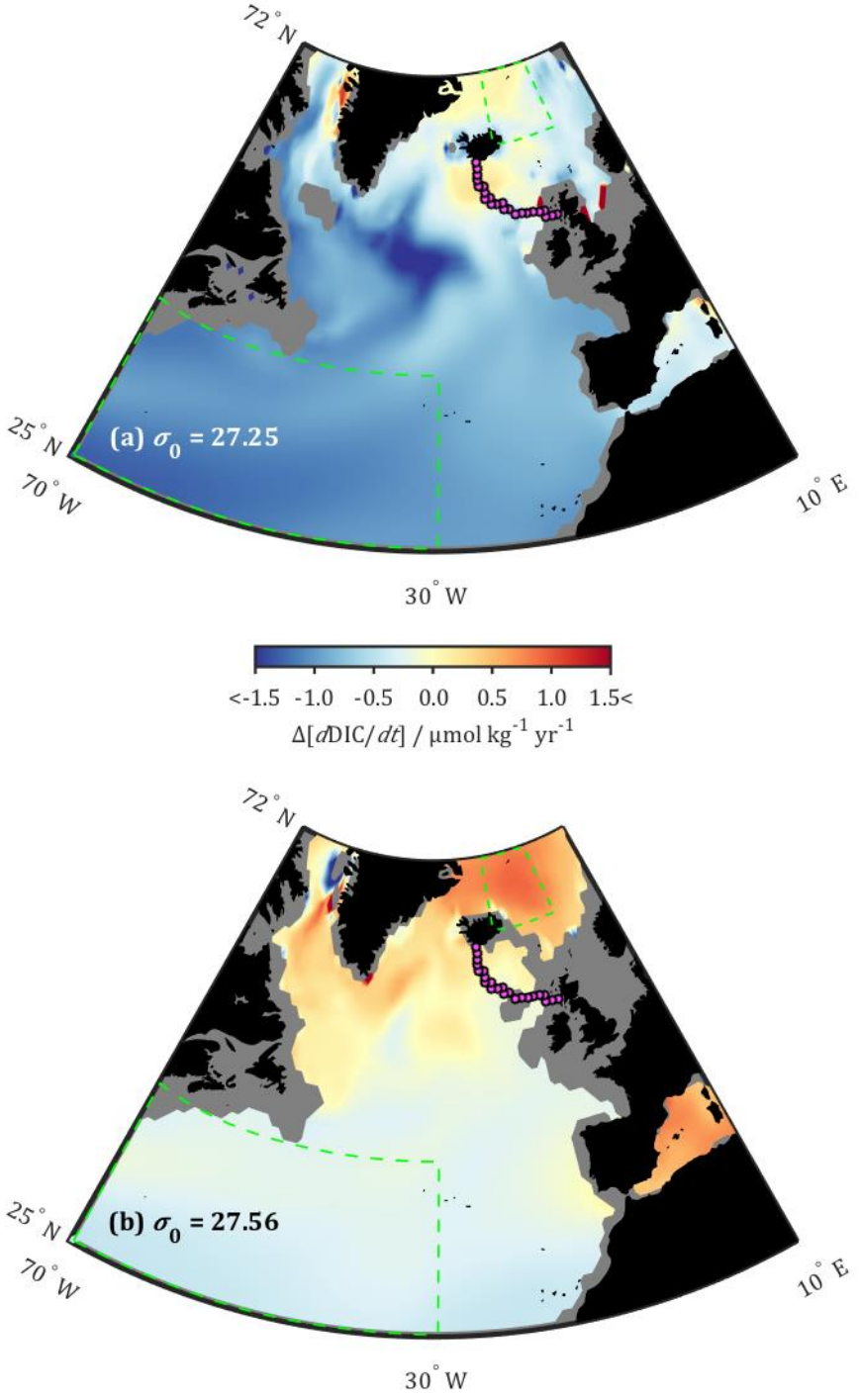

Figure 4.12. Rate of change of DIC at each 'station' in the full anthropogenic annual model data set (FAA), relative to its value at the same σ_0 level in the ideal model EEL transect data set (TAA), for (a) σ_0 = 27.25, and (b) σ_0 = 27.56, as indicated in Figure 4.11a. Positive values (red) indicate higher dDIC/dt in FAA than TAA, and negatives the opposite (blue). Magenta circles show model stations representing idealised EEL for the TAA data set (Figure 4.1). Green dashed lines enclose areas considered representative of North Atlantic and Nordic Seas for Figure 4.11.

Several conclusions can be drawn from this part of the analysis. For a significant section of the water column, several variables are changing at the same rate at the EEL as they are throughout the surrounding regions in the model domain, but different variables (and components of variables) at a given σ_0 value may not reflect changes in the same adjacent region as each other. We cannot directly transfer the findings to the observations, in particular a specific σ_0 value where the EEL switches from representing one adjacent region to the other, without a more advanced analysis of water mass circulation in the model and a full resolution of the differences between σ_0 in the model and observations (Figure 4.10a) – both of these are beyond the scope of this study – but it does seem logical that the base of the thermocline could be a point where such a switch-over happens in the real world, as that is where the main currents change between travelling from the north and from the south at the EEL (Hansen and Østerhus, 2000). Changes in these variables are also sufficiently spatially coherent that measurements of their rates along the EEL could potentially be used to track and predict similar changes far beyond its immediate surroundings.

4.5 Conclusions

Sufficient measurements have now been made along the Extended Ellett Line (EEL) transect to establish a time-series of data, from which increases in DIC can be identified throughout the water column; these can also be deconvolved into causal components. Virtually all of the increase in DIC, which is concentrated in and above the thermocline, is driven by a combination of anthropogenic CO_2 accumulation and increases in the amount of remineralised organic matter present. The latter of these is likely driven by changes in the lateral distribution of water masses along potential density surfaces. Most of the changing distribution is probably caused by a net contraction of the subpolar gyre over the time period studied, and an increasing influence of southern-sourced waters as a consequence.

Future EEL occupations will provide additional data to extend this time-series analysis, and once more consecutive years of data become available it may become possible to assess the influence of processes operating on sub-decadal timescales, for example the NAO, and other aspects of inter-annual variability. The measurements from the 2014 EEL cruise will soon be available for inclusion. The soon-to-be-released GLODAPv2 data product, which will incorporate the original GLODAP and CARINA data syntheses along with many new cruises, all having undergone an independent and consistent secondary quality-control process, will also provide a useful update to this analysis. Continued annual measurements may permit an assessment of the influence of the subpolar gyre circulation and NAO on DIC accumulation on shorter timescales than can be achieved using the existing data. A robust quantification of the inter-annual variability will also be useful to better evaluate the confidence bounds on rate-of-change calculations and times-of-emergence for long-term trends.

The isotopic data provide independent supporting evidence for the attribution of DIC changes to different driving processes, and additional isotopic measurements on future EEL occupations would be valuable; they add an extra degree of freedom which enables additional processes to be investigated. Combination of the observational data with output from model simulations has demonstrated that the spatial and temporal heterogeneity in the distribution of the observations does not adversely affect the calculated rates of change. The model data have also provided insight into the relevance of the EEL in a larger regional setting, suggesting that changes observed locally may reflect much wider scale changes occurring in the

North Atlantic and Nordic Seas. To use these results quantitatively to extrapolate EEL rates of change into the surrounding ocean basins would require first resolving precisely why offsets exist between the distribution of the observations and model outputs for the variables of interest (see Section 4.4.3.1), but they nevertheless further support continued regular monitoring of carbonate chemistry variables at the Extended Ellett Line.

5

Are coccolithophores sources or sinks of CO_2?

Abstract

Marine phytoplankton are normally oceanic sinks of carbon dioxide (CO_2), but coccolithophores also calcify so they can instead act as CO_2 sources to the atmosphere. Previous classifications of particular species as CO_2 sources or sinks have compared the production ratio, which is the ratio of calcite to organic matter production, with a threshold value at which there is no net change in the seawater partial pressure of CO_2 (pCO_2^{sw}). Some studies have assumed that this threshold is spatially and temporally homogeneous in the global surface ocean, which it is not, and others may have evaluated it erroneously. Furthermore, this threshold varies depending on the changes in total alkalinity (TA) associated with organic matter production, which are different for different coccolithophore species. In addition to the production ratio, the 'production slope', which is introduced in this chapter, can be evaluated for each species; its value relative to a threshold called the 'isocap slope' determines whether a coccolithophore is a CO_2 source or sink. The isocap slope is independent of which coccolithophore species is being considered and can be calculated exactly if the carbonate chemistry system is fully determined, or estimated from pCO_2^{sw}, seawater temperature and salinity. Spatial and temporal variability in the isocap slope is investigated using a climatological data set, and its magnitude is sufficient that some coccolithophore species could switch from being CO_2 sources to sinks both seasonally and also depending upon their geographical distribution. If there were no changes in their biology, coccolithophores would be stronger net CO_2 sinks during past climates with lower atmospheric CO_2 concentrations, whilst during past high-CO_2 events and moving into the immediate future they will become stronger net CO_2 sources, thus constituting a positive feedback on the atmospheric CO_2 concentration.

5.1. Introduction

Coccolithophores are a class of marine phytoplankton that produce calcite plates called coccoliths (Young et al., 2003). They have a more-or-less global distribution throughout the euphotic zone of the ocean (Winter et al., 1994) and are typically responsible for up to 10 % of total carbon fixation in the surface ocean, although they can sometimes account for a much greater fraction (Poulton et al., 2007). Coccolithophores provide particularly effective ballasting material in the form of dense calcite for the transfer of carbon from the surface into the interior ocean (Honjo et al., 2008; Sanders et al., 2010). In addition, they can significantly affect the carbonate chemistry of the surrounding seawater, and thus air-sea CO_2 exchange, when they bloom in large numbers (Holligan et al., 1993; Robertson et al., 1994; Buitenhuis et al., 2001). Through their net autotrophic production, coccolithophores reduce the dissolved inorganic carbon concentration (DIC) and slightly increase the total alkalinity (TA) in the surrounding seawater, which has the effect of decreasing the seawater partial pressure of CO_2 (pCO_2^{sw}). This drives an increase in the net air-to-sea transfer of carbon dioxide (CO_2), so this process is considered a CO_2 sink. Calcification, however, is a CO_2 source – although it also reduces the seawater DIC, it simultaneously decreases TA by twice as much, sufficiently that there is a net increase in pCO_2^{sw}. Whether a specific coccolithophore species acts as a CO_2 source or sink depends upon whether the combination of these two processes causes a net decrease or an increase in pCO_2^{sw} (Figure 5.1).

It has previously been suggested that a threshold value for the ratio of calcification to net autotrophic production (the production ratio, R_P) exists at which there is no net change in pCO_2^{sw} (Buitenhuis et al., 2001; Poulton et al., 2007). This threshold value is influenced by the change in TA associated with nutrient uptake during autotrophic production, which varies because this uptake stoichiometry is species-specific. Thus it becomes necessary to define a different threshold production ratio for each species. An alternative and more efficient approach is presented here, in which a 'production slope' is defined for each coccolithophore species; this is controlled by both the production ratio and the nutrient uptake stoichiometry. The production slope has a threshold called the isocap slope, which is independent of the species under consideration. Whether the production slope exceeds this threshold or not determines whether a coccolithophore is a net CO_2 source or sink.

The isocap slope can be exactly calculated if the values of at least two carbonate chemistry variables are known and thus the system is fully resolved. It can also be estimated directly from pCO_2^{sw}, using the novel approximation that lines of constant pCO_2^{sw} (called isocaps) are linear within environmentally-relevant ranges of DIC and TA variable space. This approximation and a climatological pCO_2^{sw} data set can be used to analyse previously unsuspected spatial and temporal variability in the behaviour of coccolithophores as CO_2 sources and sinks, driven by variability in the isocap slope. It also provides insight into how this behaviour was different in the past, and how it is expected to change in the future. Chemically, calcification is a positive feedback on pCO_2^{sw}, so in the absence of any biological changes, coccolithophores become stronger CO_2 sources in higher pCO_2^{sw} conditions, and stronger sinks when pCO_2^{sw} declines.

The linear approximation of the isocap slope is also of purely academic interest. To fully understand the carbonate chemistry of a seawater sample and how it will be affected by any biogeochemical process, values for at least two of the system's variables – pCO_2^{sw}, DIC, TA, pH, and the concentrations of bicarbonate and carbonate ions – must be known, permitting a full mathematical solution of the system from which the value of every other variable can be determined (Zeebe and Wolf-Gladrow, 2001). However, there are significantly more surface ocean pCO_2^{sw} data than there are for any of the other variables, and it is also the best constrained of them in the palaeorecord. This provides an incentive to develop techniques that only require pCO_2^{sw} data, like the one described here.

5.2. Methods

5.2.1. Simplified coccolithophore model

For this analysis, each coccolithophore cell is considered to consist of two pools of particulate material: one of calcium carbonate ($CaCO_3$), and one of organic matter (POM). The coccolithophore takes up various dissolved chemical species from the surrounding seawater and converts these into these two particulate forms, following the reactions outlined in section 5.2.2. The production of particulate material is assumed to be constant and the production rate of each pool relative to the other does not change, but it makes no difference to the model whether or not the absolute production rate is constant. Once in a particulate form, these chemical species can no longer influence the chemistry of the surrounding seawater. If any material is lost from these particulate pools, it is assumed to have returned to a dissolved phase in the surrounding seawater *via* the reverse of its formation reaction. The size of each pool at any time therefore represents the net of the forward and reverse reactions.

5.2.2. Production slope

Conceptually, the production slope (S_P) is the gradient of the sum of the calcification and autotrophic production vectors in DIC and TA variable space (Figure 5.1). The seawater dissolved inorganic carbon concentration (DIC) is given by:

Equation 5.1 $$\mathrm{DIC} = [\mathrm{CO_2}] + [\mathrm{HCO_3^-}] + [\mathrm{CO_3^{2-}}]$$

where the square brackets indicate the molality of the enclosed chemical species in seawater solution. The seawater partial pressure of CO_2 ($p\mathrm{CO_2^{sw}}$) is directly proportional to its dissolved concentration:

Equation 5.2 $$[\mathrm{CO_2}] = k_0 \cdot p\mathrm{CO_2^{sw}}$$

where k_0 is the equilibrium constant for the dissolution of CO_2 in seawater:

Equation 5.3 $$\mathrm{CO_{2(g)}} \overset{k_0}{\rightleftharpoons} \mathrm{CO_{2(aq)}}$$

The $p\mathrm{CO_2^{sw}}$ is therefore equal to the partial pressure of CO_2 in theoretical air in equilibrium with the seawater. An increase in $p\mathrm{CO_2^{sw}}$ drives an increase in the net sea-to-air transfer of CO_2, and a decrease in $p\mathrm{CO_2^{sw}}$ drives a decrease in this transfer.

The explicit conservative expression for TA can be used to determine the effect that biogeochemical processes will have on TA (Wolf-Gladrow et al., 2007):

Equation 5.4 $$TA = 2[Ca^{2+}] - [NO_3^-] - TPO_4 - 2TSO_4 + other\ terms$$

where the extra chemical species indicated by *other terms* are not relevant to this discussion, and TPO_4 and TSO_4 are the total concentrations of dissolved phosphate and sulfate species respectively:

Equation 5.5 $$TPO_4 = [H_3PO_4] + [H_2PO_4^-] + [HPO_4^{2-}] + [PO_4^{3-}]$$

Equation 5.6 $$TSO_4 = [HSO_4^-] + [SO_4^{2-}]$$

Calcification and autotrophic production can thus be described in terms of their effects on DIC and TA (Figure 5.1), based upon the following simplified reactions for calcification:

Equation 5.7 $$Ca^{2+} + CO_3^{2-} \longrightarrow CaCO_{3(s)}$$

where $CaCO_{3(s)}$ is PIC (particulate inorganic carbon); and for autotrophic production:

Equation 5.8
$$H_3PO_4 + \alpha HNO_3 + \beta CO_2 + \lambda H_2O + \eta H_2SO_4 \longrightarrow C_\beta H_\zeta O_\varphi N_\alpha S_\eta P_{\theta(s)} + \gamma O_2$$

where $C_\beta H_\zeta O_\varphi N_\alpha S_\eta P_{\theta(s)}$ is particulate organic matter (POM), which is equivalent stoichiometrically to β × POC (particulate organic carbon), and the coefficients denoted by Greek letters (α, β, γ, ζ, η, λ, θ and φ) take different values depending upon the stoichiometry of nutrient uptake by the phytoplankton species. For simplicity, all reactants in Equation 5.8 are shown fully-protonated; in reality, they exist in seawater in various states of dissociation, but exactly which species are involved in the reaction is unimportant in this context. For example, $[H_2SO_4]$ in normal seawater is negligible as it is virtually completely dissociated into bisulfate and sulfate ions (HSO_4^- and SO_4^{2-}). Regardless of which of these species is taken up during photosynthesis, TSO_4 (Equation 5.6) – and therefore TA (Equation 5.4) – will be changed by the same amount. Similar considerations apply to H_3PO_4, HNO_3 (which is virtually completely deprotonated to NO_3^-) and CO_2 (which affects Equation 5.1 for DIC, but not TA). An important assumption to note is that all biological uptake and excretion of N is in the form of HNO_3 and NO_3^-. Exploring the differences caused by NH_3 and/or NH_4^+ use is an important focus for future work, discussed in Section 5.3.3.1.

The following relationships can therefore be deduced between changes in DIC, TA, PIC and POC during calcification (i.e. PIC production):

Equation 5.9 $$d\mathrm{DIC}_{\mathrm{PIC}} = -d\mathrm{PIC}$$

Equation 5.10 $$d\mathrm{TA}_{\mathrm{PIC}} = -2 \cdot d\mathrm{PIC}$$

and during autotrophic production (i.e. POC production):

Equation 5.11 $$d\mathrm{DIC}_{\mathrm{POC}} = -d\mathrm{POC}$$

Equation 5.12

$$d\mathrm{TA}_{\mathrm{POC}} = \frac{1}{\beta}(\alpha + 2\eta + \theta) \cdot d\mathrm{POC}$$

The sums of these components are given by dDIC and dTA:

Equation 5.13 $$d\mathrm{DIC} = d\mathrm{DIC}_{\mathrm{PIC}} + d\mathrm{DIC}_{\mathrm{POC}}$$

Equation 5.14 $$d\mathrm{TA} = d\mathrm{TA}_{\mathrm{PIC}} + d\mathrm{TA}_{\mathrm{POC}}$$

Therefore, the relative changes in DIC and TA driven by these processes are given by:

Equation 5.15

$$\frac{\mathrm{dTA}_{\mathrm{PIC}}}{\mathrm{dDIC}_{\mathrm{PIC}}} = 2$$

for calcification, and for autotrophic production:

Equation 5.16

$$\frac{d\mathrm{TA}_{\mathrm{POC}}}{d\mathrm{DIC}_{\mathrm{POC}}} = -\frac{1}{\beta}(\alpha + 2\eta + \theta)$$

The net rates of calcification and autotrophic production can in practice be estimated from the net rates at which PIC and POC respectively are produced (Findlay et al., 2011), dPIC/dt and dPOC/dt, where t is time. A production ratio (R_{P}) of PIC and POC can thus be defined for a given organism as:

Equation 5.17

$$R_{\mathrm{P}} = \frac{d\mathrm{PIC}}{dt} \cdot \left(\frac{d\mathrm{POC}}{dt}\right)^{-1} = \frac{d\mathrm{PIC}}{d\mathrm{POC}}$$

Combining Equations 5.9 to 5.17 and letting $d\mathrm{POC} = 1$ (and therefore $d\mathrm{PIC} = R_P$, Equation 5.17), the net change in TA relative to DIC from both processes, called the production slope (S_P), is given by:

Equation 5.18

$$S_P = \frac{d\mathrm{TA}}{d\mathrm{DIC}} = \frac{d\mathrm{TA_{PIC}} + d\mathrm{TA_{POC}}}{d\mathrm{DIC_{PIC}} + d\mathrm{DIC_{POC}}} = \frac{2R_P - \frac{1}{\beta}(\alpha + 2\eta + \theta)}{R_P + 1}$$

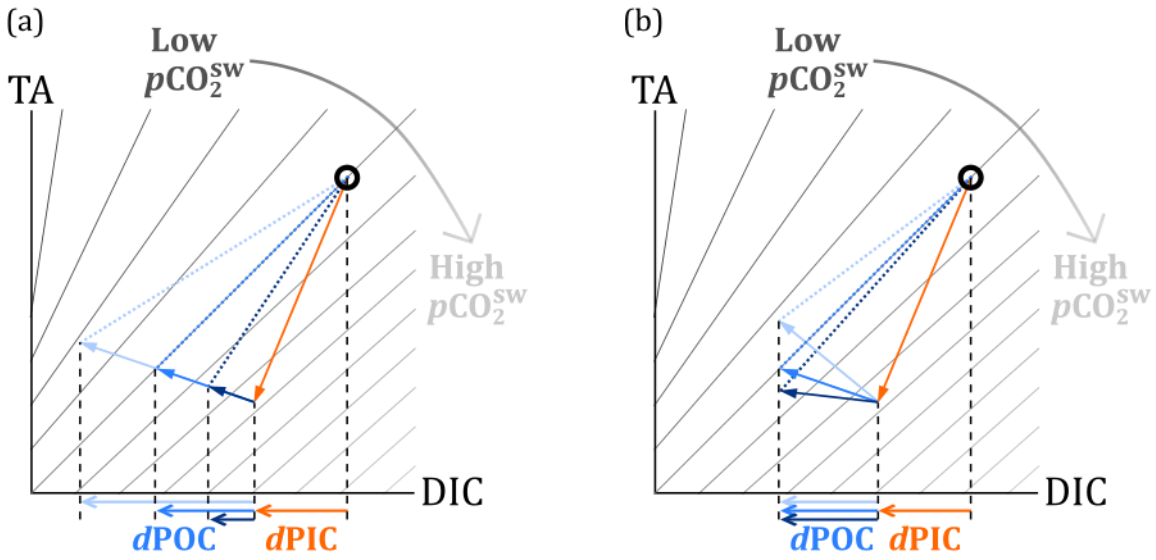

Figure 5.1. Combined effects of calcification (orange) and autotrophic production (blue) on seawater dissolved inorganic carbon (DIC), total alkalinity (TA) and partial pressure of CO_2 (pCO_2^{sw}) from an initial seawater composition indicated by the black circle. Grey diagonal lines are isocaps (contours of constant pCO_2^{sw}). In both panels, the light blue vector illustrates a CO_2 sink, medium blue is pCO_2^{sw}-neutral (i.e. $S_P = S_I$), and dark blue is a CO_2 source. The different autotrophic production vectors illustrate the effects of (a) changes in production ratio R_P at constant POM stoichiometry (i.e. constant $d\mathrm{TA_{POC}}/d\mathrm{DIC_{POC}}$, Equation 5.16), with R_P increasing from light to dark blue; and (b) changes in POM stoichiometry at constant R_P, with $d\mathrm{TA_{POC}}/d\mathrm{POC}$ increasing from dark to light blue. Dotted blue lines indicate the production slope (S_P) in each case.

5.2.3. Isocap slope

Contours of constant pCO_2^{sw} in DIC and TA phase space, called isocaps, are non-linear; their instantaneous slope at any point – $d\mathrm{TA}/d\mathrm{DIC}$ at constant pCO_2^{sw} – is the isocap slope (S_I, Figure 5.1). This is the threshold value for the production slope (S_P) at which

the coccolithophore has no net effect on pCO_2^{sw}. In this section, an exact expression for S_I is derived from the equations for DIC and TA, and the novel approximation that isocaps are linear within environmentally-relevant ranges of DIC and TA is demonstrated. This permits the estimation of S_I from only pCO_2^{sw} (S_I^{lin}), circumventing the usual requirement to have values for two carbonate system variables. The symbols S_I and S_I^{lin} are used throughout to indicate specifically which method has been used to evaluate the isocap slope for each figure and part of the discussion, but in terms of their consequences and interpretation the approximation is accurate enough that the two are effectively interchangeable (section 5.3.5.2); conclusions reached for S_I^{lin} also apply to S_I and *vice versa*.

5.2.3.1. Exact calculation

The exact value of S_I is derived from Equation 5.1 for DIC and Dickson's definition of TA (Dickson, 1981), simplified to exclude species with negligibly small concentrations in typical seawater (Zeebe and Wolf-Gladrow, 2001):

Equation 5.19 $$TA = [HCO_3^-] + 2[CO_3^{2-}] + [B(OH)_4^-] + [OH^-] - [H^+]$$

Equations 5.1 and 5.19 must be converted into functions of $[H^+]$ and $[CO_2]$. The reactions for the dynamic equilibria between the carbonate species in Equation 5.1 can be represented as:

Equation 5.20 $$CO_2 + H_2O \overset{k_1}{\rightleftharpoons} HCO_3^- + H^+$$

Equation 5.21 $$HCO_3^- \overset{k_2}{\rightleftharpoons} CO_3^{2-} + H^+$$

The stoichiometric dissociation constants k_1 and k_2 are given by:

Equation 5.22
$$k_1 = \frac{[HCO_3^-][H^+]}{[CO_2]}$$

Equation 5.23
$$k_2 = \frac{[CO_3^{2-}][H^+]}{[HCO_3^-]}$$

Rearranging Equations 5.22 and 5.23 and substituting into Equation 5.1 generates the required expression for DIC:

Equation 5.24

$$\mathrm{DIC} = [\mathrm{CO_2}]\left(1 + \frac{k_1}{[\mathrm{H^+}]} + \frac{k_1 k_2}{[\mathrm{H^+}]^2}\right)$$

For borate, the equivalent reaction and equations are:

Equation 5.25 $\mathrm{TB} = [\mathrm{B(OH)_3}] + [\mathrm{B(OH)_4^-}]$

Equation 5.26 $\mathrm{B(OH)_3} + \mathrm{H_2O} \overset{k_\mathrm{B}}{\rightleftharpoons} \mathrm{B(OH)_4^-} + \mathrm{H^+}$

Equation 5.27

$$k_\mathrm{B} = \frac{[\mathrm{B(OH)_4^-}][\mathrm{H^+}]}{[\mathrm{B(OH)_3}]}$$

and for the dissociation of water into protons and hydroxide ions:

Equation 5.28 $\mathrm{H_2O} \overset{k_\mathrm{w}}{\rightleftharpoons} \mathrm{H^+} + \mathrm{OH^-}$

Equation 5.29 $k_\mathrm{w} = [\mathrm{H^+}][\mathrm{OH^-}]$

Rearranging and substituting into Equation 5.19 generates an expression for TA:

Equation 5.30

$$\mathrm{TA} = \frac{-[\mathrm{H^+}]^4 - k_\mathrm{B}[\mathrm{H^+}]^3 + X[\mathrm{H^+}]^2 + Y[\mathrm{H^+}] + Z}{[\mathrm{H^+}]^3 + k_\mathrm{B}[\mathrm{H^+}]^2}$$

where *X*, *Y* and *Z* are functions of $[\mathrm{CO_2}]$:

Equation 5.31 $X = k_1[\mathrm{CO_2}] + k_\mathrm{B}\mathrm{TB} + k_\mathrm{w}$

Equation 5.32 $Y = (k_1 k_\mathrm{B} + 2k_1 k_2)[\mathrm{CO_2}] + k_\mathrm{B} k_\mathrm{w}$

Equation 5.33 $Z = 2k_1 k_2 k_\mathrm{B}[\mathrm{CO_2}]$

Equations 5.24 and 5.30 are then differentiated with respect to $[\mathrm{H^+}]$ at constant $[\mathrm{CO_2}]$, and the chain rule is applied to give $d\mathrm{TA}/d\mathrm{DIC}$ (i.e. S_I) in terms of $[\mathrm{H^+}]$ and $[\mathrm{CO_2}]$:

Equation 5.34

$$S_\mathrm{I} = \frac{-[\mathrm{H^+}]^4([\mathrm{H^+}] + 2k_\mathrm{B}) - ({k_\mathrm{B}}^2 + X)[\mathrm{H^+}]^3 - Y[\mathrm{H^+}](2[\mathrm{H^+}] + k_\mathrm{B}) - Z(3[\mathrm{H^+}] + 2k_\mathrm{B})}{-(k_1[\mathrm{CO_2}][\mathrm{H^+}] + 2k_1 k_2[\mathrm{CO_2}])([\mathrm{H^+}] + k_\mathrm{B})^2}$$

The values of [H^+] and [CO_2] can be determined for any given DIC and TA (Zeebe and Wolf-Gladrow, 2001), thus S_I can be calculated using Equation 5.34. Various functions of temperature and salinity for the equilibrium constants (k_1, k_2, k_B and k_w) and TB exist; the effects of different choices on S_I are evaluated and discussed in Section 5.3.5.3. Appendix 2, Section A2.1 contains a MATLAB (MathWorks) function `mph_sliso` which evaluates S_I using Equation 5.34 and version 1.1 of the CO_2SYS program for MATLAB (MathWorks) (van Heuven et al., 2011).

5.2.3.2. Linear approximation

The isocap slope (S_I) can also be estimated directly from pCO_2^{sw}, seawater temperature and salinity, using the novel approximation that isocaps are linear. Such estimates of S_I are referred to as S_I^{lin}. The accuracy of S_I^{lin} and its consequences are evaluated and discussed in Section 5.3.5.2.

The isocap slope can be estimated from pCO_2^{sw} using an equation of the form:

Equation 5.35

$$S_I \approx S_I^{lin} = a + \frac{b}{(c + pCO_2^{sw})^d}$$

where a, b, c and d are empirically-determined polynomial functions of seawater temperature and salinity. Specifically, a 4-dimensional matrix of S_I values was calculated using Equation 5.34, with dimensions TA, pCO_2^{sw}, temperature and salinity, in the following ranges: 2030 to 2600 µmol kg^{-1}, 20 to 4000 µatm, -1 to 37 °C, and 25 to 45 respectively. The equilibrium constants and [H^+] were evaluated using version 1.1 of the CO_2SYS program for MATLAB (MathWorks) (van Heuven et al., 2011) on the Free pH scale, from the following sources: carbonic acid dissociation constants k_1 and k_2 of Lueker et al. (2000); boric acid dissociation constant k_B of Dickson (1990b); ion product of water k_w of Millero (1995); and to estimate TB from salinity, the boron to chlorinity ratio of Lee et al. (2010). The mean S_I across all TA values was then calculated for each pCO_2^{sw}, temperature and salinity combination. Next, least-squares best-fit values for the coefficients a, b, c and d (Equation 5.35) were calculated for every temperature and salinity combination (Figure 5.2). Finally, polynomial functions of temperature and salinity were generated using non-linear least-squares curve fitting for a, b, c and d (Table 5.1), of the form:

Equation 5.36 $$x = x_1 + x_2T + x_3T^2 + x_4T^3 + x_5TS + x_6T^2S + x_7S + x_8S^2$$

where T is temperature in °C, S is salinity, and x represents any of a, b, c or d. Appendix 2 contains the MATLAB (MathWorks) functions which were used to carry out this curve-fitting procedure (A2.2, `generate_sliso_parameterisation`) and to apply the results to evaluate $S_{\mathrm{I}}^{\mathrm{lin}}$ (A2.3, `mph_slisolin`).

Term (multiplier)	***a***	***b***	***C***	***d***
x_1 (1)	0.98816	11.312	12.560	0.91715
x_2 (T)	-2.7845×10^{-3}	6.3984×10^{-1}	-1.2390×10^{-1}	-4.5700×10^{-3}
x_3 (T^2)	1.8609×10^{-4}	-1.7461×10^{-2}	7.7449×10^{-2}	2.4269×10^{-5}
x_4 (T^3)	-2.5893×10^{-6}	7.6719×10^{-5}	-9.2933×10^{-4}	-1.3887×10^{-6}
x_5 ($T\,S$)	4.7228×10^{-5}	-1.3161×10^{-2}	3.8589×10^{-2}	-5.1792×10^{-5}
x_6 ($T^2\,S$)	-3.8265×10^{-6}	1.0872×10^{-4}	-1.0968×10^{-3}	-1.5447×10^{-6}
x_7 (S)	7.4095×10^{-4}	0.21028	1.2782	-2.9309×10^{-3}
x_8 (S^2)	-1.6419×10^{-5}	-1.2561×10^{-3}	-8.5354×10^{-3}	5.0311×10^{-6}

Table 5.1. Coefficients for the terms in equations in the form of Equation 5.36 for the coefficients a, b, c and d in Equation 5.35. Each coefficient is the sum of the products of each multiplier and the value in each corresponding row. The calculation and additional significant figures for the coefficients are given in the MATLAB (MathWorks) function in Appendix 2, Section A2.3. For the multipliers, T is seawater temperature in °C, and S is salinity.

5.2.4. Source or sink?

The difference between the production and isocap slopes (ΔS) determines whether a coccolithophore is a net source or sink of CO_2:

Equation 5.37 $$\Delta S = S_{\mathrm{P}} - S_{\mathrm{I}}$$

The sign of ΔS matches the net change in $p\mathrm{CO}_2^{\mathrm{sw}}$: positive ΔS means that $p\mathrm{CO}_2^{\mathrm{sw}}$ is increased, and the coccolithophore is a CO_2 source; negative ΔS signifies a reduction in $p\mathrm{CO}_2^{\mathrm{sw}}$, so the coccolithophore is a CO_2 sink. These statements apply only while $d\mathrm{DIC}/dt$ is negative, which is always the case when net autotrophic production ($d\mathrm{POC}/dt$) and calcification ($d\mathrm{PIC}/dt$) rates are positive.

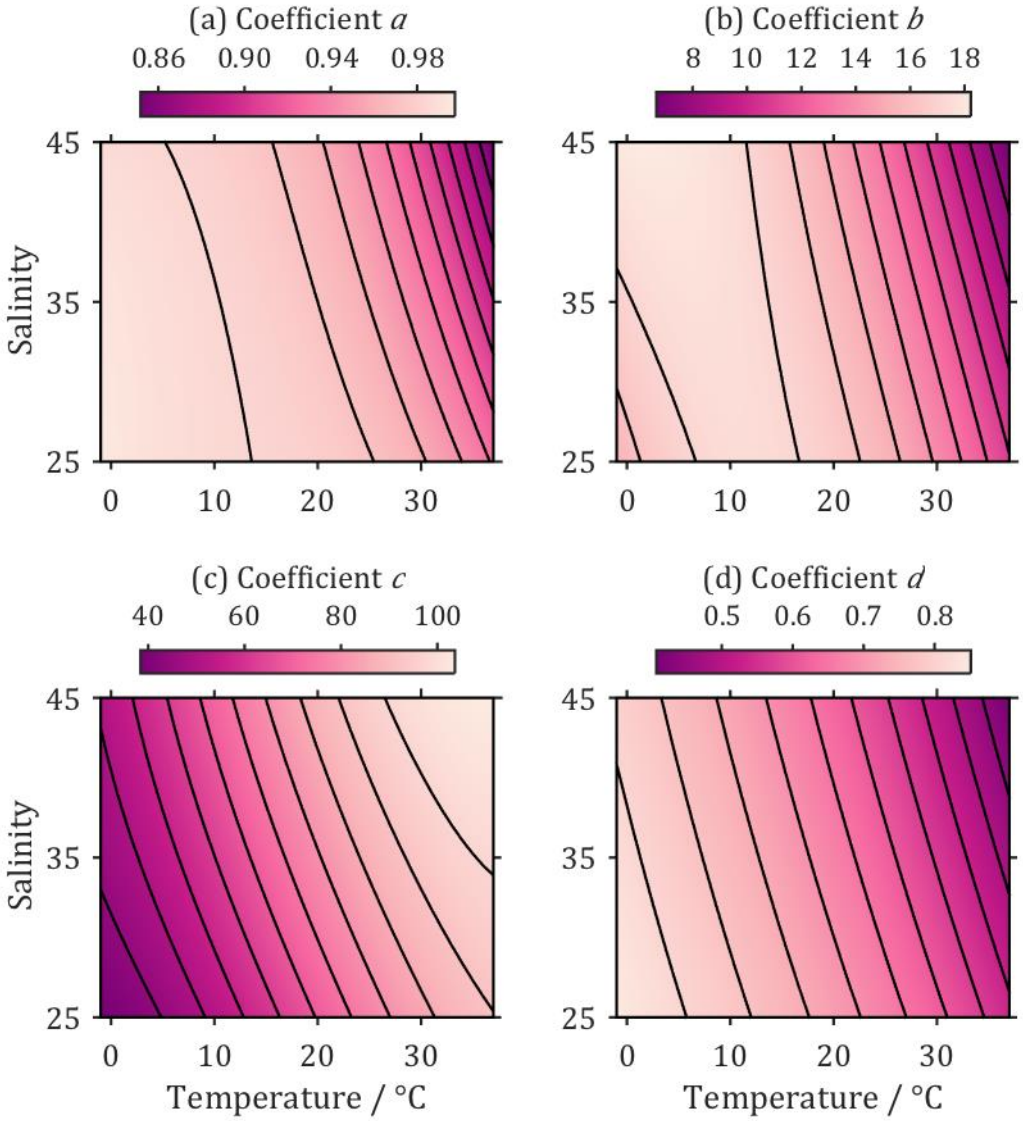

Figure 5.2. Variation of the coefficients (a) *a*, (b) *b*, (c) *c* and (d) *d* in Equation 5.35 with seawater temperature and salinity, in the ranges used to generate the linear approximation ($S_\mathrm{I}^\mathrm{lin}$). Contours are at arbitrary uniform intervals.

5.3. Results and discussion

5.3.1. Isocap slope

The isocap slope (S_I^{lin}) is dominantly controlled by pCO_2^{sw} and seawater temperature, while salinity has less influence (Figure 5.3). Increasing temperature and salinity both increase S_I^{lin}, but it has an inverse relationship with pCO_2^{sw} (Equation 5.35).

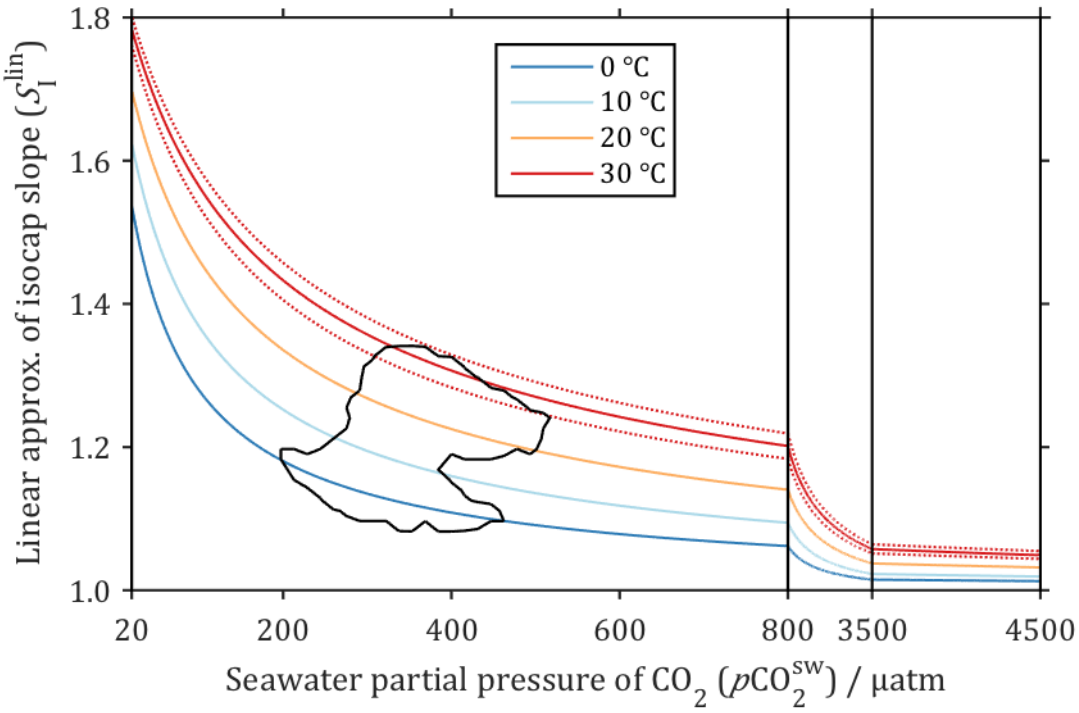

Figure 5.3. Variation of isocap slope with seawater partial pressure of CO_2 at different seawater temperatures and a salinity of 35 (solid lines), based on the linear approximation. Dotted red lines above and below the solid red 30 °C line are for salinities of 40 and 30 respectively, both at 30 °C. The black contour encompasses the distributions of pCO_2^{sw} and S_I^{lin} in the entire Takahashi et al. (2009) climatological data set (Figure 5.4).

The distribution of the isocap slope throughout the global surface ocean near the present day can be investigated using S_I^{lin} and the Takahashi et al. (2009) climatology. This global data set contains monthly mean pCO_2^{sw}, sea surface temperature (SST) and salinity gridded at 4°×5° spatial resolution, referenced to the year 2000, in non-El Niño conditions. Using Equation 5.35, S_I^{lin} was calculated for all of these data, as illustrated by Figure 5.4. As this data set is climatological, the magnitude of spatial

and seasonal variability in $S_{\mathrm{I}}^{\mathrm{lin}}$ in any individual year could exceed or fall short of that described in this section.

Annual mean $S_{\mathrm{I}}^{\mathrm{lin}}$ varies from minimum values near 1.09 at high latitudes to a maximum just over 1.32 in equatorial regions (Figure 5.4a), a range of about 0.23. Its spatial distribution is dominantly driven by SST, but the additional control of $p\mathrm{CO}_2^{\mathrm{sw}}$ is also visible in specific regions; for example, the relatively low $S_{\mathrm{I}}^{\mathrm{lin}}$ in the eastern equatorial Pacific is caused by high surface $p\mathrm{CO}_2^{\mathrm{sw}}$, driven by local upwelling of DIC-rich waters (Wang et al., 2006). Salinity has a much smaller effect on $S_{\mathrm{I}}^{\mathrm{lin}}$ than temperature or $p\mathrm{CO}_2^{\mathrm{sw}}$ (Figure 5.3). The distributions of $p\mathrm{CO}_2^{\mathrm{sw}}$ and $S_{\mathrm{I}}^{\mathrm{lin}}$ in the entire climatological data set used to generate Figure 5.4 are indicated in Figure 5.3. The total range of all monthly $S_{\mathrm{I}}^{\mathrm{lin}}$ is slightly larger, from near 1.09 to just over 1.33.

There is also significant localised seasonal variability in $S_{\mathrm{I}}^{\mathrm{lin}}$ (Figure 5.4b): its maximum annual range – defined as the difference between the maximum and minimum monthly values of $S_{\mathrm{I}}^{\mathrm{lin}}$ at each grid point in the climatological data set – is over 0.11, almost half of the global range in the annual mean. The spatial pattern in the $S_{\mathrm{I}}^{\mathrm{lin}}$ annual range emerges from the interactions of the SST and $p\mathrm{CO}_2^{\mathrm{sw}}$ seasonal cycles. Figure 5.5 shows the climatological monthly $S_{\mathrm{I}}^{\mathrm{lin}}$ at the 6 locations indicated in Figure 5.4b, along with the components of $S_{\mathrm{I}}^{\mathrm{lin}}$ driven by SST and by $p\mathrm{CO}_2^{\mathrm{sw}}$. The SST component was calculated at each grid point by evaluating $S_{\mathrm{I}}^{\mathrm{lin}}$ using the monthly values for the SST and salinity but with $p\mathrm{CO}_2^{\mathrm{sw}}$ held at its annual mean; for the $p\mathrm{CO}_2^{\mathrm{sw}}$ component, SST was instead held at its annual mean. Where seasonal SST and $p\mathrm{CO}_2^{\mathrm{sw}}$ are positively correlated, their effects on $S_{\mathrm{I}}^{\mathrm{lin}}$ cancel out to some extent and result in a small $S_{\mathrm{I}}^{\mathrm{lin}}$ annual range, while in places where they are negatively correlated, the annual range of $S_{\mathrm{I}}^{\mathrm{lin}}$ is greater. A striking feature of Figure 5.4b is the large zones with $S_{\mathrm{I}}^{\mathrm{lin}}$ annual range close to 0, in particular the oligotrophic subtropical gyres. In these regions, the seasonal cycle of $p\mathrm{CO}_2^{\mathrm{sw}}$ is dominantly driven by SST: warming decreases the solubility of CO_2 in the summer and winter cooling increases it again, but generally low wind speeds in these regions mean that the air-sea flux of CO_2 remains low regardless of the degree of SST-driven disequilibrium (Wanninkhof, 1992; Takahashi et al., 2009), so DIC and TA do not change significantly throughout the year. If DIC and TA are constant, and there is a change in temperature, then $p\mathrm{CO}_2^{\mathrm{sw}}$ changes significantly, but changes in the isocap slope S_{I} are relatively small. As a numerical example, consider a parcel of water with TA of 2330 μmol kg^{-1}, DIC of 2100 μmol kg^{-1}, temperature of 5 °C and salinity of 35. The $p\mathrm{CO}_2^{\mathrm{sw}}$ is therefore

254 µatm, and S_I is 1.19. If the temperature is increased to 25 °C and no other changes are made, the pCO_2^{sw} increases to 586 µatm, while S_I increases by 0.02 to 1.21. Returning to the original water parcel: if the temperature is held at 5 °C, the same increase in pCO_2^{sw} can be achieved by increasing DIC to 2233 µmol kg^{-1}. In this case, S_I decreases to 1.10, a much greater absolute change of 0.09. In conclusion, the isocap slope has a small annual range where pCO_2^{sw} seasonality is mainly controlled by SST; large annual ranges are found where the pCO_2^{sw} and SST seasonal cycles are decoupled. Regions with high seasonal biological uptake of CO_2 exhibit such decoupling, because primary production is more intense during the warmer, lighter summer months (Takahashi et al., 2009). These productive regions are obviously of key interest in terms evaluating the effect of coccolithophores on the global carbon cycle as CO_2 sources or sinks, and the very presence of this seasonal productivity drives large variations in isocap slope. This consideration emphasises the need to evaluate it on a case-by-case basis, and not to rely on a single, globally- or annually-averaged value.

Six locations have been selected as short case-studies to illustrate different seasonal patterns. The greatest S_I^{lin} annual range of just over 0.11 is found to the east of Japan, in the Kuroshio-Oyashio confluence region (Figure 5.5a). Here, S_I^{lin} increases from 1.11 to 1.22 from February to September because of the combined 13.2 °C increase in SST (from 1.3 to 14.5 °C) and 110 µatm decrease in pCO_2^{sw} (from 408 to 298 µatm). The latter is driven by spring phytoplankton blooms, primarily consisting of diatoms, which occur following seasonal increases in surface ocean irradiance and increased water column stratification in this region (Isada et al., 2009). Similar seasonal patterns, also mainly driven by seasonal biological activity, are observed in other regions like the Patagonian shelf (Figure 5.5b) and the subpolar North Atlantic. The former is particularly relevant because the austral spring phytoplankton blooms there often include significant abundances of coccolithophores, in particular *Emiliania huxleyi* (Painter et al., 2010; Poulton et al., 2013; Balch et al., 2014). In the subpolar North Atlantic, biological consumption of CO_2 has been estimated to reduce pCO_2^{sw} by 60 µatm during the spring and summer (Olsen et al., 2008). In some cases, the combination of SST and pCO_2^{sw} can result in a double-peak S_I^{lin} like in the subpolar North Atlantic south of Greenland where a S_I^{lin} maximum driven by pCO_2^{sw} in May is followed by a second maximum driven by both pCO_2^{sw} and SST in August (Figure 5.5c). High-magnitude S_I^{lin} seasonal cycles can also be driven by a seasonal change in

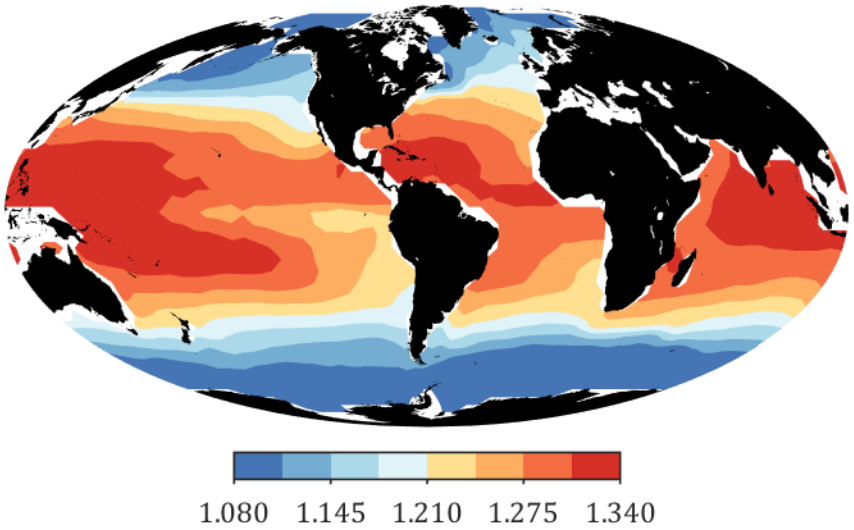

(a) Climatological annual mean isocap slope S_I^{lin}

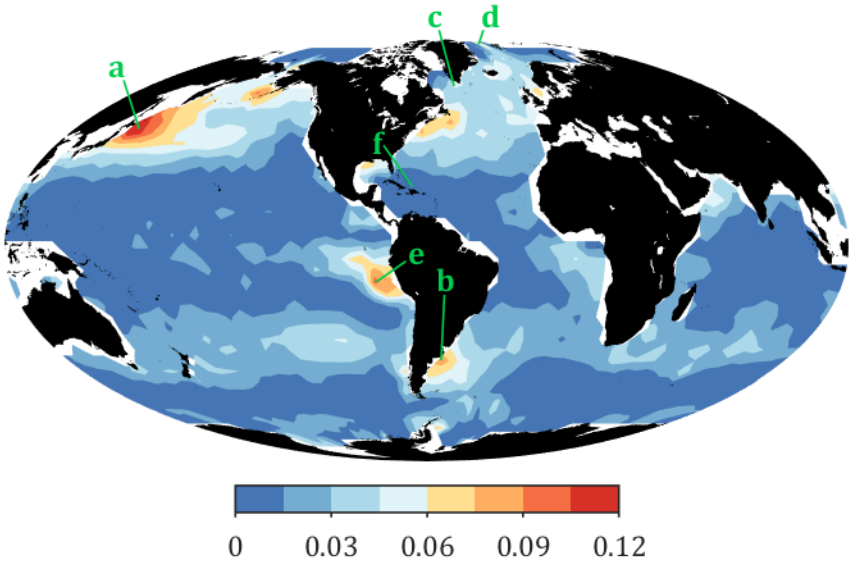

(b) Climatological annual range in isocap slope S_I^{lin}

Figure 5.4. Global distributions of isocap slope S_I^{lin} (a) annual mean and (b) annual range in the Takahashi et al. (2009) climatological data set. Green labels in (b) indicate geographical locations for Figure 5.5.

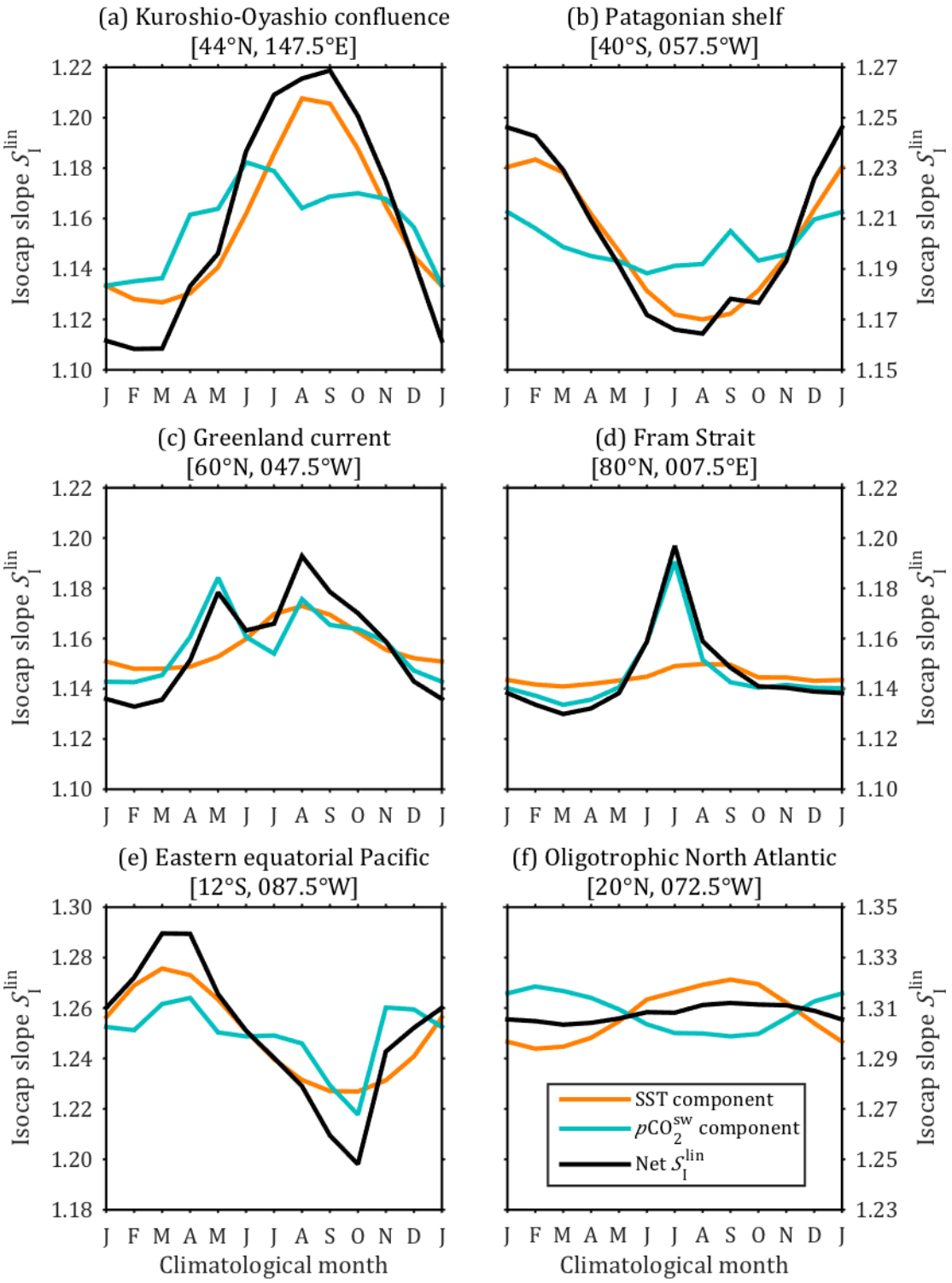

Figure 5.5. Climatological seasonal cycles in the isocap slope S_I^{lin} (black lines) and its components driven by sea surface temperature (SST) and seawater partial pressure of CO_2 (pCO_2^{sw}) (orange and blue lines respectively) at selected locations indicated in Figure 5.4. The vertical axis scale in each panel is *ad hoc*, but all panels cover the same magnitude range in S_I^{lin} (i.e. 0.12).

only one of SST or pCO_2^{sw} whilst the other remains relatively constant: in the Fram Strait (Figure 5.5d), S_I^{lin} increases strongly during the summer months, driven almost entirely by the sharp decline in pCO_2^{sw} from 315 to 190 µatm; the SST remains between 0.44 and 2.08 °C throughout the year. This pCO_2^{sw} reduction is probably due to seasonal primary productivity associated with summer sea ice melting (Bauerfeind et al., 2009). Decoupling of the SST and pCO_2^{sw} seasonal cycles is not always primarily biological. For example, in the eastern equatorial Pacific (Figure 5.5e), they are disconnected by upwelling of DIC-rich waters that occurs with particular strength during boreal autumn (Wang et al., 2006). Finally, where the pCO_2^{sw} seasonal cycle is driven by SST, for example in the oligotrophic subtropical North Atlantic (Figure 5.5f), the two components virtually cancel each other out despite individually being able to drive a non-negligible seasonal cycle of non-negligible amplitude in S_I^{lin}.

5.3.2. Production slope

The production slope (S_P) is controlled by the stoichiometry of nutrient uptake during POC production and the rate of PIC production relative to POC production (Equation 5.18); the latter is quantified by the production ratio (R_P, Equation 5.17). Table 5.2 presents a compilation of published POM stoichiometries and production ratios, as well as calculated production slopes, for the coccolithophore species *Emiliania huxleyi*, *Gephyrocapsa oceanica*, *Coccolithus pelagicus* and *Calcidiscus leptoporus*. The coefficients α, β, η and θ (for cellular particulate organic nitrogen, carbon, sulfur and phosphorus) have been normalised so that β is 106 (Appendix 3), the classic 'Redfield ratio' C to P value (Redfield et al., 1963). Several different measurements of the coefficients α, β and θ have been published for each of these coccolithophore species, which have been compiled for Table 5.2 as follows.

Langer et al. (2013) carried out culture experiments with *E. huxleyi* under different nutrient-limited conditions and reported cellular particulate organic nitrogen, carbon and phosphorus concentrations (PON, POC and POP respectively, Table A3.1). Ho et al. (2003) reported the cellular content of a wide range of elements in several phytoplankton species including *E. huxleyi* and *G. oceanica* (Table A3.2). The coefficients α and θ in Table 5.2 are the mean of results from the 'control' experiments by Langer et al. (2013) for *E. huxleyi* and the Ho et al. (2003) value. For *G. oceanica* the coefficient θ is taken directly from Ho et al. (2003), while its α is the mean of the Ho et al. (2003) value (Table A3.2) and 16.8 ± 0.6, which was reported by

Moolna and Rickaby (2012) from a culture study of this species at 'present-day' conditions. Gerecht et al. (2014a) reported cellular particulate organic nitrogen, carbon and phosphorus (PON, POC and POP) for two *C. pelagicus* subspecies at various temperatures and levels of phosphate limitation in their Table 2; as α and θ were similar across all of their experiments, the means of all of them appear in Table 5.2 to represent *C. pelagicus*. Langer et al. (2012) reported cellular PON, POC and POP for *C. leptoporus* under nitrate- and phosphate-limited and control conditions (Table A3.3). Their control and nitrate-limited ('N-limited') values for α and θ have been separately included in Table 5.2.

Cellular particulate organic sulfur (POS) is rarely measured in coccolithophore experiments. Ho et al. (2003) reported cellular POS for *E. huxleyi* and *G. oceanica* (Table A3.4), but comparable measurements were not obtained for *C. pelagicus* or *C. leptoporus*. Fortunately, it is possible to estimate cellular POS in these species from measurements of the metabolite dimethylsulfoniopropionate (DMSP), a compound produced by most coccolithophore species (Franklin et al., 2010). Matrai and Keller (1994) measured separately cellular POS and DMSP in *E. huxleyi* and several other non-coccolithophorid phytoplankton species, reporting cellular carbon to sulfur ratio of (80 ± 26):1 for *E. huxleyi*, which corresponds to η of 1.33 ± 0.43 (normalised to β = 106). In *E. huxleyi* and other non-coccolithophorid species which produce significant amounts of DSMP, the DMSP was reported to account for between 50 and 100 % of total POS (Matrai and Keller, 1994). Assuming that this holds true for the other coccolithophore species, measurements of cellular DMSP could therefore be used to estimate POS and therefore η. Franklin et al. (2010) measured cellular DMSP in all of the species in Table 5.2. Cellular POC was not measured, but can be estimated from reported cell volumes using the Menden-Deuer and Lessard (2000) cell volume-POC relationship for protist phytoplankton excluding diatoms:

Equation 5.38 $$\mathrm{POC_{cell}} = 0.216\, V^{0.939}$$

where $\mathrm{POC_{cell}}$ is the cellular POC in pg cell^{-1} and V is the cell volume in μm^3. The coefficient η was estimated for all of the species in Table 5.2 using this method, and the cellular DMSP reported by Franklin et al. (2010) from their cultures grown in K/5 media (Table A3.4). The values of η which appear in Table 5.2 are the mean of those reported by Matrai and Keller (1994), Ho et al. (2003) and Franklin et al. (2010) for *E. huxleyi*, the mean of Ho et al. (2003) and Franklin et al. (2010) for *G. oceanica*, and the estimates from only Franklin et al. (2010) for *C. pelagicus* and *C. leptoporus*.

Species	α **(N)**	β **(C)**	η **(S)**	θ **(P)**	R_P	S_P
Emiliania huxleyi	15.3[a,b]	106	1.58[b,f,g]	0.78[a,b]	0.9-1.1[a,h]	0.85-0.96
Gephyrocapsa oceanica	14.5[b,c]	106	1.18[b,g]	1.66[b]	1.5-2.9[h]	1.13-1.44
Coccolithus pelagicus	11.8[d]	106	4.24[g]	0.87[d]	1.2-1.7[d,i]	1.00-1.19
Calcidiscus leptoporus	31.1[e]	106	7.07[g]	0.53[e]	2.1-2.5[e,i]	1.22-1.31
C. leptoporus, N-limited	10.3[e]	106	7.07[g]	0.50[e]	2.1-2.5[e,i]	1.28-1.36

Table 5.2. A compilation of published values for the stoichiometric coefficients of particulate organic matter, $C_\beta H_\zeta O_\varphi N_\alpha S_\eta P_{\theta(s)}$ and the production ratio (R_P), and production slope (S_P) calculated using Equation 5.18, for 4 coccolithophore species. Only the stoichiometric coefficients relevant to this study (i.e. α, β, η and θ) are included, and they have all been normalised to β = 106. Notes: [a]Langer et al. (2013), Table A3.1; [b]Ho et al. (2003), Table A3.2; [c]Moolna and Rickaby (2012); [d]Gerecht et al. (2014a); [e]Langer et al. (2012), Table A3.3; [f]Matrai and Keller (1994); [g]Franklin et al. (2010), Table A3.4; [h]Sett et al. (2014), Table A3.5; [i]Langer et al. (2006).

Variations in R_P have a greater effect on the production slope S_P than proportionally equivalent variations in any of the stoichiometric coefficients (Figure 5.6), so ranges of R_P values have been reported in Table 5.2 and used to calculate the production slope S_P for each species, instead of averages. Sett et al. (2014) determined R_P for *E. huxleyi* and *G. oceanica* at a range of different temperature and pCO_2^{sw} conditions. The R_P values they reported at pCO_2^{sw} values closest to the present-day global average were selected (Table A3.5) and used to represent the ranges of R_P for these two species in Table 5.2. The R_P values determined for *E. huxleyi* by Langer et al. (2013) (Table A3.1) are consistent with the range given by Sett et al. (2014). Langer et al. (2006) reported R_P at a range of pCO_2^{sw} values for *C. pelagicus* and *C. leptoporus*. For *C. pelagicus*, the range of R_P in Table 5.2 is from all of the Langer et al. (2006) experiments (they found no significant control of R_P by pCO_2^{sw} for this species) combined with the results of Gerecht et al. (2014a), but excluding the latter's high-temperature subspecies *pelagicus* experiment during which anomalously low R_P was observed. For *C. leptoporus*, Table 5.2 reports the range of R_P at pCO_2^{sw} of 345 and 477 µatm for this species in Table 1 of Langer et al. (2006) and in the Control and NO_3-limited rows in Table 3 of Langer et al. (2012) (Table A3.3). Langer et al. (2012) did not find that the nutrient limitation made a significant difference to R_P.

5.3.3. Slope difference

5.3.3.1. Present day

The isocap slopes and production slopes can now be brought together to evaluate the effect of different coccolithophore species on pCO_2^{sw}, and so classify them as CO_2 sources or sinks. Figure 5.6 shows how the production slope (S_P) varies as a function of the POM stoichiometry and production ratio (R_P), and indicates the positions of the species in Table 5.2. The S_P contours at values of 1.09 and 1.33 indicate the global range of the climatological monthly isocap slope (S_I^{lin}) at the present day (Figure 5.4a) and can be used to make some first-order assessments. Coccolithophores behave as net CO_2 sinks when the slope difference ΔS is negative (i.e. $S_P < S_I$, Equation 5.37). The entire range of the production slope S_P for *E. huxleyi* (0.85-0.96) falls below the minimum value of S_I^{lin} observed in the climatological data set, 1.09 (Figure 5.4a). This means that *E. huxleyi* should always have a negative ΔS: it cannot increase pCO_2^{sw}, and cannot act as a CO_2 source. Indeed, S_I^{lin} does not fall below 1 even at very high pCO_2^{sw} and seawater temperature (Figure 5.3). A model simulation based on field and mesocosm studies of an *E. huxleyi* bloom supports the conclusion that they should act as CO_2 sinks (Buitenhuis et al., 2001). The experimentally-derived S_P for *C. pelagicus*, *G. oceanica* and *C. leptoporus* all lie partially within the climatological range of S_I^{lin} (from 1.09 to 1.33), so these species are capable of acting as CO_2 sources or sinks depending upon their precise R_P and upon their geographical location (and therefore local S_I). These species could also switch seasonally between being CO_2 sources and sinks entirely as a result of seasonal variations in S_I (Figure 5.5), even if their POM stoichiometry and R_P remain constant. The most heavily-calcified *G. oceanica*, with R_P in the upper half of its range, will always have positive ΔS and so act as a CO_2 source.

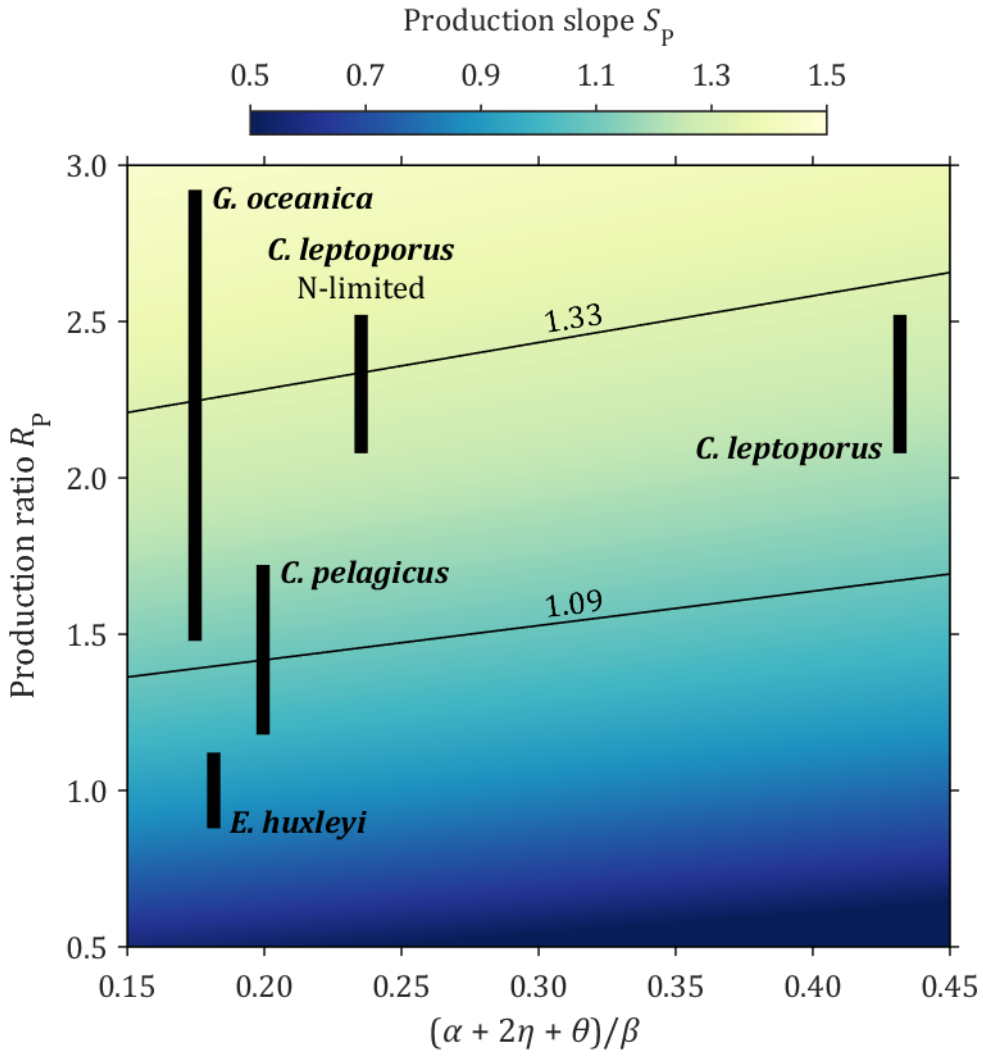

Figure 5.6. Control of production slope (S_P) by production ratio (R_P) and particulate organic matter stoichiometry. Vertical bars show the ranges of S_P calculated for the coccolithophore species in Table 5.2. Contours at S_P values of 1.09 and 1.33 indicate the total range of the climatological monthly isocap slope S_I^{lin} at near the present day (Figure 5.4).

However, there are reports of local increases in pCO_2^{sw} that have been attributed to calcification by *E. huxleyi* (Holligan et al., 1993; Robertson et al., 1994). How is this possible? If *E. huxleyi* produces POC and PIC in the ratios given in Table 5.2 it cannot increase pCO_2^{sw}, so the elevated pCO_2^{sw} must be driven by other species: either the community has negative net autotrophic production (Crawford and Purdie, 1997), or coccolithophore species with greater S_P or heterotrophic calcifiers must be present. Coccolithophores with larger cells but that are much less abundant in a community than *E. huxleyi* can still dominate seawater PIC production (Daniels et al., 2014). Alternatively, *E. huxleyi* could be producing greater quantities of PIC relative to POC and so have a much greater R_P and therefore S_P than that in Table 5.2. This species does periodically shed coccoliths (Balch et al., 1993); if these are not included in

measurements of R_P, and they do not dissolve *in situ* (i.e. they either remain *in situ* in particulate form, or sink out of the surface mixed layer) then they could be responsible for an underestimate of R_P, and therefore S_P. It is clear from Figure 5.6 that deviations in POM stoichiometry from the values in Table 5.2 are not likely to be responsible; indeed, even in the hypothetical extreme case where the cellular PON, POP and POS content were all 0 and R_P took the maximum value in the *E. huxleyi* range of 1.1, then S_P would still not exceed 1.05, which is not high enough to be a CO_2 source for any of the climatological data (Figure 5.4). It is possible that the coefficient η (for POS) could be effectively underestimated because of the simplified model of coccolithophore biology used here. Coccolithophores produce dimethyl sulfide (DMS) as a waste product (Franklin et al., 2010), which is not included in η. Therefore, DMS production could result in an underestimate of η in the same manner as how coccolith shedding could lead to an underestimate of R_P. However, increasing η decreases S_P (Equation 5.18), so this could not lead to *E. huxleyi* being a source of CO_2. Finally, if the source of N was ammonium instead of nitrate, this would alter TA in the opposite sense (Wolf-Gladrow et al., 2007), and coccolithophores can utilise ammonium as an N source (Strom and Bright, 2009). This would be reflected by using a negative value for α in Equation 5.18, and would result in a coccolithophore being a stronger CO_2 source if all other factors remained the same. For *E. huxleyi*, using the coefficients in Table 5.2 but with α changed to -15.3, the range of S_P values changes to from 1.00 to 1.10 – still almost entirely below the climatological range of S_I^{lin}, but perhaps able to generate a small CO_2 source under the lowest S_I^{lin} conditions (i.e. low temperature, high pCO_2^{sw}).

The timescale on which the effect of coccolithophores on pCO_2^{sw} is being considered has very important implications for selecting suitable values for R_P and the stoichiometric coefficients for POM. The instantaneous effect of a living coccolithophore on pCO_2^{sw} should be evaluated using the instantaneous rates of PIC and POC production and nutrient uptake. However, if R_P and the POM stoichiometry are determined from measurements of the total size of the PIC and POC pools in a coccolithophore, then the pCO_2^{sw} being evaluated is an integrated measure of the coccolithophore's effect on pCO_2^{sw} throughout its lifetime. This is the timescale implicit in the values reported in Table 5.2. In the simplified coccolithophore model used in this chapter (Section 5.2.1) there is no difference between these cases as the rate of PIC production relative to that of POC is assumed to always be the same as the total size of the PIC pool relative to the POC pool. Similarly, the relative rates at which

the nutrients which affect TA are taken up is assumed to be the same as their ratios in the POM pool. In reality these assumptions may not be true, so care must be taken to choose appropriate values for α, β, η, θ and R_P. Similarly, on timescales longer than the lifetime of a single cell, the fate of dead coccolithophores becomes important. If completely remineralised in the surface layer, they will have had no net effect on $p\mathrm{CO}_2^{\mathrm{sw}}$ despite having altered it while alive. If instead they sink out of the surface layer – perhaps a more realistic scenario (Honjo et al., 2008; Sanders et al., 2010) – then their influence on $p\mathrm{CO}_2^{\mathrm{sw}}$ is more long-lasting. If both the PIC and POC pools that make up the coccolithophore are exported from the surface layer in their entirety, then the values for the coefficients in Table 5.2 are appropriate. If any part of the coccolithophore is not exported, however, and instead remineralises in the surface layer, the coefficients would need to be adjusted to reflect this. For example, if the PIC pool was entirely exported but the POC pool was remineralised *in situ*, then over the coccolithophore's entire life cycle $d\mathrm{POC}/dt$ is 0 and so R_P is infinite. From Equation 5.18, $S_P \to 2$ as $R_P \to \infty$, so the appropriate S_P to use is 2. In the opposite hypothetical extreme where PIC was entirely remineralised *in situ* and POC exported, R_P would be 0, so S_P would take a value of $-(\alpha + 2\eta + \theta)/\beta$ (Equation 5.18). Essentially, the method presented here is independent of timescale, as long as care is taken to choose appropriate coefficients for each application.

Although in general R_P is more important than the POM stoichiometry in determining S_P, the data for *C. leptoporus* highlight the importance of taking both factors into account. The change in POM stoichiometry between a N-limited and N-replete culture experiment (Langer et al., 2012) is indicated in Figure 5.6. Significant changes in stoichiometry associated with nutrient limitation are a phenomenon common to many groups of marine phytoplankton (Geider and La Roche, 2002). The change, which is mostly driven by a reduction of cellular PON, is sufficient to change the range of S_P for *C. leptoporus* from falling entirely within with the climatological surface seawater range of S_I^{lin} to a range which partially exceeds it, despite there having been no change in R_P. The most heavily-calcified *C. leptoporus* can therefore be changed by nutrient limitation from being a CO_2 source or sink dependent upon local seawater conditions, to being virtually always a CO_2 source.

5.3.3.2. Palaeoclimatic implications

The linear approximation of the isocap slope (S_I^{lin}) can be applied to specific events in the palaeorecord by assuming that global mean surface ocean $p\mathrm{CO}_2^{\mathrm{sw}}$ remains

approximately in equilibrium with atmospheric pCO_2 on geological timescales. During the Last Glacial Maximum (LGM, 19-23 thousand years before present), the atmospheric partial pressure of CO_2 fell to 180 µatm (Monnin et al., 2001), and the annual mean sea surface temperature (SST) was up to 10 °C lower than at the present day (MARGO Project Members, 2009). In the climatological data set, the mean pCO_2^{sw}, SST and salinity are 355 µatm, 16 °C and 35 respectively, corresponding to an S_I^{lin} of 1.21. At 180 µatm, 6 °C and assuming the same salinity, S_I^{lin} increases slightly to 1.23. As its rate of change with respect to both SST and pCO_2^{sw} increases with decreasing pCO_2^{sw} (Figure 5.3), S_I^{lin} should also have exhibited greater spatial and seasonal variability. Therefore, a given coccolithophore would have been a weaker CO_2 source (or stronger CO_2 sink) during the LGM than at the present day on average, but both the magnitude and polarity of its effect on pCO_2^{sw} would be more changeable.

Conversely, during the Palaeocene-Eocene Thermal Maximum (PETM) – a hyperthermal event roughly 56 million years before present – the atmospheric CO_2 concentration (and therefore pCO_2^{sw}) was an order of magnitude higher than at the present day, possibly reaching over 4000 µatm (Zachos et al., 2008). Global mean SST was also 4-5 °C warmer than at present (Dunkley Jones et al., 2013). Under these conditions, S_I^{lin} would be effectively homogeneous at a value close to 1.03 throughout the surface ocean, much lower than at the present day, because its sensitivity to both SST and pCO_2^{sw} is greatly diminshed at high pCO_2^{sw} (Figure 5.3). Coccolithophores have been the major pelagic calcifiers throughout the Cenozoic, with modern species such as *C. pelagicus* also present during the PETM (Gibbs et al., 2006, 2013), and these species would be stronger CO_2 sources during the PETM than in the modern ocean. As a cautionary note, the exact value for S_I^{lin} during the PETM could be not so well constrained, because its calculation is based on formulae for equilibrium constants and ionic concentrations which have been empirically determined from samples of modern seawater; if there have been significant variations in the major ion composition of seawater then these expressions may not be accurate (Millero and Pierrot, 1998). Nevertheless, the conclusion that S_I^{lin} would exhibit much less heterogeneity both spatially and temporally under these much higher SST and pCO_2^{sw} conditions is robust.

5.3.3.3. Future impacts

Presently, global mean surface ocean SST and pCO_2^{sw} are increasing (Wu et al., 2011; Tjiputra et al., 2014). Although these changes have effects of opposite polarity on S_I^{lin}, the pCO_2^{sw} change dominates and so global mean S_I^{lin} is decreasing (Figure 5.3). As we continue to move towards a future, higher-CO_2 ocean, the global mean value of S_I^{lin} and its spatial and seasonal variability will decrease further, and if there are no biological changes affecting cellular stoichiometry (Table 5.2), coccolithophores would become stronger sources of CO_2 – a positive feedback that has been previously identified for calcification in general (Frankignoulle et al., 1994). Because of the opposing effects of SST and pCO_2^{sw} on S_I^{lin}, the smaller the climate sensitivity (i.e. the increase in global mean surface temperature induced by a doubling of atmospheric pCO_2), the greater this positive feedback will be. It could be offset by a decrease in the production ratio R_P (and therefore also in the production slope S_P), which some studies have suggested may happen as a result of decreased PIC production at higher pCO_2^{sw} levels (Riebesell et al., 2000; Zondervan et al., 2001, 2002; Beaufort et al., 2011; Findlay et al., 2011). However, other studies have suggested that coccolithophores could adapt to increasing SST and pCO_2^{sw}, minimising changes in their R_P (Iglesias-Rodriguez et al., 2008; Lohbeck et al., 2012; Jin et al., 2013; Schlüter et al., 2014). Coccolithophore responses to climatic change are likely to be species-specific. Increasing pCO_2^{sw} could be beneficial for autotrophic production as CO_2 is a resource in this context, but detrimental to calcification because of the associated decline in pH and consequent increased energetic cost of internal pH regulation (Gaylord et al., 2015). This contradiction might partly explain why it remains unresolved how coccolithophores – which undertake both processes – will respond to increasing pCO_2^{sw} in the future.

5.3.4. Comparisons with previous work

5.3.4.1. Erroneous calculations

Studies have sought to define particular coccolithophore species as CO_2 sources or sinks, with varying levels of success. Most discussions of this have suggested that there is a threshold value of the production ratio (R_P) – the rate of PIC production relative to that of POC (Equation 5.17) – at which pCO_2^{sw} is unaffected. It is possible to define the threshold in this way, but only for a specific POM stoichiometry. In

addition, it has been incorrectly suggested that the threshold is met when R_P is 1 (Poulton et al., 2007; Gerecht et al., 2014b). How does this misconception arise? The reaction for autotrophic production (Equation 5.8) states that production of 1 unit of POC takes up 1 unit of CO_2 from the seawater. The following reaction for calcification:

Equation 5.39 $$Ca^{2+} + 2HCO_3^- \longrightarrow CaCO_{3(s)} + CO_2 + H_2O$$

suggests that production of 1 unit of PIC returns 1 unit of CO_2 to the seawater. This leads to the mistaken conclusion that when R_P is 1, the CO_2 uptake during POC production is equal to that given out by PIC production, so there is no net change in pCO_2^{sw}. However, the dynamic equilibria between the carbonate species have been neglected (Equations 5.20 and 5.21). In reality, if CO_2 is taken up from the seawater, the positions of these equilibria will shift to partially compensate, so on timescales longer than a few seconds (i.e. enough for thermodynamic equilibrium to be established) the net change in $[CO_2]$ will be less than the amount of CO_2 removed. The changes in TA accompanying the production of PIC and POC will further alter the pCO_2^{sw}. Consequently, in terms of their effect on the seawater chemistry, the reactions for calcification given by Equations 5.7 and 5.39 – and all other variations using different combinations of the carbonate species as reactants and products – are indistinguishable, and a threshold pCO_2^{sw}-neutral value of R_P cannot be quantified intuitively in this way.

5.3.4.2. Globally homogeneous values

Other studies have evaluated a threshold for R_P more correctly, but have either assumed a single value is applicable or have not carried out a systematic analysis of spatial and temporal variability in the threshold (Buitenhuis et al., 2001; Iglesias-Rodriguez et al., 2008). Furthermore, they have not addressed the requirement to calculate the threshold differently depending on the stoichiometry of nutrient uptake, which is circumvented by using the production and isocap slopes as described in this chapter.

5.3.4.3. The buffer factor ψ

The dimensionless buffer factor ψ is the 'released CO_2 to precipitated carbonate ratio' (Frankignoulle et al., 1994). As it does not account for the effects of organic matter production, ψ in itself is not enough to determine whether a coccolithophore will be a source or sink of CO_2, but it does provide an alternative route to calculate the isocap slope (S_I). Although mainly associated with studies on coral reef calcification, where

the rate of POC production is much lower than PIC production, it has been used in several studies to quantify changes in carbonate chemistry caused by coccolithophores (Riebesell et al., 2000; Zondervan et al., 2001; Shutler et al., 2013; Gerecht et al., 2014a), and its global distribution has been investigated (Smith, 2013). However, ψ does not account for the changes in seawater TA during organic matter production. Numerically, ψ is equal to the additional reduction in DIC that would be required such that production of one unit of PIC causes no net change in $p\mathrm{CO}_2^{\mathrm{sw}}$. To illustrate the relationship between ψ and S_I, the 'isocap ratio' (R_I) is defined as the value of the production ratio R_P when its corresponding S_P for a particular POC stoichiometry (Equation 5.16) is equal to S_I, so calcification and autotrophic production are balanced such that there is no net change in $p\mathrm{CO}_2^{\mathrm{sw}}$. It then follows from Equations 5.18 and 5.40 that $\psi \to 1/R_\mathrm{I}$ as $d\mathrm{TA}_\mathrm{POC} \to 0$; ψ is numerically equal to $1/R_\mathrm{I}$ in the hypothetical case where POC production does not affect TA. The relationship between the isocap slope S_I and its value of ψ can therefore be derived geometrically:

Equation 5.40

$$S_\mathrm{I} = \frac{2}{1+\psi}$$

To demonstrate the validity of this interpretation of ψ, Figure 2 from Frankignoulle et al. (1994) has been reproduced using Equations 5.34 and 5.40 (Appendix A3, Figure A3.1).

5.3.5. Errors and limitations

5.3.5.1. Interpreting ΔS

The sign of the difference ΔS between the production slope S_P and the isocap slope S_I (Equation 5.37) determines whether a coccolithophore acts as a CO_2 source (positive ΔS) or sink (negative ΔS). When ΔS is 0, then PIC and POC production are balanced and cause no net change in $p\mathrm{CO}_2^{\mathrm{sw}}$ (medium blue vectors, Figure 5.1). This can be assessed using either the exact value of S_I (Equation 5.34) or its linear approximation $S_\mathrm{I}^{\mathrm{lin}}$ (Equation 5.35). However, DIC and TA must both be known in order to determine the rate of $p\mathrm{CO}_2^{\mathrm{sw}}$change with respect to production, which is calculated using the Revelle factor (Zeebe and Wolf-Gladrow, 2001, pp. 76–80). This also restricts comparisons between ΔS values calculated in different settings. Only when the

species being compared are taking up DIC from the seawater at the same rate and are in the same seawater conditions (i.e. the same DIC, TA, temperature and salinity) does a greater positive ΔS value guarantee a stronger CO_2 source than a smaller positive value.

The difference between S_I and S_P can be used to quantify the rate of change of DIC away from its 'equilibrium' value, relative to the PIC production rate:

Equation 5.41

$$\frac{d\mathrm{DIC}}{d\mathrm{PIC}} = \frac{2(S_P - S_I)}{S_P S_I}$$

Either SI or S_I^{lin} can be used to evaluate Equation 5.41, but to convert the DIC change into a pCO_2^{sw} change requires a fully-resolved carbonate chemistry system.

5.3.5.2. The linear approximation

The uncertainty in S_I^{lin} relative to S_I depends on the specific range of TA used to derive the functions for the coefficients a, b, c and d (Equation 5.35). The difference between S_I^{lin} and S_I (i.e. the approximation error) is greatest at the extremes of the TA range used to generate the expressions for a, b, c and d, and 0 near their centres. For this reason, the range was chosen such that present-day global mean surface ocean conditions fall close to its centre: the middle of the TA range is approximately the global mean of surface ocean TA (shallower than 10 m) in the GLODAP data set (Key et al., 2004). Figure 5.7 illustrates the approximation error as a function of DIC and TA for the ranges of TA and pCO_2^{sw} used to generate the linear approximation; the maximum absolute error is less than 0.025, which is over an order of magnitude smaller than the uncertainties in S_P in Table 5.2 and therefore not a hindrance. The error is close to 0 at the middle of the TA range, which is close to typical seawater conditions at the present day. The error also becomes closer to 0 as pCO_2^{sw} increases, because the degree of non-linearity of the isocaps decreases with increasing pCO_2^{sw}. Figure 5.7 only shows this error at a temperature of 15 °C and salinity of 35, but the pattern and magnitude of the error is similar for all other combinations of these values in the ranges used to generate the approximation.

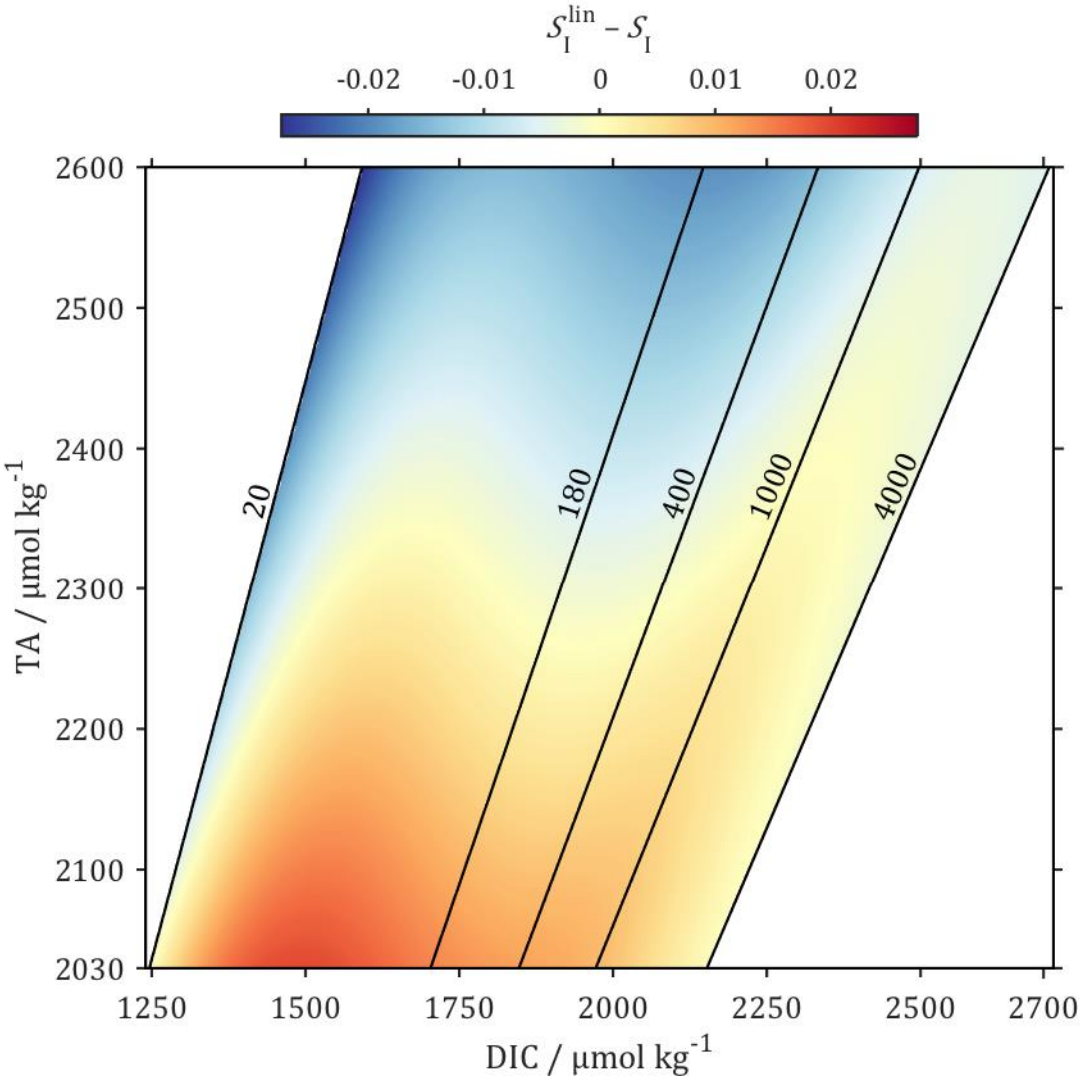

Figure 5.7. Difference between isocap slope calculated exactly (S_I, Equation 5.34) and using the linear approximation (S_I^{lin}, Equation 5.35), at a temperature of 15 °C and salinity of 35. Only the region included in the derivation of the linear approximation is coloured (i.e. 20 ≤ pCO_2^{sw} ≤ 4000 µatm). Black labelled contours show selected pCO_2^{sw} values in µatm.

5.3.5.3. Choice of constants

Several different empirical formulae exist for the equilibrium constants and ionic concentrations used to evaluate the isocap slope S_I. The differences between S_I evaluated using different expressions for these constants are negligible compared with the uncertainties in the production slope S_P for any species. Exact S_I was calculated using Equation 5.34 and every combination of relevant user-chosen constants for seawater in version 1.1 of the CO_2SYS software for MATLAB (MathWorks), at a salinity of 35, temperature of 25 °C, DIC of 2100 µmol kg^{-1} and TA of 2330 µmol kg^{-1}. There are 13 options for the carbonic acid dissociation constants k_1 and k_2, and 2 options for total boron TB, so 26 combinations in total. The mean ±

standard deviation (SD) of all these combinations for S_I was 1.197 ± 0.001, with minimum and maximum values of 1.195 and 1.120. The pCO_2^{sw} values calculated at these input conditions with the different combinations of constants were all in the range from 384 to 418 µatm, with a mean ± standard deviation of 397 ± 11 µatm. Using these pCO_2^{sw} values as inputs into the linear approximation Equation 5.35 gives a mean ± SD for S_I^{lin} of 1.191 ± 0.004, and minimum and maximum values of 1.185 to 1.196. For both S_I and S_I^{lin}, the results using the combination of constants used to generate the linear approximation (Lueker et al. (2000) for k_1 and k_2, and Lee et al. (2010) for TB) fall close to the mean of all combinations. The uncertainties in both S_I and S_I^{lin} resulting from the choice of these constants are therefore negligible because they are about 2 orders of magnitude smaller than the ranges of S_P identified for the coccolithophore species in Table 5.2.

5.4. Conclusions

Coccolithophores can be either sources or sinks of CO_2. If the production slope (S_P) for a coccolithophore species is greater than the isocap slope (S_I) for its ambient seawater environment, then it will act as a CO_2 source, or as a sink if S_P is less than S_I. The S_P depends upon the coccolithophore's ratio of PIC to POC production (R_P), and on the stoichiometry of its nutrient uptake during POC production; R_P does not in itself contain enough information to classify a coccolithophore as a CO_2 source or sink. Further investigation of the controls on the stoichiometry of nutrient uptake and production ratios of coccolithophores on different timescales is required in order to better quantify S_P and therefore carry out accurate calculations of their influence on the global carbon cycle. The S_I is dominantly controlled by the seawater temperature and pCO_2^{sw}, and it varies significantly both spatially and seasonally on a global scale. This variability is of sufficient magnitude that individual species can switch between being CO_2 sources and sinks based upon their geographical location and also seasonally, without any changes to their S_P. Because S_I has an inverse relationship with pCO_2^{sw}, coccolithophores act as a positive feedback on pCO_2^{sw} from a chemical perspective, although this could be offset if changes in pCO_2^{sw} also significantly affect their S_P, which has not been conclusively established.

6

Conclusions and outlook

Abstract

This final chapter draws together the concepts and ideas presented in all preceding chapters, and suggests other research areas where they might also be applied. The main themes discussed are on the importance of continued observations of marine carbonate chemistry in the global ocean, and how this can be achieved; on the minutiae of carrying out and reporting these measurements, in particular their precision and accuracy; and on geo-engineering possibilities for mitigating the climatic effects of anthropogenic CO_2 by increasing the capacity of the ocean to store it. Finally, future improvements that could be made to the studies forming the chapters of this thesis are suggested, along with more general ideas about present and future challenges facing the science of marine carbonate chemistry.

6.1 Continued observations

The abundance of observational marine carbonate chemistry data has increased to the point that it is now relatively difficult to create an interesting, publishable narrative or find novel insights from the results of any individual research cruise; more attention is turned towards examinations of compiled data sets (e.g. Key et al., 2010, 2004; Pfeil et al., 2013; Schmittner et al., 2013; Bakker et al., 2014; Takahashi et al., 2014b). Despite this, it remains critically important that observations are sustained; obviously, without the individual cruises taking place these combined data sets will not continue to grow, and there are still significant gaps in their spatial and temporal distributions. However, without exciting new science coming from the carbonate chemistry measurements on every cruise, funding for such observational work may become more difficult to obtain. Autonomous sensing and further integration of models and observations are two approaches which may help to ameliorate this problem. The former can take the form of adding biogeochemical sensors to autonomous sensing arrays (e.g. Martz et al., 2010), or can be based on building algorithms to predict surface ocean carbonate chemistry from satellite remote sensing data products (Sun et al., 2012). The model-based approach used to evaluate how representative the Extended Ellett Line is of the surrounding regions in Chapter 4 could be extended and applied to a global model in order to identify locations which would provide the most information, or where most uncertainties are, and so primarily target research cruises there. For example, Holden et al. (2013) were able to identify specific parts of the ocean interior where further observations of $\delta^{13}C_{DIC}$ would be critically useful, and gave suggestions for spatial targeting of future observational work. There is much scope for improvement of existing models, in particular regarding their representation of calcification; observations should be targeted to address such issues, and thus improve model parameterisations of these processes. With careful validation, model output could then also be used to determine how best to fill in gaps in observational data, and to evaluate time-of-emergence for trends in different variables. At present, the latter has been applied more to surface ocean biogeochemical variables (e.g. Henson et al., 2010) than it has in the ocean interior.

6.2 Carbonate system measurements and calculations

Although carbonate chemistry measurements are increasingly seen as routine, achieving high-quality results remains resolutely non-trivial. One aspect of this, the calculation of TA from titration data, has been discussed in detail in Chapter 2. Software such as CO_2SYS (van Heuven et al., 2011), while providing extremely useful investigative tools, hide a significant body of assumptions about the seawater chemistry which the casual user may not be aware of, giving a false sense of certainty in calculated results.

Calculation and reporting of precision is a problem for marine carbonate chemistry measurements at the present day. There are wide discrepancies in how precision is defined and calculated, and the exact calculation used is frequently explained in very vague terms, if at all. This can make it difficult or impossible to compare results between studies, as discussed in Chapter 3. In addition, precision is also routinely quoted to one-sigma precision, which is 68.3 % certainty. This means that the 'true' value of approximately 1 in every 3 measurements falls outside the quoted uncertainty range, which is perhaps inappropriate. However, for any scientist to make a unilateral switch to quoting two- or three-sigma uncertainties for measurements, corresponding to 95.4 % and 99.7 % confidence, would give the superficial appearance that their data is of poor quality, potentially hindering its publication and application.

For DIC and TA measurements, precision is often estimated as the standard deviation (SD) of (typically) 5 substandards run at the start of each analysis session. This is not ideal. Firstly, if these substandards are taken from a single large seawater sample having not been subsampled into analysis bottles, or they have otherwise undergone different processing from the samples, then the precision calculated from them does not include any uncertainty engendered by the sampling procedure. Secondly, these substandards are used to assess the running of the instrument at the start of each day. Consequently, any values considered 'wrong' by the operator are put aside, and successive substandards are measured until an 'acceptable' precision is achieved. This could lead to a false underestimate of precision. If there is any change in precision throughout the analysis session, this will also not be monitored. If these substandard measurements must be used, then the mean should be taken over many analysis sessions. It is inaccurate to assert that the SD of 5 substandards (the typical number) during each analysis session is the precision for that session, and that this

varies from day to day. One possible solution is to make greater use of replicate analyses, as in Chapter 3. It is already recommended that at least 10 % of samples – spread evenly throughout the sampling period – are collected in duplicate (Dickson et al., 2007), but the more that can be taken, the more reliably precision can be determined. Precision evaluated from these samples then includes errors introduced at all stages of the sampling and measurement processes.

Accuracy is an entirely separate issue. There is only one internationally-recognised CRM for DIC and TA measurements with which accuracy can be assessed, produced by A.G. Dickson (Scripps Institution of Oceanography, USA). Although it is of high quality, it is commonly used to calibrate measurements, in which case it cannot be used to independently assess accuracy. No effort should be spared in trying to remedy this situation, and to calibrate measurements independently of the CRM. For TA, this can be achieved for example by independently measuring the molarity of the acid titrant, while for DIC it can be done for example by using a gas loop or by preparing sodium carbonate standards (Dickson et al., 2007). Nevertheless, it remains essential to investigate the best way to calibrate data using CRM measurements, as discussed in Chapter 2 for TA, because this is all that is available for many important archival data sets.

6.3 Geo-engineering applications

A range of 'geo-engineering' techniques have been suggested to offset the adverse impacts of increasing atmospheric CO_2. Some of these are based on increasing the ocean's capacity to take up and store carbon, either by increasing the biological conversion of carbon from an inorganic to an organic form in the surface ocean, or by increasing TA. Both varieties are an application of the principles discussed in Chapter 5 for determining the influences of calcification and autotrophic production on CO_2.

The most well-known of these oceanic techniques is fertilisation by addition of iron (e.g. as Fe(II) sulfate) to iron-limited, 'high-nitrate low-chlorophyll' (HNLC) areas like the Southern Ocean. Experiments in HNLC regions have confirmed that this fertilisation can boost primary productivity and therefore biological conversion of inorganic to organic carbon in the surface layer, acting as a CO_2 sink (e.g. Coale et al., 1996; Boyd et al., 2000). In the context of Chapter 5, this corresponds to a situation where PIC production is negligible relative to POC production, so the 'production slope' (S_P) will be very small, always generating a CO_2 sink. However, as discussed in Section 5.3.3.1, if this organic carbon is not exported from the surface layer but remineralised *in situ* after the initial bloom, then no long-term net sequestration of CO_2 has taken place. In general, the associated increase in biominerals produced in the surface ocean might be expected to enhance transport into the interior ocean through the provision of ballasting material (Armstrong et al., 2001), but the local community structure is a critical factor in determining how effective this will be on a case-by-case basis. For example, at least half of the biomass of an artificially fertilised diatom-dominated bloom in the Southern Ocean was exported to deeper than 1000 m, providing successful long-term carbon sequestration (Smetacek et al., 2012). However, in a similar experiment in the Subantarctic Atlantic Ocean, the low silicic acid concentration limited the diatom population to under 10 % of the bloom biomass, and little carbon was exported to the ocean interior despite a short-term increase in net autotrophic production near the surface (Martin et al., 2013). Coupled with concerns about disruptive effects on ecosystems through changes in community structure and high levels of dissolved oxygen uptake associated with blooms, this spatial variability in efficiency – and consequent difficulties in using the results of small-scale experiments to make global predictions – has led to scepticism that this technique will provide an effective solution to the climatic effects of anthropogenic CO_2 emissions (Strong et al., 2009).

The other approach involves altering TA. As explained in Chapter 5, net calcification is a CO_2 source because of its effect on pCO_2^{sw}, and the opposite is also true – dissolution of calcium carbonate ($CaCO_3$) decreases pCO_2^{sw} and so can be considered as a CO_2 sink. This is an example of a situation where the statements in Section 5.2.4 are reversed, because $d\mathrm{DIC}/dt$ is positive; the 'production slope' could instead be called a 'dissolution slope' (S_D), and when S_D is greater than the isocap slope (S_I) there is a net CO_2 sink. Dissolution of marine carbonate sediments thus will offset the anthropogenic increase in atmospheric CO_2 by increasing the chemical capacity of the ocean to store DIC, but this will not help to offset the impacts of anthropogenic CO_2 in the immediate future, as it naturally operates on timescales much longer than a human lifetime (Archer, 2005). The process could be artificially enhanced by manually delivering ground-up carbonate minerals to the ocean surface layer. Minerals other than $CaCO_3$ have been suggested for this purpose that could be more effective at decreasing pCO_2^{sw}. The increase in TA caused by $CaCO_3$ dissolution is accompanied by an increase in DIC, which reduces S_D, thereby reducing the decrease in pCO_2^{sw} for a given amount of $CaCO_3$ dissolution in a given seawater composition. Minerals with greater S_D will be more effective CO_2 sinks, in terms of the change in pCO_2^{sw} per unit increase in TA. For example, olivine has the chemical formula $(Mg,Fe)_2SiO_4$, so its dissolution does not affect DIC but does increase TA; its S_D is ∞. As a numerical illustration, consider a water parcel at 15 °C, with a salinity of 35, DIC of 2100 μmol kg^{-1}, TA of 2330 μmol kg^{-1}, and no dissolved silicate; its initial pCO_2^{sw} is 391 μatm (van Heuven et al., 2011). Increasing TA by 50 μmol kg^{-1} by dissolution of $CaCO_3$ is accompanied by an increase in DIC of 25 μmol kg^{-1}, and pCO_2^{sw} drops by 34 μatm, to 357 μatm. If the same TA increase was instead achieved by $(Mg,Fe)_2SiO_4$ dissolution, then DIC does not change, the silicate concentration increases by 25 μmol kg^{-1}, and pCO_2^{sw} falls by 75 μatm, to 316 μatm. Olivine is widely available as a key component of mafic igneous rocks, and this geo-engineering potential has been the subject of investigation (e.g. Köhler et al., 2010). However, its iron and silicate content means that its dissolution in seawater also has a fertilisation effect (Köhler et al., 2013), and the adverse consequences associated with this, which are discussed in the previous paragraph, may also be applicable.

6.4 Future work

My specific plans for future work directly related to the content of individual chapters are discussed directly in those chapters. For example, the Calkulate script presented in Chapter 2 will be further developed, and its CO_2 loss correction scheme tested experimentally. The GLODAPv2 data product, once released, will be used to update the analysis presented in Chapter 4. All of Chapters 2 to 5 are in the process of being prepared for independent publication, and a version of Chapter 3 is currently undergoing peer review (Humphreys et al., 2015). The following paragraphs describe in more general terms the outlook for specific areas or research in which I intend to be involved in the future.

One area in which studies which combine observations with model output will be important is the continental shelf seas. These shallow, coastal ocean areas have a far more complex suite of physical and biological processes operating on the carbonate chemistry system than those affecting the open ocean. As a result, while these regions are considered globally to be a net sink for atmospheric CO_2 (Cai, 2011; Laruelle et al., 2014), individual shelf seas can instead act as CO_2 sources (Dai et al., 2013). Whether each region is a CO_2 source or sink usually is a result of a unique combination of factors, making it very difficult to predict how a specific sea will behave without first making detailed observations. These observations need to be at a high enough spatial resolution to discover small-scale processes while still covering a large enough geographical area to represent the entire shelf sea. Temporally, they need to be frequent enough to resolve seasonal cycles and also must be carried out for at least a full year. Clearly, this represents an enormous undertaking that would be financially and logistically restricted from being carried out indefinitely. When the opportunity presents itself to make observations in these settings it is therefore critical to do so in parallel with modelling studies, for example in the UK Shelf Seas Biogeochemistry research programme, which is currently underway. Amongst other goals, this aims to quantify the air-sea flux of CO_2 for the European continental shelf sea, and also to investigate if there is significant transport of carbon from the shelf sea into the adjacent open ocean. The observational data collected in such programmes can be tested against simulated output and thus used to improve available models. Once validated, the model output can be used to fill gaps and extend the understanding of the system generated from the observations. This will ensure that the final conclusions of the expensive and exhausting observational programme are applicable not only to the specific time period and location of the observations, but in a more

universal sense. While of course many studies on wide-ranging subjects have already been conducted in which these aims have been fulfilled, many more have not integrated observations with model output despite these potential gains.

The scientific community must continue its efforts to compile and perform secondary quality control on biogeochemical observations to provide historical context for new and repeated measurements, but it will become increasingly important to integrate data from sources other than traditional research cruises, like Argo floats and sustained observation platforms attached to moorings. The soon-to-be-released data synthesis GLODAPv2 will be an invaluable resource, but while all of the cruises it includes have been compared using cross-over analysis (Tanhua, 2010) and adjusted for consistency or excluded where necessary, there is no established method in place by which data collected from different platforms can be compatibly and reproducibly assimilated. Version 3 of the Surface Ocean CO_2 Atlas (SOCAT), which is also approaching completion and release, does contain data from a range of different observational platforms, and it features an expanded data flagging system to account for this and allow these data to be easily identified. Efforts should also be made to include a wider range of variables: for example, the previous generation of GLODAP and CARINA (Key et al., 2004, 2010) included stable isotopic data for DIC which had not undergone secondary quality control, necessitating the creation of independent data products for this variable (Schmittner et al., 2013; Becker et al., 2015). This raises the possibility of inconsistencies in the variables and cruises which are duplicated by the different data products, and increases the time which must be spent prior to any analysis simply making these datasets compatible with each other. As more and more data are generated in the future, increasing automation of these quality-control procedures will become essential. This is especially important as they typically rely upon hours of unfunded, voluntary work for many of the scientists involved.

6.5 Concluding remarks

The science of marine carbonate chemistry has never been so important to study as it is at the present day. As anthropogenic CO_2 continues to accumulate in the global ocean, the corresponding changes in its chemistry – like the decline in pH – will become increasingly pronounced, along with their ramifications. To answer critical questions about the magnitude and impacts of these changes in the coming century, it is essential first to understand how this complex system works and interacts now. The research community must embrace new sources of data and new methods of analysis, and carefully consider how to incorporate them into existing schemes.
To predict and prepare for the future, we must first understand the present.

A1

Calkulate functions

This appendix contains the MATLAB (MathWorks) functions used to calculate total alkalinity from open-cell titration data described in Chapter 2.

A1.1 Main Calkulate function

```
function [TA_final,E0_final,t,sc,meanT,pipmass,f2xint] = calkulate( ...
    datfile,acidmolar,acidrho,tit5vol,pipvol,sal,dic,phos,sc,tforce,z)
%calkulate Calculates total alkalinity from .dat file output by VINDTA
% Matthew P. Humphreys, 2015-01-20. Last updated 2015-02-16 [v0.1.1]
% This calculates total alkalinity (TA) from the .dat files output by the
%  VINDTA instrument (Marianda). The method is based on the Gran plot (G52)
%  as modified by Hansson & Jagner (HJ73) and Bradshaw et al. (BBSW81).
% However, DIC takes a fixed value which is not permitted to change during
%  the iterative process.
% See end of main function for citation list & reference codes.

%% === USER INPUTS and example values ===
% datfile = '3-1  14  (1500)1110.dat'; % 'filename.dat' from VINDTA
% tit5vol = 4.9831; % Titrino pipette volume/mL at "5mL" dispensed
% acidmolar = 0.10496; % Acid molarity / mol/L
% acidrho = 1.0212; % Acid density / kg/L
% pipvol = 100; % TA pipette volume / mL
% sal = 33.384;
% dic = 2022.04 * 1e-6; % DIC / mol/kg
% phos = 0.48 * 1e-6; % Phosphate / mol/kg
% sc = []; % Leave empty or input structure containing all constants' codes
% tforce = []; % Leave empty to use titration file temperature
% z = 0.1; % CO2 loss correction factor of B92

%% === SELECT CONSTANTS ===
if isempty(sc)
% Ionic concentrations
sc.TSO4 = 'MR66'; % Total sulfate: MR66,KDCP67
sc.THF = 'W71'; % Total fluoride: W71,R65,KDCP67
sc.TB = 'LKB10'; % Total boron: LKB10,U74,KDCP67
% Dissociation constants
sc.kHSO4 = 'D90b'; % Sulfate: D90b,WM13
sc.kHF = 'PF87'; % Fluoride: PF87,DR79
sc.k1k2 = 'LDK00'; % Carbonic acid K1&K2: LDK00,GP89
end %if

%% === READ VINDTA OUTPUT: .dat FILE ===
% This gives the option of inputting the titration data directly as a table
if ischar(datfile)
    t = calk_datfile(datfile);
else
    t = datfile;
end %if
```

```
% Correct cell temperature to <tforce>, if required
if ~isempty(tforce)
    t.t(:) = tforce;
end %if

% Initial .dat file calculations
t.vol = t.vol_raw * tit5vol/5; % Volume acid added / mL
t.tk = t.t + 273.15; % Cell temperature / K
t.mass = t.vol*1e-3 * acidrho; % Acid added / kg

% Seawater sample analysis density (MP81) & associated calculations
piprho = calk_MP81(t.t(1),sal) * 1e-3; % Sample analysis density / kg/L
pipmass = pipvol * piprho * 1e-3; % Sample mass / kg
acidmolal = acidmolar/acidrho; % Acid molality / mol/kg

%% === NERNST EQUATION CONSTANTS ===
% Constants R & F are 2010 CODATA recommended values
%  from http://physics.nist.gov/cuu/Constants
R =  8.3144621; % Gas constant / J/mol/K
F = 96.4853365; % Faraday constant / kC/mol
t.nernst = R * t.tk / F; % J/kC

%% === IONIC CONCENTRATIONS ===
% Total Sulfate / mol/kg
switch sc.TSO4
    case 'MR66',   TSO4 = calk_MR66(sal); % MR66 (recommended by DSC07)
    case 'KDCP67', TSO4 = 4.008 / 142.041; % KDCP67 (synthetic seawater)
end %switch
% Total Fluoride / mol/kg
switch sc.THF
    case 'W71',    THF = calk_W71(sal); % W71
    case 'R65',    THF = calk_R65(sal); % R65 (recommended by DSC07)
    case 'KDCP67', THF = 0.003 / 41.988; % KDCP67 (synthetic sw)
end %switch
% Total Boron / mol/kg
switch sc.TB
    case 'LKB10',  TB = calk_LKB10(sal); % LKB10
    case 'U74',    TB = calk_U74(sal); % U74
    case 'KDCP67', TB = 0.026 / 61.8317; % KDCP67 (synthetic sw)
end %switch

%% === DISSOCIATION CONSTANTS - all converted to Free pH scale ===
% Bisulfate kHSO4
switch sc.kHSO4
    case 'D90b', [~,pkHSO4] = calk_D90(t.tk,sal); % D90b (rec. DSC07)
    case 'WM13', pkHSO4 = calk_WM13(t.tk,sal); % WM13
end %switch
t.kHSO4 = 10.^-pkHSO4;
t.t2f = log10(1 + TSO4./t.kHSO4); % pH scale conversion: Total to Free
% Fluoride kHF
switch sc.kHF
    case 'PF87', pkHF_T = calk_PF87(t.tk,sal); % PF87 (rec. DSC07)
        t.kHF = 10.^-(pkHF_T + t.t2f);
    case 'DR79', pkHF = calk_DR79(t.tk,sal); % DR79
        t.kHF = 10.^-pkHF;
end %switch
t.s2f = log10(1 + TSO4./t.kHSO4 + THF./t.kHF); % pH conv.: SWS to Free
% Carbonic acid K1 and K2
switch sc.k1k2
    case 'LDK00', [pk1_T,pk2_T] = calk_LDK00(t.tk,sal); % LDK00 (rec. DSC07)
        t.k1 = 10.^-(pk1_T + t.t2f);
        t.k2 = 10.^-(pk2_T + t.t2f);
    case 'GP89', [pk1_SWS,pk2_SWS] = calk_GP89(t.tk,sal); % GP89
        t.k1 = 10.^-(pk1_SWS + t.s2f);
        t.k2 = 10.^-(pk2_SWS + t.s2f);
end %switch
% Boric acid (D90a)
pKB = calk_D90(t.tk,sal); % D90a (rec. DSC07)
t.kB = 10.^-(pKB + t.t2f);
```

```
% Water and phosphoric acid (KP67,DR79,JW79,M95,DSC07)
[pkw_T,pkP1_T,pkP2_T,pkP3_T] = calk_DSC07(t.tk,sal);
t.kw = 10.^-(pkw_T + t.t2f);
t.kP1 = 10.^-(pkP1_T + t.t2f);
t.kP2 = 10.^-(pkP2_T + t.t2f);
t.kP3 = 10.^-(pkP3_T + t.t2f);

% Dilution correction factor
t.masscxn = pipmass ./ (pipmass + t.mass);

%% === INITIAL ESTIMATES for TA and E0 ===
% Originally from G52, used by HJ73 and BBSW81, written here from
%  DAA03 eq'ns (10) and (11). NB: DAA03's "F1" is the others' "F2". Here,
%  I use the label G.
t.G = (pipmass + t.mass) .* exp(t.emf ./ t.nernst); % DAA03 eq'n (10)
t.Glogic = t.G > 0.1*max(t.G); % This may need to be adjusted. It
% should catch the +ve linear section on the right hand side of
% scatter(t.vol,t.G). This value is only used the first time,
% not for subsequent iterations.

%% === ITERATION PRE-ALLOCATIONS ===
ta = NaN(10,1);
e0 = NaN(size(ta));
% I = 1;

%% === ITERATION BEGINS ===
for I = 1:length(ta)

f2fit = regstats(t.G(t.Glogic(:,I),I),t.mass(t.Glogic(:,I)), ...
    'linear','beta');
f2xint = -f2fit.beta(1)/f2fit.beta(2);
ta(I) = f2xint * acidmolal/pipmass; % TA / mol/kg
% DAA03 eq'n (11):
if I == 1
    t.e0(:,I) = t.emf - t.nernst ...
        .* log((t.mass-f2xint)*acidmolal ...
        ./ (pipmass+t.mass));
else
    t.e0(:,I) = t.emf - t.nernst ...
        .* log(((t.mass-f2xint)*acidmolal ...
        - pipmass*(t.hf(:,I-1) + t.hso4(:,I-1))) ...
        ./ (pipmass+t.mass));
end %if else

t.e0(~t.Glogic(:,I),I) = NaN;
e0(I) = nanmean(t.e0(:,I)); % E0 / mV

%% === pH CALCULATION ===
% Modified Gran calculation from BBSW81's Appendix 2: based on HJ73, but
%  with phosphate & silicate effects added in.
t.h(:,I) = 10.^((t.emf - e0(I))./(log(10)*t.nernst)); % HJ73 eq'n (19)
t.ph(:,I) = -log10(t.h(:,I)); % Free scale

%% === CO2 LOSS CORRECTION ===
% Using B92 equations 24 and 25
t.FZ(:,I) = (t.h(:,I).^2 + t.k1.*t.h(:,I) + t.k1.*t.k2) ...
    ./ ((1+z).*t.h(:,I).^2 + t.k1.*t.h(:,I) + t.k1.*t.k2);
t.dic(:,I) = dic * t.FZ(:,I);

%% === OTHER PROTON EQUATIONS ===
% As for pH calculation, based on HJ73 and BBSW81
% (Silicate only affects the DIC determination, so is not included)
t.bicarb(:,I) = t.masscxn.*t.dic(:,I)./(t.h(:,I)./t.k1 + 1); % HJ73 eq. 20
t.hso4(:,I) = t.masscxn.*TSO4./(1 + t.kHSO4./t.h(:,I));      % HJ73 eq. 21
t.hf(:,I) = t.masscxn.*THF./(1 + t.kHF./t.h(:,I));           % HJ73 eq. 22
t.borate(:,I) = t.masscxn.*TB./(t.h(:,I)./t.kB + 1);         % HJ73 eq. 23
t.oh(:,I) = t.kw ./ t.h(:,I);                                % HJ73 eq. 24
% BBSW81 Appendix 2, eq'n for [H3PO4]-[HPO42-]:
t.p_p2(:,I) = phos * (1 - t.kP1.*t.kP2./(t.h(:,I).^2)) ...
    ./ (1 + t.kP1./t.h(:,I) ...
    + t.kP2.*t.kP3./t.h(:,I).^2 + t.kP1.*t.kP2.*t.kP3./t.h(:,I).^3);
% NB: [PO43-] is negligible in F2 pH range (BBSW81 Appendix 2)
```

```
%% === EXTEND TABLE to house iterated variables on first loop ===
if I == 1
    itvars = t.Properties.VariableNames(20:end); % !UNSTABLE!
    for V = 1:length(itvars)
        t.(itvars{V}) = [t.(itvars{V}) NaN(height(t),length(ta)-1)];
    end %for V
    t.Glogic(isnan(t.Glogic)) = 0;
    t.Glogic = logical(t.Glogic);
end %if

%% === CALCULATE F2, GET NEXT ESTIMATES of TA and E0 ===
% HJ73 eq'n (16), including phosphate like BBSW81 Appendix 2, but
%  remaining in the pH Free scale, and in mass not volume:
if I < length(ta)
    t.G(:,I+1) = (pipmass + t.mass).*(t.h(:,I) + t.hso4(:,I) ...
        + t.hf(:,I) - t.bicarb(:,I) + t.p_p2(:,I) - t.oh(:,I) ...
        - t.borate(:,I));
    t.Glogic(:,I+1) = t.ph(:,I) < 4 ...
        & t.ph(:,I) > 3;
end %if

%% === EVALUATION OF F1 and CALCULATION OF DIC ===
% I do not currently evaluate F1 or iterate a value for DIC, because:
%  (1) It should not affect the TA value
%  (2) Titration is open cell, so iterated DIC value is not meaningful
%  (3) There should always be an independently-measured DIC value to input
% So DIC is instead held constant at this input value.
% In case (3) is ever false, it may be worth writing up the DIC iteration
%  part (from HJ73 & BBSW81 Appendix 2; the latter includes a silicate
%  correction).
% Also, experimenting with input DIC suggests that it does not
%  significantly affect the TA result: changing DIC from 2000 to 1000
%  micromol/kg changes TA by only 2 micromol/kg. Permitting smaller changes
%  in DIC during the calculation therefore should make only negligible
%  changes to TA (i.e. much less than the measurement precision).

% === ITERATION ENDS
end %for I

%% === GET FINAL OUTPUTS ===
TA_final = ta(end) * 1e6; % micromol/kg
E0_final = e0(end); % mV
meanT = mean(t.t); % degC

%% === REFERENCES ===
%    G52: Gran, 1952, Analyst 77
%    R65: Riley, 1965, Deep-Sea Res 12(2)
%   MR66: Morris & Riley, 1966, Deep-Sea Res 13(4
% KDCP67: Kester et al., 1967, Limnol Oceanogr 12(1)
%   KP67: Kester & Pytkowicz, 1967, Limnol Oceanogr 12(2)
%  WLD69: Wooster et al., 1969, Limnol Oceanogr 14(3)
%    W71: Warner, 1971, Deep-Sea Res 18(12)
%   HJ73: Hansson & Jagner, 1973, Anal Chim Acta 65(2)
%    U74: Uppstrom, 1974, Deep-Sea Res 21(2)
%   DR79: Dickson & Riley, 1979, Mar Chem 7(2)
%   JW79: Johansson & Wedborg, 1979, Mar Chem 8(1)
% BBSW81: Bradshaw et al., 1981, Earth Planet Sci Lett 55(1)
%   MP81: Millero & Poisson, 1981, Deep-Sea Res Pt A 28(6)
%   PF87: Perez & Fraga, 1987, Mar Chem 21(2)
%   GP89: Goyet & Poisson, 1989, Deep-Sea Res Pt A 36(11)
%   D90a: Dickson, 1990, Deep-Sea Res Pt A 37(5)
%   D90b: Dickson, 1990, J Chem Thermodyn 22(2)
%    B92: Butler, 1992, Mar Chem 38(3-4)
%  CRP94: Clegg et al., 1994, J Chem Soc F Trans 90(13)
%    M95: Millero, 1995, Geochim Cosmochim Acta 59(4)
%  LDK00: Lueker et al., 2000, Mar Chem 70(1-3)
%  DAA03: Dickson et al., 2003, Mar Chem 80(2-3)
%  DSC07: Dickson et al., 2007. PICES Special Publication 3.
%  LKB10: Lee et al., 2010, Geochim Cosmochim Acta 74(6)
%   WM13: Waters & Millero, 2013, Mar Chem 149

end %function calkulate
```

A1.2 Calkulate subfunctions

```
function t = calk_datfile(filename)
%calk_datfile Load VINDTA titration data from .dat file
% Input <filename> = 'filename.dat'; output <t> = titration data

% Load titration data from .dat file
fileid = fopen(filename,'r');
tdata = textscan(fileid,'%f%f%f', 'headerlines',2);
fclose(fileid);

% Extract titration variables
t.vol_raw  = tdata{1}; % Volume of acid added / mL
t.emf      = tdata{2}; % Electrode EMF        / mV
t.t        = tdata{3}; % Temperature          / deg C
t = struct2table(t);

end %function calk_datfile



function TSO4 = calk_MR66(sal)
%calk_MR66 Total sulfate in seawater / mol/kg
% Input <sal> = salinity; output <TSO4> = total sulfate / mol/kg
% Total sulfate = [sulfate(2-)] + [bisulfate(-)]

% Sulfate:chlorinity (MR66)
SO4_Cl = 0.14000;

% Atomic mass (DSC07)
SO4_mass = 32.065 + 4*15.999; % g/mol

% Salinity:chlorinity (WLD69,DSC07)
TSO4 = (SO4_Cl/SO4_mass) * sal/1.80655; % mol/kg

end %function calk_MR66



function TF = calk_R65(sal)
%calk_R65 Total fluorine <TF> in seawater / mol/kg
% Input <sal> = salinity; output <TF> = total fluorine / mol/kg
% Total fluorine = [fluoride(-)] + [hydrogen fluoride]

% Fluorine:chlorinity (R65)
F_Cl = 6.7e-5;

% Atomic mass (DSC07)
F_mass = 18.998; % g/mol

% Salinity:chlorinity (WLD69,DSC07)
TF = (F_Cl/F_mass) * sal/1.80655; % mol/kg

end %function calk_W71



function TF = calk_W71(sal)
%calk_W71 Total fluorine <TF> in seawater / mol/kg
% Input <sal> = salinity; output <TF> = total fluorine / mol/kg
% Total fluorine = [fluoride(-)] + [hydrogen fluoride]

% Fluorine:chlorinity (W71)
F_Cl = 6.75e-5;

% Atomic mass (DSC07)
F_mass = 18.998; % g/mol

% Salinity:chlorinity (WLD69,DSC07)
TF = (F_Cl/F_mass) * sal/1.80655; % mol/kg

end %function calk_W71
```

```
function TB = calk_U74(sal)
%calk_U74 Total boron <TB> in seawater / mol/kg
% Input <sal> = salinity; output <TB> = total boron / mol/kg
% Total boron = [boric acid] + [borate(-)]

% Boron:chlorinity (U74)
B_Cl = 0.232;

% Atomic mass (DSC07)
B_mass = 10.811; % g/mol

% Salinity:chlorinity (WLD69,DSC07)
TB = (1e-3*B_Cl/B_mass) * sal/1.80655; % mol/kg

end %function calk_U74



function pkHF = calk_DR79(tk,sal)
%calk_DR79 HF stoichiometric dissociation constant <pkHF>, pH-Free
% Reaction: HF <=> H{+} + F{-}
% Inputs <tk> = temperature / K, <sal> = salinity
% Output <pkHF> = stoich. diss. constant, Free pH scale

% Ionic strength (DSC07)
ionstr = 19.924 * sal ./ (1000 - 1.005 * sal);

% Calculate pkHF (DR79)
ln_kF = 1590.2./tk - 12.641 + 1.525*sqrt(ionstr) + log(1 - 0.001005*sal);
pkHF = -log10(exp(ln_kF));

end %function calk_DR79



function rho = calk_MP81(t,sal)
%calk_MP81 Seawater density <rho> / kg/m^3 at pressure = 1 atmosphere
% Inputs <t> = temperature / deg C, <sal> = salinity
% Output <rho> = density / kg/m^3

% Calculate density (MP81)
rho  = 999.842594                          ...
     +   6.793952e-2 * t                   ...
     -   9.095290e-3 * t.^2                ...
     +   1.001685e-4 * t.^3                ...
     -   1.120083e-6 * t.^4                ...
     +   6.536336e-9 * t.^5                ...
 + (     0.824493                          ...
     -   4.0899e-3   * t                   ...
     +   7.6438e-5   * t.^2                ...
     -   8.2467e-7   * t.^3                ...
     +   5.3875e-9   * t.^4 ) .*sal        ...
 + ( -   5.72466e-3                        ...
     +   1.0227e-4   * t                   ...
     -   1.6546e-6   * t.^2 ) .*sal.^1.5 ...
 +       4.8314e-4             .*sal.^2   ;

end %function calk_MP81



function pkHF_T = calk_PF87(tk,sal)
%calk_PF87 HF stoichiometric dissociation constant <pkHF>, pH-Total
% Reaction: HF <=> H{+} + F{-}
% Inputs <tk> = temperature / K, <sal> = salinity
% Output <pkHF> = stoich. diss. constant, Total pH scale

% Calculate pkHF (PF87)
ln_bHF = -874./tk - 0.111.*sal.^0.5 + 9.68;
ln_kHF = -ln_bHF;
pkHF_T = -log10(exp(ln_kHF));

end %function calk_PF87
```

```
function [pk1_SWS,pk2_SWS] = calk_GP89(tk,sal)
%calk_GP89 Carbonic acid stoichiometric dissociation constants, pH-SWS
% Reaction: CO2 + H2O <=> HCO3{-} + H{+} <=> CO3{2-} + 2H{+}
% Inputs <tk> = temperature / K, <sal> = salinity
% Outputs <pk1_SWS>, <pk2_SWS> = stoich. diss. constants, SWS pH scale

% Calculate constants (GP89)
pk1_SWS =  812.27./tk + 3.356 - 0.00171*sal.*log(tk) + 0.000091*sal.^2;
pk2_SWS = 1450.87./tk + 4.604 - 0.00385*sal.*log(tk) + 0.000182*sal.^2;

end %function calk_GP89



function [pkB_T,pkHSO4] = calk_D90(tk,sal)
%calk_D90 Boric acid (pH-Total) & bisulfate (pH-Free) eq'm constants
% Inputs <tk> = temperature / K, <sal> = salinity
% Outputs <pkB_T>, <pkHSO4> = equilibrium constants

%% BORIC ACID - Total pH scale (D90a)
% Reaction: B(OH)3 + H2O <=> B(OH)4{-} + H{+}
% D90a, equation 23
ln_KB = (-8966.90   -  2890.53  *sal.^0.5 - 77.942   *sal ...
        + 1.728*sal.^1.5 - 0.0996*sal.^2) ./ tk ...
     +    148.0248 +   137.1942*sal.^0.5 +   1.62142*sal ...
     - (   24.4344 +    25.085 *sal.^0.5 +   0.2474 *sal) .* log(tk) ...
     +      0.053105*sal.^0.5 .* tk;
pkB_T = -log10(exp(ln_KB));

%% BISULFATE - Free pH scale (D90b)
% Reaction: HSO4{-} <=> SO4{2-} + H{+}
% D90b is paywalled, so equations here are as reprinted by DSC07
ionstr = 19.942*sal ./ (1000 - 1.005*sal); % Ionic strength
ln_KS = -4276.1./tk + 141.328 - 23.093*log(tk) ...
    + ((-13856./tk) + 324.57 - 47.986*log(tk)) .* ionstr.^0.5 ...
    + ((35474./tk) - 771.54 + 114.723*log(tk)) .* ionstr ...
    - (2698./tk) .* ionstr.^1.5 ...
    + (1776./tk) .* ionstr.^2 ...
    + log(1 - 0.001005*sal);
pkHSO4 = -log10(exp(ln_KS));

end %function calk_D90



function [pk1_T,pk2_T] = calk_LDK00(tk,sal)
%calk_LDK00 Carbonic acid stoichiometric dissociation constants, pH-Total
% Reaction: CO2 + H2O <=> HCO3{-} + H{+} <=> CO3{2-} + 2H{+}
% Inputs <tk> = temperature / K, <sal> = salinity
% Outputs <pk1_T>, <pk2_T> = stoich. diss. constants, Total pH scale

% Calculate constants (LDK00)
pk1_T = 3633.86./tk - 61.2172 + 9.6777.*log(tk) ...
    - 0.011555*sal + 0.0001152*sal.^2;
pk2_T = 471.78./tk + 25.929 - 3.16967.*log(tk) ...
    - 0.01781*sal + 0.0001122*sal.^2;

end %function calk_LDK00
```

```
function [pkw_T,pkP1_T,pkP2_T,pkP3_T] = calk_DSC07(tk,sal)
%calk_DSC07 Water & phosphoric acid dissociation constants, pH-Total
% Inputs <tk> = temperature / K, <sal> = salinity
% Outputs <pkw_T>, <pkP1_T>, <pkP2_T>, <pkP3_T>
%   = stoich. diss. constants, Total pH scale

% These equations are all taken from DSC07, but they are originally from
%  M95; DSC07 have subtracted 0.015 from the constant term in each case,
%  to approximately convert pH-SWS to pH-Total.

%% WATER (DSC07)
% kw = [H+][OH-]
ln_kw = (-13847.26./tk) + 148.9652 - 23.6521*log(tk) ...
    + ((118.67./tk) - 5.977 + 1.0495*log(tk)) .* sal.^0.5 ...
    - 0.01615 * sal;
pkw_T = -log10(exp(ln_kw));

%% PHOSPHORIC ACID
% These equations, first presented by M95, are based on a composite of data
%  from KP67, DR79 and JW79. NB: the equations below are from DSC07.
% kP1 = [H+][H2PO4-]/[H3PO4]
ln_kP1 = -4576.752./tk + 115.525 - 18.453*log(tk) ...
    + (-106.736./tk + 0.69171) .* sal.^0.5 ...
    + (-0.65643./tk - 0.01844) .* sal;
pkP1_T = -log10(exp(ln_kP1));
% kP2 = [H+][HPO42-]/[H2PO4-]
ln_kP2 = -8814.715./tk + 172.0883 - 27.927*log(tk) ...
    + (-160.34./tk + 1.3566) .* sal.^0.5 ...
    + (0.37335./tk - 0.05778) .* sal;
pkP2_T = -log10(exp(ln_kP2));
% kP3 = [H+][PO43-]/[HPO42-]
ln_kP3 = -3070.75./tk - 18.141 ...
    + (17.27039./tk + 2.81197) .* sal.^0.5 ...
    + (-44.99486./tk - 0.09984) .* sal;
pkP3_T = -log10(exp(ln_kP3));

end %function calk_DSC07



function TB = calk_LKB10(sal)
%calk_LKB10 Total boron <TB> in seawater / mol/kg
% Input <sal> = salinity; output <TB> = total boron / mol/kg
% Total boron = [boric acid] + [borate(-)]

B_sal = 0.1336;      % = boron/salinity / (mg/kg)/â (LKB10)
B = B_sal * sal;     % = boron / mg/kg
B_RAM = 10.811e3;    % = relative atomic mass of boron / mg/mol (DSC07)
TB = B/B_RAM;        % = total boron / mol/kg

end %function calk_LKB10
```

```
function pkHSO4 = calk_WM13(tk,sal)
%calk_WM13 Bisulfate dissociation constant, pH-Free
% Reaction: HSO4{-} <=> SO4{2-} + H{+}
% Inputs <tk> = temperature / K, <sal> = salinity
% Outputs <pkB_T>, <pkHSO4> = equilibrium constants

%% Equation 29
% Constants (from Corrigendum to WM13, Table 6)
c1  =  4.24666         ;
c2  = -0.152671        ;
c3  =  2.67059   * 1e-2;
c4  = -4.2128    * 1e-5;
c5  =  0.2542181       ;
c6  = -5.09534   * 1e-3;
c7  =  7.1589    * 1e-4;
c8  = -2.91179   * 1e-3;
c9  =  2.09968   * 1e-5;
c10 = -4.03724   * 1e-5;
% Equation
log10_KK = (c1 + c2*tk + c3*tk.*log(tk) + c4*tk.^2) .* sal.^0.5 ...
        + (c5 + c6*tk + c7*tk.*log(tk))           .* sal      ...
        + (c8 + c9*tk)                          .* sal.^1.5 ...
        +  c10                                  * sal.^2   ;

%% Equation (30)
% Constants (taken directly from CRP94)
a1  =    562.69486        ;
a2  = -  102.5154         ;
a3  = -    1.117033 * 1e-4;
a4  =      0.2477538      ;
a5  = -13273.75           ;
% Equation
log10_Ko = a1 + a2*log(tk) + a3*tk.^2 + a4*tk + a5./tk;

%% Calculate pkHSO4 (WM13)
pkHSO4 = -(log10_KK + log10_Ko);

end %function calk_WM13
```

A2

MATLAB functions for Chapter 5

This appendix contains the MATLAB (MathWorks) functions used to evaluate the exact isocap slope (S_I) (A2.1), and to generate and evaluate its linear approximation (S_I^{lin}) (A2.2 and A2.3 respectively). These require version 1.1 of the CO_2SYS program for MATLAB (van Heuven et al., 2011); this program and relevant documentation can be downloaded from http://cdiac.ornl.gov/oceans/co2rprt.html.

A2.1 Calculate exact S_I

```
function sliso =
mph_sliso(PAR1,PAR2,PAR1TYPE,PAR2TYPE,SAL,TEMP,PRES,SI,PHOS,K1K2CONSTANTS,KSO4CON
STANT)
%mph_sliso Calculates exact isocap slope using CO2SYS
% Written by Matthew P. Humphreys, last updated 2015-03-03
% === INPUTS ===
% PAR1: vector of carbonate chemistry variable 1, see CO2SYS documentation
% PAR2: vector of carbonate chemistry variable 2, see CO2SYS documentation
% PAR1TYPE: type of carbonate chem. variable 1, see CO2SYS documentation
% PAR2TYPE: type of carbonate chem. variable 2, see CO2SYS documentation
% SAL: salinity
% TEMP: temperature / ∞C
% PRES: pressure / dbar
% SI: silicate / ?mol/kg
% PHOS: phosphate / ?mol/kg
% K1K2CONSTANTS: carbonic acid dissoc. constants, see CO2SYS documentation
% KSO4CONSTANT: total boron and bisulfate dissoc., see CO2SYS documentation
% === OUTPUT ===
% sliso: exact isocap slope

co2s = CO2SYS(PAR1,PAR2,PAR1TYPE,PAR2TYPE,SAL,TEMP,TEMP,PRES,PRES, ...
    SI,PHOS,3,K1K2CONSTANTS,KSO4CONSTANT);

CO2 = co2s(:, 8) * 1e-6;
H   = co2s(:,28) * 1e-6;
k1  = co2s(:,54);
k2  = co2s(:,55);
kw  = co2s(:,58);
kB  = co2s(:,59);
TB  = co2s(:,79) * 1e-6;

X = k1.*CO2 + kB.*TB + kw;
Y = (k1.*kB + 2*k1.*k2).*CO2 + kB.*kw;
Z = 2*k1.*k2.*kB.*CO2;

sliso = (-H.^4.*(H + 2*kB) - (kB.^2 + X).*H.^3 - Y.*H.*(2*H + kB) ...
    - Z.*(3*H + 2*kB)) ./ (-(k1.*CO2.*H + 2*k1.*k2.*CO2) .* (H + kB).^2);

end %function mph_sliso
```

A2.2 Generate expressions for coefficients *a*, *b*, *c* and *d*

```
function abcd_fit = generate_sliso_parameterisation
%generate_sliso_parameterisation Fits coefficients for the linear
% approximation to the isocap slope, a/(b+c.pCO2)^d
% Written by Matthew P. Humphreys, last updated 2015-03-03
% Output abcd_fit is copied into function mph_slisolin()

%% Setup gradients
pco2 = ([20:10:400 425:25:1500 1500:50:2000 2100:100:4000])';
t = -1:2:37;
s = 25:1:45;
p = 5;
si = 0;
phos = 0;
ta = (2030:10:2600)';

% Calculate isocaps and their fit coefficients
slisofit = NaN(length(t),4,length(s));
isocaps_std = NaN(length(t),length(s),length(pco2));
isocaps = isocaps_std;

for S = 1:length(s)
    for T = 1:length(t)

        disp([num2str((S-1)*length(t)+T) ...
            '/' num2str(length(t)*length(s))]);

        for P = 1:length(pco2)

            isocaps(T,S,P) = mean(mph_sliso(ta,pco2(P),1,4,s(S),t(T), ...
                p,si,phos,10,3));
            isocaps_std(T,S,P) = std(mph_sliso(ta,pco2(P),1,4, ...
                s(S),t(T),p,si,phos,10,3));

        end %for P

        % Set up fit type and options.
        ft = fittype('a+b/(c+x)^d', 'independent','x', 'dependent','y');
        opts = fitoptions('method','nonlinearleastsquares');
        opts.Display = 'off';
        opts.StartPoint = [1 15 60 0.7];

        % Fit model to data
        fitresult = fit(pco2,squeeze(isocaps(T,S,:)),ft,opts);
        slisofit(T,:,S) = coeffvalues(fitresult);

    end %for T
end %for S

%% Parameterise the coefficients
tvec = repmat(t',[length(s) 1]);
svec = repmat(s,[length(t) 1]);
svec = svec(:);
for C = 1:4
    isovec.(['c' num2str(C)]) = slisofit(:,C,:);
    isovec.(['c' num2str(C)]) = isovec.(['c' num2str(C)])(:);
    abcd_fit.(['c' num2str(C)]) = regstats(isovec.(['c' num2str(C)]), ...
        [tvec tvec.^2 tvec.^3 tvec.*svec svec.*tvec.^2 svec svec.^2], ...
        'linear',{'beta' 'yhat' 'rsquare'});
end %for C

end %function generate_eqratio_parameterisation
```

A2.3 Calculate S_I^{lin} from pCO_2^{sw}, temperature and salinity

```
function [slisolin,abcd] = mph_slisolin(pco2,tvec,svec)
%mph_slisolin Calculates linear approximation to isocap slope
% Written by Matthew P. Humphreys, last updated 2015-03-03
% ==== INPUTS ===
% pco2: column vector or single value of pCO2sw / ?atm
% tvec: column vector or single value of temperature / ∞C
% svec: column vector or single value of salinity
% NB - tvec and svec must always be the same size as each other
%    - pco2 must be the same size as tvec and svec unless pco2 is a single
%      value or tvec and svec are both single values
% === OUTPUTS ===
% slisolin: linear approximation of isocap slope
% abcd: columns are a, b, c and d at corresponding row in input vectors

%% Define abcd coefficients
abcd_fit.a.beta = [9.881636599862392e-01;
                  -2.784543166903102e-03;
                   1.860900378580598e-04;
                  -2.589312833034023e-06;
                   4.722792899496479e-05;
                  -3.826460112690743e-06;
                   7.409460579217958e-04;
                  -1.641945979129400e-05];

abcd_fit.b.beta = [1.131151913010460e+01;
                   6.398374670363518e-01;
                  -1.746141025849049e-02;
                   7.671910811203251e-05;
                  -1.316098749414350e-02;
                   1.087205118509660e-04;
                   2.102829120389100e-01;
                  -1.256070118425023e-03];

abcd_fit.c.beta = [1.256037743216081e+01;
                  -1.239014655272715e-01;
                   7.744897863536181e-02;
                  -9.293268335286905e-04;
                   3.858929513108719e-02;
                  -1.096813555333075e-03;
                   1.278247367117405e+00;
                  -8.535374679418109e-03];

abcd_fit.d.beta = [9.171528209365897e-01;
                  -4.569952888401074e-03;
                   2.426885402002241e-05;
                  -1.388709728915260e-06;
                  -5.179150949034683e-05;
                  -1.544717005017022e-06;
                  -2.930874540047260e-03;
                   5.031075218501546e-06];

%% Generate predictor matrix
pmx = [tvec tvec.^2 tvec.^3 tvec.*svec svec.*tvec.^2 svec svec.^2];
abcd = NaN(length(tvec),4);

%% Calculate y=a+b/(c+x)^d coefficients
letters = {'a' 'b' 'c' 'd'};
for C = 1:4
    abcd(:,C) = abcd_fit.(letters{C}).beta(1) ...
        + pmx * abcd_fit.(letters{C}).beta(2:end);
end %for C

%% Calculate isocap slope
slisolin = abcd(:,1) + abcd(:,2)./(abcd(:,3) + pco2).^abcd(:,4);

end %function mph_slisolin
```

A3

Stoichiometry of coccolithophore particulate organic and inorganic matter, and calculation of ψ from S_I

This appendix to Chapter 5 contains the raw data collected from the published literature, and the calculations carried out upon it, used to generate Table 5.2. See Chapter 5 for a full explanation of the abbreviations and symbols used. Figure A3.2 is a reproduction of Figure 2 of Frankignoulle et al. (1994) in order to support the interpretation of ψ described in Chapter 5 and Equation 5.40.

Experiment	**Coefficient (element)**	**POX / pg cell^{-1}**	**POX / pmol cell^{-1}**	**Normalised to β = 106**
Control PO_4	α (N)	1.62 ± 0.03	0.116 ± 0.002	17.7 ± 0.4
Control PO_4	β (C)	8.31 ± 0.11	0.692 ± 0.009	106
Control PO_4	θ (P)	0.10 ± 0.00	0.0032 ± 0.0000	0.49 ± 0.01
Control NO_3	α (N)	1.45 ± 0.03	0.104 ± 0.002	15.9 ± 0.6
Control NO_3	β (C)	8.30 ± 0.28	0.691 ± 0.023	106
Control NO_3	θ (P)	0.09 ± 0.00	0.0029 ± 0.0000	0.45 ± 0.02

Table A3.1. Cellular organic elemental stoichiometry data for *Emiliania huxleyi* from Langer et al. (2013). Langer et al. (2013) also report PIC of 8.40 ± 0.24 pg cell^{-1} and 9.43 ± 0.50 pg cell^{-1} for the Control PO_4 and NO_3 experiments respectively, from which R_P values of 1.01 ± 0.03 and 1.14 ± 0.07 can be calculated. The X in POX refers to the element in brackets in the Coefficient column for each row.

Species	Coefficient (element)	Ho et al. (2003)	Normalised to β = 106
E. huxleyi	α (N)	8.8 ± 2.9	12.3 ± 5.5
E. huxleyi	β (C)	76 ± 23	106
E. huxleyi	η (S)	0.77 ± 0.02	1.07 ± 0.33
E. huxleyi	θ (P)	1	1.39 ± 0.42
G. oceanica	α (N)	7.3 ± 1.3	12.1 ± 3.1
G. oceanica	β (C)	64 ± 12	106
G. oceanica	η (S)	1.00 ± 0.07	1.66 ± 0.33
G. oceanica	θ (P)	1	1.66 ± 0.31

Table A3.2. Cellular organic elemental stoichiometry data for *Emiliania huxleyi* and *Gephyrocapsa oceanica* from Ho et al. (2003).

Experiment	Coefficient (element)	POX / pg cell^{-1}	POX / pmol cell^{-1}	Normalised to β = 106
Control	α (N)	10.45 ± 1.38	0.75 ± 0.10	31.1 ± 4.5
Control	β (C)	30.53 ± 1.79	2.54 ± 0.15	106
Control	θ (P)	0.39 ± 0.04	0.013 ± 0.001	0.53 ± 0.06
NO_3-limited	α (N)	4.79 ± 1.00	0.34 ± 0.07	10.3 ± 2.3
NO_3-limited	β (C)	42.37 ± 3.16	3.53 ± 0.26	106
NO_3-limited	θ (P)	0.52 ± 0.07	0.017 ± 0.002	0.50 ± 0.08

Table A3.3. Cellular organic elemental stoichiometry data for *Calcidiscus leptoporus* from Langer et al. (2012). Langer et al. (2012) also report PIC of 70.81 ± 4.50 pg cell^{-1} and 107.13 ± 5.26 pg cell^{-1} for the Control and NO_3-limited experiments respectively, from which R_P values of 2.32 ± 0.15 and 2.53 ± 0.23 can be calculated. The X in POX refers to the element in brackets in the Coefficient column for each row.

Species	Cell volume / µm^3	POC / pg cell^{-1}	POC / pmol cell^{-1}	DMSP / pg cell^{-1}	DMSP / pmol cell^{-1}	η
E. huxleyi	25	4.4	0.37	1.1	0.0082	2.35
G. oceanica	99	16.2	1.35	1.2	0.0089	0.70
C. pelagicus	1316	183	15.3	95	0.708	4.91
C. leptoporus	278	42.6	3.55	15.2	0.113	3.39

Table A3.4. Cellular sulfur stoichiometry from Franklin et al. (2010), with cellular POC calculated using Equation 5.37 following Menden-Deuer and Lessard (2000). Values of the coefficient η are relative to β = 106.

Species	Temperature / °C	pCO_2^{sw} / µatm	R_P
G. oceanica	15	430	1.52
G. oceanica	20	413	1.73
G. oceanica	25	377	2.84
E. huxleyi	10	375	0.90
E. huxleyi	15	400	0.93
E. huxleyi	20	431	1.12

Table A3.5. Production ratios R_P for *Gephyrocapsa oceanica* and *Emiliania huxleyi* from Sett et al. (2014) supplementary tables S1 and S2.

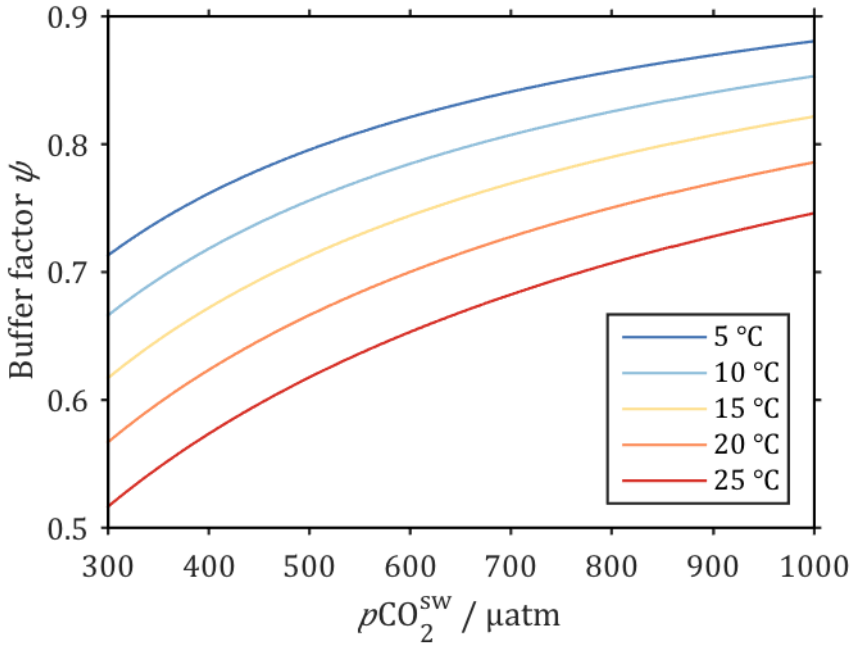

Figure A3.1. Replication of Figure 2 from Frankignoulle et al. (1994) with ψ calculated using Equations 5.34 and 5.40. Total alkalinity = 2400 µmol kg^{-1}, salinity = 35. There are slight differences between the original graph and this replication, probably because different expressions were used for the various equilibrium constants and ionic concentrations, but the overall patterns and range of values are virtually the same.

References

Ahn, J., Brook, E.J., Mitchell, L., Rosen, J., McConnell, J.R., Taylor, K., Etheridge, D., Rubino, M., 2012. Atmospheric CO_2 over the last 1000 years: A high-resolution record from the West Antarctic Ice Sheet (WAIS) Divide ice core. Global Biogeochem. Cy. 26, GB2027. doi:10.1029/2011GB004247

Álvarez, M., Lo Monaco, C., Tanhua, T., Yool, A., Oschlies, A., Bullister, J.L., Goyet, C., Metzl, N., Touratier, F., McDonagh, E., Bryden, H.L., 2009. Estimating the storage of anthropogenic carbon in the subtropical Indian Ocean: a comparison of five different approaches. Biogeosciences 6, 681–703. doi:10.5194/bg-6-681-2009

Anderson, L.A., 1995. On the hydrogen and oxygen content of marine phytoplankton. Deep-Sea Res. Pt I 42, 1675–1680. doi:10.1016/0967-0637(95)00072-E

Anderson, L.A., Sarmiento, J.L., 1994. Redfield ratios of remineralization determined by nutrient data analysis. Global Biogeochem. Cy. 8, 65–80. doi:10.1029/93GB03318

Andres, R.J., Boden, T.A., Bréon, F.-M., Ciais, P., Davis, S., Erickson, D., Gregg, J.S., Jacobson, A., Marland, G., Miller, J., Oda, T., Olivier, J.G.J., Raupach, M.R., Rayner, P., Treanton, K., 2012. A synthesis of carbon dioxide emissions from fossil-fuel combustion. Biogeosciences 9, 1845–1871. doi:10.5194/bg-9-1845-2012

Archer, D., 2005. Fate of fossil fuel CO_2 in geologic time. J. Geophys. Res. 110, C09S05. doi:10.1029/2004JC002625

Armstrong, R.A., Lee, C., Hedges, J.I., Honjo, S., Wakeham, S.G., 2001. A new, mechanistic model for organic carbon fluxes in the ocean based on the quantitative association of POC with ballast minerals. Deep-Sea Res. Pt II 49, 219–236. doi:10.1016/S0967-0645(01)00101-1

Atamanchuk, D., Tengberg, A., Thomas, P.J., Hovdenes, J., Apostolidis, A., Huber, C., Hall, P.O.J., 2014. Performance of a lifetime-based optode for measuring partial pressure of carbon dioxide in natural waters. Limnol. Oceanogr. Methods 12, 63–73. doi:10.4319/lom.2014.12.63

Bakker, D.C.E., Pfeil, B., Smith, K., Hankin, S., Olsen, A., Alin, S.R., Cosca, C., Harasawa, S., Kozyr, A., Nojiri, Y., O'Brien, K.M., Schuster, U., Telszewski, M., Tilbrook, B., Wada, C., Akl, J., Barbero, L., Bates, N.R., Boutin, J., Bozec, Y., Cai, W.-J., Castle, R.D., Chavez, F.P., Chen, L., Chierici, M., Currie, K., de Baar, H.J.W., Evans, W., Feely, R.A., Fransson, A., Gao, Z., Hales, B., Hardman-Mountford, N.J., Hoppema, M., Huang, W.-J., Hunt, C.W., Huss, B., Ichikawa, T., Johannessen, T., Jones, E.M., Jones, S.D., Jutterström, S., Kitidis, V., Körtzinger, A., Landschützer, P., Lauvset, S.K., Lefèvre, N., Manke, A.B., Mathis, J.T., Merlivat, L., Metzl, N., Murata, A., Newberger, T., Omar, A.M., Ono, T., Park, G.-H., Paterson, K., Pierrot, D., Ríos, A.F., Sabine, C.L., Saito, S., Salisbury, J., Sarma, V.V.S.S., Schlitzer, R., Sieger, R., Skjelvan, I., Steinhoff, T., Sullivan, K.F., Sun, H., Sutton, A.J., Suzuki, T., Sweeney, C., Takahashi, T., Tjiputra, J., Tsurushima, N., van Heuven, S.M.A.C., Vandemark, D., Vlahos, P., Wallace, D.W.R., Wanninkhof, R., Watson, A.J., 2014. An update to the Surface Ocean CO_2 Atlas (SOCAT version 2). Earth Syst. Sci. Data 6, 69–90. doi:10.5194/essd-6-69-2014

Balch, W.M., Drapeau, D.T., Bowler, B.C., Lyczkowski, E.R., Lubelczyk, L.C., Painter, S.C., Poulton, A.J., 2014. Surface biological, chemical, and optical properties of the Patagonian Shelf coccolithophore bloom, the brightest waters of the Great Calcite Belt. Limnol. Oceanogr. 59, 1715–1732. doi:10.4319/lo.2014.59.5.1715

Balch, W.M., Kilpatrick, K., Holligan, P.M., Cucci, T., 1993. Coccolith Production and Detachment by *Emiliania huxleyi* (Prymnesiophyceae). J. Phycol. 29, 566–575. doi:10.1111/j.0022-3646.1993.00566.x

Barron, J.L., Dyrssen, D., Jones, E.P., Wedborg, M., 1983. A comparison of computer methods for seawater alkalinity titrations. Deep-Sea Res. Pt A 30, 441–448. doi:10.1016/0198-0149(83)90077-8

Bartlett, M.S., 1935. Some Aspects of the Time-Correlation Problem in Regard to Tests of Significance. J. Roy. Stat. Soc. 98, 536–543. doi:10.2307/2342284

Bates, N.R., Astor, Y.M., Church, M.J., Currie, K., Dore, J.E., González-Dávila, M., Lorenzoni, L., Muller-Karger, F., Olafsson, J., Santana Casiano, J.M., 2014. A time-series view of changing ocean chemistry due to ocean uptake of anthropogenic CO_2 and ocean acidification. Oceanography 27, 126–141. doi:10.5670/oceanog.2014.16

Bates, N.R., Best, M.H.P., Neely, K., Garley, R., Dickson, A.G., Johnson, R.J., 2012. Detecting anthropogenic carbon dioxide uptake and ocean acidification in the North Atlantic Ocean. Biogeosciences 9, 2509–2522. doi:10.5194/bg-9-2509-2012

Bauerfeind, E., Nöthig, E.-M., Beszczynska, A., Fahl, K., Kaleschke, L., Kreker, K., Klages, M., Soltwedel, T., Lorenzen, C., Wegner, J., 2009. Particle sedimentation patterns in the eastern Fram Strait during 2000–2005: Results from the Arctic long-term observatory HAUSGARTEN. Deep-Sea Res. Pt I 56, 1471–1487. doi:10.1016/j.dsr.2009.04.011

Beaufort, L., Probert, I., de Garidel-Thoron, T., Bendif, E.M., Ruiz-Pino, D., Metzl, N., Goyet, C., Buchet, N., Coupel, P., Grelaud, M., Rost, B., Rickaby, R.E.M., de Vargas, C., 2011. Sensitivity of coccolithophores to carbonate chemistry and ocean acidification. Nature 476, 80–83. doi:10.1038/nature10295

Becker, M., Andersen, N., Fiedler, B., Fietzek, P., Körtzinger, A., Steinhoff, T., Friedrichs, G., 2012. Using cavity ringdown spectroscopy for continuous monitoring of $\delta^{13}C(CO_2)$ and fCO_2 in the surface ocean. Limnol. Oceanogr. Methods 10, 752–766. doi:10.4319/lom.2012.10.752

Becker, M., Tanhua, T., Humphreys, M.P., Erlenkeuser, H., Andersen, N., Körtzinger, A., 2015. An internally consistent collection of ocean $\delta^{13}C$ data. Manuscript in preparation.

Boyd, P.W., Watson, A.J., Law, C.S., Abraham, E.R., Trull, T., Murdoch, R., Bakker, D.C.E., Bowie, A.R., Buesseler, K.O., Chang, H., Charette, M., Croot, P., Downing, K., Frew, R., Gall, M., Hadfield, M., Hall, J., Harvey, M., Jameson, G., LaRoche, J., Liddicoat, M., Ling, R., Maldonado, M.T., McKay, R.M., Nodder, S., Pickmere, S., Pridmore, R., Rintoul, S., Safi, K., Sutton, P., Strzepek, R., Tanneberger, K., Turner, S., Waite, A., Zeldis, J., 2000. A mesoscale phytoplankton bloom in the polar Southern Ocean stimulated by iron fertilization. Nature 407, 695–702. doi:10.1038/35037500

Bradshaw, A.L., Brewer, P.G., 1988. High precision measurements of alkalinity and total carbon dioxide in seawater by potentiometric titration — 1. Presence of unknown protolyte(s)? Mar. Chem. 23, 69–86. doi:10.1016/0304-4203(88)90023-0

Bradshaw, A.L., Brewer, P.G., Shafer, D.K., Williams, R.T., 1981. Measurements of total carbon dioxide and alkalinity by potentiometric titration in the GEOSECS program. Earth Planet. Sci. Lett. 55, 99–115. doi:10.1016/0012-821X(81)90090-X

Bresnahan Jr., P.J., Martz, T.R., Takeshita, Y., Johnson, K.S., LaShomb, M., 2014. Best practices for autonomous measurement of seawater pH with the Honeywell Durafet. Methods Oceanogr. 9, 44–60. doi:10.1016/j.mio.2014.08.003

Bretherton, C.S., Widmann, M., Dymnikov, V.P., Wallace, J.M., Bladé, I., 1999. The Effective Number of Spatial Degrees of Freedom of a Time-Varying Field. J. Clim. 12, 1990–2009. doi:10.1175/1520-0442(1999)012<1990:TENOSD>2.0.CO;2

Brewer, P.G., 1978. Direct observation of the oceanic CO_2 increase. Geophys. Res. Lett. 5, 997–1000. doi:10.1029/GL005i012p00997

Brewer, P.G., Sarmiento, J.L., Smethie, W.M., 1985. The Transient Tracers in the Ocean (TTO) program: The North Atlantic Study, 1981; The Tropical Atlantic Study, 1983. J. Geophys. Res. Oceans 90, 6903–6905. doi:10.1029/JC090iC04p06903

Buitenhuis, E.T., van der Wal, P., de Baar, H.J.W., 2001. Blooms of *Emiliania huxleyi* are sinks of atmospheric carbon dioxide: A field and mesocosm study derived simulation. Global Biogeochem. Cy. 15, 577–587. doi:10.1029/2000GB001292

Burkholder, K.C., Lozier, M.S., 2011. Mid-depth Lagrangian pathways in the North Atlantic and their impact on the salinity of the eastern subpolar gyre. Deep-Sea Res. Pt I 58, 1196–1204. doi:10.1016/j.dsr.2011.08.007

Butler, J.N., 1992. Alkalinity titration in seawater: How accurately can the data be fitted by an equilibrium model? Mar. Chem. 38, 251–282. doi:10.1016/0304-4203(92)90037-B

Byrne, R.H., Robert-Baldo, G., Thompson, S.W., Chen, C.T.A., 1988. Seawater pH measurements: an at-sea comparison of spectrophotometric and potentiometric methods. Deep-Sea Res. Pt A 35, 1405–1410. doi:10.1016/0198-0149(88)90091-X

Byrne, R.H., Yao, W., 2008. Procedures for measurement of carbonate ion concentrations in seawater by direct spectrophotometric observations of Pb(II) complexation. Mar. Chem. 112, 128–135. doi:10.1016/j.marchem.2008.07.009

Cai, W.-J., 2011. Estuarine and Coastal Ocean Carbon Paradox: CO_2 Sinks or Sites of Terrestrial Carbon Incineration? Annu. Rev. Marine Sci. 3, 123–145. doi:10.1146/annurev-marine-120709-142723

Caldeira, K., Wickett, M.E., 2003. Anthropogenic carbon and ocean pH. Nature 425, 365–365. doi:10.1038/425365a

Chen, G.-T., Millero, F.J., 1979. Gradual increase of oceanic CO_2. Nature 277, 205–206. doi:10.1038/277205a0

Clarke, J.S., Achterberg, E.P., Mowlem, M.C., 2015a. Developments in pCO_2 measurement technology for use in marine environments. Manuscript in preparation.

Clarke, J.S., Achterberg, E.P., Rérolle, V., Floquet, C., Mowlem, M.C., 2015b. Characterisation and deployment of an immobilised pH sensor spot for ocean pH measurements. Submitted manuscript.

Coale, K.H., Johnson, K.S., Fitzwater, S.E., Gordon, R.M., Tanner, S., Chavez, F.P., Ferioli, L., Sakamoto, C., Rogers, P., Millero, F., Steinberg, P., Nightingale, P., Cooper, D., Cochlan, W.P., Landry, M.R., Constantinou, J., Rollwagen, G., Trasvina, A., Kudela, R., 1996. A massive phytoplankton bloom induced by an ecosystem-scale iron fertilization experiment in the equatorial Pacific Ocean. Nature 383, 495–501. doi:10.1038/383495a0

Colbourn, G., Ridgwell, A., Lenton, T.M., 2015. The time scale of the silicate weathering negative feedback on atmospheric CO_2. Global Biogeochem. Cy. 2014GB005054. doi:10.1002/2014GB005054

Collins, W.J., Bellouin, N., Doutriaux-Boucher, M., Gedney, N., Halloran, P., Hinton, T., Hughes, J., Jones, C.D., Joshi, M., Liddicoat, S., Martin, G., O'Connor, F., Rae, J., Senior, C., Sitch, S., Totterdell, I., Wiltshire, A., Woodward, S., 2011. Development and evaluation of an Earth-System model – HadGEM2. Geosci. Model Dev. 4, 1051–1075. doi:10.5194/gmd-4-1051-2011

Coplen, T.B., 1995. Reporting of stable carbon, hydrogen, and oxygen isotopic abundances, in: Reference and Intercomparison Materials for Stable Isotopes of Light Elements. Proceedings of a Consultants Meeting Held in Vienna, 1-3 December 1993. International Atomic Energy Agency.

Crawford, D.W., Purdie, D.A., 1997. Increase of pCO_2 during blooms of *Emiliania huxleyi*: Theoretical considerations on the asymmetry between acquisition of HCO_3^- and respiration of free CO_2. Limnol. Oceanogr. 42, 365–372. doi:10.4319/lo.1997.42.2.0365

Dai, M., Cao, Z., Guo, X., Zhai, W., Liu, Z., Yin, Z., Xu, Y., Gan, J., Hu, J., Du, C., 2013. Why are some marginal seas sources of atmospheric CO_2? Geophys. Res. Lett. 40, 2154–2158. doi:10.1002/grl.50390

Daniels, C.J., Sheward, R.M., Poulton, A.J., 2014. Biogeochemical implications of comparative growth rates of *Emiliania huxleyi* and *Coccolithus* species. Biogeosciences 11, 6915–6925. doi:10.5194/bg-11-6915-2014

Dickson, A.G., 1993. The measurement of sea water pH. Mar. Chem. 44, 131–142. doi:10.1016/0304-4203(93)90198-W

Dickson, A.G., 1992. The development of the alkalinity concept in marine chemistry. Mar. Chem. 40, 49–63. doi:10.1016/0304-4203(92)90047-E

Dickson, A.G., 1990a. Standard potential of the reaction: $AgCl_{(s)} + 0.5\ H_{2(g)} = Ag_{(s)} + HCl_{(aq)}$, and the standard acidity constant of the ion HSO_4^- in synthetic sea water from 273.15 to 318.15 K. J. Chem. Thermodyn. 22, 113–127. doi:10.1016/0021-9614(90)90074-Z

Dickson, A.G., 1990b. Thermodynamics of the dissociation of boric acid in synthetic seawater from 273.15 to 318.15 K. Deep-Sea Res. Pt A 37, 755–766. doi:10.1016/0198-0149(90)90004-F

Dickson, A.G., 1981. An exact definition of total alkalinity and a procedure for the estimation of alkalinity and total inorganic carbon from titration data. Deep-Sea Res. Pt A 28, 609–623. doi:10.1016/0198-0149(81)90121-7

Dickson, A.G., Afghan, J.D., Anderson, G.C., 2003. Reference materials for oceanic CO_2 analysis: a method for the certification of total alkalinity. Mar. Chem. 80, 185–197. doi:10.1016/S0304-4203(02)00133-0

Dickson, A.G., Millero, F.J., 1987. A comparison of the equilibrium constants for the dissociation of carbonic acid in seawater media. Deep-Sea Res. Pt A 34, 1733–1743. doi:10.1016/0198-0149(87)90021-5

Dickson, A.G., Riley, J.P., 1979. The estimation of acid dissociation constants in sea-water media from potentiometric titrations with strong base. II. The dissociation of phosphoric acid. Mar. Chem. 7, 101–109. doi:10.1016/0304-4203(79)90002-1

Dickson, A.G., Sabine, C.L., Christian, J.R., 2007. Guide to best practices for ocean CO_2 measurements. PICES Special Publication 3.

Doney, S.C., Fabry, V.J., Feely, R.A., Kleypas, J.A., 2009. Ocean Acidification: The Other CO_2 Problem. Annu. Rev. Marine Sci. 1, 169–192. doi:10.1146/annurev.marine.010908.163834

Dore, J.E., Lukas, R., Sadler, D.W., Church, M.J., Karl, D.M., 2009. Physical and biogeochemical modulation of ocean acidification in the central North Pacific. Proc. Natl. Acad. Sci. U.S.A. 106, 12235–12240. doi:10.1073/pnas.0906044106

Dunkley Jones, T., Lunt, D.J., Schmidt, D.N., Ridgwell, A., Sluijs, A., Valdes, P.J., Maslin, M., 2013. Climate model and proxy data constraints on ocean warming across the Paleocene–Eocene Thermal Maximum. Earth Sci. Rev. 125, 123–145. doi:10.1016/j.earscirev.2013.07.004

Dunne, J.P., Sarmiento, J.L., Gnanadesikan, A., 2007. A synthesis of global particle export from the surface ocean and cycling through the ocean interior and on the seafloor. Global Biogeochem. Cy. 21, GB4006. doi:10.1029/2006GB002907

Dyrssen, D., Sillén, L.G., 1967. Alkalinity and total carbonate in sea water. A plea for *p*-*T*-independent data. Tellus A 19, 113–121. doi:10.3402/tellusa.v19i1.9755

Eakins, B.W., Sharman, G.F., 2010. Volumes of the World's Oceans from ETOPO1. NOAA National Geophysical Data Center, Boulder, CO.

Egleston, E.S., Sabine, C.L., Morel, F.M.M., 2010. Revelle revisited: Buffer factors that quantify the response of ocean chemistry to changes in DIC and alkalinity. Global Biogeochem. Cy. 24, GB1002. doi:10.1029/2008GB003407

Ekstrom, J.A., Suatoni, L., Cooley, S.R., Pendleton, L.H., Waldbusser, G.G., Cinner, J.E., Ritter, J., Langdon, C., van Hooidonk, R., Gledhill, D., Wellman, K., Beck, M.W., Brander, L.M., Rittschof, D., Doherty, C., Edwards, P.E.T., Portela, R., 2015. Vulnerability and adaptation of US shellfisheries to ocean acidification. Nature Clim. Change 5, 207–214. doi:10.1038/nclimate2508

Falkowski, P., Scholes, R.J., Boyle, E., Canadell, J., Canfield, D., Elser, J., Gruber, N., Hibbard, K., Högberg, P., Linder, S., Mackenzie, F.T., Iii, B.M., Pedersen, T., Rosenthal, Y., Seitzinger, S., Smetacek, V., Steffen, W., 2000. The Global Carbon Cycle: A Test of Our Knowledge of Earth as a System. Science 290, 291–296. doi:10.1126/science.290.5490.291

Feely, R.A., Sabine, C.L., Lee, K., Berelson, W., Kleypas, J., Fabry, V.J., Millero, F.J., 2004. Impact of Anthropogenic CO_2 on the $CaCO_3$ System in the Oceans. Science 305, 362–366. doi:10.1126/science.1097329

Findlay, H.S., Calosi, P., Crawfurd, K.J., 2011. Determinants of the PIC:POC response in the coccolithophore *Emiliania huxleyi* under future ocean acidification scenarios. Limnol. Oceanogr. 56, 1168–1178. doi:10.4319/lo.2011.56.3.1168

Francey, R.J., Trudinger, C.M., van der Schoot, M., Law, R.M., Krummel, P.B., Langenfelds, R.L., Paul Steele, L., Allison, C.E., Stavert, A.R., Andres, R.J., Rödenbeck, C., 2013. Atmospheric verification of anthropogenic CO_2 emission trends. Nature Clim. Change 3, 520–524. doi:10.1038/nclimate1817

Frankignoulle, M., 1994. A complete set of buffer factors for acid/base CO_2 system in seawater. J. Marine Syst. 5, 111–118. doi:10.1016/0924-7963(94)90026-4

Frankignoulle, M., Canon, C., Gattuso, J.-P., 1994. Marine calcification as a source of carbon dioxide: Positive feedback of increasing atmospheric CO_2. Limnol. Oceanogr. 39, 458–462. doi:10.4319/lo.1994.39.2.0458

Franklin, D.J., Steinke, M., Young, J., Probert, I., Malin, G., 2010. Dimethylsulphoniopropionate (DMSP), DMSP-lyase activity (DLA) and dimethylsulphide (DMS) in 10 species of coccolithophore. Mar. Ecol. Prog. Ser. 410, 13–23. doi:10.3354/meps08596

Friis, K., Körtzinger, A., Pätsch, J., Wallace, D.W.R., 2005. On the temporal increase of anthropogenic CO_2 in the subpolar North Atlantic. Deep-Sea Res. Pt I 52, 681–698. doi:10.1016/j.dsr.2004.11.017

Fritsch, F., Carlson, R., 1980. Monotone Piecewise Cubic Interpolation. SIAM J. Numer. Anal. 17, 238–246. doi:10.1137/0717021

García, H.E., Gordon, L.I., 1992. Oxygen Solubility in Seawater: Better Fitting Equations. Limnol. Oceanogr. 37, 1307–1312.

Gaylord, B., Kroeker, K.J., Sunday, J.M., Anderson, K.M., Barry, J.P., Brown, N.E., Connell, S.D., Dupont, S., Fabricius, K.E., Hall-Spencer, J.M., Klinger, T., Milazzo, M., Munday, P.L., Russell, B.D., Sanford, E., Schreiber, S.J., Thiyagarajan, V., Vaughan, M.L.H., Widdicombe, S., Harley, C.D.G., 2015. Ocean acidification through the lens of ecological theory. Ecology 96, 3–15. doi:10.1890/14-0802.1

Geider, R., La Roche, J., 2002. Redfield revisited: variability of C:N:P in marine microalgae and its biochemical basis. Eur. J. Phycol. 37, 1–17. doi:10.1017/S0967026201003456

Gerecht, A.C., Šupraha, L., Edvardsen, B., Probert, I., Henderiks, J., 2014a. High temperature decreases the PIC / POC ratio and increases phosphorus requirements in *Coccolithus pelagicus* (Haptophyta). Biogeosciences 11, 3531–3545. doi:10.5194/bg-11-3531-2014

Gerecht, A.C., Šupraha, L., Edvardsen, B., Probert, I., Henderiks, J., 2014b. High temperature decreases the PIC / POC ratio and increases phosphorus requirements in *Coccolithus pelagicus* (Haptophyta). Biogeosciences Discuss. 11, 1021–1051. doi:10.5194/bgd-11-1021-2014

Gibbs, S.J., Bralower, T.J., Bown, P.R., Zachos, J.C., Bybell, L.M., 2006. Shelf and open-ocean calcareous phytoplankton assemblages across the Paleocene-Eocene Thermal Maximum: Implications for global productivity gradients. Geology 34, 233–236. doi:10.1130/G22381.1

Gibbs, S.J., Poulton, A.J., Bown, P.R., Daniels, C.J., Hopkins, J., Young, J.R., Jones, H.L., Thiemann, G.J., O'Dea, S.A., Newsam, C., 2013. Species-specific growth response of coccolithophores to Palaeocene-Eocene environmental change. Nature Geosci. 6, 218–222. doi:10.1038/ngeo1719

Goericke, R., Fry, B., 1994. Variations of marine plankton $\delta^{13}C$ with latitude, temperature, and dissolved CO_2 in the world ocean. Global Biogeochem. Cy. 8, 85–90. doi:10.1029/93GB03272

González-Dávila, M., Santana-Casiano, J.M., Rueda, M.J., Llinás, O., 2010. The water column distribution of carbonate system variables at the ESTOC site from 1995 to 2004. Biogeosciences 7, 3067–3081. doi:10.5194/bg-7-3067-2010

Goodkin, N.F., Levine, N.M., Doney, S.C., Wanninkhof, R., 2011. Impacts of temporal CO_2 and climate trends on the detection of ocean anthropogenic CO_2 accumulation. Global Biogeochem. Cy. 25, GB3023. doi:201110.1029/2010GB004009

Goyet, C., Poisson, A., 1989. New determination of carbonic acid dissociation constants in seawater as a function of temperature and salinity. Deep-Sea Res. Pt A 36, 1635–1654. doi:10.1016/0198-0149(89)90064-2

Gran, G., 1952. Determination of the Equivalence Point in Potentiometric Titrations. Part II. Analyst 77, 661–671. doi:10.1039/AN9527700661

Gregg, W.W., Rousseaux, C.S., 2014. Decadal trends in global pelagic ocean chlorophyll: A new assessment integrating multiple satellites, in situ data, and models. J. Geophys. Res. Oceans 119, 5921–5933. doi:10.1002/2014JC010158

Griffith, D.R., McNichol, A.P., Xu, L., McLaughlin, F.A., Macdonald, R.W., Brown, K.A., Eglinton, T.I., 2012. Carbon dynamics in the western Arctic Ocean: insights from full-depth carbon isotope profiles of DIC, DOC, and POC. Biogeosciences 9, 1217–1224. doi:10.5194/bg-9-1217-2012

Griffiths, C.R. (Ed.), 2012. RRS *Discovery* cruise D379, Southampton to Reykjavik, Extended Ellett Line. Scottish Association for Marine Science, Oban, UK pp. 184.

Griffiths, C.R., Holliday, N.P. (Eds.), 2013. RRS James Cook, Cruise JC086: Glasgow to Glasgow, Extended Ellett Line, 6th May 2013 > 26th May 2013. Scottish Association for Marine Science, Oban, UK.

Gruber, N., 2009. Carbon cycle: Fickle trends in the ocean. Nature 458, 155–156. doi:10.1038/458155a

Gruber, N., Keeling, C.D., Bacastow, R.B., Guenther, P.R., Lueker, T.J., Wahlen, M., Meijer, H.A.J., Mook, W.G., Stocker, T.F., 1999. Spatiotemporal patterns of carbon-13 in the global surface oceans and the oceanic Suess effect. Global Biogeochem. Cy. 13, 307–335. doi:199910.1029/1999GB900019

Gruber, N., Sarmiento, J.L., Stocker, T.F., 1996. An improved method for detecting anthropogenic CO_2 in the oceans. Global Biogeochem. Cy. 10, 809–837. doi:10.1029/96GB01608

Hall, T.M., Haine, T.W.N., Waugh, D.W., 2002. Inferring the concentration of anthropogenic carbon in the ocean from tracers. Global Biogeochem. Cy. 16, 1131. doi:10.1029/2001GB001835

Hansen, B., Østerhus, S., 2000. North Atlantic–Nordic Seas exchanges. Prog. Oceanogr. 45, 109–208. doi:10.1016/S0079-6611(99)00052-X

Hansson, I., Jagner, D., 1973. Evaluation of the accuracy of Gran plots by means of computer calculations: Application to the potentiometric titration of the total alkalinity and carbonate content in sea water. Anal. Chim. Acta 65, 363–373. doi:10.1016/S0003-2670(01)82503-4

Hartman, S., Esposito, M., Achterberg, E., 2014a. Discrete Carbon Dioxide Data Obtained During the R/V Discovery EEL_2011_D365 Cruise Along Extended Ellett Line. Carbon Dioxide Information Analysis Center, Oak Ridge National Laboratory, U.S. Department of Energy, Oak Ridge, TN, USA. doi:10.3334/CDIAC/OTG.CLIVAR_EEL_2011_D365

Hartman, S., Griffiths, A., Achterberg, E., 2014b. Discrete Carbon Dioxide Data Obtained During the R/V Discovery EEL_2012_D379 Cruise Along Extended Ellett Line. Carbon Dioxide Information Analysis Center, Oak Ridge National Laboratory, U.S. Department of Energy, Oak Ridge, TN, USA. doi:10.3334/CDIAC/OTG.CLIVAR_EEL_2012_D379

Hartman, S., Menzel, J.L., Achterberg, E., 2014c. Discrete Carbon Dioxide Data Obtained During the R/V James Cook EEL_2013_JC86 Cruise Along Extended Ellett Line. Carbon Dioxide Information Analysis Center, Oak Ridge National Laboratory, U.S. Department of Energy, Oak Ridge, TN, USA. doi:10.3334/CDIAC/OTG.CLIVAR_EEL_2013_JC86

Hátún, H., Payne, M.R., Beaugrand, G., Reid, P.C., Sandø, A.B., Drange, H., Hansen, B., Jacobsen, J.A., Bloch, D., 2009. Large bio-geographical shifts in the north-eastern Atlantic Ocean: From the subpolar gyre, via plankton, to blue whiting and pilot whales. Prog. Oceanogr. 80, 149–162. doi:10.1016/j.pocean.2009.03.001

Hátún, H., Sandø, A.B., Drange, H., Hansen, B., Valdimarsson, H., 2005. Influence of the Atlantic Subpolar Gyre on the Thermohaline Circulation. Science 309, 1841–1844. doi:10.1126/science.1114777

Heimann, M., Maier-Reimer, E., 1996. On the relations between the oceanic uptake of CO_2 and its carbon isotopes. Global Biogeochem. Cy. 10, 89–110. doi:199610.1029/95GB03191

Henson, S.A., Sanders, R., Madsen, E., 2012. Global patterns in efficiency of particulate organic carbon export and transfer to the deep ocean. Global Biogeochem. Cy. 26, GB1028. doi:10.1029/2011GB004099

Henson, S.A., Sarmiento, J.L., Dunne, J.P., Bopp, L., Lima, I., Doney, S.C., John, J., Beaulieu, C., 2010. Detection of anthropogenic climate change in satellite records of ocean chlorophyll and productivity. Biogeosciences 7, 621–640. doi:10.5194/bg-7-621-2010

Hernández-Ayón, J.M., Belli, S.L., Zirino, A., 1999. pH, alkalinity and total CO_2 in coastal seawater by potentiometric titration with a difference derivative readout. Anal. Chim. Acta 394, 101–108. doi:10.1016/S0003-2670(99)00207-X

Hernández-Ayón, J.M., Zirino, A., Dickson, A.G., Camiro-Vargas, T., Valenzuela, E., 2007. Estimating the contribution of organic bases from microalgae to the titration alkalinity in coastal seawaters. Limnol. Oceanogr. Methods 5, 225–232. doi:10.4319/lom.2007.5.225

Hester, K.C., Peltzer, E.T., Kirkwood, W.J., Brewer, P.G., 2008. Unanticipated consequences of ocean acidification: A noisier ocean at lower pH. Geophys. Res. Lett. 35, L19601. doi:10.1029/2008GL034913

Heuzé, C., Heywood, K.J., Stevens, D.P., Ridley, J.K., 2014. Changes in global ocean bottom properties and volume transports in CMIP5 models under climate change scenarios. J. Climate. doi:10.1175/JCLI-D-14-00381.1

Heuzé, C., Heywood, K.J., Stevens, D.P., Ridley, J.K., 2013. Southern Ocean bottom water characteristics in CMIP5 models. Geophys. Res. Lett. 40, 1409–1414. doi:10.1002/grl.50287

Hieronymus, M., Nycander, J., 2013. The budgets of heat and salinity in NEMO. Ocean Model. 67, 28–38. doi:10.1016/j.ocemod.2013.03.006

Holden, P.B., Edwards, N.R., Müller, S.A., Oliver, K.I.C., Death, R.M., Ridgwell, A., 2013. Controls on the spatial distribution of oceanic $\delta^{13}C_{DIC}$. Biogeosciences 10, 1815–1833. doi:10.5194/bg-10-1815-2013

Holliday, N.P., Cunningham, S., 2013. The Extended Ellett Line: Discoveries from 65 years of marine observations west of the UK. Oceanography 26, 156–163. doi:10.5670/oceanog.2013.17

Holligan, P.M., Fernández, E., Aiken, J., Balch, W.M., Boyd, P., Burkill, P.H., Finch, M., Groom, S.B., Malin, G., Muller, K., Purdie, D.A., Robinson, C., Trees, C.C., Turner, S.M., van der Wal, P., 1993. A biogeochemical study of the coccolithophore, *Emiliania huxleyi*, in the North Atlantic. Global Biogeochem. Cy. 7, 879–900. doi:10.1029/93GB01731

Honjo, S., Manganini, S.J., Krishfield, R.A., Francois, R., 2008. Particulate organic carbon fluxes to the ocean interior and factors controlling the biological pump: A synthesis of global sediment trap programs since 1983. Prog. Oceanogr. 76, 217–285. doi:10.1016/j.pocean.2007.11.003

Ho, T.-Y., Quigg, A., Finkel, Z.V., Milligan, A.J., Wyman, K., Falkowski, P.G., Morel, F.M.M., 2003. The Elemental Composition of Some Marine Phytoplankton. J. Phycol. 39, 1145–1159. doi:10.1111/j.0022-3646.2003.03-090.x

Hughes, S.L., Holliday, N.P., Gaillard, F., 2012. Variability in the ICES/NAFO region between 1950 and 2009: observations from the ICES Report on Ocean Climate. ICES J. Mar. Sci. 69, 706–719. doi:10.1093/icesjms/fss044

Humphreys, M.P., Achterberg, E.P., Griffiths, A.M., McDonald, A., Boyce, A.J., 2015. Measurements of the stable isotope composition of dissolved inorganic carbon in the Northeastern Atlantic and Nordic Seas during summer 2012. Earth Syst. Sci. Data Discuss. 8, 57–82. doi:10.5194/essdd-8-57-2015

Humphreys, M.P., Achterberg, E.P., Griffiths, A.M., McDonald, A., Boyce, A.J., 2014a. UKOA measurements of the stable isotope composition of dissolved inorganic carbon in the Northeastern Atlantic and Nordic Seas during summer 2012. British Oceanographic Data Centre, Natural Environment Research Council, UK. doi:10/xpj

Humphreys, M.P., Achterberg, E.P., Griffiths, A.M., McDonald, A., Boyce, A.J., 2014b. Ellett Line measurements of stable isotope composition of dissolved inorganic carbon in the Northeastern Atlantic and Nordic Seas during summer 2012. British Oceanographic Data Centre, Natural Environment Research Council, UK. doi:10/xph

Hurrell, J.W., Kushnir, Y., Ottersen, G., Visbeck, M., 2003. An Overview of the North Atlantic Oscillation, in: The North Atlantic Oscillation: Climatic Significance and Environmental Impact. American Geophysical Union, pp. 1–35.

Iglesias-Rodriguez, M.D., Halloran, P.R., Rickaby, R.E.M., Hall, I.R., Colmenero-Hidalgo, E., Gittins, J.R., Green, D.R.H., Tyrrell, T., Gibbs, S.J., Dassow, P. von, Rehm, E., Armbrust, E.V., Boessenkool, K.P., 2008. Phytoplankton Calcification in a High-CO_2 World. Science 320, 336–340. doi:10.1126/science.1154122

Ilyina, T., Zeebe, R.E., Brewer, P.G., 2010. Future ocean increasingly transparent to low-frequency sound owing to carbon dioxide emissions. Nature Geosci. 3, 18–22. doi:10.1038/ngeo719

IPCC, 2013. Climate Change 2013: The Physical Science Basis. Contribution of Working Group I to the Fifth Assessment Report of the Intergovernmental Panel on Climate Change. Cambridge University Press, Cambridge, UK and New York, NY, USA. doi:10.1017/CBO9781107415324

Isada, T., Kuwata, A., Saito, H., Ono, T., Ishii, M., Yoshikawa-Inoue, H., Suzuki, K., 2009. Photosynthetic features and primary productivity of phytoplankton in the Oyashio and Kuroshio–Oyashio transition regions of the northwest Pacific. J. Plankton Res. 31, 1009–1025. doi:10.1093/plankt/fbp050

Jin, P., Gao, K., Beardall, J., 2013. Evolutionary Responses of a Coccolithophorid *Gephyrocapsa Oceanica* to Ocean Acidification. Evolution 67, 1869–1878. doi:10.1111/evo.12112

Johansson, O., Wedborg, M., 1982. On the evaluation of potentiometric titrations of seawater with hydrochloric acid. Oceanol. Acta 5, 209–218.

Johnson, C., Inall, M., Häkkinen, S., 2013. Declining nutrient concentrations in the northeast Atlantic as a result of a weakening Subpolar Gyre. Deep-Sea Res. Pt I 82, 95–107. doi:10.1016/j.dsr.2013.08.007

Johnson, K.M., King, A.E., Sieburth, J.M., 1985. Coulometric TCO_2 analyses for marine studies; an introduction. Mar. Chem. 16, 61–82. doi:10.1016/0304-4203(85)90028-3

Keeling, C.D., 1979. The Suess effect: ^{13}Carbon-^{14}Carbon interrelations. Environ. Int. 2, 229–300. doi:10.1016/0160-4120(79)90005-9

Kester, D.R., Duedall, I.W., Connors, D.N., Pytkowicz, R.M., 1967. Preparation of artificial seawater. Limnol. Oceanogr. 12, 176–179. doi:10.4319/lo.1967.12.1.0176

Key, R.M., Kozyr, A., Sabine, C.L., Lee, K., Wanninkhof, R., Bullister, J.L., Feely, R.A., Millero, F.J., Mordy, C., Peng, T.-H., 2004. A global ocean carbon climatology: Results from Global Data Analysis Project (GLODAP). Global Biogeochem. Cy. 18, GB4031. doi:10.1029/2004GB002247

Key, R.M., Tanhua, T., Olsen, A., Hoppema, M., Jutterström, S., Schirnick, C., van Heuven, S., Kozyr, A., Lin, X., Velo, A., Wallace, D.W.R., Mintrop, L., 2010. The CARINA data synthesis project: introduction and overview. Earth Syst. Sci. Data 2, 105–121. doi:10.5194/essd-2-105-2010

Khatiwala, S., Primeau, F., Hall, T., 2009. Reconstruction of the history of anthropogenic CO_2 concentrations in the ocean. Nature 462, 346–349. doi:10.1038/nature08526

Kieke, D., Rhein, M., Stramma, L., Smethie, W.M., Bullister, J.L., LeBel, D.A., 2007. Changes in the pool of Labrador Sea Water in the subpolar North Atlantic. Geophys. Res. Lett. 34, L06605. doi:10.1029/2006GL028959

Kim, H.-C., Lee, K., 2009. Significant contribution of dissolved organic matter to seawater alkalinity. Geophys. Res. Lett. 36, L20603. doi:10.1029/2009GL040271

Köhler, P., Abrams, J.F., Völker, C., Hauck, J., Wolf-Gladrow, D.A., 2013. Geoengineering impact of open ocean dissolution of olivine on atmospheric CO_2, surface ocean pH and marine biology. Environ. Res. Lett. 8, 014009. doi:10.1088/1748-9326/8/1/014009

Köhler, P., Hartmann, J., Wolf-Gladrow, D.A., 2010. Geoengineering potential of artificially enhanced silicate weathering of olivine. Proc. Natl. Acad. Sci. U.S.A. 107, 20228–20233. doi:10.1073/pnas.1000545107

Körtzinger, A., Quay, P.D., Sonnerup, R.E., 2003. Relationship between anthropogenic CO_2 and the ^{13}C Suess effect in the North Atlantic Ocean. Global Biogeochem. Cy. 17, 5–1–5–20. doi:10.1029/2001GB001427

Körtzinger, A., Send, U., Lampitt, R.S., Hartman, S., Wallace, D.W.R., Karstensen, J., Villagarcia, M.G., Llinás, O., DeGrandpre, M.D., 2008. The seasonal pCO_2 cycle at 49°N/16.5°W in the northeastern Atlantic Ocean and what it tells us about biological productivity. J. Geophys. Res. 113, C04020. doi:10.1029/2007JC004347

Langer, G., Geisen, M., Baumann, K.-H., Kläs, J., Riebesell, U., Thoms, S., Young, J.R., 2006. Species-specific responses of calcifying algae to changing seawater carbonate chemistry. Geochem. Geophys. Geosyst. 7, Q09006. doi:10.1029/2005GC001227

Langer, G., Oetjen, K., Brenneis, T., 2013. Coccolithophores do not increase particulate carbon production under nutrient limitation: A case study using Emiliania huxleyi (PML B92/11). J. Exp. Mar. Biol. Ecol. 443, 155–161. doi:10.1016/j.jembe.2013.02.040

Langer, G., Oetjen, K., Brenneis, T., 2012. Calcification of Calcidiscus leptoporus under nitrogen and phosphorus limitation. J. Exp. Mar. Biol. Ecol. 413, 131–137. doi:10.1016/j.jembe.2011.11.028

Laruelle, G.G., Lauerwald, R., Pfeil, B., Regnier, P., 2014. Regionalized global budget of the CO_2 exchange at the air-water interface in continental shelf seas. Global Biogeochem. Cy. 28, 2014GB004832. doi:10.1002/2014GB004832

Leakey, R.J.G. (Ed.), 2012. UK Ocean Acidification Research Programme Arctic Cruise Report. Scottish Association for Marine Science, Oban, UK pp. 310.

Le Bris, N., Birot, D., 1997. Automated pH-ISFET measurements under hydrostatic pressure for marine monitoring application. Anal. Chim. Acta 356, 205–215. doi:10.1016/S0003-2670(97)00533-3

Leduc, A.O.H.C., Munday, P.L., Brown, G.E., Ferrari, M.C.O., 2013. Effects of acidification on olfactory-mediated behaviour in freshwater and marine ecosystems: a synthesis. Philos. Trans. R. Soc. Lond. B Biol. Sci. 368, 20120447. doi:10.1098/rstb.2012.0447

Lee, K., Kim, T.-W., Byrne, R.H., Millero, F.J., Feely, R.A., Liu, Y.-M., 2010. The universal ratio of boron to chlorinity for the North Pacific and North Atlantic oceans. Geochim. Cosmochim. Acta 74, 1801–1811. doi:10.1016/j.gca.2009.12.027

Lee, K., Tong, L.T., Millero, F.J., Sabine, C.L., Dickson, A.G., Goyet, C., Park, G.-H., Wanninkhof, R., Feely, R.A., Key, R.M., 2006. Global relationships of total alkalinity with salinity and temperature in surface waters of the world's oceans. Geophys. Res. Lett. 33, L19605. doi:10.1029/2006GL027207

Le Quéré, C., Raupach, M.R., Canadell, J.G., Marland, G., Bopp, L., Ciais, P., Conway, T.J., Doney, S.C., Feely, R.A., Foster, P., Friedlingstein, P., Gurney, K., Houghton, R.A., House, J.I., Huntingford, C., Levy, P.E., Lomas, M.R., Majkut, J., Metzl, N., Ometto, J.P., Peters, G.P., Prentice, I.C., Randerson, J.T., Running, S.W., Sarmiento, J.L., Schuster, U., Sitch, S., Takahashi, T., Viovy, N., van der Werf, G.R., Woodward, F.I., 2009. Trends in the sources and sinks of carbon dioxide. Nature Geosci. 2, 831–836. doi:10.1038/ngeo689

Le Quéré, C., Takahashi, T., Buitenhuis, E.T., Rödenbeck, C., Sutherland, S.C., 2010. Impact of climate change and variability on the global oceanic sink of CO_2. Global Biogeochem. Cy. 24, GB4007. doi:10.1029/2009GB003599

Lohbeck, K.T., Riebesell, U., Reusch, T.B.H., 2012. Adaptive evolution of a key phytoplankton species to ocean acidification. Nature Geosci. 5, 346–351. doi:10.1038/ngeo1441

Lohmann, K., Drange, H., Bentsen, M., 2008. Response of the North Atlantic subpolar gyre to persistent North Atlantic oscillation like forcing. Clim. Dyn. 32, 273–285. doi:10.1007/s00382-008-0467-6

Lueker, T.J., Dickson, A.G., Keeling, C.D., 2000. Ocean pCO_2 calculated from dissolved inorganic carbon, alkalinity, and equations for K_1 and K_2: validation based on laboratory measurements of CO_2 in gas and seawater at equilibrium. Mar. Chem. 70, 105–119. doi:10.1016/S0304-4203(00)00022-0

Lynch-Stieglitz, J., Stocker, T.F., Broecker, W.S., Fairbanks, R.G., 1995. The influence of air-sea exchange on the isotopic composition of oceanic carbon: Observations and modeling. Global Biogeochem. Cy. 9, 653–666. doi:10.1029/95GB02574

Madec, G., 2008. NEMO reference manual, ocean dynamic component: NEMO–OPA. Note du Pôle de modélisation, Institut Pierre Simon Laplace, France, Technical Report 27.

Manning, A.C., Keeling, R.F., 2006. Global oceanic and land biotic carbon sinks from the Scripps atmospheric oxygen flask sampling network. Tellus B 58, 95–116. doi:10.1111/j.1600-0889.2006.00175.x

Marcet, A., 1822. Some Experiments and Researches on the Saline Contents of Sea-Water, Undertaken with a View to Correct and Improve Its Chemical Analysis. Phil. Trans. R. Soc. Lond. 112, 448–456. doi:10.1098/rstl.1822.0034

MARGO Project Members, 2009. Constraints on the magnitude and patterns of ocean cooling at the Last Glacial Maximum. Nature Geosci. 2, 127–132. doi:10.1038/ngeo411

Marion, G.M., Millero, F.J., Camões, M.F., Spitzer, P., Feistel, R., Chen, C.-T.A., 2011. pH of seawater. Mar. Chem. 126, 89–96. doi:10.1016/j.marchem.2011.04.002

Martin, P., van der Loeff, M.R., Cassar, N., Vandromme, P., d' Ovidio, F., Stemmann, L., Rengarajan, R., Soares, M., González, H.E., Ebersbach, F., Lampitt, R.S., Sanders, R., Barnett, B.A., Smetacek, V., Naqvi, S.W.A., 2013. Iron fertilization enhanced net community production but not downward particle flux during the Southern Ocean iron fertilization experiment LOHAFEX. Global Biogeochem. Cy. 27, 871–881. doi:10.1002/gbc.20077

Martz, T.R., Carr, J.J., French, C.R., DeGrandpre, M.D., 2003. A Submersible Autonomous Sensor for Spectrophotometric pH Measurements of Natural Waters. Anal. Chem. 75, 1844–1850. doi:10.1021/ac020568l

Martz, T.R., Connery, J.G., Johnson, K.S., 2010. Testing the Honeywell Durafet® for seawater pH applications. Limnol. Oceanogr. Methods 8, 172–184. doi:10.4319/lom.2010.8.172

Martz, T.R., Jannasch, H.W., Johnson, K.S., 2009. Determination of carbonate ion concentration and inner sphere carbonate ion pairs in seawater by ultraviolet spectrophotometric titration. Mar. Chem. 115, 145–154. doi:10.1016/j.marchem.2009.07.002

Matrai, P.A., Keller, M.D., 1994. Total organic sulfur and dimethylsulfoniopropionate in marine phytoplankton: intracellular variations. Mar. Biol. 119, 61–68. doi:10.1007/BF00350107

Matsumoto, K., Gruber, N., 2005. How accurate is the estimation of anthropogenic carbon in the ocean? An evaluation of the ΔC* method. Global Biogeochem. Cy. 19, GB3014. doi:200510.1029/2004GB002397

McDougall, T.J., Barker, P.M., 2011. Getting started with TEOS-10 and the Gibbs Seawater (GSW) Oceanographic Toolbox. SCOR/IAPSO WG127.

McGrath, T., Kivimäe, C., Tanhua, T., Cave, R.R., McGovern, E., 2012a. Inorganic carbon and pH levels in the Rockall Trough 1991–2010. Deep-Sea Res. Pt I 68, 79–91. doi:10.1016/j.dsr.2012.05.011

McGrath, T., Nolan, G., McGovern, E., 2012b. Chemical characteristics of water masses in the Rockall Trough. Deep-Sea Res. Pt I 61, 57–73. doi:10.1016/j.dsr.2011.11.007

McNeil, B.I., Matear, R.J., Tilbrook, B., 2001a. Does carbon 13 track anthropogenic CO_2 in the Southern Ocean? Global Biogeochem. Cy. 15, 597–613. doi:10.1029/2000GB001352

McNeil, B.I., Tilbrook, B., Matear, R.J., 2001b. Accumulation and uptake of anthropogenic CO_2 in the Southern Ocean, south of Australia between 1968 and 1996. J. Geophys. Res. 106, 31431–31,445. doi:10.1029/2000JC000331

McNichol, A., Quay, P.D., Gagnon, A.R., Burton, J.R., 2010. Collection and measurement of carbon isotopes in seawater DIC, in: The GO-SHIP Repeat Hydrography Manual: A Collection of Expert Reports and Guidelines. IOCCP Report No. 14, ICPO Publication Series No. 134, Version 1.

Mehrbach, C., Culberson, C.H., Hawley, J.E., Pytkowicz, R.M., 1973. Measurement of the Apparent Dissociation Constants of Carbonic Acid in Seawater at Atmospheric Pressure. Limnol. Oceanogr. 18, 897–907. doi:10.4319/lo.1973.18.6.0897

Menden-Deuer, S., Lessard, E.J., 2000. Carbon to volume relationships for dinoflagellates, diatoms, and other protist plankton. Limnol. Oceanogr. 45, 569–579. doi:10.4319/lo.2000.45.3.0569

Millero, F.J., 2007. The Marine Inorganic Carbon Cycle. Chem. Rev. 107, 308–341. doi:10.1021/cr0503557

Millero, F.J., 1995. Thermodynamics of the carbon dioxide system in the oceans. Geochim. Cosmochim. Acta 59, 661–677. doi:10.1016/0016-7037(94)00354-O

Millero, F.J., Pierrot, D., 1998. A Chemical Equilibrium Model for Natural Waters. Aquat. Geochem. 4, 153–199. doi:10.1023/A:1009656023546

Millero, F.J., Poisson, A., 1981. International one-atmosphere equation of state of seawater. Deep-Sea Res. Pt A 28, 625–629. doi:10.1016/0198-0149(81)90122-9

Mintrop, L., Pérez, F.F., González-Dávila, M., Santana-Casiano, J.M., Körtzinger, A., 2000. Alkalinity determination by potentiometry: intercalibration using three different methods. Cienc. Mar. 26, 23–27. doi:10.7773/cm.v26i1.573

Monnin, E., Indermühle, A., Dällenbach, A., Flückiger, J., Stauffer, B., Stocker, T.F., Raynaud, D., Barnola, J.-M., 2001. Atmospheric CO_2 Concentrations over the Last Glacial Termination. Science 291, 112–114. doi:10.1126/science.291.5501.112

Moolna, A., Rickaby, R.E.M., 2012. Interaction of the coccolithophore *Gephyrocapsa oceanica* with its carbon environment: response to a recreated high-CO_2 geological past. Geobiology 10, 72–81. doi:10.1111/j.1472-4669.2011.00308.x

Morris, A.W., Riley, J.P., 1966. The bromide/chlorinity and sulphate/chlorinity ratio in sea water. Deep-Sea Res. 13, 699–705. doi:10.1016/0011-7471(66)90601-2

Morse, J.W., Arvidson, R.S., Lüttge, A., 2007. Calcium Carbonate Formation and Dissolution. Chem. Rev. 107, 342–381. doi:10.1021/cr050358j

Muller, F.L.L., Bleie, B., 2008. Estimating the organic acid contribution to coastal seawater alkalinity by potentiometric titrations in a closed cell. Anal. Chim. Acta 619, 183–191. doi:10.1016/j.aca.2008.05.018

Munday, P.L., Cheal, A.J., Dixson, D.L., Rummer, J.L., Fabricius, K.E., 2014. Behavioural impairment in reef fishes caused by ocean acidification at CO_2 seeps. Nature Clim. Change 4, 487–492. doi:10.1038/nclimate2195

Olafsson, J., Olafsdottir, S.R., Benoit-Cattin, A., Danielsen, M., Arnarson, T.S., Takahashi, T., 2009. Rate of Iceland Sea acidification from time series measurements. Biogeosciences 6, 2661–2668. doi:10.5194/bg-6-2661-2009

Olsen, A., Brown, K.R., Chierici, M., Johannessen, T., Neill, C., 2008. Sea-surface CO_2 fugacity in the subpolar North Atlantic. Biogeosciences 5, 535–547. doi:10.5194/bg-5-535-2008

Olsen, A., Ninnemann, U., 2010. Large $\delta^{13}C$ Gradients in the Preindustrial North Atlantic Revealed. Science 330, 658–659. doi:10.1126/science.1193769

Olsen, A., Omar, A.M., Bellerby, R.G.J., Johannessen, T., Ninnemann, U., Brown, K.R., Olsson, K.A., Olafsson, J., Nondal, G., Kivimäe, C., Kringstad, S., Neill, C., Olafsdottir, S., 2006. Magnitude and origin of the anthropogenic CO_2 increase and ^{13}C Suess effect in the Nordic seas since 1981. Global Biogeochem. Cy. 20, GB3027. doi:10.1029/2005GB002669

Ono, T., Saino, T., Kurita, N., Sasaki, K., 2004. Basin-scale extrapolation of shipboard pCO_2 data by using satellite SST and Chl*a*. Int. J. Remote Sens. 25, 3803–3815. doi:10.1080/01431160310001657515

O'Sullivan, D.W., Millero, F.J., 1998. Continual measurement of the total inorganic carbon in surface seawater. Mar. Chem. 60, 75–83. doi:10.1016/S0304-4203(97)00079-0

Painter, S.C., Poulton, A.J., Allen, J.T., Pidcock, R., Balch, W.M., 2010. The COPAS'08 expedition to the Patagonian Shelf: Physical and environmental conditions during the 2008 coccolithophore bloom. Cont. Shelf Res. 30, 1907–1923. doi:10.1016/j.csr.2010.08.013

Perez, F.F., Fraga, F., 1987. Association constant of fluoride and hydrogen ions in seawater. Mar. Chem. 21, 161–168. doi:10.1016/0304-4203(87)90036-3

Pérez, F.F., Vázquez-Rodríguez, M., Mercier, H., Velo, A., Lherminier, P., Ríos, A.F., 2010. Trends of anthropogenic CO_2 storage in North Atlantic water masses. Biogeosciences 7, 1789–1807. doi:10.5194/bg-7-1789-2010

Pfeil, B., Olsen, A., Bakker, D.C.E., Hankin, S., Koyuk, H., Kozyr, A., Malczyk, J., Manke, A., Metzl, N., Sabine, C.L., Akl, J., Alin, S.R., Bates, N., Bellerby, R.G.J., Borges, A., Boutin, J., Brown, P.J., Cai, W.-J., Chavez, F.P., Chen, A., Cosca, C., Fassbender, A.J., Feely, R.A., González-Dávila, M., Goyet, C., Hales, B., Hardman-Mountford, N., Heinze, C., Hood, M., Hoppema, M., Hunt, C.W., Hydes, D., Ishii, M., Johannessen, T., Jones, S.D., Key, R.M., Körtzinger, A., Landschützer, P., Lauvset, S.K., Lefèvre, N., Lenton, A., Lourantou, A., Merlivat, L., Midorikawa, T., Mintrop, L., Miyazaki, C., Murata, A., Nakadate, A., Nakano, Y., Nakaoka, S., Nojiri, Y., Omar, A.M., Padin, X.A., Park, G.-H., Paterson, K., Perez, F.F., Pierrot, D., Poisson, A., Ríos, A.F., Santana-Casiano, J.M., Salisbury, J., Sarma, V.V.S.S., Schlitzer, R., Schneider, B., Schuster, U., Sieger, R., Skjelvan, I., Steinhoff, T., Suzuki, T., Takahashi, T., Tedesco, K., Telszewski, M., Thomas, H., Tilbrook, B., Tjiputra, J., Vandemark, D., Veness, T., Wanninkhof, R., Watson, A.J., Weiss, R., Wong, C.S., Yoshikawa-Inoue, H., 2013. A uniform, quality controlled Surface Ocean CO_2 Atlas (SOCAT). Earth Syst. Sci. Data 5, 125–143. doi:10.5194/essd-5-125-2013

Poulton, A.J., Adey, T.R., Balch, W.M., Holligan, P.M., 2007. Relating coccolithophore calcification rates to phytoplankton community dynamics: Regional differences and implications for carbon export. Deep-Sea Res. Pt II 54, 538–557. doi:10.1016/j.dsr2.2006.12.003

Poulton, A.J., Painter, S.C., Young, J.R., Bates, N.R., Bowler, B., Drapeau, D., Lyczsckowski, E., Balch, W.M., 2013. The 2008 Emiliania huxleyi bloom along the Patagonian Shelf: Ecology, biogeochemistry, and cellular calcification. Global Biogeochem. Cy. 27, 2013GB004641. doi:10.1002/2013GB004641

Quay, P.D., Sonnerup, R., Stutsman, J., Maurer, J., Körtzinger, A., Padin, X.A., Robinson, C., 2007. Anthropogenic CO_2 accumulation rates in the North Atlantic Ocean from changes in the $^{13}C/^{12}C$ of dissolved inorganic carbon. Global Biogeochem. Cy. 21, GB1009. doi:10.1029/2006GB002761

Quay, P.D., Tilbrook, B., Wong, C.S., 1992. Oceanic Uptake of Fossil Fuel CO_2: Carbon-13 Evidence. Science 256, 74 –79. doi:10.1126/science.256.5053.74

Quay, P., Sonnerup, R., Westby, T., Stutsman, J., McNichol, A., 2003. Changes in the $^{13}C/^{12}C$ of dissolved inorganic carbon in the ocean as a tracer of anthropogenic CO_2 uptake. Global Biogeochem. Cy. 17, 1004. doi:10.1029/2001GB001817

Raupach, M.R., Quéré, C.L., Peters, G.P., Canadell, J.G., 2013. Anthropogenic CO_2 emissions. Nature Clim. Change 3, 603–604. doi:10.1038/nclimate1910

Raven, J., Caldeira, K., Elderfield, H., Hoegh-Guldberg, O., Liss, P., Riebesell, U., Turley, C., Watson, A., 2005. Ocean acidification due to increasing atmospheric carbon dioxide. Policy Document 12/05, Royal Society, London, UK.

Read, J.F. (Ed.), 2011. RRS *Discovery* Cruise 365: 11 May-02 Jun 2011, The Extended Ellett Line 2011. National Oceanography Centre, Southampton, UK.

Read, J.F. (Ed.), 2010. RRS *Discovery* Cruise 351: 10-28 May 2010, The Extended Ellett Line 2010. National Oceanography Centre, Southampton, UK.

Redfield, A.C., Ketchum, B.H., Richards, F.A., 1963. The influence of organisms on the composition of sea-water, in: The Sea. Interscience, New York, pp. 26–77.

Rérolle, V.M.C., Floquet, C.F.A., Harris, A.J.K., Mowlem, M.C., Bellerby, R.R.G.J., Achterberg, E.P., 2013. Development of a colorimetric microfluidic pH sensor for autonomous seawater measurements. Anal. Chim. Acta 786, 124–131. doi:10.1016/j.aca.2013.05.008

Rérolle, V.M.C., Floquet, C.F.A., Mowlem, M.C., Connelly, D.P., Achterberg, E.P., Bellerby, R.R.G.J., 2012. Seawater-pH measurements for ocean-acidification observations. Trends Anal. Chem. 40, 146–157. doi:10.1016/j.trac.2012.07.016

Reverdin, G., 2010. North Atlantic Subpolar Gyre Surface Variability (1895–2009). J. Climate 23, 4571–4584. doi:10.1175/2010JCLI3493.1

Riahi, K., Rao, S., Krey, V., Cho, C., Chirkov, V., Fischer, G., Kindermann, G., Nakicenovic, N., Rafaj, P., 2011. RCP 8.5—A scenario of comparatively high greenhouse gas emissions. Clim. Chang. 109, 33–57. doi:10.1007/s10584-011-0149-y

Ribas-Ribas, M., Rérolle, V.M.C., Bakker, D.C.E., Kitidis, V., Lee, G.A., Brown, I., Achterberg, E.P., Hardman-Mountford, N.J., Tyrrell, T., 2014. Intercomparison of carbonate chemistry measurements on a cruise in northwestern European shelf seas. Biogeosciences 11, 4339–4355. doi:10.5194/bg-11-4339-2014

Riebesell, U., Zondervan, I., Rost, B., Tortell, P.D., Zeebe, R.E., Morel, F.M.M., 2000. Reduced calcification of marine plankton in response to increased atmospheric CO_2. Nature 407, 364–367. doi:10.1038/35030078

Riley, J.P., 1965. The occurrence of anomalously high fluoride concentrations in the North Atlantic. Deep-Sea Res. 12, 219–220. doi:10.1016/0011-7471(65)90027-6

Robertson, J.E., Robinson, C., Turner, D.R., Holligan, P., Watson, A.J., Boyd, P., Fernandez, E., Finch, M., 1994. The impact of a coccolithophore bloom on oceanic carbon uptake in the northeast Atlantic during summer 1991. Deep-Sea Res. Pt I 41, 297–314. doi:10.1016/0967-0637(94)90005-1

Sabine, C.L., Feely, R.A., 2001. Comparison of recent Indian Ocean anthropogenic CO_2 estimates with a historical approach. Global Biogeochem. Cy. 15, 31–42.

Sabine, C.L., Feely, R.A., Gruber, N., Key, R.M., Lee, K., Bullister, J.L., Wanninkhof, R., Wong, C.S., Wallace, D.W.R., Tilbrook, B., Millero, F.J., Peng, T.-H., Kozyr, A., Ono, T., Rios, A.F., 2004. The Oceanic Sink for Anthropogenic CO_2. Science 305, 367–371. doi:10.1126/science.1097403

Sabine, C.L., Tanhua, T., 2010. Estimation of Anthropogenic CO_2 Inventories in the Ocean. Annu. Rev. Marine Sci. 2, 175–198. doi:10.1146/annurev-marine-120308-080947

Saito, H., Tamura, N., Kitano, H., Mito, A., Takahashi, C., Suzuki, A., Kayanne, H., 1995. A compact seawater pCO_2 measurement system with membrane equilibrator and nondispersive infrared gas analyzer. Deep-Sea Res. Pt I 42, 2025–2033. doi:10.1016/0967-0637(95)00090-9

Sanders, R., Morris, P.J., Poulton, A.J., Stinchcombe, M.C., Charalampopoulou, A., Lucas, M.I., Thomalla, S.J., 2010. Does a ballast effect occur in the surface ocean? Geophys. Res. Lett. 37, L08602. doi:10.1029/2010GL042574

Schlüter, L., Lohbeck, K.T., Gutowska, M.A., Gröger, J.P., Riebesell, U., Reusch, T.B.H., 2014. Adaptation of a globally important coccolithophore to ocean warming and acidification. Nature Clim. Change 4, 1024–1030. doi:10.1038/nclimate2379

Schmittner, A., Gruber, N., Mix, A.C., Key, R.M., Tagliabue, A., Westberry, T.K., 2013. Biology and air–sea gas exchange controls on the distribution of carbon isotope ratios ($\delta^{13}C$) in the ocean. Biogeosciences 10, 5793–5816. doi:10.5194/bg-10-5793-2013

Schröder, C.R., Weidgans, B.M., Klimant, I., 2005. pH Fluorosensors for use in marine systems. Analyst 130, 907–916. doi:10.1039/B501306B

Sett, S., Bach, L.T., Schulz, K.G., Koch-Klavsen, S., Lebrato, M., Riebesell, U., 2014. Temperature Modulates Coccolithophorid Sensitivity of Growth, Photosynthesis and Calcification to Increasing Seawater pCO_2. PLoS ONE 9, e88308. doi:10.1371/journal.pone.0088308

Sherwin, T. (Ed.), 2009. RRS Discovery, Cruise D340a: Reykjavik to Dunstaffnage via Rockall and the Wyville Thomson Ridge, 10 June to 25 June 2009. Scottish Association for Marine Science, Oban, UK.

Shi, D., Xu, Y., Hopkinson, B.M., Morel, F.M.M., 2010. Effect of Ocean Acidification on Iron Availability to Marine Phytoplankton. Science 327, 676–679. doi:10.1126/science.1183517

Shiller, A.M., 1981. Calculating the Oceanic CO_2 Increase: A Need for Caution. J. Geophys. Res. 86. doi:198110.1029/JC086iC11p11083

Shutler, J.D., Land, P.E., Brown, C.W., Findlay, H.S., Donlon, C.J., Medland, M., Snooke, R., Blackford, J.C., 2013. Coccolithophore surface distributions in the North Atlantic and their modulation of the air-sea flux of CO_2 from 10 years of satellite Earth observation data. Biogeosciences 10, 2699–2709. doi:10.5194/bg-10-2699-2013

Simpson, S.D., Munday, P.L., Wittenrich, M.L., Manassa, R., Dixson, D.L., Gagliano, M., Yan, H.Y., 2011. Ocean acidification erodes crucial auditory behaviour in a marine fish. Biol. Lett. rsbl20110293. doi:10.1098/rsbl.2011.0293

Smetacek, V., Klaas, C., Strass, V.H., Assmy, P., Montresor, M., Cisewski, B., Savoye, N., Webb, A., d' Ovidio, F., Arrieta, J.M., Bathmann, U., Bellerby, R., Berg, G.M., Croot, P., Gonzalez, S., Henjes, J., Herndl, G.J., Hoffmann, L.J., Leach, H., Losch, M., Mills, M.M., Neill, C., Peeken, I., Röttgers, R., Sachs, O., Sauter, E., Schmidt, M.M., Schwarz, J., Terbrüggen, A., Wolf-Gladrow, D., 2012. Deep carbon export from a Southern Ocean iron-fertilized diatom bloom. Nature 487, 313–319. doi:10.1038/nature11229

Smith, S.V., 2013. Parsing the Oceanic Calcium Carbonate Cycle: A Net Atmospheric Carbon Dioxide Source, or a Sink? Limnol. Oceanogr. e-Books pp. 42. doi:10:4319/svsmith.2013.978-0-9845591-2-1

Sonnerup, R.E., McNichol, A.P., Quay, P.D., Gammon, R.H., Bullister, J.L., Sabine, C.L., Slater, R.D., 2007. Anthropogenic $\delta^{13}C$ changes in the North Pacific Ocean reconstructed using a multiparameter mixing approach (MIX). Tellus B 59, 303–317. doi:10.1111/j.1600-0889.2007.00250.x

Sonnerup, R.E., Quay, P.D., 2012. ^{13}C constraints on ocean carbon cycle models. Global Biogeochem. Cy. 26, GB2014. doi:10.1029/2010GB003980

Sonnerup, R.E., Quay, P.D., McNichol, A.P., Bullister, J.L., Westby, T.A., Anderson, H.L., 1999. Reconstructing the oceanic ^{13}C Suess Effect. Global Biogeochem. Cy. 13, 857–872. doi:10.1029/1999GB900027

Steinfeldt, R., Rhein, M., Bullister, J.L., Tanhua, T., 2009. Inventory changes in anthropogenic carbon from 1997–2003 in the Atlantic Ocean between 20°S and 65°N. Global Biogeochem. Cy. 23, GB3010. doi:10.1029/2008GB003311

Stendardo, I., Kieke, D., Rhein, M., Gruber, N., Steinfeldt, R., 2015. Interannual to decadal oxygen variability in the mid-depth water masses of the eastern North Atlantic. Deep-Sea Res. Pt I 95, 85–98. doi:10.1016/j.dsr.2014.10.009

Strom, S.L., Bright, K.J., 2009. Inter-strain differences in nitrogen use by the coccolithophore *Emiliania huxleyi*, and consequences for predation by a planktonic ciliate. Harmful Algae 8, 811–816. doi:10.1016/j.hal.2007.10.005

Strong, A., Chisholm, S., Miller, C., Cullen, J., 2009. Ocean fertilization: time to move on. Nature 461, 347–348. doi:10.1038/461347a

Sun, Q., Tang, D., Wang, S., 2012. Remote-sensing observations relevant to ocean acidification. Int. J. Remote Sens. 33, 7542–7558. doi:10.1080/01431161.2012.685978

Suzuki, T., Ishii, M., Aoyama, M., Christian, J.R., Enyo, K., Kawano, T., Key, R.M., Kosugi, N., Kozyr, A., Miller, L.A., Murata, A., Nakano, T., Ono, T., Saino, T., Sasaki, K., Sasano, D., Takatani, Y., Wakita, M., Sabine, C., 2013. PACIFICA Data Synthesis Project. ORNL/CDIAC-159, NDP-092. Carbon Dioxide Information Analysis Center, Oak Ridge National Laboratory, U.S. Department of Energy, Oak Ridge, TN, USA. doi:10.3334/CDIAC/OTG.PACIFICA_NDP092

Takahashi, T., Sutherland, S.C., Chipman, D.W., Goddard, J.G., Ho, C., Newberger, T., Sweeney, C., Munro, D.R., 2014a. Climatological distributions of pH, pCO_2, total CO_2, alkalinity, and $CaCO_3$ saturation in the global surface ocean, and temporal changes at selected locations. Mar. Chem. 164, 95–125. doi:10.1016/j.marchem.2014.06.004

Takahashi, T., Sutherland, S.C., Kozyr, A., 2014b. Global Ocean Surface Water Partial Pressure of CO_2 Database: Measurements Performed During 1957-2013 (Version 2013). ORNL/CDIAC-160, NPD-088(V2013). Carbon Dioxide Information Analysis Center, Oak Ridge National Laboratory, U.S. Department of Energy, Oak Ridge, TN, USA.

Takahashi, T., Sutherland, S.C., Wanninkhof, R., Sweeney, C., Feely, R.A., Chipman, D.W., Hales, B., Friederich, G., Chavez, F., Sabine, C., Watson, A., Bakker, D.C.E., Schuster, U., Metzl, N., Yoshikawa-Inoue, H., Ishii, M., Midorikawa, T., Nojiri, Y., Körtzinger, A., Steinhoff, T., Hoppema, M., Olafsson, J., Arnarson, T.S., Tilbrook, B., Johannessen, T., Olsen, A., Bellerby, R., Wong, C.S., Delille, B., Bates, N.R., de Baar, H.J.W., 2009. Climatological mean and decadal change in surface ocean pCO_2, and net sea–air CO_2 flux over the global oceans. Deep-Sea Res. Pt II 56, 554–577. doi:10.1016/j.dsr2.2008.12.009

Tanhua, T., 2010. MATLAB Toolbox to perform secondary quality control on hydrographic data. ORNL/CDIAC-158. Carbon Dioxide Information Analysis Center, Oak Ridge National Laboratory, U.S. Department of Energy, Oak Ridge, TN, USA. doi:10.3334/CDIAC/otg.CDIAC_158

Tanhua, T., Körtzinger, A., Friis, K., Waugh, D.W., Wallace, D.W.R., 2007. An estimate of anthropogenic CO_2 inventory from decadal changes in oceanic carbon content. Proc. Natl. Acad. Sci. U.S.A. 104, 3037 –3042. doi:10.1073/pnas.0606574104

Tanhua, T., van Heuven, S., Key, R.M., Velo, A., Olsen, A., Schirnick, C., 2010. Quality control procedures and methods of the CARINA database. Earth Syst. Sci. Data 2, 35–49. doi:10.5194/essd-2-35-2010

Tanhua, T., Wallace, D.W.R., 2005. Consistency of TTO-NAS inorganic carbon data with modern measurements. Geophys. Res. Lett. 32, L14618. doi:10.1029/2005GL023248

Taylor, J.K., Smith, S.W., 1959. Precise Coulometric Titration of Acids and Bases. J. Res. Natl. Bur. Stand. 63A, 153–159.

Taylor, K.E., Stouffer, R.J., Meehl, G.A., 2011. An Overview of CMIP5 and the Experiment Design. Bull. Amer. Meteor. Soc. 93, 485–498. doi:10.1175/BAMS-D-11-00094.1

Thacker, W.C., 2012. Regression-based estimates of the rate of accumulation of anthropogenic CO_2 in the ocean: A fresh look. Mar. Chem. 132–133, 44–55. doi:10.1016/j.marchem.2012.02.004

Thomas, H., Prowe, A.E.F., Lima, I.D., Doney, S.C., Wanninkhof, R., Greatbatch, R.J., Schuster, U., Corbière, A., 2008. Changes in the North Atlantic Oscillation influence CO_2 uptake in the North Atlantic over the past 2 decades. Global Biogeochem. Cy. 22, GB4027. doi:200810.1029/2007GB003167

Thompson, M., Howarth, R.J., 1973. The rapid estimation and control of precision by duplicate determinations. Analyst 98, 153–160. doi:10.1039/AN9739800153

Tjiputra, J.F., Olsen, A., Bopp, L., Lenton, A., Pfeil, B., Roy, T., Segschneider, J., Totterdell, I., Heinze, C., 2014. Long-term surface pCO_2 trends from observations and models. Tellus B 66, 23083. doi:10.3402/tellusb.v66.23083

Van Heuven, S., Pierrot, D., Rae, J.W.B., Lewis, E., Wallace, D.W.R., 2011. CO_2SYS v 1.1, MATLAB program developed for CO_2 system calculations. ORNL/CDIAC-105b. Carbon Dioxide Information Analysis Center, Oak Ridge National Laboratory, U.S. Department of Energy, Oak Ridge, TN, USA.

Vázquez-Rodríguez, M., Pérez, F.F., Velo, A., Ríos, A.F., Mercier, H., 2012. Observed acidification trends in North Atlantic water masses. Biogeosciences 9, 5217–5230. doi:10.5194/bg-9-5217-2012

Vázquez-Rodríguez, M., Touratier, F., Lo Monaco, C., Waugh, D.W., Padin, X.A., Bellerby, R.G.J., Goyet, C., Metzl, N., Ríos, A.F., Pérez, F.F., 2009. Anthropogenic carbon distributions in the Atlantic Ocean: data-based estimates from the Arctic to the Antarctic. Biogeosciences 6, 439–451. doi:10.5194/bg-6-439-2009

Wallace, D.W.R., 1995. Monitoring Global Ocean Carbon Inventories. OOSDP, Texas A & M University, College Station, TX.

Wang, X., Christian, J.R., Murtugudde, R., Busalacchi, A.J., 2006. Spatial and temporal variability of the surface water pCO_2 and air-sea CO_2 flux in the equatorial Pacific during 1980–2003: A basin-scale carbon cycle model. J. Geophys. Res. 111. doi:10.1029/2005JC002972

Wanninkhof, R., 1992. Relationship Between Wind Speed and Gas Exchange Over the Ocean. J. Geophys. Res. 97, 7373–7382. doi:10.1029/92JC00188

Warner, T.B., 1971. Normal fluoride content of seawater. Deep-Sea Res. 18, 1255–1263. doi:10.1016/0011-7471(71)90030-1

Waters, J.F., Millero, F.J., 2013. The free proton concentration scale for seawater pH. Mar. Chem. 149, 8–22. doi:10.1016/j.marchem.2012.11.003

Waugh, D.W., Hall, T.M., McNeil, B.I., Key, R., Matear, R.J., 2006. Anthropogenic CO_2 in the oceans estimated using transit time distributions. Tellus B 58, 376–389. doi:10.1111/j.1600-0889.2006.00222.x

Weiss, R.F., 1974. Carbon dioxide in water and seawater: the solubility of a non-ideal gas. Mar. Chem. 2, 203–215. doi:10.1016/0304-4203(74)90015-2

Winter, A., Jordan, R.W., Roth, P.H., 1994. Biogeography of living coccolithophores in ocean waters, in: Coccolithophores. Cambridge University Press, pp. 161–177.

Wolf-Gladrow, D.A., Zeebe, R.E., Klaas, C., Körtzinger, A., Dickson, A.G., 2007. Total alkalinity: The explicit conservative expression and its application to biogeochemical processes. Mar. Chem. 106, 287–300. doi:10.1016/j.marchem.2007.01.006

Wu, Z., Huang, N.E., Wallace, J.M., Smoliak, B.V., Chen, X., 2011. On the time-varying trend in global-mean surface temperature. Clim. Dyn. 37, 759–773. doi:10.1007/s00382-011-1128-8

Yashayaev, I., van Aken, H.M., Holliday, N.P., Bersch, M., 2007. Transformation of the Labrador Sea Water in the subpolar North Atlantic. Geophys. Res. Lett. 34, L22605. doi:10.1029/2007GL031812

Yool, A., Popova, E.E., Anderson, T.R., 2013a. MEDUSA-2.0: an intermediate complexity biogeochemical model of the marine carbon cycle for climate change and ocean acidification studies. Geosci. Model Dev. 6, 1767–1811. doi:10.5194/gmd-6-1767-2013

Yool, A., Popova, E.E., Coward, A.C., Bernie, D., Anderson, T.R., 2013b. Climate change and ocean acidification impacts on lower trophic levels and the export of organic carbon to the deep ocean. Biogeosciences 10, 5831–5854. doi:10.5194/bg-10-5831-2013

Young, J., Geisen, M., Cros, L., Kleijne, A., Sprengel, C., Probert, I., Østergaard, J., 2003. A guide to extant coccolithophore taxonomy. J. Nannoplankt. Res. Special Issue 1.

Zachos, J.C., Dickens, G.R., Zeebe, R.E., 2008. An early Cenozoic perspective on greenhouse warming and carbon-cycle dynamics. Nature 451, 279–283. doi:10.1038/nature06588

Zeebe, R.E., Wolf-Gladrow, D., 2001. CO_2 in Seawater: Equilibrium, Kinetics, Isotopes, Elsevier Oceanography Series 65. Elsevier Ltd.

Zhu, Q., Aller, R.C., Fan, Y., 2005. High-Performance Planar pH Fluorosensor for Two-Dimensional pH Measurements in Marine Sediment and Water. Environ. Sci. Technol. 39, 8906–8911. doi:10.1021/es051023m

Zondervan, I., Rost, B., Riebesell, U., 2002. Effect of CO_2 concentration on the PIC/POC ratio in the coccolithophore *Emiliania huxleyi* grown under light-limiting conditions and different daylengths. J. Exp. Mar. Biol. Ecol. 272, 55–70. doi:10.1016/S0022-0981(02)00037-0

Zondervan, I., Zeebe, R.E., Rost, B., Riebesell, U., 2001. Decreasing marine biogenic calcification: A negative feedback on rising atmospheric pCO_2. Global Biogeochem. Cy. 15, 507–516. doi:10.1029/2000GB001321